Durham University

Durham E-Theses

The Design and Use of Supramolecular Gels as Crystallisation Media

JAMES PHILIP SMITH

How to cite:

SMITH, JAMES PHILIP (2022) The Design and Use of Supramolecular Gels as Crystallisation Media. Doctoral thesis, Durham University.

Use policy

The full-text may be used and/or reproduced, and given to third parties in any format or medium, without prior permission or charge, for personal research or study, educational, or not-for-profit purposes provided that:

- a full bibliographic reference is made to the original source
- a https://etheses.durham.ac.uk/id/eprint/14316/ is made to the metadata record in Durham E-Theses
- the full-text is not changed in any way

The full-text must not be sold in any format or medium without the formal permission of the copyright holders.

Please consult the full Durham E-Theses policy for further details.

Academic Support Office, The Palatine Centre, Durham University, Stockton Road, Durham, DH1 3LE
e-mail: e-theses.admin@durham.ac.uk Tel: +44 0191 334 6107
https://etheses.durham.ac.uk

The Design and Use of Supramolecular Gels as Crystallisation Media

A thesis submitted in partial fulfilment of the requirements for the degree of *Doctor of Philosophy*.

James P. Smith

Department of Chemistry
Durham University

2021

Abstract

The solid-state of pharmaceuticals is a critical area of research for pharmaceuticals companies, primarily due to the impact the solid form can have on the physicochemical properties of a drug. Some of these forms can be challenging to isolate experimentally, thus new techniques to screen for unidentified forms and to control crystallisation outcomes are required to reduce the risk of forms being identified late in product development. This work focuses on the design and use of supramolecular gels to crystallise pharmaceutical compounds and attempt to control the crystallisation outcomes. The work builds on previous studies by the Steed group.

Chapter One focuses on the design of bis(urea) supramolecular gels using a 4,4-methylenebis(2,6-diethylphenyl) spacer group, which has previously been the core structure of numerous versatile molecular gelators, with the aim to build on our understanding of the structural factors that may promote or prevent gelation for this system. A methodical stepwise approach to crystallise these gelators successfully yielded the first reported crystal structure of a bis(urea) derived from the 4,4-methylenebis(2,6-diethylphenyl) spacer, providing valuable insight to the molecular conformation and intermolecular interactions formed. The findings corroborate the results of previous computational crystal structure prediction studies on gelators derived from the 4,4-methylenebis(2,6-diethylphenyl) spacer.

A further study investigates the development and use of API-mimetic supramolecular gelators as crystallisation media for two polymorphic AstraZeneca active compounds (AZD-6140 and AZD-2281) to influence the crystallisation outcomes. Whilst a new nitrobenzene solvated of AZD-2281 is reported, the gels failed to influence crystal factors, such as the polymorphic form, crystal habit or size. This is despite an extensive screening procedure using a wide range of solvents and gelator/substrate concentration ratios. An initial proof of concept is also reported to demonstrate the gelation capability of free and pinacol protected boronic acid gelators. This provides the foundations for further work to investigate whole molecule API-mimicking gelators by exploiting reversible covalent bond formation between diol groups and boronic acid functionalities.

The final two studies investigate the self-assembly behaviour of novel bis(acyl-semicarbazide) compounds. A series of aliphatic and aromatically spaced bis(acyl-

semicarbazides) with chiral 1-R-phenylethyl/1-S-phenyl ethyl and achiral benzyl end groups are synthesised and characterised. A crystallisation screening of these compounds, including racemic mixtures of the pure R,R and S,S enantiomers, resulted in thirteen single crystal structures of these compounds being determined. The resulting structures provide insight to their self-assembly behaviour. The aromatic-spacer compounds exhibit dimer assembly without infinite unidirectional hydrogen bond synthons that may promote anisotropic assembly. This lack explains their poor gelation profile. Two distinct conformations (linear and folded conformations) were observed in the structures for malonyl- and succinyl-spaced compounds. The linear conformations assemble via urea α-tape synthons, which are thought to give rise to gelation behaviour. The folded conformers, which are stabilised by an intramolecular hydrogen bond, assemble into bilayer arrangements with hydrophilic cores and hydrophobic surfaces. Ultrasound is required in many solvents to induced gelation of the malonyl and succinyl-spaced compounds and this is attributed to the requirement to disrupt the intramolecular hydrogen bond and induce a conformational change. Only linear conformers and urea α-tape assembly were identified for the oxalyl- and adipic-spaced compounds with both spacers yielding highly versatile gelators. The impact of chirality on gelation behaviour is also described, with chiral compounds exhibiting superior gelation behaviour to their achiral counterparts. Racemic mixtures of R,R and S,S enantiomers also exhibit significantly reduced gelation behaviour compared to the enantiomerically pure components, likely due to enabling crystallisation in centrosymmetric space groups. The sensitivity of gels to anions were explored, with most gels undergoing a gel-sol upon the addition of trace amounts of anionic salts. However, the chiral oxalyl-spaced gelators are highly resistant to anion-disruption, maintaining gelation upon addition of up to 10 molar equivalents of anions. This was shown to be useful in the crystallisation of the salt procaine hydrochloride, with the oxalyl-based gelator the only compound able to form stable gels in the presence of the API salt and facilitate API crystallisation. The bis(acyl-semicarbazide) gels were also used to crystallise a range of pharmaceuticals to influence the crystallisation outcomes, including via an API-mimetic approach and attempts to achieve chiral resolution of chiral APIs. Whilst in most cases the crystallisation outcomes were not influenced by the presence of gel fibres, one new form of polymorphic RMOY was successfully isolated from chlorobenzene gels of chiral adipic-

spaced bis(acyl-semicarbazide) gelators.

Declaration

The work detailed in this thesis was carried out in the Department of Chemistry at Durham university between October 2016 to June 2021, under the supervision of Professor Jonathan W. Steed and Dr David Berry of Durham University and Dr James F. McCabe of AstraZeneca, Macclesfield. This work has not previously been submitted for a degree at this or any other institution.

Crystallographic data for structures **3.2f**, **4.1**$_{Rac}$, **4.2**$_{RR}$, **4.2**$_{Rac}$, **4.3**$_{SS}$, **4.6**$_{RR}$ were collected and processed by Dr Dmitry Yufit and Dr Andrei Batsanov at station I19 of the Diamond Light Source synchrotron. Dr Yufit also assisted in refining the structures of **2a**, **3.2c**, **3.2e**, **4.1**$_{RR}$, **4.3**$_{Rac}$, and **4.4**$_{SS}$. The compound RMOY was first synthesised and supplied by the Preuss Group at the University of Guelph. Solid-state NMR and 2D solution-state NMR experiments were performed by Dr David Apperly and Dr Juan Aguilar Malavia respectively. Differential Scanning Calorimetry experiments were run by Mr Douglas W. Carswell. All other results are the product of independent work and investigation by the author.

Statement of Copyright

The copyright of this thesis rests with the author. No quotation from it should be published without the author's prior written consent and information derived from it should be acknowledged.

Funding

This work was funded by the Engineering and Physical Sciences Research Council (EPSRC) and AstraZeneca.

Acknowledgements

There are a number of key colleagues and friends who have made this journey possible for me who have earned my eternal gratitude. Firstly, my supervisor Jon Steed, whose vast scientific knowledge and extraordinary ideas were an invaluable resource throughout my time in Durham. Moreover, I will always be grateful for the encouragement, support, and patience he has shown me over the last few years, especially when times were tough. I also thank Dr David Berry, who taught me many skills in pharmaceutical characterisation early on and provided much needed reassurance and advice for entering the world of 'proper chemistry' as a fellow pharmacist. I am also deeply grateful for the valuable input to this work from my industrial collaborator Dr Jim McCabe and for setting my initial assignment to explore the solid-state of two AstraZeneca compounds. I could not have completed this work without significant help from Drs Dmitry Yufit and Andrei Basantov. Their expertise and assistance in my all single-crystal X-ray diffraction work was of critical importance. I would also like to acknowledge Dr Juan Aguilar Malavia for his help in acquiring 2D-NMR data and his training in how to interpret the resulting spectra, and Leon Bowen for his support and training in electron microscopy. I am greatly appreciative to the Thompson group for free access to their rheometer. Further appreciation is shown to Gary Oswald, David Apperley and Douglas Carswell for their guidance and support with XRPD, solid-state NMR and DSC respectively.

On a personal note, my parents, Liz and Phil, and my sister, Joanna, have always been the foundations of my support, and somehow extended themselves even further to support me through this entire experience. My girlfriend Laylee has been the perfect partner to have by my side as I tackled the final stages of my PhD. Her understanding and loving nature, in addition to her fierce and unwavering belief in me, has been a huge source of positivity which I have been able to draw strength from when times were tough. My fellow past and present Steed group colleagues have my gratitude for always supporting me and sharing their experiences (both in science and in life). In particular I'd like to thank Jess, Amy, Brette, Luke and Lottie, for keeping me sane when positive results were elusive. I also attribute my 'mild' caffeine addiction to these folks and our shared coffee breaks. Finally, I wish to thank my colleagues in Global Regulatory Affairs – Vaccines at Pfizer, and in particular my line manager Dr

Matthew Marsden, for their support in helping me finish my thesis during what can best be described as a chaotic and challenging time.

Table of Contents

Chapter 1 - Introduction

1.1 Solid-state forms of pharmaceuticals

The solid form of any given compound can significantly impact its physicochemical properties, thus when developing solid-form materials, manufacturers should consider the solid-state of each component within their product. This is particularly critical for solid-dosage forms of active pharmaceutical ingredients (APIs), where the final formulation must consistently achieve a bioavailability that delivers a drug blood concentration within the therapeutic window.[1–3] These solid forms can broadly be categorised as crystalline or amorphous.

Crystalline solids exhibit long range order with molecules assembled in a three-dimensional lattice. This lattice is built up by a repetitive group of atoms known as the unit cell. Strong and regular supramolecular interactions are typically observed in crystalline forms. Sometimes, the same molecule can self-assemble into multiple distinct lattice arrangements. This is the phenomenon of polymorphism with each distinct crystal form being known as a polymorph. Polymorphs can generally be divided into two subtypes: packing and conformational polymorphs. Packing polymorphism is where the molecule adopts a near-identical conformation in both crystal forms, whilst conformational polymorphism arises when a crystallisation substrate adopts a different conformation in each form resulting in a different packing arrangement (***Figure 1-1***).[4]

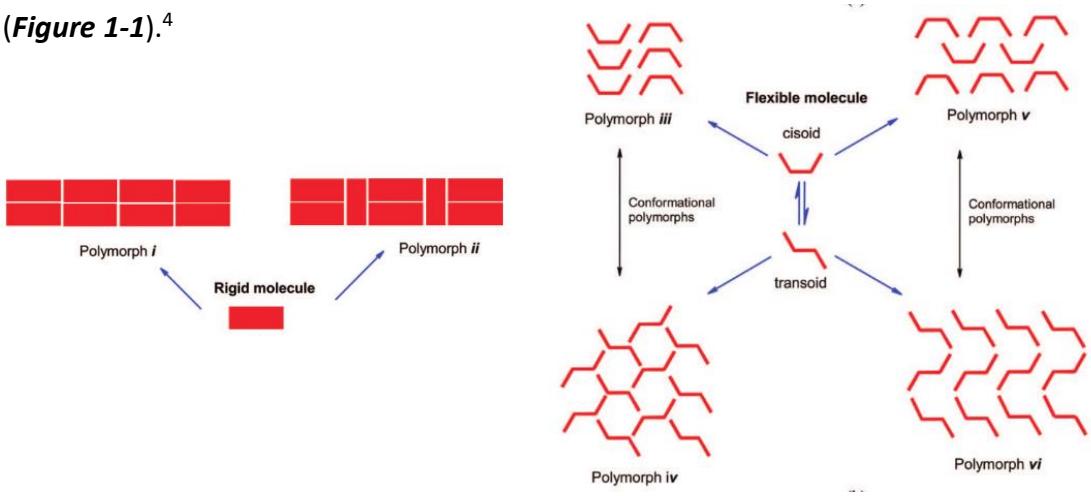

Figure 1-1. (a) Packing polymorphism occurs when the molecule maintains the same conformation in both crystal forms. **(b)** Conformational polymorphism occurs when the molecule adopts different conformation resulting in the distinct crystal lattice arrangements. Adapted from reference 4 with permission.

Despite being identical in terms of chemical composition, each polymorph can display significant difference in their physicochemical properties, including solubility, dissolution rate, chemical stability, hygroscopy, processability and melting point,[5–8] thus it is an essential consideration for a wide range of R&D industries, including agriculture, explosives, dyes and pharmaceuticals.[9,10] Each polymorph has a relative stability which is determined by its free energy. The form with the lowest free energy under given conditions is referred to as the thermodynamically stable form, whilst the other polymorphs with higher free energies are considered metastable forms. If crystal forms are close in free energy, then the likelihood of them co-existing and crystallising under identical conditions is increased.[11–15] This is known as concomitant polymorphism and can be undesirable for pharmaceutical manufacturers where isolating a pure single form may be critical to ensure product stability and performance.[10] There are also numerous reports of disappearing polymorphs, whereby a new crystal form has been identified, but attempts to yield the polymorph from subsequent crystallisation experiments using the same experimental conditions are unsuccessful.[14,16,17] The 'disappearance' of these forms is often attributed to the unintentional seeding with microscopic seeds of a more thermodynamically stable form. Disappearing polymorph also pose a serious issue for manufacturers, particularly from an intellectual property perspective, and much time and resource, including the development of inventive procedures, may be required to recrystallise and characterise the vanished metastable form.

When the API molecules contains an ionizable basic or acidic functionality they can be formulated as a multicomponent crystalline form known as a salt. In salts, the API acid or basic group is ionised and interacts with a counterion of the opposite charge. Hydrochloride salts are most used for basic drugs, whilst sodium is the most common counterion used for acid drug salts. Pharmaceutical salt selection has classically been utilised for resolving the low aqueous solubility of APIs.[18] There is also growing interest in neutral multi-component crystals. These are referred to as solvates when one component is a solvent or hydrates if that solvent is water.[19] If neither component is a solvent, they are referred to as a co-crystal. There has been growing interest in co-crystals over the past decade, with numerous licensed formulations of APIs now available on the market and many more co-crystal forms patented and in development for commercial use.[20] This has partly been driven by the emergence of crystal

engineering and a growing understanding of common supramolecular interactions.[21] Like salts, co-crystals can significantly improve the physicochemical properties of the compounds, in particular the solubility and bioavailability.[22] Unlike salts, they do not require an ionizable functionality within the drug molecule. The classification of multicomponent crystalline systems has been slightly ambiguous over the past decade, but a widely accepted classification system has now been proposed by Grothe *et al.* (***Figure 1-2***).[23] Whilst pharmaceutical patents on co-crystals have been rarely observed, they are expected to increase drastically due to advancements and clarifications in the regulatory requirements from world leading regulatory agencies such as the Food and Drugs Administration (FDA) and European Medicines Agency (EMA).[24–26] Specifically, it has been confirmed that co-crystals of marketed APIs can be filed under the same abridged Marketing Authorisation Application pathways as generic medicines, providing they do not have an inferior efficacy or safety profile. These expedited approval pathways to market further increase the attractiveness of co-crystal formulations.

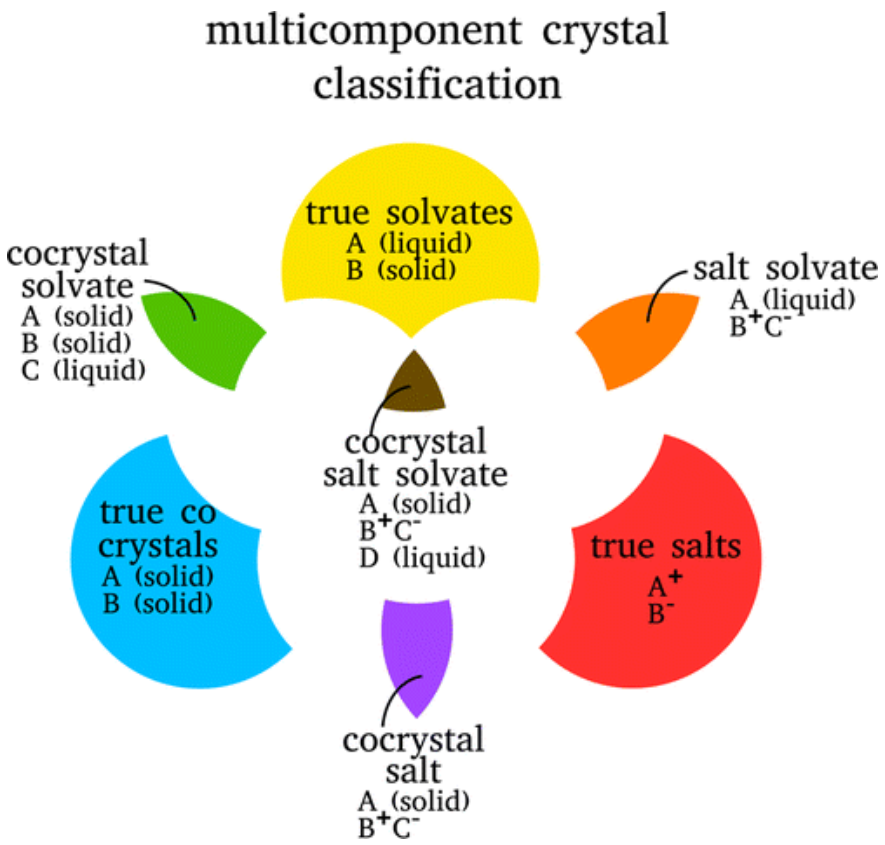

Figure 1-2. The proposed classification system for multicomponent crystals as proposed by Grothe *et al*. This classification system was inspired by Aitipamula *et al.*, who raised concerns regarding FDA classifications of multi-component crystals. Adapted from reference 23 with permission.

In contrast to crystalline forms, in the amorphous state there is a lack of structural or long-range order with relatively weak or few intermolecular interactions between neighbouring molecules. This low propensity of strong intermolecular interactions means amorphous forms are typically more soluble than crystalline forms, making them attractive options for applications where high solubility is desirable. However, the lack of long-range order also means that amorphous forms are less thermodynamically stable than crystalline forms and they can tend to crystallise over time. Thus, amorphous forms commonly need to be stabilised with a polymer or small molecule additive(s).[27,28] The basis of these stabilization methods is to keep the API molecules separated and restrict their aggregation.

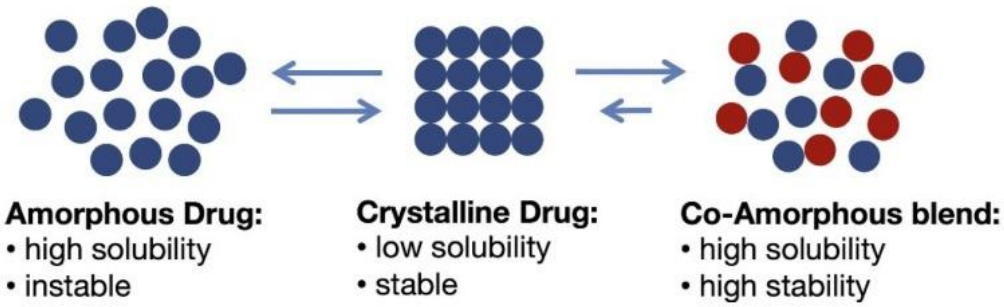

Figure 1-3. The instability of amorphous forms and low solubility of crystalline drug may be overcome by producing co-amorphous blends. Adapted from reference 28 with permission.

There are now various licensed medicines with APIs formulated in the amorphous state,[29,30] although it is worth noting that the U.S Food and Drug Administration classify the amorphous state of a drug the same as crystalline polymorphs. It is likely many more amorphous formulations will be developed in the futures due to the enhanced solubility that the amorphous state offers, particularly as API molecules are generally increasing in size and thus decreasing in aqueous solubility. However, it is still the case that most licensed solid-dosage forms contain API in a crystalline form and there is still a great need to develop robust crystallisation screening procedures to ensure the form with the most favourable physicochemical properties is identified and selected for development.

1.2 Crystallisation and polymorphism

Crystallisation is a self-assembly process that occurs under non-equilibrium conditions consisting of two main steps; nucleation and crystal growth. Nucleation is the initial step, whereby solute molecules initially aggregate into microscopic ordered lattices called nuclei. Nucleation can occur when there are no existing crystals in the solution (primary nucleation) or when crystalline seeds are present in solution (secondary nucleation). Secondary nucleation, also known as homogenous seeding, is commonly utilised in industries to control and expedite the crystallisation process.[31] Primary nucleation can be divided further into homogenous and heterogenous nucleation.[32] Homogenous nucleation is where nuclei form in the absence of any other particulates and is energetically unfavourable due to the large energetic barrier to generating a new phase. Heterogenous nucleation occurs when a solid phase already exists in the system in the form of foreign particulates. This lowers the energy barrier to nucleation, as a new solid phase does not need to be formed, which consequently accelerates the nucleation process. Homogenous nucleation is thought to occur very rarely in reality, with heterogenous nucleation nearly always attributed as the source of primary nucleation.[33]

The exact mechanisms of nucleation are complex and not fully understood. Classical nucleation theory states that the molecules in solution start to assemble into ordered clusters via a one-step process until the nuclei grow above a critical size.[34] At this point, macroscopic crystal growth occurs, whereby substrate molecules from solution are adsorbed to the surface of the growing crystal to form additional lattice layers. If nuclei fail to reach the critical size, they redissolve into solution. Unlike nucleation, the crystal growth phase is energetically favourable as the increase in crystal size reduces the interfacial energy between solid crystalline phase and solution.[35] Whilst classical nucleation theory provides an approximate description of the nucleation process, it is limited when used to predict or calculate nucleation rates and critical sizes. This is due to a number of assumptions, including that all nuclei are spherical and that molecules are incorporated sequentially rather than multiple molecules being incorporated in parallel.[36] A two-step nucleation theory is largely considered to provide a more accurate account of nucleation and is supported by computational models and experimental observations.[37] The two-step model proposes that molecules initially

aggregate to form highly concentrated colloidal particulates with less order than that proposed in classical nucleation theory.[38–40] The molecules in these particulates then slowly rearrange to form a highly ordered nuclei (**Figure 1-4**).

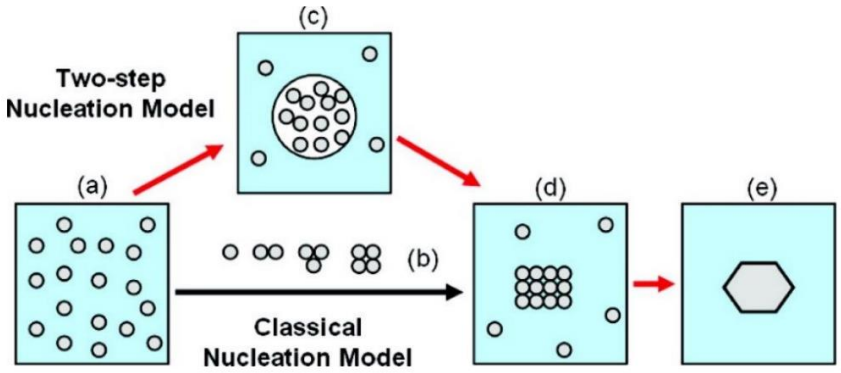

Figure 1-4. A schematic to show the classical and two-step nucleation pathways. **(a)** The start point for both theories is a supersaturated solution. **(b)** In classical nucleation theory, solute molecules aggregate to form highly ordered clusters below the critical nuclei size. These clusters continue to grow until they reach the critical nuclei size. **(c)** In the two-step model, high local concentrations of solute initially result in the formation of colloidal clusters, which then slowly rearrange to form highly ordered nuclei above the critical size. Once nuclei surpass r_{crit} **(d)** then energetically favourable macroscopic crystal growth can occur **(e)**. Adapted from reference 40.

As mentioned in section 1.1, each polymorphic form has a relative stability which is defined by the associated free energy. Ostwald's step rule states that most commonly metastable polymorphs crystallise before thermodynamically stable forms.[41] This is because metastable forms are generally significantly closer in energy to the solution phase than the thermodynamically stable form is. Instead, the thermodynamically stable form is obtained via a series of metastable forms, with each dissolving and recrystallising into the next most stable form to minimises changes in free energy. This cycle is repeated until the thermodynamically stable form is crystallised and observations of this behaviour has often been reported in the literature.[42–45] The practical implication of this theory is it should be possible to isolate each kinetic form by slightly varying the kinetic conditions of the system. However, Ostwald's rule is not definite and serves more as a guideline for what is expected. Indeed, there are reports of the Ostwald stages purposefully being 'leapfrogged'.[46,47] Metastable forms in the solid-state are also energetically driven to transform into the thermodynamically stable form over time.[48–50] Transformations to more stable forms can be extremely slow, and often metastable forms can be highly stable under ambient conditions.

External factors such as temperature, pressure and humidity often have a significant impact on the solid-solid transition rate.[51,52]

Interestingly the thermodynamic relationship between two polymorphs can be either monotropic or enantiotropic. A monotropic relationship exists if one form is more stable than the other under all conditions, regardless of external factors such as temperature, pressure or solute concentration. In practical terms this means that the transformation from the higher energy form to the lower energy form is essentially an irreversible process. Meanwhile, in an enantiotropic relationship, certain conditions exists at which the stability order of the two forms inverts and the possibility of reversible transitions between the two forms arises through alteration of the external conditions (**Figure 1-5**).[53,54] The conditions at which the order of stability inverts is known as the transition point, and is commonly either a specific temperature or pressure. If the conditions are kept at the transition point, the two forms would be expected to co-exist. Surpassing the transition point does not typically result in an immediate transition from one form to the other. Indeed, measurable levels of transformation may not be observable until the system is pushed further away from the transition point.[48]

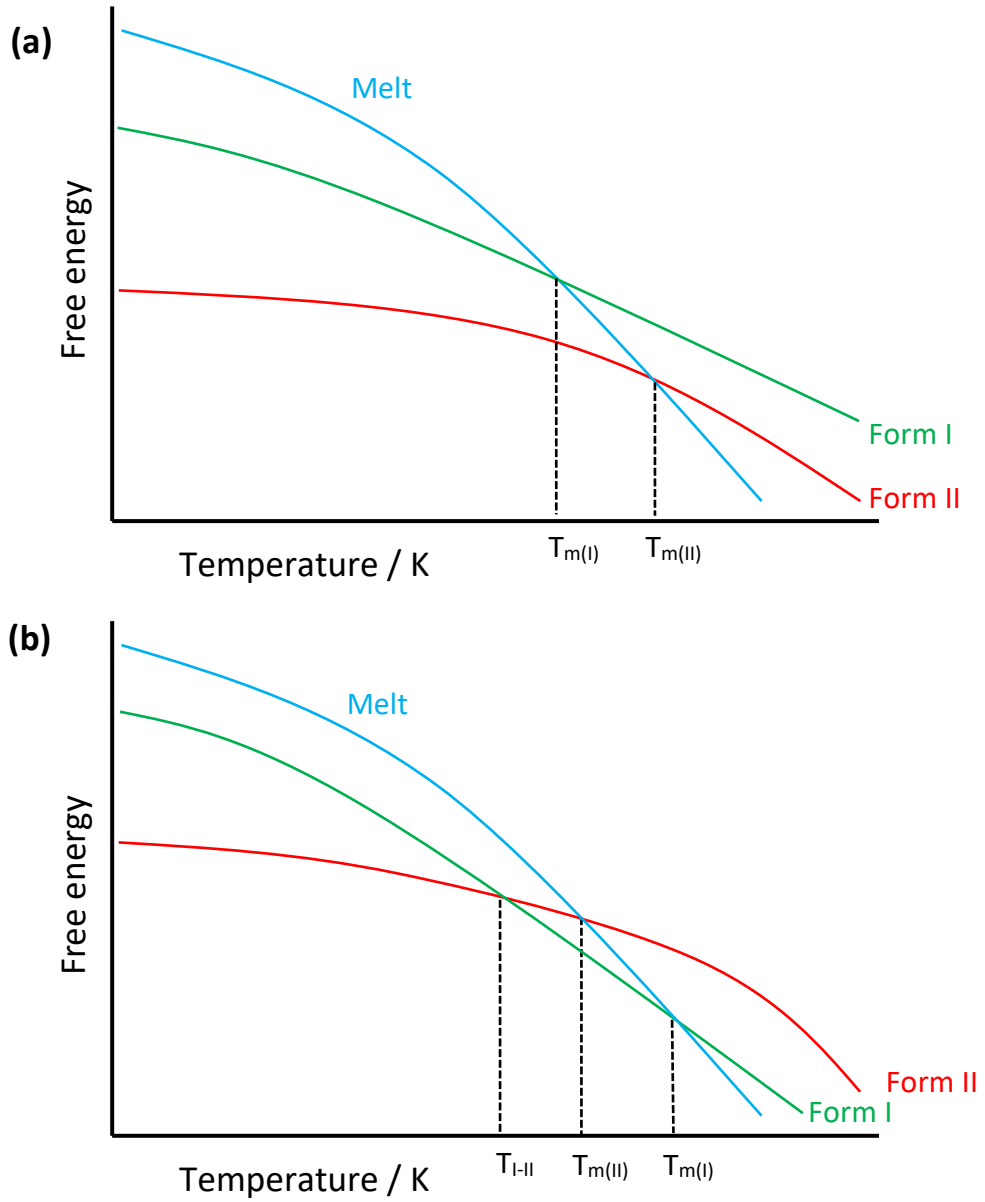

Figure 1-5. (a) A plot of free energy vs temperature for polymorphs I and II in a monotropic system. Form II has a lower relative free energy than form I, and therefore is the thermodynamically stable form, across all temperatures up to the respective melt points (T_m). **(b)** A plot of the free energy vs temperature for forms I and II for an enantiotropic system. Form II is the thermodynamically stable form at temperatures below the solid-state transition temperature (T_{I-II}) and form I is the thermodynamically stable form above this transition temperature. At the transition point, the barrier to nucleation may still be high, and a measurable transition from one form to the other may only be measurable at points further away from T_{I-II}.

The relative stability of polymorphs can often be established experimentally through slurry experiments, whereby a mixture of two or more polymorphs of the API are mixed in a minimal volume of an inert solvent over time.[55] Over time the composition of the mixture should change with an increase in the more stable form and a decrease in the amount of metastable forms. This is due to the higher solubility of the metastable forms, which results in the metastable crystals dissolving more rapidly than

the stable form until the solvent is supersaturated. This is then followed by recrystallisation as the more stable form due to seeding.

Crystallization conditions may be described as thermodynamic or kinetic. Thermodynamic conditions are those that are close to equilibrium, such as low degree of supersaturation. This results in relatively few nuclei forming and maturing via Ostwald ripening, which can eventually grow into large single crystals of the thermodynamically stable form. Examples of crystallisation methods that may achieve thermodynamic conditions include slow cooling or evaporation experiments, where the solution can be kept near the border between supersaturation and saturation for extended periods of time. Kinetic conditions are those where the system is far from equilibrium, which increases the rate of nucleation and can leapfrog the Ostwald ripening process. They typically result in the formation of many smaller crystals of metastable forms.[56] Techniques used to achieve kinetic crystallisation conditions include using solutions with high degrees of supersaturation, or inducing sudden changes to the system, for example crash cooling solutions (or melts) or sublimation via rapid heating.[57] In the pharmaceutical industry, using a wide range of crystallisation conditions and techniques is critical in order to increase the chances of identifying and characterising as many polymorphic forms as possible.

1.3 Solid-state characterisation of APIs

The solid-state of pharmaceuticals can be characterised using a wide range of techniques. The most widely used is x-ray powder diffraction (XRPD), which provides a 'fingerprint' of diffraction peaks which are unique to any given crystal form and can be used to distinguish between polymorphs, co-crystals, salts and solvates.[58–62] This non-destructive technique can also be used to quantify the crystallinity and composition of mixtures, which is particularly useful when investigating concomitant crystal forms or pharmaceutical blends.[63] XRPD experiments are generally relatively short, although exposure times may be extended for samples with low crystallinity and weak diffraction. Furthermore, some instruments can be used to run experiments at various temperatures and pressures, enabling forms that are stable under more extreme conditions to be characterised and may also aid identification of phase transitions.[64] There are very few limitations of XRPD, thus it is universally applied to characterise the solid-state of APIs. However, single crystal x-ray diffraction (SCXRD) remains the gold

standard for the characterisation of crystalline forms as it can be used to determine the structure of the three-dimensional crystal lattice, the conformation of the molecules and the key intermolecular interactions driving self-assembly. Whilst highly desirable, structure determination via SCXRD can be challenging due to the requirement for diffraction-quality single crystals, which can be difficult to obtain, particularly for metastable forms.[61,65,66] Methods for determining and refining crystal structures from powder diffraction data have been developed, but are yet to be a standard process generally due to the requirement for high-quality synchrotron diffraction data.[67]

The molecular environment in solid forms, including the nature of supramolecular intermolecular interactions, can be probed through non-destructive spectroscopic techniques, such as infrared (IR) and Raman. They can be particularly useful for observing API salt disproportionation within pharmaceutical blends or formulations.[68–70] Their use in distinguishing between polymorphic forms can be hindered by low resolution when the spectra of two forms seem closely matched. However if two polymorphs do produce distinct spectra, then they can be used to monitor and quantify the crystal forms present in a pharmaceutical blend throughout the manufacturing process and under different storage conditions.[71–75] One benefit of these methods is that they can often be used to take measurements *in-situ* by using probes, which enables the kinetics of solid-state transitions to be closely monitored throughout pharmaceutical processes.[50,76–79] They can even be used to control crystallisation of APIs by detecting the presence of undesirable polymorphs and providing signal feedback to adjust crystallisation conditions.[80] Raman spectroscopy can be particularly useful when looking at hydrated forms or the effects of humidity on solid phase due to water being 'Raman inactive'.[81]

Another widely used technique to detect and characterise polymorphism is solid-state NMR (ss-NMR), primarily ^{13}C ss-NMR. These NMR methods can be used to quantify polymorph composition both within formulations[82,83] and can be used to solve problems not easily resolved through diffraction techniques, for example identifying cases of dynamic disorder.[84] A disadvantage of ss-NMR is the requirement for relatively large amounts of material compared to the other solid-state characterisation techniques. This can particularly be an issue in early-stage development where the API may be extremely limited. Furthermore, it typically has a lower sensitivity compared

with Raman and IR spectroscopy for identifying trace amounts of a polymorphic form in mixtures.[58,85–87]

Thermoanalytical methods are also widely used to establish the relative stability and transitional behaviour of polymorphic forms. Differential scanning calorimetry (DSC) can be used to identify form transitions, such as melting, desolvation, polymorph transformations and glass transitions, and is widely relied upon to establish polymorph thermodynamic stabilities and behaviour.[88] The method works by measuring the power required to heat the sample against a reference and plotting the difference as a function of temperature. The utility of DSC using standard heating rates may be limited in incidences where thermal events overlap one another, for example if one lower-melting polymorph melts then recrystallizes into a new form which concurrently melts.[89] This prevents establishment of polymorphic purity via DSC and makes accurate determination of thermodynamic values, such as enthalpy of melting, impossible. Increasing the rate of heating by high-speed DSC may improve the results by inhibiting the recrystallization of a new form, thus preventing a concomitant melting endotherms.[90,91]

Hot-stage microscopy can be used to further validate observations from DSC/TGA and to produce samples of polymorphs that transition at various temperatures.[92,93] The technique also enables optical characterisation of the crystalline form, providing information on the crystal habit, dimensions, desolvation and degree of crystallinity.[94] Furthermore, it can be used to screen for co-crystals through the Kofler mixed fusion method.[95,96] In this method, the component with the highest melting point is melted and allowed to recrystallise on a slide, before the second component is melted to form an interface which solubilises the first component to form a eutectic phase. This then can recrystallise to give a region of solid co-crystalline phase.

1.4 Key examples of polymorphic APIs

Cases of polymorphism in APIs are common and frequently identified for two predominant reasons. The first is neatly summarised by the American microscopist Walter McCrone, who famously stated that “every compound has different polymorphic forms and that, in general, the number of forms known for a given compound is proportional to the time and money spent in research on that

compound".[97] Although the idea that every crystalline substance is polymorphic has faced growing skepticism over the years, the latter point remains true in that the more money and time spent researching a compound generally results in more crystalline forms being identified. In particular, pharmaceutical companies extensively screen for crystal forms of novel APIs to ensure that the thermodynamically form has been identified, avoiding any unwelcome form changes that may sabotage therapeutic performance whilst also meeting global regulatory requirements.[98] Additionally, each polymorph is potentially a patentable invention, as demonstrated by the case of Ranitidine,[99] thus pharmaceutical companies expend time and resources screening for potential forms in order to extend or protect market exclusivity status. The second reason for the high number of identified cases of polymorphism in APIs is due to the generally flexible nature of the molecules, with API molecules exhibiting 5.6 rotatable bonds on average, which increases the potential for conformational polymorphs.[100]

The vast research into the solid-state of pharmaceuticals has unveiled numerous key examples of the significant impact that polymorphism can have on physicochemical properties and the performance of API formulations. A classic example of this is the pro-drug chloramphenicol palmitate (compound **1.1**). This antibacterial agent is known to have 3 polymorphic forms; form A is the thermodynamically stable form, with form B being metastable and form C being unstable at room temperature.[101] In order to be activated, chloramphenicol palmitate must be hydrolysed by intestinal esterases, with the extent of hydrolysis dependent upon the dissolution rate and API aqueous solubility.[102] Form A exhibits poor aqueous solubility, thus enzymatic hydrolysis cannot occur to a significant extent and form A is considered biologically inactive when administered orally. Form B has a much greater solubility and thus undergoes a higher extent of hydrolysis, achieving a 7-fold increase in serum chloramphenicol concentrations compared with form A.[103] Hence, there is a 10% limit of Form A permitted in licensed oral formulations enforced by regulatory agencies.

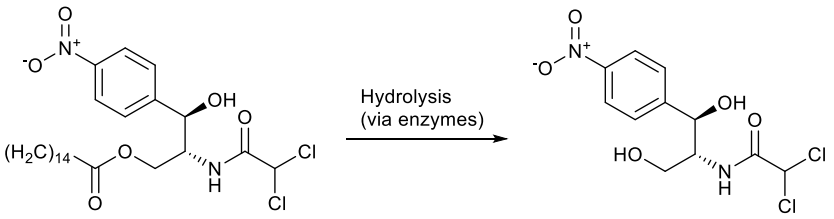

1.1 **1.2**

Figure 1-6. In vivo enzymatic hydrolysis of the pro-drug chloramphenicol palmitate (**1.1**) generates the biologically active chloramphenicol (**1.2**). The extent of hydrolysis is largely determined by the aqeuous solubibility of chloramphenicol palmitate, which is significantly affected by the polymorphic form.

The most notorious example of API polymorphism is arguably provided by the HIV protease inhibitor Ritonavir (compound **1.3**).[104] When introduced to the market in 1996, only one crystal form of ritonavir (form I) had been identified and control of crystal form was not a regulatory requirement due to being marketed in an oral liquid and a semi-solid capsule formulation.

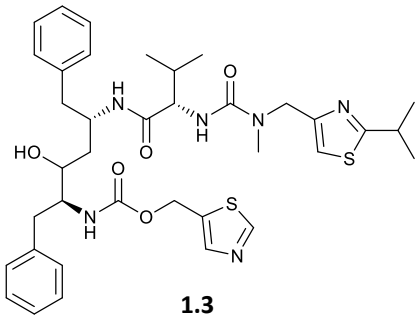

1.3

A previously unidentified form of ritonavir (form II) was observed as precipitate in semi-solid capsule formulations after they started to fail batch tests. It was found that form II is 50 % less soluble that form I, which resulted in a significantly reduced bioavailability. Structural analysis of forms I and II uncovered a conformational difference between the two forms, chiefly due to form I adopting a trans configuration about the carbamate torsion angle, whilst form II assumes a cis configuration.[105,106] Investigations found that form II is challenging to crystallise due to the cis-conformer being energetically unfavourable in solution. However, in the solid-state the *cis* conformer in form II is stabilised by $R_2^2(9)$ hydrogen bond synthons, whereby the alcohol group acts as both hydrogen donor and acceptor giving rise to a synergistic effect enhancing the hydrogen bonding (**Figure 1-7**). Furthermore, form I rapidly transitions into the thermodynamically stable form II when seeded with trace amounts of Form II. In the manufacturing process, a cis-cyclic carbamate impurity present in the bulk ritonavir product was identified as a heterogenous seed for the crystallisation of

form II which consequently results in crystals of form I transforming into crystals of form II.

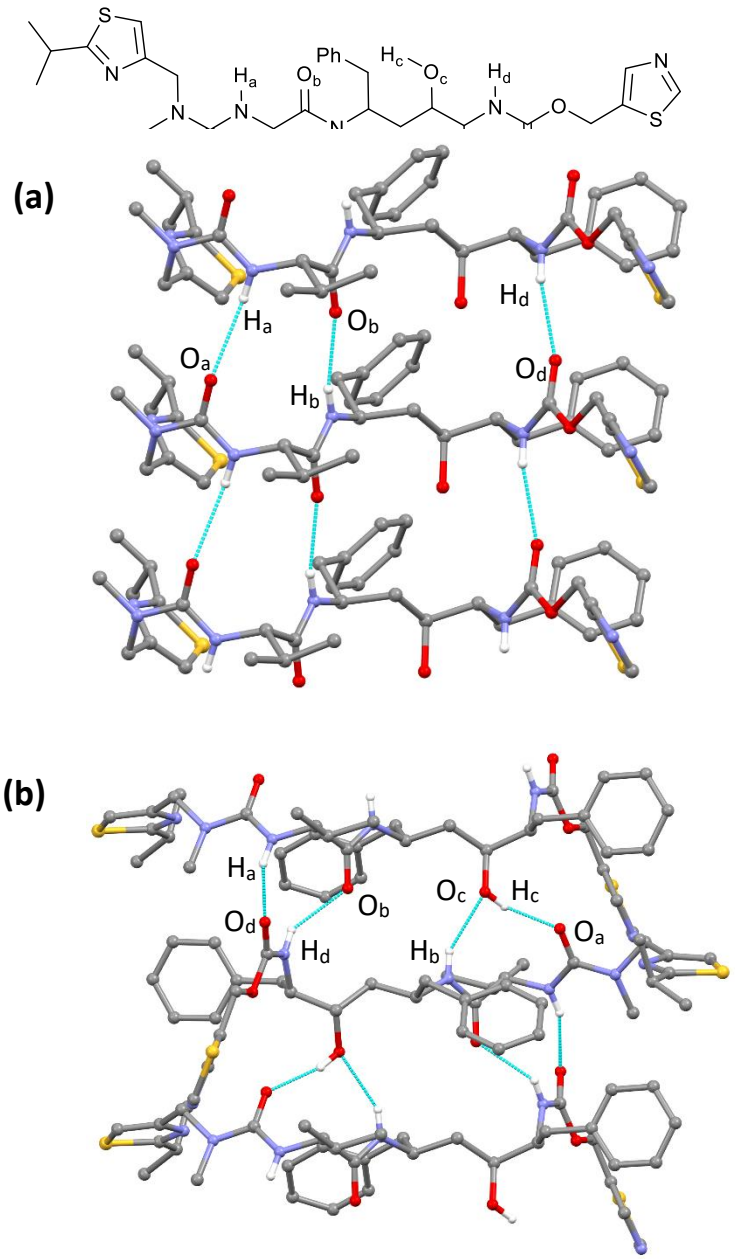

Figure 1-7. The hydrogen bond networks in **(a)** form I and **(b)** form II of Ritonavir. In form II the hydroxyl group acts as both a hydrogen bond donor and acceptor, and this interaction is largely attributed with the improved stability of the cis-conformer in the solid state compared with when in solution. The hydrogen bond donors and acceptors have been labelled according to the scheme above for clarity.

The manufacturers could no longer guarantee stability the formulations over the product shelf life, leading to the withdrawal of both products from the market for 2 years whilst a new amorphous formulation was devised.[107,108] Later studies also identified a further three crystal forms of ritonavir, including a metastable polymorph, a hydrate and a formamide solvate.[109] The ritonavir case enforced reforms in the

regulatory considerations for solid state formulations, and highlights the need for exhaustive form screening in early stage development.[12,110]

A similar case was reported with the anti-Parkinson's drug, rotigotine (compound **1.4**). Rotigotine has been a known chemical entity since the mid-1980s and marketed in 2006 as 'Neupro' transdermal patches, having been filed as a monomorphic compound. However, in 2008 a novel form (form II) of rotigotine precipitated from formulations after storage at 40°C for a minimum of 10 days (**Figure *1-8***).[111] Form II has an higher stability and lower solubility compared with form I, which significantly reduces transdermal drug delivery and causes rotigotine to crystallise from the patches. Form I was confirmed as a metastable form and a monotropic relationship has been established between form I and form II. The European Medicines Agency (EMA) ruled that manufacturers must withdraw the formulation from the market and reformulate the drug, despite conversion from form I to form II appearing to be slow under ambient conditions. Later analysis of form I identified that the molecules had assumed a curious conformation which should have provoked further research into crystal form in early phase development, demonstrating the benefit of in silico prediction tools and thorough experimental form screening.[112]

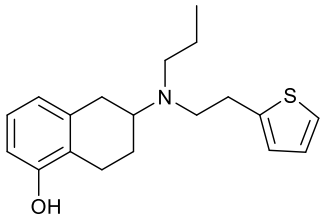

1.4

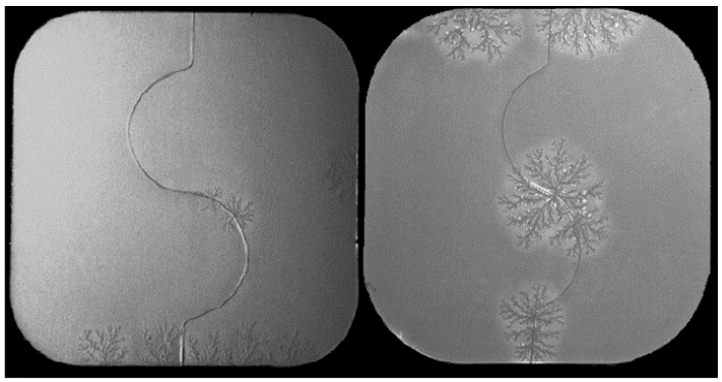

Figure 1-8. Form 2 of Rotigotine crystallising from Neupro patches which resulted in the withdrawal of Neupro patches from the market. Image adapted from reference 111.

The common over-the-counter analgesic and antipyretic paracetamol, also known as acetaminophen, provides an interesting example of how polymorphism can significantly impact the processibility of a compound. Paracetamol is known to have three anhydrous crystalline forms (forms I-III), with form I being the thermodynamically stable form under ambient conditions.[113–115] Form II exhibits favourable compressibility and can be incorporated into tablets via direct compression,[116] whereby excipients and API are simply mixed to form a homogenous

blend, before being compressed into pellets. However, form I is renowned for its poor compressibility and results in defective chipped or capped tablets when formulated into tablets via direct compression. Therefore, extra steps in the tablet production process, such as wet granulation, are required to improve the compressibility of form I.[117] The crystal structures of form I and form II reveal the same hydrogen bonds to form molecular layers, but the planarity of the layers in each form differ.[118] Those in form I are in a puckered or zig-zagged structure, which prevents layers gliding over one another and hence decreases the compressibility of the form (**Figure 1-9**). The layers in form II are planar, allowing the hydrogen bonding sheets to slide over one another, improving behaviour under compression.[119] Furthermore, form II was initially highly elusive due to seeds of the thermodynamically stable form I.[120] To produce crystals of pure form II, the crystals need to be removed from the mother liquor before seeds of form I started to appear.

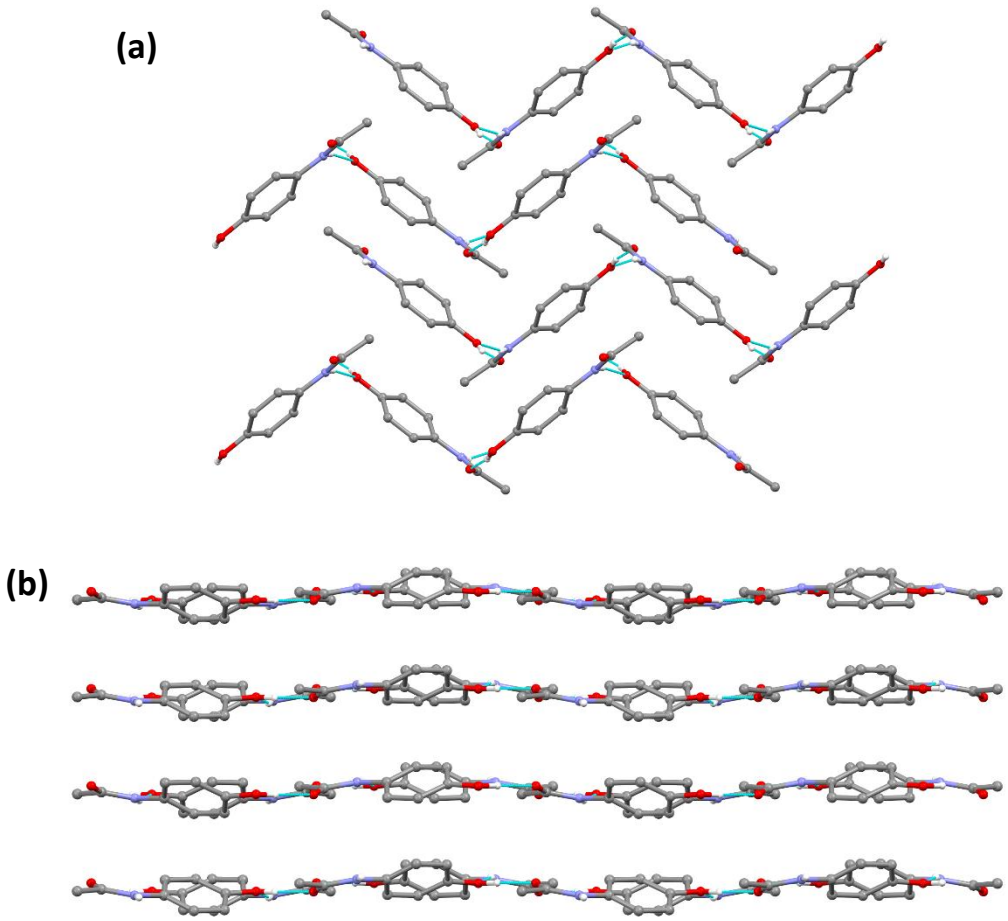

Figure 1-9. Images of the crystal packing of paracetamol in forms I and forms II. **(a)** The zig-zag hydrogen bonding sheets in form I of paracetamol is attributed with its poor compressibility, whilst **(b)** the planar hydrogen bonding sheets observed in form II improves the compressibility and enables tablets to be produced via direct compression. Images were generated using CSD entries HXACAN24 (form II) and HXACAN27 (form I).

Carbamazepine is highly polymorphic with over 50 forms reported including five anhydrous forms[121,122], numerous solvates[123] and many co-crystals.[124–126] Many of these solvate and co-crystal forms are themselves polymorphic.[127] Anhydrous forms I-IV all exhibit carbamazepine molecules forming the same hydrogen bond dimer. Meanwhile form V is catemeric with carbamazepine molecules forming C(4) hydrogen bond synthons between amide functionalities (**Figure 1-10**). Form III is the thermodynamically stable form under ambient conditions and is used in pharmaceutical formulations. However, kinetic forms I, II and IV can all crystallise readily and concomitantly with form III from solution. This has resulted in carbamazepine becoming a key test compound for methods designed to control polymorphism and isolate a single crystal form.

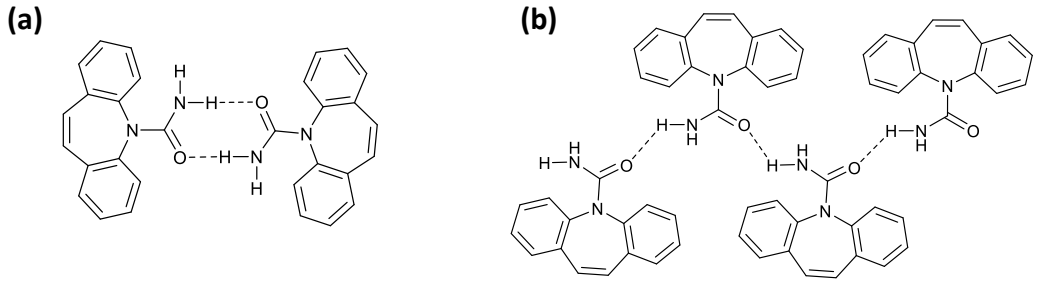

Figure 1-10. (a) The hydrogen bonded dimer present in anhydrous forms I-IV of carbamazepine. **(b)** The C(4) hydrogen bond synthon exhibited in catemeric form V of carbamazepine.

Form V of carbamazepine does not readily crystallise. It was first predicted computationally and then obtained experimentally using seeds of form II of the structurally related compound 10,11-dihydrocarbamazepine (DHC).[122] Form II of DHC is isostructural with form V of carbamazepine and exhibits the same C(4) hydrogen bond synthons. This example highlights how both the use of computational prediction methods and investigating structurally related compounds can aid the identification of novel polymorphic forms. It also demonstrates that crystal forms can be highly elusive, and a wide range of crystallisation methods may be required to uncover novel forms. This point is further emphasised by the antituberculosis drug isoniazid (**1.5**) and structurally related analogue iproniazid (**1.6**).

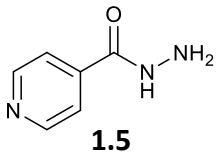

1.5

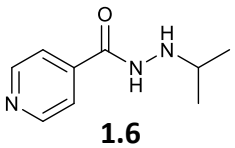

1.6

Despite being first synthesised in 1952, isoniazid which was long thought to be monomorphic due to only one form being identified over many decades.[128] This stable form of isoniazid (now known as form I) exhibits a head to tail arrangement of isoniazid molecules, with N1-H···N3 and N2-H···N1 hydrogen bonds forming between adjacent molecules (**Figure 1-11**). However, two new forms have since been isolated and characterised through melt crystallisations and crystallisations under nanoconfinement.[129] A single crystal of form II has been characterised via SCXRD with the structure revealing dimer formation via N1-H···O=C hydrogen bonding. This example of API polymorphism further demonstrates the need for thorough and extensive screening for polymorphic forms utilising numerous different methods. Further work by Taylor *et al* demonstrated how crystal structural prediction (CSP) techniques are able to predict these elusive forms of isoniazid. In addition, three forms of iproniazid were also identified. Exhaustive crystallisation screening of iproniazid via solution-phase, melt and high-pressure crystallisation experiments resulted in these three forms being obtained experimentally, demonstrating the benefit of using computational prediction methods to direct experimental screening and reduce the risk of failing to identify potential polymorphs.

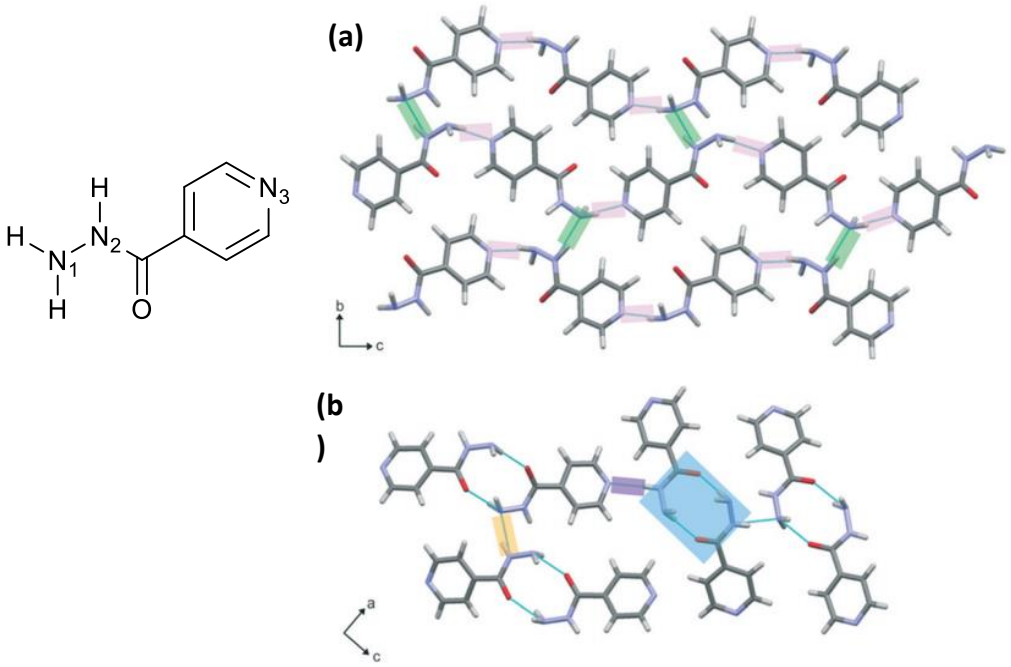

Figure 1-11. (a) Molecular packing of isoniazid in form I. N1-H···N3 (in pink) and N2-H···N1 (in green) form between adjacent molecules. **(b)** Molecular packing in novel form II reveals dimer formation via N1-H···O hydrogen bonds, with N2-H···N3 hydrogen bonds (in purple) and N2-H···N1 interactions (in orange) also being formed. Adapted from reference 129.

Finally, the pharmaceutical precursor 5-methyl-2-[(2-nitrophenyl)amino]-3thiophenecarbonitrile (**1.7**), also known as ROY, offers a well-documented example of polymorphism which has gathered significant interest from researchers over time. ROY is highly polymorphic, with fourteen forms characterised experimentally, [130–135] and further forms predicted computationally.[136] What is most striking about this compound is how vastly its solid appearance can change, with crystals being either red, orange or yellow depending on polymorphic form (**Figure 1-12**). The polymorphs arise due to conformational flexibility around the C–N–C–S torsion angle, with torsion angles between 21-58 ° yielding red crystals or orange crystals, whilst an angle greater than 67 ° resulting in yellow crystals.[137] Furthermore, the different polymorphs have been shown to crystallise concomitantly due to a narrow free-energy range between forms, resulting in poor thermodynamic selectivity.[135,138] Thus, ROY has become a model compound for testing whether polymorph selectivity can be achieved by a given technique or procedure.[138,139]

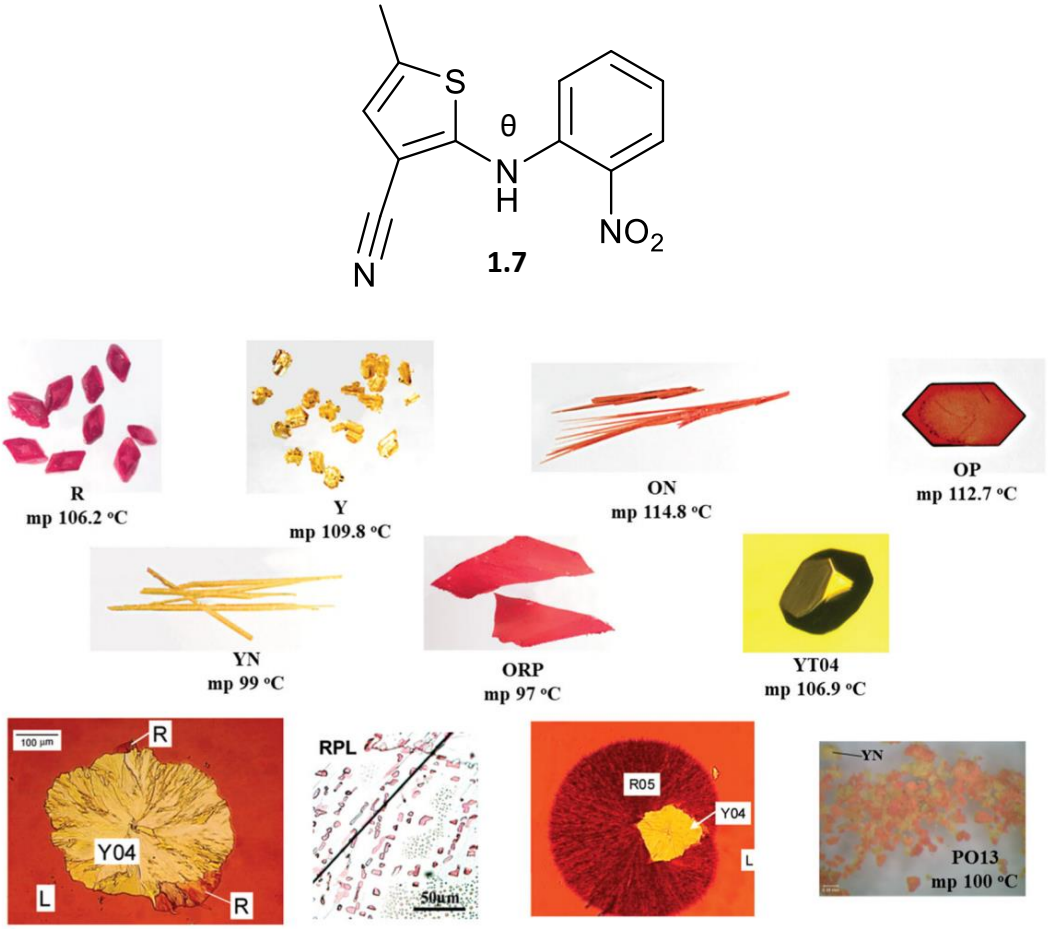

Figure 1-12. The colour and melting points (mp) of many of the forms of ROY (**1.7**). The different polymorphs and colours arise due to the conformational flexibility around the C–N–C–S torsion angle (θ). Adapted from reference 137.

1.5 Introduction to gels

Gels are materials that exhibit unique physical properties, behaving as conventional solids through shape retention and their ability to support weight, whilst exhibiting fluid-like behaviour under the application of stress. These distinct properties mean gels are ideal for use across a broad range of modern day applications and are utilised in lubricants, cosmetics, food products, explosives and medicinal products.[140–147] The IUPAC definition of a gel stands as "a colloidal network that is expanded throughout its whole volume by a fluid".[148] Indeed, gels are predominantly comprised of a fluid phase that is immobilised by a solid phase, which typically makes up 1 to 2 % of the gel composition. The solid phase forms a vast fibrous network with a high surface area that can immobilise the fluid phase through surface tension. Whilst immobilization of the liquid phase prevents macroscopic flow, diffusion through the liquid phase still occur and is critical for the use of gels in specific applications such as protein

separation, extractions of toxic ions and the controlled release of drugs from gel-matrix formulations. Water,[149,150] organic solvents[151–153] and ionic liquids[154–156] can all employed as the fluid component in gel formation and are respectively termed hydrogels, organogels and ionogels. Additionally, gases can be used as the fluid phase to produce aerogels, which are lightweight materials with porous structures and extraordinary surface areas, making them well suited for a range of potential applications, including drug delivery,[157] water purification[158] and electrochemical capacitor applications.[159] The fact gels are comprised mostly of a fluid phase makes their solid-like bulk properties highly fascinating.

Traditionally, the solid phase in gels comprises long chain polymers capable of forming solid networks through physical interactions of cross-linking between chains. However, since the 1990s there has been a rapidly growing interest in supramolecular or low molecular weight gelators (LMWGs).[160] In a supramolecular gel, the formation of the fibrous network is initiated on the mesoscopic level through the self-assembly of a small molecule into anisotropic architectures, such as fibres or scrolls, which is the primary gel structure. These architectures then aggregate to form fibrils (the secondary structures) which then entangle to form the vast gel network. Typically, supramolecular gels can be formed by dissolving the gelator in a suitable solvent via heating and then cooling the resulting solution below a critical temperature, known as the sol-gel transition temperature (T_g), at which point the gel forms. Other methods of inducing gelation include exposure to light,[161] changes in pH,[162] ultrasound[163,164] and use of additives, such as metallic salts.[165,166]

The gelation process may be considered very similar to crystallisation, with both occurring under supersaturation and comprising of nucleation and growth phases. It has even been suggested that gelation is essentially an arrested crystallisation and that gels are metastable forms that precede crystalline phases.[167] Indeed, there have been reports of gels transitioning into crystalline phases over time.[168–170] The gelator concentration and stoichiometric ratio with the solvent may play a key role in determining whether gelation or crystallisation occur, and there are examples of gels forming above a measurable critical gelation concentration (CGC) and crystallisation occurring below this concentration.[171]

When compared to polymer gels, supramolecular gels are relatively fragile due to the weaker nature of the non-covalent interactions which drive fibre formation. Indeed, supramolecular gels are reversible and typically return to their sol state via different mechanisms, such as heating, exposure to light[172] or the use of additives that may disrupt supramolecular interactions, such as anions. This fragility can limit the applications of a supramolecular gel, particularly where gel manipulation or shaping is required.[173]

1.6 Designing supramolecular gelators

Much work to develop guidance on how to design and produce reliable supramolecular gelators has been undertaken. Whilst identifying consistent rules remains a challenge, due to a limited understanding on the mechanism of gel self-aggregation and how the gelator structures can impact it,[174–176] much progress has been made such that supramolecular gelators can be designed with some success.

The formation of one-dimensional fibres is driven on the mesoscopic level by unidirectional non-covalent interactions, including hydrogen bonding, π-stacking,[177,178] halogen bonding[179,180] and salt interactions.[181,182] Indeed, whilst past discoveries of LMWGs heavily relied on serendipity, a growing knowledge of these supramolecular interactions and the field of crystal engineering has enabled some gelators to be purposefully designed through the inclusion of functionalities capable of forming unidirectional intermolecular interactions.[183] These gels may be formed by a single molecular species or may be multicomponent whereby the fibrous networks consists of two or more molecular entities which interact with one another and self-assemble into anisotropic structures.[264] As with the co-crystal field, a growing understanding of supramolecular interactions has played a key role in the development of multi-component gels.

Hydrogen bonding functionalities are commonly utilised to encourage gelation behaviour due to their highly directional and relatively strong nature. In particular, amides and peptides are often incorporated into LMWG molecules, due to their tendency to form infinite chain synthons through N–H···O=C hydrogen bonds can promote the formation of anisotropic architectures (**Figure 1-13**). Similarly, urea groups can assemble via $R_2^1(6)$ hydrogen bond motifs with intermolecular hydrogen

bonds forming between N–H in one molecule to a single urea carbonyl in the adjacent molecule. This can result in the unidirectional molecular aggregation via the infinite α-tape arrangement.

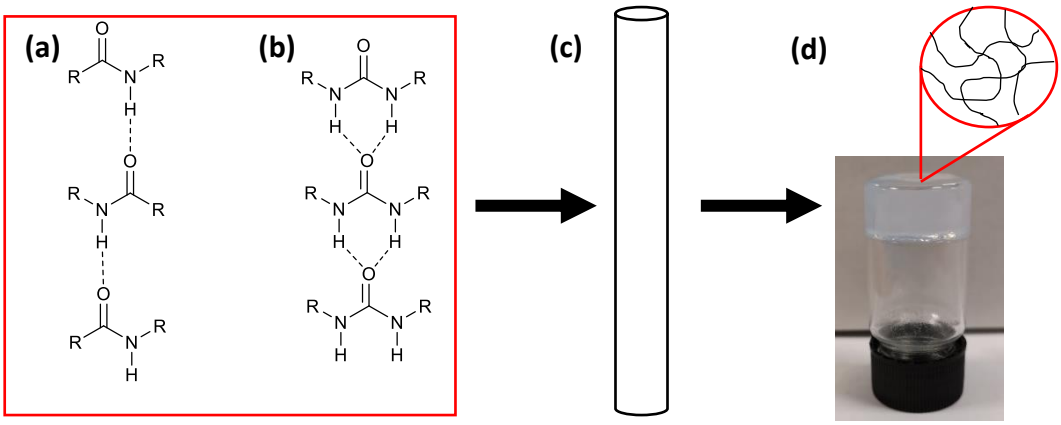

Figure 1-13. Unidimensional hydrogen bond synthons that anisotropic aggregation include the (a) C4 amide synthons and (b) $R2\ 1(6)$ urea α-tape synthons. (c) Molecular assembly driven by these synthons can result in the formation of fibres. (d) The fibres then entangle to form the vast fibrous network capable of immobilising bulk solutions.

The additional hydrogen bond donor present in the urea functionality means they typically form stronger gels than their amide/peptide counterparts. Similarly, increasing the number of amide or urea functionalities within the molecule tends to yield more effective gelators, with bis(ureas) and bis(amides) commonly used to yield LMWGs.[101–104] Although it is also worth noting that increasing the number of hydrogen bond donors and acceptors in the molecule may disrupt the infinite hydrogen bond synthons driving anisotropic aggregation or result in rapid assembly in more than one dimension.[128,188] Interestingly the relative orientation of the urea groups in bis(urea) LMWGs can have a significant impact on gelation behaviour, as was demonstrated in previous work by the Steed group (**Figure *1-14***).[189] In this work, a series of bis(urea) compounds were derived with varying length of the aliphatic spacer group. When the number of methylene units was even, gelation behaviour was observed. Conversely, compounds with an odd number of methylene units in the spacer group were non-gelators. This was attributed to the expected relative orientation of the urea groups when assuming an all-trans conformation is adopted by the spacer groups. An anti-parallel orientation (where n = even) promoted gelation, whilst a parallel orientation (where n = odd) results in poor gelation behaviour.

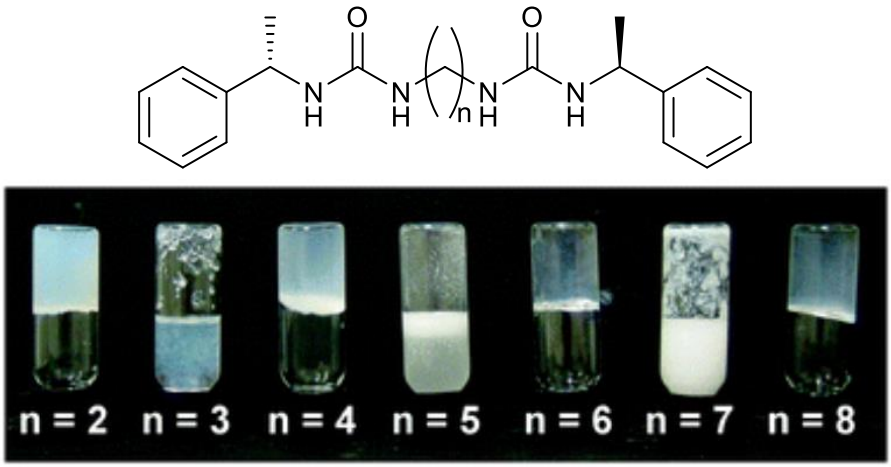

Figure 1-14. Work by the Steed group has demonstrated that the relative orientation of urea groups in bis(urea) molecules is key for enabling gelation behaviour, with anti-parallel urea groups (n = even) resulting in gel formation, whilst a parallel orientation (n= odd) results in a non-gelator. Adapted from reference 189 with permission.

The gelation of urea-derived compounds can be further encouraged by incorporating a methylene unit between urea functionality and aryl end groups.[188,190] This reduces steric hindrance around the urea group and improves the likelihood of α-tape assembly. Phenyl groups with electron-withdrawing substituents can also form C-$H_{(aryl)}\cdots O_{(urea)}$ interactions when directly adjacent to urea functionalities. [191] These essentially block the carbonyl acceptor from partaking in μ-tape synthons. The addition of the methylene spacer between urea functionalities and end group can prevent these intramolecular interactions forming, again freeing up the urea group to partake in α-tape synthons.

It is common practice for researchers to synthesis a series of structurally related compounds based on known LMWGs (which may have been identified themselves through serendipity).[192–198] In these situations, a functional group may be substituted or altered, but the key gelation functionalities and/or linker group are maintained within the LMWG molecule to increase the likelihood that gelation behaviour will be observed in the child compounds. Furthermore, the structural modifications to the functional group can alter or tune the properties and behaviours of the LMWG which may improve their suitability for the proposed application.[199] Seemingly small changes in the molecular structure, such as the position of ring substituents, can significantly impact gelation behaviour.[190,200] This is often due to changes in the supramolecular synthons that can be formed or the gelator solubility.[188]

Indeed, the solubility of a LMWG in the desired solvent(s) plays a critical role in its success as a molecular gelator. LMWGs should exhibit what is often referred to as a 'Goldilocks' solubility to enable gels to form. This ensures the gelator can be dissolved in and form supersaturated solution in the solvent, which can then result in the formation of a fibrous network. Calculating the dissolution or solubility parameters for a system can sometimes be used to predict whether a molecule will be a gelator or non-gelator in a given solvent, but this can be challenging.[201–204] Whether or not a solvent will be gelled is due to a number of complex factors, including the polarity of the solvent, solvent-gelator interactions and how the solvent impacts gelator-gelator interactions.[204] Given that LMWG compounds can be very diverse, a given method to predict gelation behaviour on solubility parameters may provide accurate predictions for a series of structurally-related analogues, but generally cannot be applied universally.[205] As a result, researchers typically test the versatility of potential gelators by screening them experimentally in a selection of different solvents. Naturally, the properties of the solvent can significantly impact or alter the properties of the gel, including the fibre morphology and rheological profile.[206–209]

Finally, chiral moieties are often incorporated into potential LMWGs to increase the likelihood of gelation occurring. Indeed, most LMWGs contain chiral substituents with the pure enantiomer being an effective gelator, whilst the racemic mixtures or achiral analogues exhibit little to no gelation behaviour.[210–212] The lack of mirror or inversion symmetry in chiral compounds means that they are limited to crystallising in the Sohncke space groups. This is considered to frustrate crystallisation and increase the likelihood of anisotropic assembly into fibres. Cases where mixtures of the enantiomers enhance gelation properties are rare but have occasionally been reported.[213–215] In these instances, it has been proposed that the improved gelation properties may be due to enantiomerically pure and racemic fibres forming concomitantly, with enhanced intermolecular forces forming between the two types of fibres.[213]

1.7 Characterisation of gels

Gel fibrils are challenging to characterise due only comprising 1 to 2 % w/v of the total gel composition, in addition to their small size and dynamic nature. Therefore, gels are typically characterised via their bulk properties. One such key property of gels to

characterise is their rheology. A simple benchtop observation, known as the inversion test, can be performed to qualitatively assess the rheology and determine whether a gel may have formed. Here the vial is simply upturned and if the gel holds its shape and does not flow, then it may be classed as a gel. Whilst the simplest method to determine whether a gel has formed, it has significant limitations. Most notably, it cannot distinguish between a gel or a highly viscous suspension.[216] Instead, measuring the rheological properties using a rheometer offers a more reliable method to identify gels.[217] In gels, the storage modulus (G') is an order of magnitude greater than the loss modulus (G") and remains constant as oscillatory shear is applied up to the yield stress of the gel.[218,219] The yield stress can be determined through stress-sweep rheometry experiments, with the gel breaking and liquefying once the yield stress is surpassed. The higher the yield stress, the stronger the gel.

Obtaining a single crystal structure of gelators themselves can provide invaluable insight to their structural organisation and how the molecules may assemble to form gel fibres. This can also aid gelator engineering by identifying key functionalities and supramolecular synthons that may drive gelation. Yet the task of obtaining a single crystal of a gelator is notoriously challenging. If a single crystal can be obtained, the crystalline and xerogel phases can be compared by solid-state characterisation techniques, such as XRPD, IR/Raman spectroscopy and solid-state NMR.[219,220] The theory is that removal of the solvent leaves behind the solid fibrous network of gelator and these solid-state techniques can be utilised to determine whether the molecular arrangements and intermolecular interactions are identical or distinct in the crystalline and fibrous phases. Whilst these are quick and readily accessible techniques, studies have demonstrated that the removal of solvent from gels can result in phase transitions, thus there is always a risk that the xerogel fibres may not be wholly representative of the solvated fibres.[221,222] Computational methods are frequently utilised in parallel with solid-state characterisation of gels in ordered to model the molecular packing within gel fibres and to better understand the nature of the supramolecular interactions driving gelation.[223–225] Further techniques, such as fibre X-ray diffraction,[226] small angle X-ray scattering (SAXS) and small-angle neutron scattering (SANS)[227] can be utilised to explore the wet gel phase but access to the required equipment can be limited. When used, these techniques can provide valuable

information regarding the mechanism of gelation[228] and interactions between gelator and solutes.[229]

Microscopy techniques can provide valuable insights on the fibrous architectures on the nanoscale. Scanning electron microscopy (SEM) and Transmission Electron Microscopy (TEM) are two widely utilised methods to achieve this. These techniques can provide valuable information on the size, nature and chirality of the fibres, and can be used to model and predict the self-assembly behaviour on the molecular level when combined with computational methods. Due the requirements for samples to be imaged in a vacuum chamber, gel samples need to be either dried down into their xerogel state or frozen and studied at cryogenic temperatures.[230] Organic samples also need to be coated with a conductive metal such as chromium, platinum, or gold, for SEM or with carbon for TEM prior to imaging to reduce charging effects and improve image quality. Environmental-SEM can be used to image wet samples but the gaseous environment in the sample chamber reduces the distance over which the electron beam can be used, meaning that it may not achieve sufficient magnification and resolution to image fibres at the low end of the nanoscale.

Solution NMR experiments can also be used to look at gel formation and gelator interactions.[231] Although molecules in the gel-phase are typically invisible to solution-state NMR due to the low mobility of the self-assembled molecules, solution state NMR can be used to investigate the assembly process, as the resonance peaks typically broaden and undergo shifts in frequency and decreases in intensity as the molecules in solution self-assemble into gelatinous aggregates. [232] Indeed, solution-state NMR has been utilised successfully to investigate the kinetics of gel network formation, [265] the thermal stability of gels,[266] the surface chemistry of fibres[233] and how additives interact with gelators.[267]

1.8 General considerations for gels as crystallisation media

Gels have been used as crystal growth media since the late 19th century where Liesegang observed the crystallization of inorganic salts in gelatine hydrogels. Thus for over a century polymer gels have been used to crystallize range of compounds, including organic compounds, inorganic compounds, proteins and viruses.[234–241] Crystals grown in gels frequently display superior properties to those yielded from

solution, including a larger size, greater optical quality and fewer defects. This can primarily be attributed to the suppression of convection eddy currents, slower diffusion of solute through the gel media and the ability of the gel fibres to facilitate heterogenous nucleation. Interestingly, a recent study published by the Edkins group demonstrated via neutron spectroscopy experiments that that diffusion of API molecules when in close proximity of gel fibres can actually be faster than in solution of the same polar solvent system (in this case 7:3 v/v ethanol:water).[242] This faster solute diffusion is hypothesised to be due to the hydrophobic nature of the gel fibres which disrupts the hydrogen bonding of the solvent and thus lowers the viscosity in the immediate locality of the gel fibres.

In more recent years, attention has started to turn from using polymer gels as crystallisation media to using supramolecular gels instead. One of these reasons for this is that gel-sol transitions can often be induced via the use of additives without the requirement for heat. This can be highly favourable and enable the easy retrieval of crystals via filtration. This was demonstrated in previous work by the Steed group. [243] In this work, a range of bis(urea) gelators that were used as crystallisation media of a range of pharmaceutical substrates. Dissolution of these gels can be initiated by the addition of anions to the system, which disrupts the α-tape synthons and induce a gel-sol transition (**Figure 1-15**). Whilst a useful trait of supramolecular gels, the study also revealed the need for caution when using anion addition to retrieve crystals, as some API crystals were observed to dissolve due to API molecules interacting with the anions and disrupting the crystalline order.

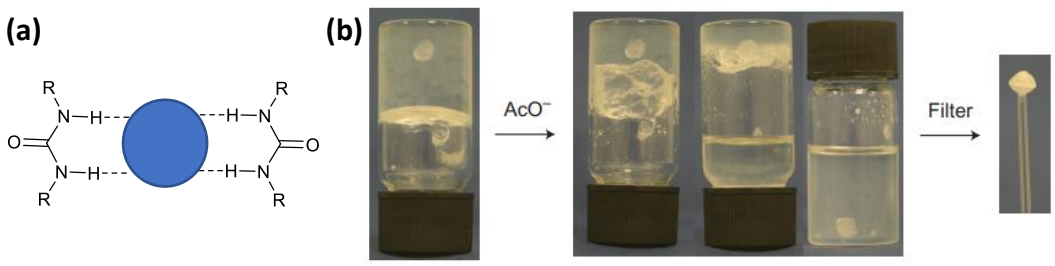

Figure 1-15. (a) Anions disrupt the urea α-tape hydrogen bonding synthons in supramolecular urea-derived gels. **(b)** This results in the disassembly of gel fibres and a gel-sol transition, enabling crystals to be conveniently retrieved via filtration of the sol. Figure adapted from reference 243.

Work by Fang *et al*. has also demonstrated that this anion effect can be concentration dependent and that the addition of tetrabutylammonium (TBA) salts, at concentrations less than 0.01 molar equivalents to the gelator, can actually enhance the strength and elasticity of bis(urea) gels.[244] This was attributed to a salting out effect via NMR titrations, whereby the addition of TBA salt decreases the solubility of the gelator which results in more gelator molecules aggregating to form fibres and increasing the overall strength of the gel. At higher concentration of TBA salts, a gel-sol transition is induced. The gels in this study were also utilised to crystallise organic semi-conductors, although the gels had no significant impact on crystallisation outcomes. Again, the crystals can be retrieved via filtration after the addition of anions at sufficient concentrations (above 0.01 molar equivalents).

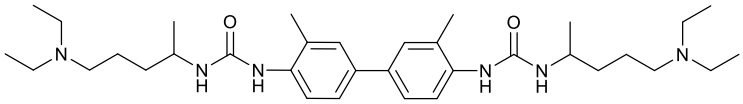

1.8

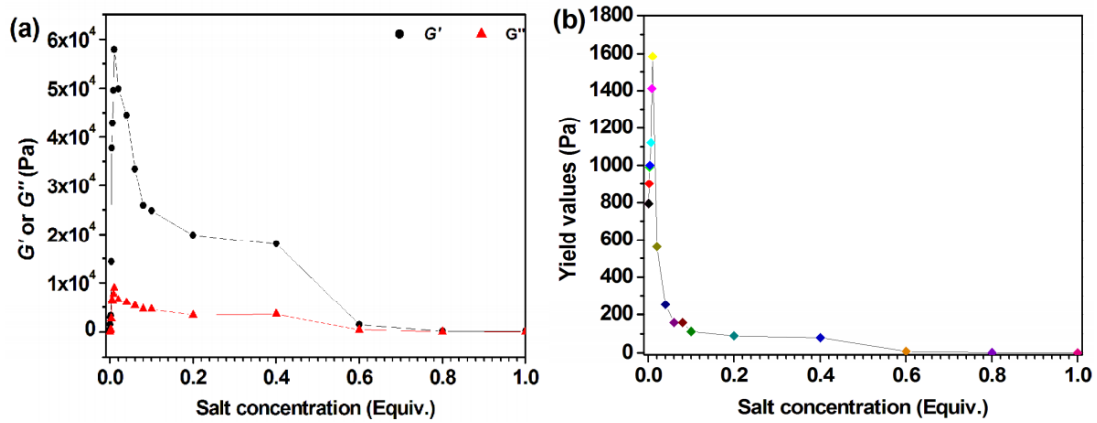

Figure 1-16. When low molar equivalents of TBA salts up to 0.02 molar equivalents are added to 2% w/v m-xylene gels of **1.8**, the **(a)** G', G" values and **(b)** yield stress sharply increase due to a salting out effect. As the salt concentration is further increased, the yield stress sharply decreases and the gel transitions to a sol state due to disruption of supramolecular interactions between gelator molecules. Adapted from reference 244.

It is worth noting that crystallisation substrates themselves can have significant impacts on supramolecular gel behaviour and properties. This was demonstrated by the Smith group who showed that multicomponent gels consisting of Lysine-based dendrons and alkyl amines were able to crystallise caffeine and carbamazepine (CBZ) although had no impact on the crystallisation outcomes.[245] Interestingly, the presence of CBZ actually enhances the gelation behaviour of decylamine and a G2-Lys dendron multicomponent gel at room temperature, whilst gelation is not achieved at room

temperature in the absence of CBZ.[246] Gelation occurs due to a hydrogen bond, or potential ion transfer, between the CO_2H functionality in the G2-Lys dendron (**1.9**) and NH_2 in the monoamine (**1.10**). However, aspirin and indomethacin, which both contain carboxylic acid groups, disrupted gelation and crystallisation of the APIs, due to the $CO_2H\cdots HN_2$ synthon formed between the API molecular and amine gelator component being more thermodynamically favourable than the synthon form between the amine and Lys-based dendron required for gels to form. As a result, the multicomponent gel failed to form, and API crystallisation was also inhibited.

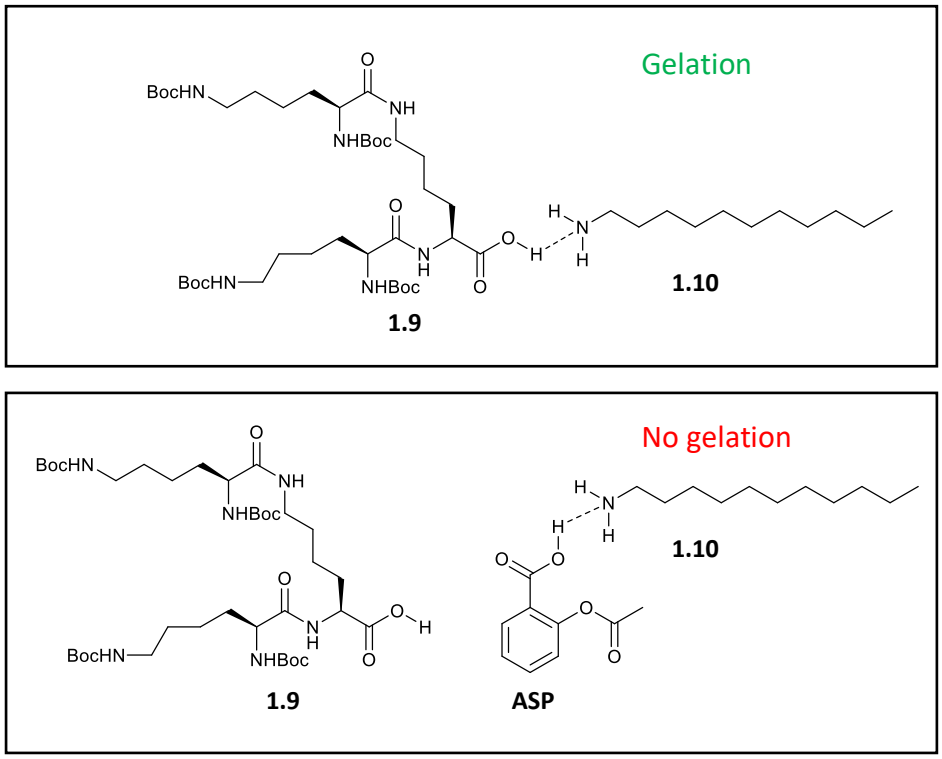

Figure 1-17. (a) Gelation of the G2-Lys dendron (1.9) and decylamine (1.10) occurs due to the formation of a hydrogen bond between CO_2H and NH_2 in the two components. **(b)** The addition of substrates containing CO_2H groups, such as aspirin (ASP), results in competitive $CO_2H\cdots NH_2$ interactions which can disrupt gel formation, as well as crystallisation of the substrate.

Work by Kumari *et al.* has shown the degree of interaction between crystallisation substrate and gelator is influenced by the gelator concentration and the molar ratio of gelator to substrate.[229] The study reports the use of SANS, microscopy and rheology to demonstrate that nucleation of solute and gelator are largely independent of one another with minimal interaction between gel fibres and solute nuclei. This is especially the case when the nucleation of one of the species (either gelator or substrate) is significantly faster than the other. However, under specific conditions the

nucleation of both substrate and gelator occur simultaneously and competitively. When this occurs the gel strength and structure can be significantly impacted (**Figure 1-18**).

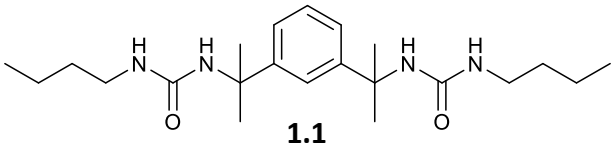

1.1

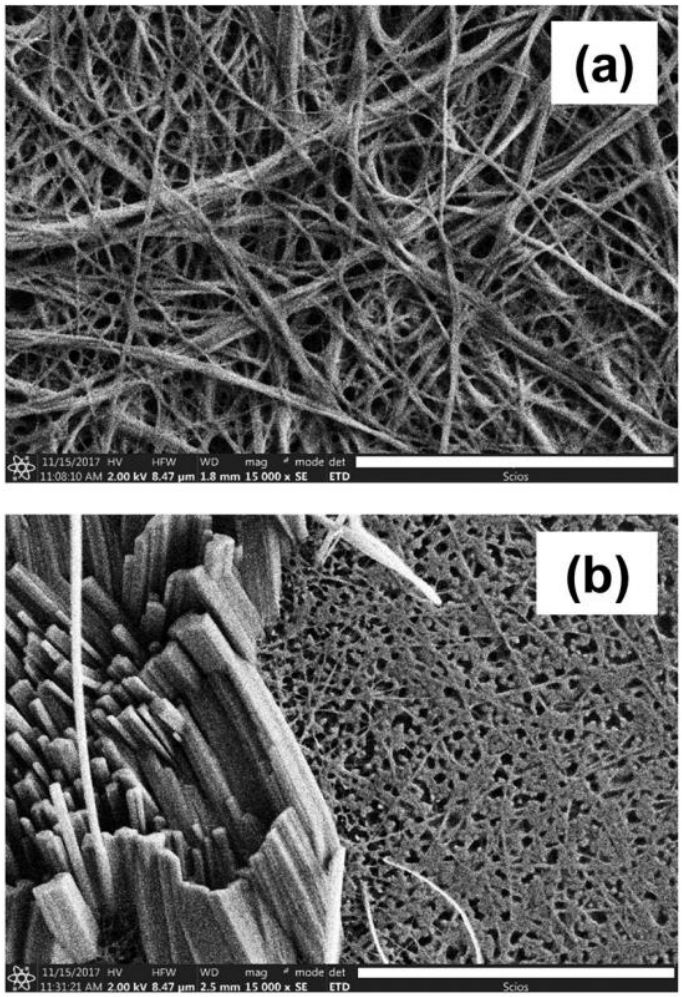

Figure 1-18. SEM images of 0.12 % (w/v) toluene xerogels of **1.11 (a)** alone and **(b)** in the presence of 0.2 % (w/v) of carbamazepine. The images clearly reveal a change in fibre morphology, size and extent of bundling which indicates that the carbamazepine has influenced the fibril formation and properties. Scale bars represent 4 µm. Adapted from reference 229

1.9 Using gels to influence or control crystallisation outcomes

Recent work in the field has focused on designing gels that can influence the properties of the crystals obtained, such as the crystal morphology or polymorphic form. These gels can then be used as part of wider solid-state screening methods to control crystal properties/form and even identify novel forms. Both polymer and supramolecular gels have been used in this application to date.

Sudha *et al.* reported the use of gel media to isolate stable form I and metastable form II of paracetamol.[247] In this column system, needles of form II formed at the surface of the gel media, whilst prisms of form I crystallised at the bottom of the gel (**Figure 1-19**). The difference in form was attributed to the faster evaporation of solvent at the surface of the gel, resulting in higher concentration of paracetamol near the gel-air interface which enables the nucleation of metastable form II. In comparison, the concentration at the bottom of the gel is comparatively low and therefore nucleation and growth of form I occurs. This system enables the two forms to be separated and isolated with ease.

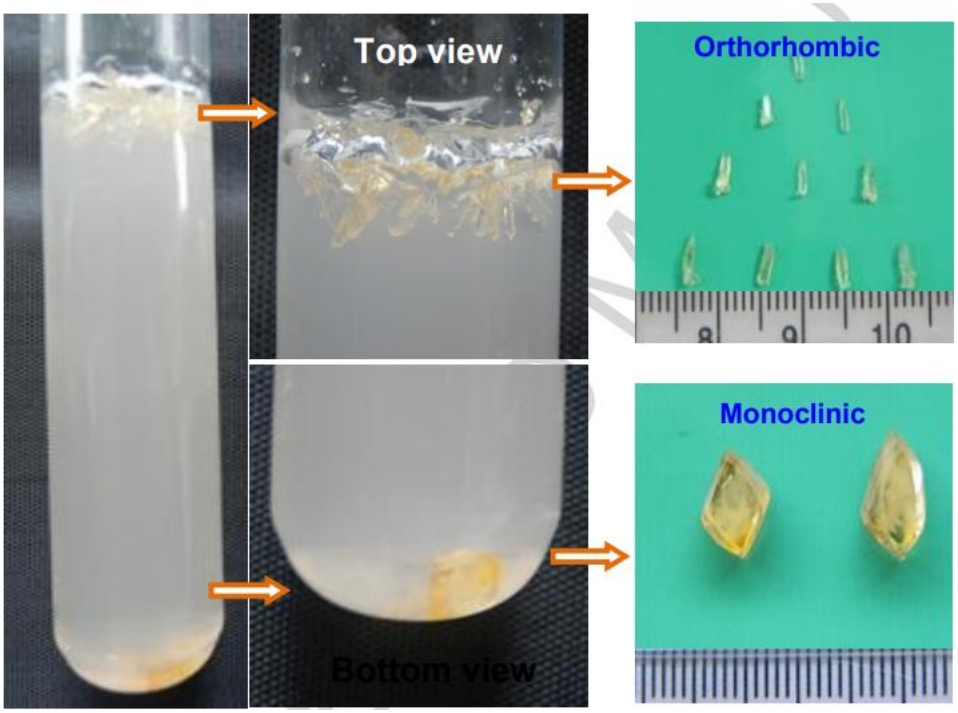

Figure 1-19. Work from Sudha *et al*. demonstrated how gel columns can be used to isolate stable monoclonic form I and metastable orthorhombic form II of paracetamol. The latter crystallises at the surface of the gel due to accelerated solvent evaporation resulting in higher local solute concentrations compared with in the body of the gel. Adapted from reference 247.

Work by Trout *et al.* used a novel polymer microgel with tuneable mesh sizes to control polymorphic form of ROY and carbamazepine, which influence polymorphic outcome through confinement effects and interactions between gel fibre surfaces and substrates, in addition to gel-facilitated nucleation which is dependent upon the polymer-mesh sizes and chemical composition.[248] These polymer gels swell upon immersion in solution and the degree of swelling, which is governed by polymer sub-chain length, ultimately determines the mesh size which can be finely tuned. For carbamazepine it was found that polymer chains over 400 g/mol in size, only form II of

CBZ was produced, whereas using polymers with molecular weight less than 400 g/mol resulted in a loss of polymorph selectivity (**Figure 1-20**). The intermolecular interactions are prominently similar in both form I and form II of CBZ, making the selectivity achieved in this work extraordinary. High degrees of selectivity for the metastable R form of ROY at polymer molecular weight of 575 g/mol are also achieved in this system, with ROY being notorious its concomitant polymorphs.[131,135]

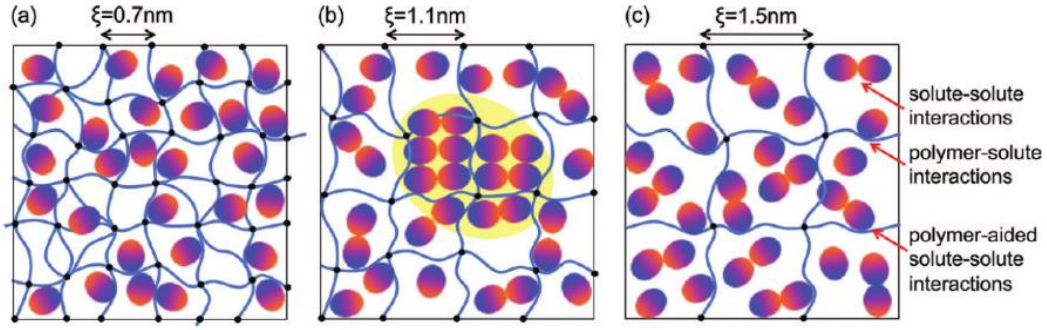

Figure 1-20. Schematic illustrating the mesh size effect on nucleation. When mesh sizes are too small, polymer-solute interactions dominate, preventing solute-solute interactions and thus nuclei formation. If mesh sizes are too large, there is no size restriction on nuclei and nucleation will take longer, thus less control over polymorphic form. At the right size, polymer-solute interactions and spatial confinement encourage solute-solute interactions, enabling controlled nuclei formation and crystal growth. Adapted from reference 248

One of the challenges of using polymer gels to influence crystallisation outcomes is that their synthesis and modification can often be complex. However, nanocellulose offers an option than can be readily modified and nanocellulose organogels have been utilised to good effect for API-crystallisations. Nanocellulose has readily accessible hydroxyl groups at its surface which can easily be modified to produce functional groups which will interact with the crystallisation substrate (**Figure 1-21**).[249,250] In particular, carboxylated nanocellulose (c-NC) has been used to facilitate API crystallisation.[251,252] In these examples, the surface of c-NC fibres were made more hydrophobic by the addition of lipophilic amines, which form ionic interactions between the ammonium cation and carboxylic acids present on the n-NC surface. These hydrophobic surfaces can then attract hydrophobic drugs, increasing local substrate concentrations and provide a surface that can encourage nucleation. These gels have been used to crystallise a wide range of API compounds and successfully aided the identification of a novel DMSO solvate of sulfapyridine.[251] They have also been shown to influence polymorphic form, crystal morphology and even have amorphized previously crystalline API compounds.[252]

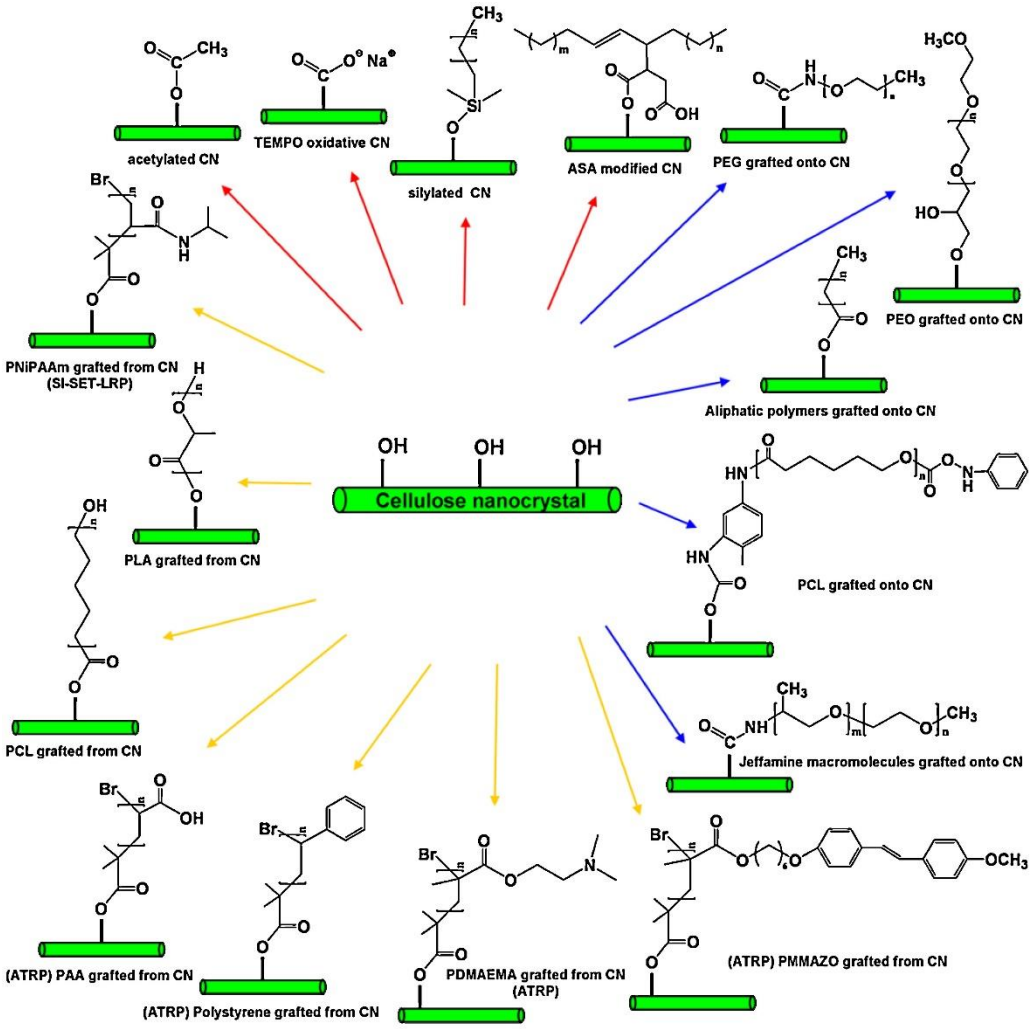

Figure 1-21. Some of the common surface modifications of nanocellulose that can be achieved. This synthetic malleability enables nanocellulose gelators to be designed to specifically interact with desired crystallisation substrates. Adapted from reference 250.

A similar approach to target hydrophobic APIs has also been achieved via the incorporation of calixarenes into supramolecular gelators to facilitate the crystallisation of hydrophobic drugs.[253] Gelators **1.12** and **1.13/1.14** were designed with the intention to produce gel fibres with calixarene cavities exposed on their surface. These cavities are hydrophobic and act as nucleation sites for hydrophobic APIs by providing pockets in which the APIs can bind to. Gelator **1.12** is a single component gelator with four hydrazide which are proposed to drive anisotropic assembly with molecules packing together in a head-to-tail formation. Gelators **1.13** and **1.14** form a two-component gel, with the well-documented guest-host chemistry of crown ethers and ammonium groups being utilised to promote gelation in the two-component system (**Figure 1-22**). The individual **1.13** and **1.14** components being non-gelators when used in the absence of the other. Gelation of **1.13/1.14** could be reversed by the addition of potassium ions which displace the ammonium groups from

the crown ethers via competitive binding. A limitation of both these gel systems is their lack of versatility with **1.12** only gelling 1,2-dibromoethane at 1 % (w/v), whilst **1.13/1.14** only gel 1,2,4-trichlorobenzene at 6 % (w/v).

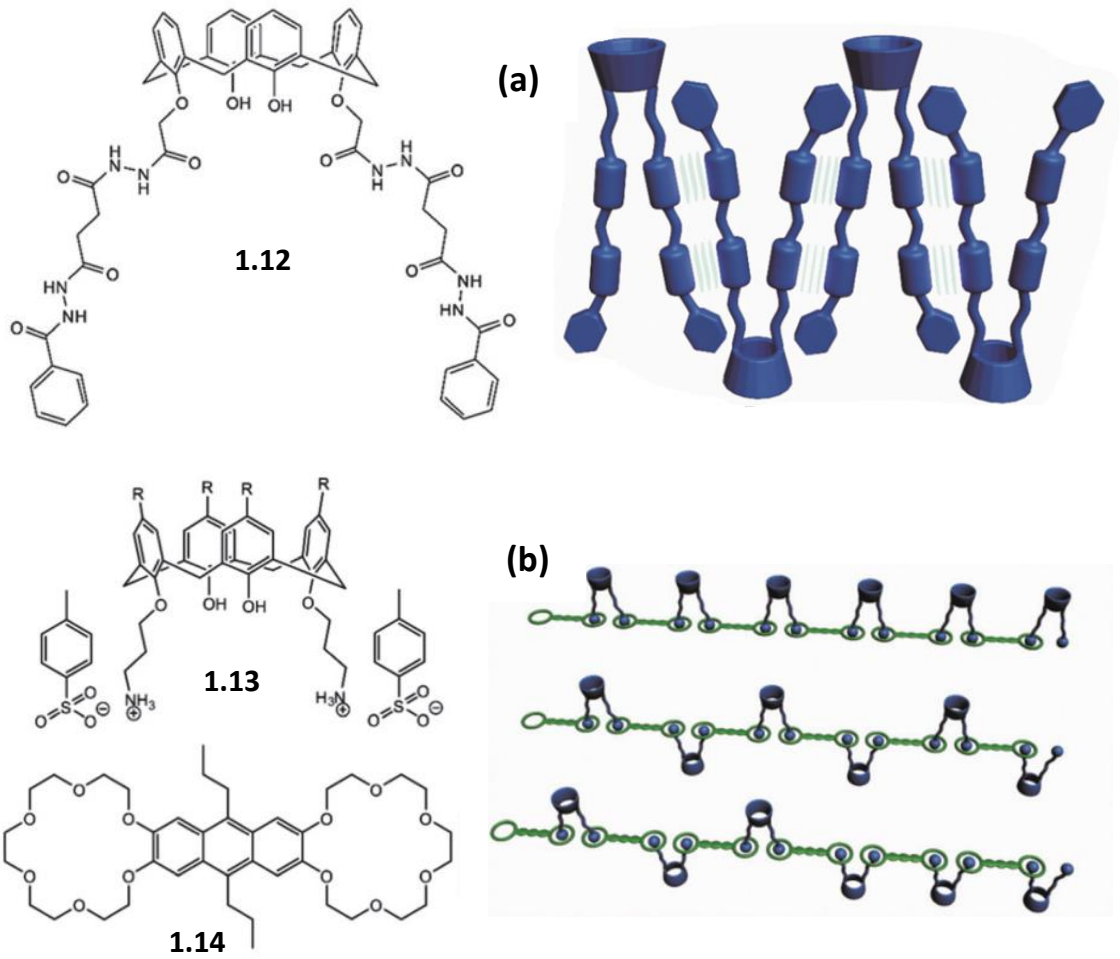

Figure 1-22. (a) Schematic to show the proposed self-assembly behaviour of single component gelator **1.12**. Molecules are thought to assemble in an anisotropic manner via hydrogen bonding between hydrazide functionalities with molecules packing in a head to tail formation. **(b)** Schematic showing the proposed gelation mechanism of two-component gels formed from **1.13** and **1.14**. The crown ethers in **1.14** (in green) form guest-host complexes with the ammonium groups in **1.13** (in blue) resulting in anisotropic assembly. Adapted from reference 253.

Gels of **1.12** in 1,2-dibromomethane and 1,2,4-trichlorobenzene gels of **1.13/1.14** were used as crystallisation media for hydrophobic compounds paracetamol, fenbufen, monobenzone and chlorphenesin. The gels crystallise the known polymorphic forms of most of the substrates which are also obtained from solution experiments, thus the gels failed to significantly impact crystallisation. The exception to this was chlorphenesin of which a new form crystallised from gels of **1.13/1.14**. Single crystals of this form, suitable for SCXRD characterisation, were then grown from solution. The

resulting crystal structure reveals a Z' of 2 and further demonstrates the applicability of using supramolecular gels to crystallise APIs and obtain novel forms.

The small molecular nature of LMWGs means they are generally and comparatively simple to synthesise when compared to most polymer gels. This has made it easier for researchers to develop molecular gels that are tailored to interact with a specific crystallisation substrate. The first example of using a supramolecular gel as crystallisation media which impacts crystal properties was reported by Estroff *et al* in 2004. They used a supramolecular hydrogelator (**1.15**) to crystallise calcite.[254] The gelator was designed using the knowledge of Ca^{2+} cation binding by carboxylic acids groups. It was found that the crystal morphology changed when left longer in the gel (**Figure 1-23**). This was attributed to free gelator molecules in solution adsorbing to the surface of calcite crystals at sites of imperfections. Over time, more gelator molecules accumulate at these sites and modify the morphology of the crystals. This example shows the potential for supramolecular gelator molecules to interact with the crystallisation substrate and influence the crystal morphology.

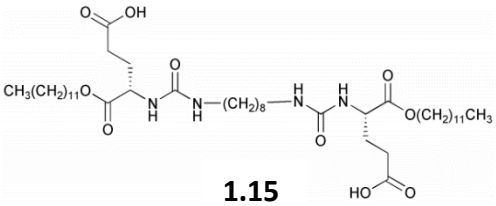

1.15

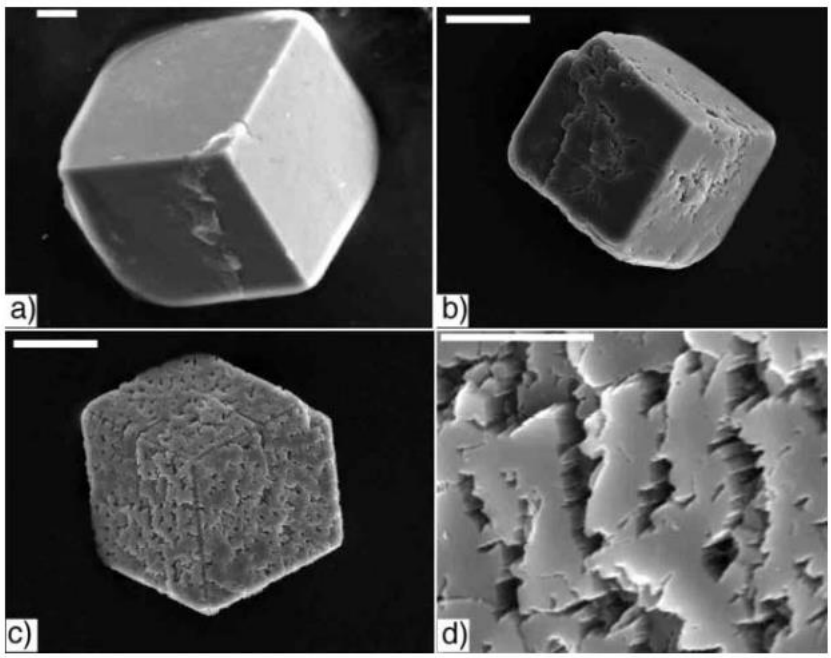

Figure 1-23. Calcite crystals removed from hydrogels of **1.15** after **(a)** 3.5 hours, **(b)** 10.5 hours and **(c)** 24 hours. **(d)** A magnified image of the crystal surface after 24 hours. The surface of the crystals become more etched and irregular over time spent in the gel. Adapted from reference 254.

Caruso and colleagues demonstrated that tannic acid-titanium(IV) supramolecular metallogels can also have a significant impact on crystal morphology and size when applied to the gel-phase crystallisation of caffeine, carbamazepine and piroxicam (**Figure 1-24**).[255] The morphology and size is also dependent upon substrate concentration. Additionally, the gels influence the polymorphic forms of carbamazepine obtained, with the dihydrate form being the dominant for from the gels whilst form III is the dominant form obtained control experiments in solution (albeit both formed concomitantly in gel and control crystallisations). The authors noted that further studies are required to understand why the gels have this impact on the crystallisation outcomes due to the complexity of factors that influence gel-phase crystallisation. With this system, crystal retrieval can be achieved via the addition of solid mass of pyrocatechol to the gel surface. The pyrocatechol competes with tannic acid to bind the titanium cation and results in disassembly of the gel enabling crystals to be filtered out with ease. Interestingly, the study also demonstrates that the API-loaded gels achieved sustainable API-release, which may form a basis for API delivery systems going forwards. Indeed, this application of supramolecular gels has been a focus for many researchers.[256–258]

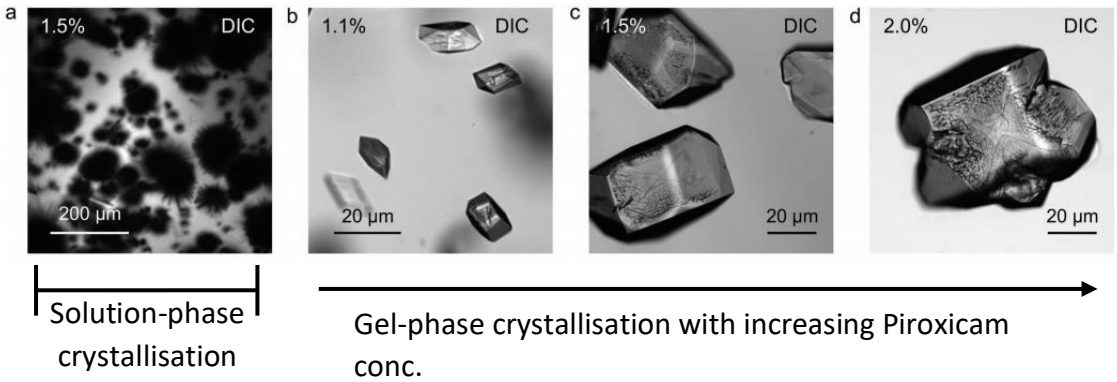

Figure 1-24. Morphology and size differences between **(a)** solution phase crystallisation and **(b-d)** gel-phase crystallisations of piroxicam. As the piroxicam concentration is increased, the size of crystals obtained from the gels increases. The concentration documented in each imaged is the piroxicam concentration as % w/v. Adapted from reference 255.

One approach to influence crystallisation is to design LMWGs containing functionalities that mimic those present in the crystallisation substrate. The rationale behind this approach is that the gel fibres provide a templated nucleation surface with the capacity to form favourable interactions with the substrate, lowering the activation enthalpy barrier to crystallization. The first example of this was reported by the Steed group, where a cisplatin-mimetic gelator (**1.16**) was used to crystallise cisplatin.[259]

Cisplatin is a chemotherapeutic agent used in a wide range of cancers and displays a particularly poor solubility in the majority of organic solvents. Indeed, the gelator and API are not soluble in any mutual solvent tested. Therefore, a bilayer diffusion set up was utilised, whereby a cisplatin-DMF solution was layered on preformed cisplatin-mimetic and generic gels alike, enabling diffusion of cisplatin into the gel phase. These crystallisations led to the discovery of a novel crystal habit of the known DMF solvate of cisplatin that was temperature dependent and only observed in the mimetic gelator. Low temperature crystallizations in all gels tested resulted in the formation of plate-like crystals with irregular shapes, whilst crystals obtained from xylene gels of the mimetic gel at room temperature yielded a substantial amount of hexagonal plate-like crystals, in addition to a few irregular shaped crystals. This observation indicates that the API-mimetic gel facilitates selective adsorption of the gelator to the fastest growing face of the cisplatin crystal. Additionally, when the experiment was repeated using dimethyl acetamide (DMA) in place of DMF, a novel DMA hemisolvate was obtained. Whilst xylene gels of both cisplatin-mimetic gelator and generic gelator generated the novel DMA solvate, only the mimetic gelator produced high-quality rectangular plate-like crystals that could be characterised via SCXRD, whereas the generic gelator produced small masses of poor-quality microcrystals. The influence of the mimetic gelator is proposed to be due structural and geometric recognition between cisplatin and the gelator, with both components likely interacting via Pt-Pt and/or ammine-chloride hydrogen bonds. This work demonstrates how gels can be used to obtain high quality crystals of poorly soluble compounds, as well as in the identification and characterisation of novel crystal forms.

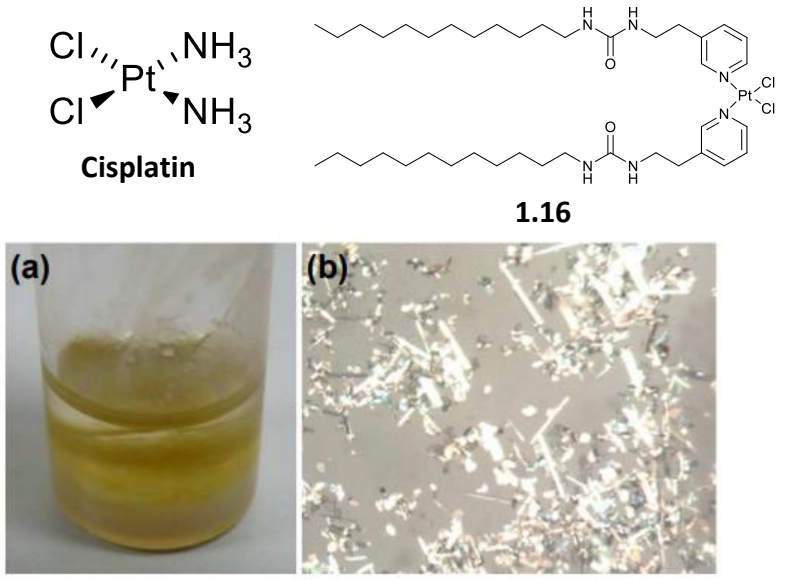

Cisplatin **1.16**

Figure 1-25. (a) Photograph of the o-xylene gel of cisplatin-mimetic **1.16** layered with a solution of cisplatin in DMF. **(b)** Image of the crystals grown at the gel-sol interface using this API-mimetic system. Adapted from reference 259.

Further work from the Steed group has demonstrated the significant impact that API-mimetic gels can have as crystallisation media. In one such study, a ROY-mimetic gelator (**1.17**) was synthesised and used to crystallise ROY, in addition to solution and generic gel crystallisations, whereby the generic gelator (**1.18**) exhibits minimal structural similarity to ROY.[260] The study found that the toluene gel of the ROY-mimetic gelator consistently resulted in the crystallization of the metastable red (R) form of ROY, whereas crystallisation from solution and toluene gels of gelators bearing no resemblance to ROY leads to the stable yellow (Y) form precipitating (***Figure 1-26***).

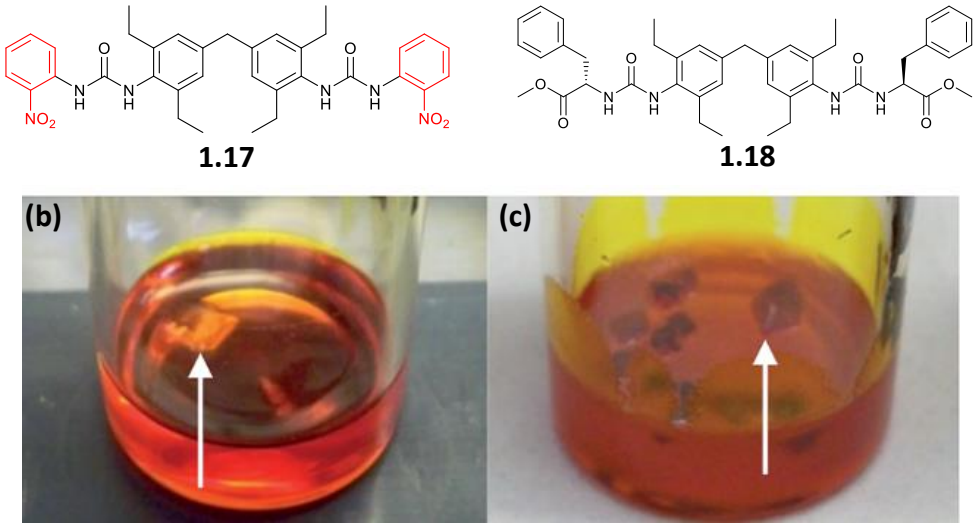

Figure 1-26. (a) A large crystal of stable Y form grown in a toluene gel of generic gelator **1.18** and **(b)** crystals of metastable R form of ROY grown in toluene gel of ROY-mimetic gelator **1.17**. It is proposed that in the ROY-mimetic toluene gel the nitrophenylaniline moieties present at the surface of gel fibres and attain a similar conformation to the thiophene group in the R conformation of ROY, facilitating epitaxial growth of this metastable crystal form. The API mimetic functionality in **1.17** is in red for clarity. Adapted from Reference 260.

Through use of computational crystal structure prediction (CSP) methods, which had previously been utilised in determining the molecular arrangement in gel fibres, it was identified that the nitrophenylaniline moieties would be expected to present at the surface of the gel fibres, thus are easily accessible to ROY molecules. Furthermore, the urea-nitroaniline unit presented a close steric and electrostatic match with the thiophene orientation in the R conformation of ROY, leading to the conclusion that the periodic urea-nitroaniline groups present in the mimetic gelator are able to facilitate epitaxial growth of the metastable R form and demonstrates that mimetic-gelators can control crystallisation outcomes.

API-mimetic gels aminoglutethimide-derived bis(urea) organogelators to influence the crystallisation outcomes for polymorphic compounds barbital (BAR) and thalidomide (THL).[261] BAR has 6 known polymorphs with forms I, III and V exhibiting similar relative packing energies and typically crystallise concomitantly.[262] Meanwhile racemic THL has two known forms termed α and β, which also crystallise concomitantly from nitromethane solution.[263] The study demonstrated that gels of an API-mimetic bis(urea) (**1.19**) were able to selectively crystallise the kinetic form III of BAR and kinetic form α of THL, whilst solution-phase and non-mimetic gel experiments yielded mixtures of polymorphic forms (**Figure 1-27**). This is hypothesised to be due to the surface of the mimetic gel fibres interacting more favourably with the nuclei of these kinetic forms and thus serving as templates for these forms exclusively.

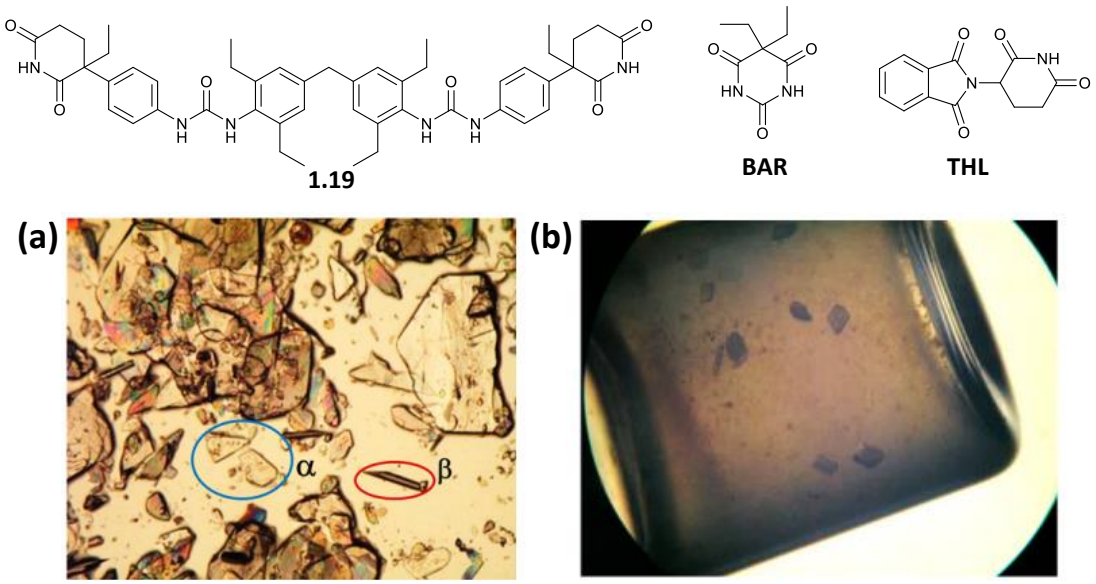

Figure 1-27. Nitromethane gels of **1.19** were able to selectively crystallise the kinetic form III of barbital (BAR) and form α of (±)-thalidomide (THL). **(a)** Image of α and β of THL (crystallised concomitantly from nitromethane solution) which can be distinguished by their distinct morphologies. **(b)** Image crystalline plates of form α in the nitromethane gel of API-mimetic **1.19**. Adapted from reference 261.

1.10 Project overview

This work aims to further the field of designing supramolecular gelators, with a focus on how molecular assembly and supramolecular motifs can encourage or discourage gelation. By identifying the structural trends that promote molecular gelation, supramolecular a range of LMWGs can be designed and synthesised which can then utilised as crystallisation media in solid-state screens of APIs. The goal from this work is to develop a library of LMWGs that gel a wide range of solvents that can be used as crystallisation media for APIs and attempt to understand factors that may promote or inhibit gelation of these compounds. The eventual goal is for researchers to have access to a series of diverse LMWGs (i.e. a 'toolkit' of LMWGs) with various distinct structural features that could be selected for use as crystallisation media based on structural mimicry or potential for interacting with the target API. Gel-phase crystallisations could then be completed in combination with standard established crystallisation screening techniques, to potentially identify novel crystal forms and control crystallisation outcomes in early-phase development.

In the first part of this work, we present a systematic study to investigate the effects of substituent groups on the gelation and self-assembly behaviour of bis(urea) compounds derived from a 4,4-methylenebis(2,6-diethylphenyl) spacer (4,4-MDEP).

Bis(urea)s derived from 4,4-MDEP have frequently yielded highly versatile and effective molecular gels and have become a cornerstone for gelator design in the Steed group. This work focuses on understanding what types of substituent groups promote gelation of 4,4-MDEP analogues and what groups may discourage gelation behaviour. The findings can then be used to inform future bis(urea) gelator design using 4,4-MDEP as a spacer, which could then be included in the 'toolkit' of LMWGs for pharmaceutical crystallisations. In this work, gels formed by the synthesised 4,4-MDEP analogues are characterised through rheology, SEM, ball-drop experiments and XRPD. Attempts were then made to crystallise the 4,4-MDEP compounds with the aim to grow single crystals that could be investigated via SCXRD analysis. The resulting structures could provide valuable insight to the molecular conformation, packing tendencies and intermolecular synthons that may encourage or discourage gelation of 4,4-MDEP bis(urea) analogues. As previously discussed, crystallisation effective gelators can be challenging and this work presents a methodical process that can used to try to encourage crystallisation over gelation for these compounds. Prior to this work a crystal structure of a 4,4-MDEP bis(urea) had never been reported.

The second chapter of work describes an approach to design and produce API-mimetic bis(urea) gelators that can be used in solid-state screens of two AstraZeneca APIs, AZD2281 and AZD6140, which both exhibit polymorphism. The primary aim is to investigate the effect that API-mimetic gelators may have on crystallisation outcomes when utilised as crystallisation media. The gelation and self-assembly behaviour of the synthesised bis(urea) compounds were characterised , including via SCXRD, to understand any presence (or absence) of gelation behaviour. Solution and gel-phase crystallisations of each API compound were undertaken, using both API-mimetic gelators and generic gelators bearing minimal resemblance to the API molecules. Various API and gelator concentrations were tested to attempt to find conditions under which the API and gel fibres would interact and influence crystallisation. The API material obtained from crystallisation experiments was characterised using X-ray diffraction, DSC and IR spectroscopy and compared with experimental data for the known polymorphic forms.

The penultimate chapter describes the design and crystallisation of a series of chiral and achiral symmetrical bis(acyl-semicarbazide) molecules. The acyl-semicarbazide functionality has rarely been reported in gelator structures, but theoretically the

molecules could form strong, unidirectional hydrogen bond synthons typically associated with versatile gelation behaviour. The Steed group has heavily relied upon using 4,4-MDEP as the core for LMWG compounds. However, sometimes incorporating a desirable functional end group to mimic or interact with a crystallisation substrate can result in a lack of gelation, either through poor solubility or disruption of gel-promoting supramolecular synthons. Identifying additional spacer functionalities that yield highly effective gels could increase structural diversity of LMWGs in the gelator toolkit. In this chapter, a range of bis(acyl-semicarbazides) were synthesised and attempts to grow single crystals of these compounds were made. The solved and refined crystal structures that were obtained provide an understanding for how many structural features impact self-assembly behaviour of the bis(acyl-semicarbazides), including aliphatic vs aromatic spacer groups, aliphatic spacer length and the chirality of the functional end groups. Similar to chapter 1, the focus in this chapter is understanding the molecular packing and supramolecular synthons that can be formed by potential gelator molecules, with the objective to identify any structure motifs that may promote or discourage gelation of bis(acyl)-semicarbazide compounds.

The final chapter then explores the gelation behaviour of the same series of bis(acyl-semicarbazide) compounds. The gels formed were characterised and through rheology, SEM and ball-drop experiments and the gels of all analogues were compared, using the understanding of molecular conformations and self-assembly from the crystal structures reported in the preceding chapter to hypothesise about the bulk gel properties. The effects of anion addition on the gel rheological and morphologies were also explored. These designer gels were then used in a wide range of pharmaceutical crystallisations to see if they could influence the crystallisation of drugs, including via API-mimetic crystallisations, crystallisation of an anionic API-salt and attempts to achieve chiral resolution of racemic API compounds.

1.11 References

1 H. Al-Obaidi, M. Majumder and F. Bari, *Curr. Pharm. Des.*, 2016, **23**, 350–361.

2 R. Censi and P. Di Martino, *Molecules*, 2015, **20**, 18759–18776.

3 J. Varshosaz, E. Ghassami and S. Ahmadipour, *Curr. Pharm. Des.*, 2018, **24**, 2473–2496.

4 A. Nangia, *Acc. Chem. Res.*, 2008, **41**, 595–604.

5 J. Bernstein, *Cryst. Growth Des.*, 2011, **11**, 632–650.

6 S. R. Vippagunta, H. G. Brittain and D. J. W. Grant, *Adv. Drug Deliv. Rev.*, 2001, **48**, 3–26.

7 J. Bernstein, *Polymorphism in Molecular Crystals*, Oxford University Press., 2010.

8 E. H. Lee, *Asian J. Pharm. Sci.*, 2014, **9**, 163–175.

9 Michael E Aulton, *Aulton's Pharmaceutics*, Harcourt Publishers Limited, London, 2013, vol. 4.

10 D. Singhal and W. Curatolo, *Adv. Drug Deliv. Rev.*, 2004, **56**, 335–347.

11 S. Roy, R. Banerjee, A. Nangia and G. J. Kruger, *Chem. - A Eur. J.*, 2006, **12**, 3777–3788.

12 L. X. Yu, M. S. Furness, A. Raw, K. P. Woodland Outlaw, N. E. Nashed, E. Ramos, S. P. F. Miller, R. C. Adams, F. Fang, R. M. Patel, F. O. Holcombe, Y. Y. Chiu and A. S. Hussain, *Pharm. Res.*, 2003, 20, 531–536.

13 V. J. Smith, C. G. Marais, K. Suwińska, J. Lipkowski, A. Szumna, C. Esterhuysen and L. J. Barbour, *CrystEngComm*, 2015, **17**, 5129–5133.

14 P. G. Jones, H. Hopf, A. Silaghi and C. Näther, *Acta Crystallogr. Sect. C Cryst. Struct. Commun.*, 2011, **67**, 405–408.

15 P. Munshi and T. N. G. Row, *Cryst. Growth Des.*, 2006, **6**, 708–718.

16 D.-K. Bucar, R. W. Lancaster and J. Bernstein, *Angew. Chemie - Int. Ed.*, 2015, **54**, 6972–6993.

17 H. M. Cuppen, M. M. H. Smets, A. M. Krieger, J. A. Van Den Ende, H. Meekes, E. R. H. Van Eck and C. H. Görbitz, *Cryst. Growth Des.*, 2019, **19**, 1709–1719.

18 D. P. Elder, R. Holm and H. L. De Diego, *Int. J. Pharm.*, 2013, **50**, 6665–6672.

19 A. M. Healy, Z. A. Worku, D. Kumar and A. M. Madi, *Adv. Drug Deliv. Rev.*, 2017, **117**, 25–46.

20 A. Kumar, S. Kumar and A. Nanda, *Adv. Pharm. Bull.*, 2018, **8**, 855–863.

21 D. J. Berry and J. W. Steed, *Adv. Drug Deliv. Rev.*, 2017, **117**, 3–24.

22 I. Sathisaran and S. V. Dalvi, *Pharmaceutics*, 2018, 10.

23 E. Grothe, H. Meekes, E. Vlieg, J. H. Ter Horst and R. De Gelder, *Cryst. Growth Des.*, 2016, **16**, 3237–3243.

24 A. R. Thayyil, T. Juturu, S. Nayak and S. Kamath, *Adv. Pharm. Bull.*, 2020, **10**, 203–212.

25 Center of Drug Evaluation and Research, *Regulatory classification of pharmaceutical co-crystals, guidance for industry*, 2018.

26 EMA, *Reflection paper on the use of cocrystals and other solid state forms of active substances in medicinal products*, 2015.

27 H. Grohganz, P. A. Priemel, K. Löbmann, L. H. Nielsen, R. Laitinen, A. Mullertz, G. Van Den Mooter and T. Rades, *Expert Opin. Drug Deliv.*, 2014, **11**, 977–989.

28 A. Karagianni, K. Kachrimanis and I. Nikolakakis, *Pharmaceutics*, 2018, **10**, 98.

29 P. Kanaujia, P. Poovizhi, W. K. Ng and R. B. H. Tan, *Powder Technol.*, 2015, **285**, 2–15.

30 N. M. Belozerova, P. Bilski, M. Jarek, J. Jenczyk, S. E. Kichanov, D. P. Kozlenko, J. Mielcarek, A. Pajzderska and J. Wąsicki, *RSC Adv.*, 2020, **10**, 33585–33594.

31 J. Ulrich and M. J. Jones, in *Industrial Crystallization Process Monitoring and Control*, eds. H. J. M. Kramer and A. Chianese, Wiley-VCH Verlag GmbH, 2012, pp. 127–138.

32 E. Ruckenstein, G. O. Berim and G. Narsimhan, *Adv. Colloid Interface Sci.*, 2015, **215**, 13–27.

33 R. P. Sear, *CrystEngComm*, 2014, **16**, 6506–6522.

34 D. Erdemir, A. Y. Lee and A. S. Myerson, *Acc. Chem. Res.*, 2009, **42**, 621–629.

35 K. Sangwal, in *Nucleation and Crystal Growth*, ed. K. Sangwal, John Wiley & Sons, New Jersey, 2018, pp. 361–421.

36 S. Karthika, T. K. Radhakrishnan and P. Kalaichelvi, *Cryst. Growth Des.*, 2016, **16**, 6663–6681.

37 J. Cookman, V. Hamilton, S. R. Hall and U. Bangert, *Sci. Rep.*, 2020, **10**, 19156.

38 P. G. Vekilov, *J. Cryst. Growth*, 2005, **275**, 65–76.

39 P. G. Vekilov, *Nanoscale*, 2010, **2**, 2346–2357.

40 J. Chen, B. Sarma, J. M. B. Evans and A. S. Myerson, *Cryst. Growth Des.*, 2011, **11**, 887–895.

41 J. Nývlt, *Cryst. Res. Technol.*, 1995, **30**, 443–449.

42 A. L. Washington, M. E. Foley, S. Cheong, L. Quffa, C. J. Breshike, J. Watt, R. D. Tilley and G. F. Strouse, *J. Am. Chem. Soc.*, 2012, **134**, 17046–52.

43 J. C. Burley, M. J. Duer, R. S. Stein and R. M. Vrcelj, *Eur. J. Pharm. Sci.*, 2007, **31**, 271–276.

44 G. G. Z. Zhang, C. Gu, M. T. Zell, R. Todd Burkhardt, E. J. Munson and D. J. W. Grant, *J. Pharm. Sci.*, 2002, **91**, 1089–1100.

45 G. T. Rengarajan, D. Enke, M. Steinhart and M. Beiner, *Phys. Chem. Chem. Phys.*, 2011, **13**, 1367–1374.

46 C. Chen, O. Cook, C. E. Nicholson and S. J. Cooper, *Cryst. Growth Des.*, 2011, **11**, 2228–2237.

47 C. E. Nicholson and S. J. Cooper, *Crystals*, 2011, **1**, 195–205.

48 J. Anwar and D. Zahn, *Adv. Drug Deliv. Rev.*, 2017, **117**, 47–70.

49 N. Zencirci, T. Gelbrich, D. C. Apperley, R. K. Harris, V. Kahlenberg and U. J. Griesser, *Cryst. Growth Des.*, 2010, **10**, 302–313.

50 S. Jiang, P. J. Jansens and J. H. Ter Horst, *Cryst. Growth Des.*, 2010, **10**, 2123–2128.

51 K. Matsuo and M. Matsuoka, *J. Chem. Eng. Japan*, 2007, **40**, 541–549.

52 T. Suzuki, T. Araki, H. Kitaoka and K. Terada, *Int. J. Pharm.*, 2010, **402**, 110–116.

53 H. Tomkowiak, A. Olejniczak and A. Katrusiak, *Cryst. Growth Des.*, 2013, **13**, 121–125.

54 K. Kawakami, *J. Pharm. Sci.*, 2007, **96**, 982–989.

55 C. H. Gu, V. Young and D. J. W. Grant, *J. Pharm. Sci.*, 2001, **90**, 1878–1890.

56 S. M. Reutzel-Edens, *Curr. Opin. Drug Discov. Dev.*, 2006, **9**, 806–815.

57 M. D. Ward, *Curr. Opin. Colloid Interface Sci.*, 1997, **2**, 51–64.

58 S. S. Kumar, S. Rana and A. Nangia, *Chem. - An Asian J.*, 2013, **8**, 1551–1568.

59 J. S. Song and Y. T. Sohn, *J. Pharm. Investig.*, 2012, **42**, 127–131.

60 P. Láng, E. Várkonyi, J. Ulrich, P. Szabó-Révész and Z. Aigner, *J. Pharm. Biomed. Anal.*, 2015, **102**, 229–235.

61 R. Perumal and S. Moorthy Babu, *Curr. Appl. Phys.*, 2010, **10**, 858–865.

62 J. Lu, J. Wang, Z. Li and S. Rohani, *African J. Pharm. Pharmacol.*, 2012, **6**, 269–277.

63 J.-B. Qiu, G. Li, Y. Sheng and M.-R. Zhu, *J. Pharm. Biomed. Anal.*, 2015, **107**, 298–303.

64 L. yu Wang, L. Zhu, Z. liang Sha, X. chao Li, Y. fei Wang, L. bin Yang and X. yu Zhao, *J. Therm. Anal. Calorim.*, 2017, **127**, 1533–1542.

65 F. T. Martins, A. O. Legendre, S. B. Honorato, A. P. Ayala, A. C. Doriguetto and J. Ellena, *Cryst. Growth Des.*, 2010, **10**, 1885–1891.

66 N. Chieng, T. Rades and J. Aaltonen, *J. Pharm. Biomed. Anal.*, 2011, **55**, 618–644.

67 P. Y. Zavalij and S. M. Whittingham, *Rigaku J.*, 2004, **21**, 2–14.

68 P. S. Wray, W. E. Sinclair, J. W. Jones, G. S. Clarke and D. Both, *Int. J. Pharm.*, 2015, **493**, 198–207.

69 A. V. Ewing, P. S. Wray, G. S. Clarke and S. G. Kazarian, *J. Pharm. Biomed. Anal.*, 2015, **111**, 248–256.

70 H. Nie, Z. Liu, B. C. Marks, L. S. Taylor, S. R. Byrn and P. J. Marsac, *J. Pharm. Biomed. Anal.*, 2016, **118**, 328–337.

71 M. Farias and R. Carneiro, *Molecules*, 2014, **19**, 128–138.

72 S. F. Barakh Ali, Z. Rahman, S. Dharani, H. Afrooz and M. A. Khan, *J. Pharm. Sci.*, 2019, **108**, 1211–1219.

73 A. Borrego-Sánchez, A. Hernández-Laguna and C. I. Sainz-Díaz, *J. Mol. Model.*, 2017, **23**, 106.

74 M. Antonio and R. M. Maggio, *J. Pharm. Biomed. Anal.*, 2018, **149**, 603–611.

75 M. C. Hennigan and A. G. Ryder, *J. Pharm. Biomed. Anal.*, 2013, **72**, 163–171.

76 H. Park, H. Nie, A. Dhiman, V. Tomar and Q. T. Zhou, *Mol. Pharm.*, 2020, **17**, 3043–3052.

77 C. Starbuck, A. Spartalis, L. Wai, J. Wang, P. Fernandez, C. M. Lindemann, G. X. Zhou and Z. Ge, *Cryst. Growth Des.*, 2002, **2**, 515–522.

78 R. D. Oparin, Y. A. Vaksler, M. A. Krestyaninov, A. Idrissi, S. V. Shishkina and M. G. Kiselev, *J. Supercrit. Fluids*, 2019, **152**, 104547.

79 M. Inoue, H. Hisada, T. Koide, J. Carriere, R. Heyler and T. Fukami, *Org. Process Res. Dev.*, 2017, **21**, 262–265.

80 H. Pataki, I. Csontos, Z. K. Nagy, B. Vajna, M. Molnar, L. Katona and G. Marosi, *Org. Process Res. Dev.*, 2013, **17**, 493–499.

81 M. A. dos S. Farias, F. L. F. Soares and R. L. Carneiro, *J. Pharm. Biomed. Anal.*, 2016, **121**, 209–214.

82 Y. lee Hong, G. N. Manjunatha Reddy and Y. Nishiyama, *Solid State Nucl. Magn. Reson.*, 2020, **106**, 101651.

83 M. Zielińska-pisklak, D. M. Pisklak and I. Wawer, *J. Pharm. Sci.*, 2012, **101**, 1763–1772.

84 R. K. Harris, *J. Pharm. Pharmacol.*, 2007, **59**, 225–239.

85 K. E. Dempah, D. H. Barich, A. M. Kaushal, Z. Zong, S. D. Desai, R. Suryanarayanan, L. Kirsch and E. J. Munson, *AAPS PharmSciTech*, 2013, **14**, 19–28.

86 F. G. Vogt, G. R. Williams, M. N. Johnson and R. C. B. Copley, *Cryst. Growth Des.*, 2013, **13**, 5353–5367.

87 P. Láng, V. Kiss, R. Ambrus, G. Farkas, P. Szabó-Révész, Z. Aigner and E. Várkonyi, *J. Pharm. Biomed. Anal.*, 2013, **84**, 177–183.

88 J. L. Ford and T. E. Mann, *Adv. Drug Deliv. Rev.*, 2012, 64, 422–430.

89 E. Verdonck, K. Schaap and L. C. Thomas, *Int. J. Pharm.*, 1999, **192**, 3–20.

90 C. McGregor, M. H. Saunders, G. Buckton and R. D. Saklatvala, *Thermochim. Acta*, 2004, **417**, 231–237.

91 C. McGregor and E. Bines, *Int. J. Pharm.*, 2008, **350**, 48–52.

92 M. R. A. Bakar, Z. K. Nagy and C. D. Rielly, *J. Therm. Anal. Calorim.*, 2010, **99**, 609–619.

93 N. Stieger, M. Aucamp, S. W. Zhang and M. M. De Villiers, *Am. Pharm. Rev.*, 2012, **15**, 32–36.

94 A. Kumar, P. Singh and A. Nanda, *Appl. Microsc.*, 2020, **50**, 1–12.

95 D. J. Berry, C. C. Seaton, W. Clegg, R. W. Harrington, S. J. Coles, P. N. Horton, M. B. Hursthouse, R. Storey, W. Jones, T. Friščić and N. Blagden, *Cryst. Growth Des.*, 2008, **8**, 1697–1712.

96 G. L. Perpétuo, G. O. Chierice, L. T. Ferreira, T. F. C. Fraga-Silva, J. Venturini, M. S. P. Arruda, G. Bannach and R. A. E. Castro, *Thermochim. Acta*, 2017, **651**, 1–10.

97 J. Haleblian and W. McCrone, *J. Pharm. Sci.*, 1969, 58, 911–929.

98 G. Saurabh and C. Kaushal, *J. Chem. Pharm. Res.*, 2011, 3, 6–17.

99 S. Agatonovic-Kustrin, T. Rades, V. Wu, D. Saville and I. G. Tucker, *J. Pharm. Biomed. Anal.*, 2001, **25**, 741–750.

100 G. Vistoli, A. Pedretti and B. Testa, *Drug Discov. Today*, 2008, **13**, 285–94.

101 M. M. De Villiers, J. G. Van der Watt and A. P. Lotter, *Drug Dev. Ind. Pharm.* , 1991, **17**, 1295–1303.

102 A. Glazko, H. Carnes, A. Kazenko, L. Wolf and T. Reutner, *Antibiot. Annu.*, 1957, **5**, 792–802.

103 T. Maeda, H. Takenaka, Y. Yamahira and T. Noguchi, *Chem Pharm Bull (Tokyo).*, 1980, **28**, 431–436.

104 J. Bauer, S. Spanton, R. Henry, J. Quick, W. Dziki, W. Porter and J. Morris, *Pharm. Res.*, 2001, **18**, 859–866.

105 P. T. A. Galek, F. H. Allen, L. Fábián and N. Feeder, *CrystEngComm*, 2009, **11**, 2634–2639.

106 A. Nangia, *J. Indian Inst. Sci.*, 2007, 87, 133–147.

107 D. Law, E. A. Schmitt, K. C. Marsh, E. A. Everitt, W. Wang, J. J. Fort, S. L. Krill and Y. Qiu, *J. Pharm. Sci.*, 2004, **93**, 563–570.

108 D. Law, S. L. Krill, E. A. Schmitt, J. J. Fort, Y. Qiu, W. Wang and W. R. Porter, *J. Pharm. Sci.*, 2001, **90**, 1015–1025.

109 S. L. Morissette, S. Soukasene, D. Levinson, M. J. Cima and O. Almarsson, *PNAS*, 2003, **100**, 2180–2184.

110 A. Raw and M. S. Furness, *Adv. Drug Deliv. Rev.*, 2004, **56**, 397–414.

111 I. B. Rietveld and R. Céolin, *J. Pharm. Sci.*, 2015, **104**, 4117–4122.

112 G. Goldbeck, E. Pidcock and C. R. Groom, *CCDC White Pap.*, 2011, 1–8.

113 L. H. Thomas, C. Wales, L. Zhao and C. C. Wilson, *Cryst. Growth Des.*, 2011, **11**, 1450–1452.

114 P. Di Martino, P. Conflant, M. Drache, J. P. Huvenne and A. M. Guyot-Hermann, *J. Therm. Anal.*, 1997, **48**, 447–458.

115 M. A. Perrin, M. A. Neumann, H. Elmaleh and L. Zaske, *Chem. Commun.*, 2009, 3181–3183.

116 P. Di Martino, A. M. Guyot-Hermann, P. Conflant, M. Drache and J. C. Guyot, *Int. J. Pharm.*, 1996, **128**, 1–8.

117 E. Joiris, P. Di Martino, C. Berneron, A. M. Guyot-Hermann and J. C. Guyot, *Pharm. Res.*, 1998, **15**, 1122–1130.

118 D. A. Druzhbin, T. N. Drebushchak, V. S. Min'kov and E. V Boldyreva, *J. Struct. Chem.*, 2015, **56**, 317–323.

119 J.-P. Brog, C.-L. Chanez, A. Crochet and K. M. Fromm, *RSC Adv.*, 2013, **3**, 16905.

120 G. Nicnols and C. S. Frampton, *J. Pharm. Sci.*, 1998, **87**, 684–693.

121 A. L. Grzesiak, M. Lang, K. Kim and A. J. Matzger, *J. Pharm. Sci.*, 2003, **92**, 2260–2271.

122 J. B. Arlin, L. S. Price, S. L. Price and A. J. Florence, *Chem. Commun.*, 2011, **47**, 7074–7076.

123 A. Johnston, B. F. Johnston, A. R. Kennedy and A. J. Florence, *CrystEngComm*, 2008, **10**, 23–25.

124 M. Ullah, I. Hussain and C. C. Sun, *Drug Dev. Ind. Pharm.*, 2016, **42**, 969–976.

125 N. Qiao, K. Wang, W. Schlindwein, A. Davies and M. Li, *Eur. J. Pharm. Biopharm.*, 2013, **83**, 415–426.

126 Z. Rahman, R. Samy, V. A. Sayeed and M. A. Khan, *Pharm. Dev. Technol.*, 2012, **17**, 457–465.

127 R. Yutani, R. Haku, R. Teraoka, C. Tode, T. Koide, S. Kitagawa, T. Sakane and T. Fukami, *Crystals*, 2019, **9**, 553–564.

128 S. R. Kennedy, C. D. Jones, D. S. Yufit, C. E. Nicholson, S. J. Cooper and J. W. Steed, *CrystEngComm*, 2018, **20**, 1390–1398.

129 K. Zhang, N. Fellah, A. G. Shtukenberg, X. Fu, C. Hu and M. D. Ward, *CrystEngComm*, 2020, **22**, 2705–2708.

130 L. Yu, G. A. Stephenson, C. A. Mitchell, C. A. Bunnell, S. V. Snorek, J. J. Bowyer, T. B. Borchardt, J. G. Stowell and S. R. Byrn, *J. Am. Chem. Soc.*, 2000, **122**, 585–591.

131 S. Chen, I. A. Guzei and L. Yu, *J. Am. Chem. Soc.*, 2005, **127**, 9881–9885.

132 L. Yu, *Acc. Chem. Res.*, 2010, **43**, 1257–1266.

133 X. Li, X. Ou, H. Rong, S. Huang, J. Nyman, L. Yu and M. Lu, *Cryst. Growth Des.*, 2020, **20**, 7093–7097.

134 A. Tyler, R. Ragbirsingh, C. J. McMonagle, P. G. Waddell, S. E. Heaps, J. W. Steed, P. Thaw, M. J. Hall and M. R. Probert, *Chem*, 2020, **6**, 1755–1765.

135 A. Lévesque, T. Maris and J. D. Wuest, *J. Am. Chem. Soc.*, 2020, **142**, 11873–11883.

136 M. Vasileiadis, A. V. Kazantsev, P. G. Karamertzanis, C. S. Adjiman and C. C. Pantelides, *Acta Crystallogr. Sect. B Struct. Sci.*, 2012, **68**, 677–685.

137 B. A. Nogueira, C. Castiglioni and R. Fausto, *Commun. Chem.*, 2020, **3**, Article 34, 1–12.

138 A. Singh, I. S. Lee and A. S. Myerson, *Cryst. Growth Des.*, 2009, **9**, 1182–1185.

139 I. Ziemecka, S. Gokalp, S. Stroobants, F. Brau, D. Maes and A. De Wit, *Crystals*, 2019, **9**, 351–361.

140 A. Fernandez-Barbero, I. J. Suarez, B. Sierra-Martin, A. Fernandez-Nieves, F. J. de las Nieves, M. Marquez, J. Rubio-Retama and E. Lopez-Cabarcos, *Adv. Colloid Interface Sci.*, 2009, **147**, 88–108.

141 H. Bunzen and E. Kolehmainen, *Molecules*, 2013, **18**, 3745–3759.

142 Y. S. R. Elnaggar, W. M. El-Refaie, M. A. El-Massik and O. Y. Abdallah, *J. Control. Release*, 2014, **180**, 10–24.

143 S. Banerjee and S. Bhattacharya, *Crit. Rev. Food Sci. Nutr.*, 2012, **52**, 334–346.

144 J. H. Jung, J. H. Lee, J. R. Silverman and G. John, *Chem. Soc. Rev.*, 2013, **42**, 924–936.

145 A. V. Goponenko and Y. A. Dzenis, *Polym.*, 2016, **101**, 415–449.

146 W. T. Truong, Y. Su, J. T. Meijer, P. Thordarson and F. Braet, *Chem. - An Asian J.*, 2011, **6**, 30–42.

147 Z. Wei, J. H. Yang, J. Zhou, F. Xu, M. Zrínyi, P. H. Dussault, Y. Osada and Y. M. Chen, *Chem. Soc. Rev.*, 2014, **43**, 8114–8131.

148 J. V. Alemán, A. V. Chadwick, J. He, M. Hess, K. Horie, R. G. Jones, P. Kratochvíl, I. Meisel, I. Mita, G. Moad, S. Penczek and R. F. T. Stepto, *Pure Appl. Chem.*, 2007, **79**, 1801–1829.

149 N. A. Peppas, Adv. Mater. 2006, 18, 1345–1360.

150 E. M. Ahmed, *J. Adv. Res.*, 2015, **6**, 105–121.

151 D. J. Abdallah and R. G. Weiss, *Adv. Mater.*, 2000, **12**, 1237–1247.

152 S. Murdan, *Expert Opin. Drug Deliv.*, 2005, **2**, 489–505.

153 A. Vintiloiu and J.-C. Leroux, *J. Control. Release*, 2008, **125**, 179–192.

154 M. A. Néouze, J. Le Bideau, P. Gaveau, S. Bellayer and A. Vioux, *Chem. Mater.*, 2006, **18**, 3931–3936.

155 A. Vioux, L. Viau, S. Volland and J. Le Bideau, *Comptes Rendus Chim.*, 2010, **13**, 242–255.

156 J. Le Bideau, L. Viau and A. Vioux, *Chem. Soc. Rev.*, 2011, **40**, 907–925.

157 P. Veres, A. M. López-Periago, I. Lázár, J. Saurina and C. Domingo, *Int. J. Pharm.*, 2015, **496**, 360–370.

158 B. Lee, S. Lee, M. Lee, D. H. Jeong, Y. Baek, J. Yoon and Y. H. Kim, *Nanoscale*, 2015, **7**, 6782–6789.

159 J.-Y. Hong, J. J. Wie, Y. Xu and H. S. Park, *Phys. Chem. Chem. Phys.*, 2015, **17**, 30946–30962.

160 R. G. Weiss, *J. Am. Chem. Soc.*, 2014, **136**, 7519–7530.

161 C. D. Jones and J. W. Steed, *Chem. Soc. Rev.*, 2016, **45**, 6546–6596.

162 G. Ghosh, R. Barman, J. Sarkar and S. Ghosh, *J. Phys. Chem. B*, 2019, **123**, 5909–5915.

163 M. Himabindu and A. Palanisamy, *Gels*, 2017, **3**, 12.

164 J. Bachl, D. Sampedro, J. Mayr and D. Díaz Díaz, *Phys. Chem. Chem. Phys.*, 2017, **19**, 22981–22994.

165 A. Z. Cardoso, L. L. E. Mears, B. N. Cattoz, P. C. Griffiths, R. Schweins and D. J. Adams, *Soft Matter*, 2016, **12**, 3612–3621.

166 R. Kuosmanen, K. Rissanen and E. Sievänen, *Chem. Soc. Rev.*, 2020, **49**, 1977–1998.

167 J. L. Andrews, E. Pearson, D. S. Yufit, J. W. Steed and K. Edkins, *Cryst. Growth Des.*, 2018, **18**, 7690–7700.

168 E. C. Barker, A. D. Martin, C. J. Garvey, C. Y. Goh, F. Jones, M. Mocerino, B. W. Skelton, M. I. Ogden and T. Becker, *Soft Matter*, 2017, **13**, 1006-1011

169 J. Cui, Z. Shen and X. Wan, *Langmuir*, 2010, **26**, 97–103.

170 T. Yuan, Y. Xu, J. Fei, H. Xue, X. Li, C. Wang, G. Fytas and J. Li, *Angew. Chemie - Int. Ed.*, 2019, **58**, 11072–11077.

171 A. Vidyasagar and K. M. Sureshan, *Angew. Chemie - Int. Ed.*, 2015, **54**, 12078–82.

172 X. Tong, Y. Qiu, X. Zhao, B. Xiong, R. Liao, H. Peng, Y. Liao and X. Xie, *Soft Matter*, 2019, **15**, 6411–6417.

173 P. R. A. Chivers and D. K. Smith, *Nat. Rev. Mater.*, 2019, **4**, 463–478.

174 M. Liu, G. Ouyang, D. Niu and Y. Sang, *Org. Chem. Front.*, 2018, 5.

175 E. R. Draper and D. J. Adams, *Chem*, 2017, 3.

176 P. K. Hashim, J. Bergueiro, E. W. Meijer and T. Aida, *Prog. Polym. Sci.*, 2020, **105**, 101250.

177 T. Steiner, *Angew. Chem. Int. Ed.*, 2002, **41**, 48–76.

178 S. S. Babu, V. K. Praveen and A. Ajayaghosh, *Chem. Rev.*, 2014, **114**, 1973–2129.

179 S. Bhattacharjee and S. Bhattacharya, *Langmuir*, 2016, **32**, 4270–4277.

180 L. Meazza, J. A. Foster, K. Fucke, P. Metrangolo, G. Resnati and J. W. Steed, *Nat. Chem.*, 2013, **5**, 42–47.

181 R. Roy, T. K. Adalder and P. Dastidar, *Chem. - An Asian J.*, 2018, **13**, 552–559.

182 U. K. Das, D. R. Trivedi, N. N. Adarsh and P. Dastidar, *J. Org. Chem.*, 2009, **74**, 7111–7121.

183 R. Parveen and P. Dastidar, *Chem. - A Eur. J.*, 2016, **22**, 9257–9266.

184 J. A. Foster, R. M. Edkins, G. J. Cameron, N. Colgin, K. Fucke, S. Ridgeway, A. G. Crawford, T. B. Marder, A. Beeby, S. L. Cobb and J. W. Steed, *Chem. Eur. J.*, 2014, **20**, 279–291.

185 S. J. Wezenberg, C. M. Croisetu, M. C. A. Stuart and B. L. Feringa, *Chem. Sci.*, 2016, **7**, 4341–4346.

186 Z. Qi, P. Malo de Molina, W. Jiang, Q. Wang, K. Nowosinski, A. Schulz, M. Gradzielski and C. A. Schalley, *Chem. Sci.*, 2012, **3**, 2073.

187 M.-O. M. Piepenbrock, N. Clarke, J. A. Foster and J. W. Steed, *Chem. Commun.*, 2011, **47**, 2095–2097.

188 F. Piana, D. H. Case, S. M. Ramalhete, G. Pileio, M. Facciotti, G. M. Day, Y. Z. Khimyak, J. Angulo, R. C. D. Brown and P. A. Gale, *Soft Matter*, 2016, **12**, 4034–4043.

189 M. O. M. Piepenbrock, G. O. Lloyd, N. Clarke and J. W. Steed, *Chem. Commun.*, 2008, 2644–2646.

190 A. E. Hooper, S. R. Kennedy, C. D. Jones and J. W. Steed, *Chem. Commun.*, 2016, **52**, 198–201.

191 L. S. Reddy, S. Basavoju, V. R. Vangala and A. Nangia, *Cryst. Growth Des.*, 2006, **6**, 161–173.

192 Z. Li, L. E. Buerkle, M. R. Orseno, K. A. Streletzky, S. Seifert, A. M. Jamieson and S. J. Rowan, *Langmuir*, 2010, **26**, 10093–100101.

193 K. L. Morris, L. Chen, A. Rodger, D. J. Adams and L. C. Serpell, *Soft Matter*, 2015, **11**, 1174–1181.

194 S. Awhida, E. R. Draper, T. O. McDonald and D. J. Adams, *J. Colloid Interface Sci.*, 2015, **455**, 24–31.

195 W. J. Peveler, H. Packman, S. Alexander, R. R. Chauhan, L. M. Hayes, T. J. Macdonald, J. K. Cockcroft, S. Rogers, D. G. A. L. Aarts, C. J. Carmalt, I. P. Parkin and J. C. Bear, *Soft Matter*, 2018, **14**, 8821–8827.

196 B. Hu, W. Sun, H. Li, H. Sui and S. Li, *Int. J. Pharm.*, 2018, **547**, 637–647.

197 A. R. Meyer, C. R. Bender, D. M. Dos Santos, F. I. Ziembowicz, C. P. Frizzo, M. A. Villetti, J. M. Reichert, N. Zanatta, H. G. Bonacorso and M. A. P. Martins, *Soft Matter*, 2018, **14**, 6716–6727.

198 T. Das, M. Häring, D. Haldar and D. Díaz Díaz, *Biomater. Sci.*, 2018, **6**, 38–59.

199 D. Ghosh, R. Bjornsson and K. K. Damodaran, *Gels*, 2020, **6**, 41–58.

200 D. Ghosh, M. T. Mulvee and K. K. Damodaran, *Molecules*, 2019, 24, DOI:10.3390/molecules24193472.

201 M. L. Muro-Small, J. Chen and A. J. McNeil, *Langmuir*, 2011, **27**, 13248–13253.

202 A. R. Hirst, I. A. Coates, T. R. Boucheteau, J. F. Miravet, B. Escuder, V. Castelletto, I. W. Hamley and D. K. Smith, *J. Am. Chem. Soc.*, 2008, **130**, 9113–9121.

203 Y. Lan, M. G. Corradini, R. G. Weiss, S. R. Raghavan and M. A. Rogers, *Chem. Soc. Rev.*, 2015, **44**, 6035–6058.

204 Y. Lan, M. G. Corradini, X. Liu, T. E. May, F. Borondics, R. G. Weiss and M. A. Rogers, *Langmuir*, 2014, **30**, 14128–14142.

205 D. Rosa Nunes, M. Raynal, B. Isare, P. A. Albouy and L. Bouteiller, *Soft Matter*, 2018, **14**, 4805–4809.

206 M. Bielejewski, A. Łapiński, R. Luboradzki and J. Tritt-Goc, *Tetrahedron*, 2011, **67**, 7222–7230.

207 Y. Jeong, K. Hanabusa, H. Masunaga, I. Akiba, K. Miyoshi, S. Sakurai and K. Sakurai, *Langmuir*, 2005, **21**, 586–594.

208 S. Bartocci, I. Morbioli, M. Maggini and M. Mba, *J. Pept. Sci.*, 2015, **21**, 871–878.

209 D. Mandal, S. Dinda, P. Choudhury and P. K. Das, *Langmuir*, 2016, **32**, 9780–9789.

210 K. McAulay, B. Dietrich, H. Su, M. T. Scott, S. Rogers, Y. K. Al-Hilaly, H. Cui, L. C. Serpell, A. M. Seddon, E. R. Draper and D. J. Adams, *Chem. Sci.*, 2019, **10**, 7801–7806.

211 J. Makarević, M. Jokić, Z. Raza, Z. Štefanić, B. Kojić-Prodić and M. Žinić, *Chem. - A Eur. J.*, 2003, **9**, 5567-80.

212 V. Čaplar, L. Frkanec, N. Š. Vujičić and M. Žinić, *Chem. - A Eur. J.*, 2010, **16**, 3066–3082.

213 D. A. Tómasson, D. Ghosh, Z. Kržišnik, L. H. Fasolin, A. A. Vicente, A. D. Martin, P. Thordarson and K. K. Damodaran, *Langmuir*, 2018, **34**, 12957-12967.

214 M. Qin, Y. Zhang, C. Xing, L. Yang, C. Zhao, X. Dou and C. Feng, *Chem. - A Eur. J.*, 2021, **27**, 3119–3129.

215 Z. Shen, T. Wang and M. Liu, *Langmuir*, 2014, **30**, 10772–10778.

216 R. G. Weiss and P. Terech, *Molecular gels: Materials with self-assembled fibrillar networks*, Springer Netherlands, 2006.

217 A. Dawn and H. Kumari, *Chem. - A Eur. J.*, 2018, **24**, 762–776.

218 P. Terech, D. Pasquier, V. Bordas and C. Rossat, *Langmuir*, 2000, **16**, 4485–4494.

219 G. Yu, X. Yan, C. Han and F. Huang, *Chem. Soc. Rev.*, 2013, **42**, 6697–6722.

220 Nonappa and E. Kolehmainen, *Soft Matter*, 2016, **12**, 6015–6026.

221 L. L. E. Mears, E. R. Draper, A. M. Castilla, H. Su, Zhuola, B. Dietrich, M. C. Nolan, G. N. Smith, J. Doutch, S. Rogers, R. Akhtar, H. Cui and D. J. Adams, *Biomacromolecules*, 2017, **18**, 3531–3540.

222 B. Bai, Z. Li, H. Wang, M. Li, Y. Ozaki and J. Wei, *R. Soc. Open Sci.*, 2018, **5**, 170492.

223 S. Baddi, S. S. Madugula, D. S. Sarma, Y. Soujanya and A. Palanisamy, *Langmuir*, 2016, **32**, 889–899.

224 C. D. Jones, H. T. D. Simmons, K. E. Horner, K. Liu, R. L. Thompson and J. W. Steed, *Nat. Chem.*, 2019, **11**, 375–381.

225 M. G. F. Angelerou, P. W. J. M. Frederix, M. Wallace, B. Yang, A. Rodger, D. J. Adams, M. Marlow and M. Zelzer, *Langmuir*, 2018, **34**, 6912–6921.

226 E. R. Draper, K. L. Morris, M. A. Little, J. Raeburn, C. Colquhoun, E. R. Cross, T. O. McDonald, L. C. Serpell and D. J. Adams, *CrystEngComm*, 2015, **17**, 8047–8057.

227 K. Morishima, X. Li, K. Oshima, Y. Mitsukami and M. Shibayama, *J. Chem. Phys.*, 2018, **149**, 163301.

228 S. A. Jamieson, K. W. K. Tong, W. A. Hamilton, L. He, M. James and P. Thordarson, *Langmuir*, 2014, **30**, 13987–13993.

229 A. Dawn, M. Mirzamani, C. D. Jones, D. S. Yufit, S. Qian, J. W. Steed and H. Kumari, *Soft Matter*, 2018, **14**, 9489.

230 C. Marmorat, A. Arinstein, N. Koifman, Y. Talmon, E. Zussman and M. Rafailovich, *Sci. Rep.*, 2016, **6**, 25495.

231 B. Escuder, M. LLusar and J. F. Miravet, *J. Org. Chem.*, 2006, **71**, 7747–7752.

232 M. Wallace, J. A. Iggo and D. J. Adams, *Soft Matter*, 2015, **11**, 7739–7747.

233 M. Wallace, J. A. Iggo and D. J. Adams, *Soft Matter*, 2017, **13**, 1716–1727.

234 C. Biertümpfel, J. Basquin, D. Suck and C. Sauter, in *Acta Crystallographica Section D: Biological Crystallography*, 2002, vol. 58, pp. 1657–1659.

235 B. Lorber, C. Sauter, A. Theobald-Dietrich, A. Moreno, P. Schellenberger, M. C. Robert, B. Capelle, S. Sanglier, N. Potier and R. Giege, *Prog. Biophys. Mol. Biol.*, 2009, **101**, 13–25.

236 B. Lorber, C. Sauter, M. C. Robert, B. Capelle and R. Giegé, *Acta Crystallogr. Sect. D Biol. Crystallogr.*, 1999, **55**, 1491–1494.

237 D. K. Kumar and J. W. Steed, *Chem. Soc. Rev.*, 2014, **43**, 2080–2088.

238 Y. Li, D. Guo and B. Zheng, *RSC Adv.*, 2012, **2**, 4857.

239 E. Ramachandran and S. Natarajan, *Indian J. Pure Appl. Phys.*, 2005, **43**, 372–376.

240 A. R. Patel and A. Venkateswara Rao, *Bull. Mater. Sci.*, 1982, 4, 527–548.

241 M. Pauchet, T. Morelli, S. Coste, J. J. Malandain and G. Coquerel, *Cryst. Growth Des.*, 2006, **6**, 1881–1889.

242 T. Seydel, R. M. Edkins, C. D. Jones, J. A. Foster, R. Bewley, J. A. Aguilar and K. Edkins, *Chem. Commun.*, 2018, **54**, 6340–6343.

243 J. A. Foster, M. M. Piepenbrock, G. O. Lloyd, N. Clarke, J. A. K. Howard and J. W. Steed, *Nat. Chem.*, 2010, **2**, 1037–43.

244 S. Gao, S. Wang, J. Ma, Y. Wu, X. Fu, R. K. Marella, K. Liu and Y. Fang, *Langmuir*, 2016, **32**, 12805–12813.

245 J. Buendía, E. Matesanz, D. K. Smith and L. Sánchez, *CrystEngComm*, 2015, **17**, 8146–8152.

246 W. Edwards and D. K. Smith, *J. Am. Chem. Soc.*, 2013, **135**, 5911–5920.

247 C. Sudha, P. Parimaladevi and K. Srinivasan, *Mater. Sci. Eng. C*, 2015, **47**, 150–155.

248 Y. Diao, K. E. Whaley, M. E. Helgeson, M. A. Woldeyes, P. S. Doyle, A. S. Myerson, T. A. Hatton and B. L. Trout, *J. Am. Chem. Soc.*, 2012, **134**, 673–684.

249 D. Alain, *Mater. Today*, 2013, **16**, 220–227.

250 A. Sharma, M. Thakur, M. Bhattacharya, T. Mandal and S. Goswami, *Biotechnol. Reports*, 2019, **21**, DOI:10.1016/j.btre.2019.e00316.

251 C. Ruiz-Palomero, S. R. Kennedy, M. L. Soriano, C. D. Jones, M. Valcarcel and J.

W. Steed, *Chem. Commun.*, 2016, **52**, 7782–7785.

252 M. Banerjee, S. Saraswatula, L. G. Willows, H. Woods and B. Brettmann, *J. Mater. Chem. B*, 2018, **6**, 7317–7328.

253 L. Kaufmann, S. R. Kennedy, C. D. Jones and J. W. Steed, *Chem. Commun.*, 2016, **52**, 10113–10116.

254 L. A. Estroff, L. Addadi, S. Weiner and A. D. Hamilton, *Org. Biomol. Chem.*, 2004, **2**, 137–141.

255 M. A. Rahim, Y. Hata, M. Björnmalm, Y. Ju and F. Caruso, *Small*, 2018, **14**, 1801202.

256 A. K. Patterson and D. K. Smith, *Chem. Commun.*, 2020, **56**, 11046–11049.

257 M. reza Saboktakin and R. M. Tabatabaei, *Int. J. Biol. Macromol.*, 2015, **75**, 426–436.

258 S. Bernhard and M. W. Tibbitt, *Adv. Drug Deliv. Rev.*, 2021, **171**, 240–256.

259 A. Dawn, K. S. Andrew, D. S. Yufit, Y. Hong, J. P. Reddy, C. D. Jones, J. A. Aguilar and J. W. Steed, *Cryst. Growth Des.*, 2015, **15**, 4591–4599.

260 J. A. Foster, K. K. Damodaran, A. Maurin, G. M. Day, H. P. G. Thompson, G. J. Cameron, J. C. Bernal and J. W. Steed, *Chem. Sci.*, 2017, **8**, 78–84.

261 B. Saikia, M. T. Mulvee, I. Torres-Moya, B. Sarma and J. W. Steed, *Cryst. Growth Des.*, 2020, **20**, 7978–7996.

262 N. Zencirci, U. J. Griesser, T. Gelbrich, D. C. Apperley and R. K. Harris, *Mol. Pharm.*, 2014, **11**, 338–350.

263 J. C. Reepmeyer, M. O. Rhodes, D. C. Cox and J. V. Silverton, *J. Chem. Soc. Perkin Trans. 2*, 1994, **9**, 2063–2067.

264 J. Raeburn and D. J. Adams, *Chem. Commun.*, 2015, **51**, 5170-5180

265 D. L. VanderHart, J. F. Douglas, S. D. Hudson, J. M. Antonucci, and E. A. Wilder, *Langmuir,* 2011, **27**, 1745–1757

266 S. S. Rohner, J. Ruiz-Olles and D. K. Smith, *RSC Adv.*, 2015, **5**, 27190-27196

267 S. M. Ramalhete, K. P. Nartowski, N. Sarathchandra, J. S. Foster, A. N. Round, J. Angulo, G. O. Lloyd, Y. Z. Khimyak, *Chemistry*., 2017, **23**, 8014-8024

Chapter 2 - Gelation and Crystallisation of the 'Magic Spacer'

2.1 Introduction

Past discoveries of LMWGs have largely depended on serendipity, but in recent times LMWGs have been designed by incorporating functionalities known to promote supramolecular gelation and by modifying the structures of known LMWGs. Over many years, the Steed group have reported numerous bis(urea) LMWGs, with many being structural modifications of 4,4-methylenebis(2,6-diethylphenyl) (4,4-MDEP) core spacer group (**2.0**).[1–3] Affectionately nicknamed the 'magic spacer' within the Steed group, bis(urea) compounds derived from 4,4-MDEP have consistently demonstrated gelation with remarkable versatility. Despite being used utilised in numerous published and unpublished LMWGs, little is known about why this spacer is generally so effective at bringing about gelation behaviour. It is assumed that urea α-tape synthons drive gelation behaviour of the LMWGs, with some crystal structure prediction (CSP) calculations on 4,4-MDEP analogue **2.1** previously showing that experimental XRPD patterns of these compounds match computational crystal structures that exhibit α-tape synthons. However, no crystal structures of 4,4-MDEP bis(urea) analogues have previously been obtained due to the tendency of compounds containing it to gel rather than crystallise. Whilst, It is important to note that gel fibres are often highly polymorphic and molecular packing arrangements in crystal structures may not be representative of the packing in gel fibres,[3,4] such crystal structures still provide valuable information regarding molecular conformations and packing tendencies that can potentially explain effective gelation behaviour.[1,5,6]

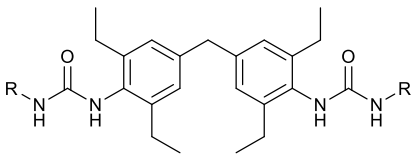

2.0

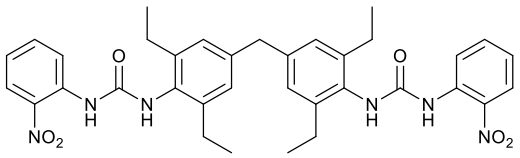

2.1

This work investigates the impact of different R-substituents on 4,4-MDEP bis(urea) derivatives on gelation behaviour and continues to describe an approach to grow single crystals of these compounds. A range of symmetrical 4,4-MDEP bis(urea) LMWGs are synthesised and their gelation capacity explored in a range of solvents. Attempts to grow single crystals of all these compounds were made to understand the

molecular conformations and molecular packing arrangements exhibited by the 4,4-MDEP analogues. The method utilised to promote crystallisation over gelation involved lowering the LMWG concentration below the critical gelation concentration (CGC) and adjusting environmental conditions accordingly.

One analogue was purposefully designed to generate steric hinderance near the urea functionalities by using *t*-butyl end groups. It was hypothesised that these steric effects may slow down unidirectional urea α-tape assembly and give the best chance for multidirectional crystal growth to occur. A single crystal of this analogue was successfully prepared and analysed via SCXRD. The crystal structure provides the first experimental crystallographic insight to the molecular packing behaviour of a 4,4-MDEP derived bis(urea) gelator.

2.2 Design and Synthesis

Bis(urea) 4,4-MDEP analogues **2a-g** were synthesised via reacting 4,4-methylenebis(2,6-diethylphenyl isocyanate) with 2.1 molar equivalents of the corresponding primary amines. The general synthetic procedure involved reacting the reagents under reflux in chloroform or THF, with a precipitate forming in most cases (**Scheme 2-1.** The general synthetic procedure for compounds **2a-g.**). This precipitate could be purified via washing with the reaction solvent and diethyl ether and then drying in a drying pistol under vacuum at 110 °C. The full synthetic details are outlined in the experimental section.

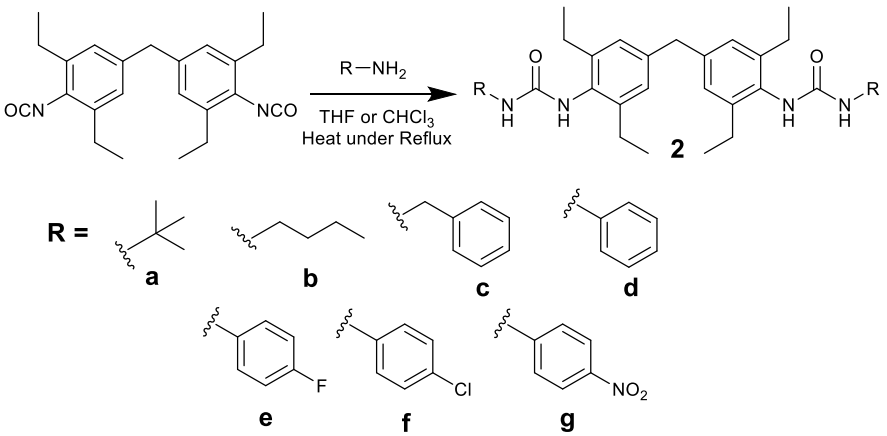

Scheme 2-1. The general synthetic procedure for compounds **2a-g.**

The R-groups used were chosen to explore how different structural features influence crystallisation and gelation behaviour of 4,4-MDEP analogues, including comparisons between aromatic and aliphatic end groups. It was hoped that crystal structures for all

compounds would provide a valuable and well-rounded insight to the molecular conformations and self-assembly behaviours adopted by 4,4-MDEP derivatives.

The *t*-butyl and *n*-butyl groups allow the effect of aliphatic branching on of short aliphatic groups to be explored. The use of phenyl and benzyl end groups enables the exploration of the effect of spacing between aromatic end group and urea functionalities on self-assembly behaviour and probes the influence of steric bulk near the urea carbonyl acceptor. Furthermore, the effects of electron-withdrawing substituents (F, Cl and NO_2) on the phenyl group are also of interest. The initial hypothesis was that electron-withdrawing substituents would increase the acidity of the urea NH functionalities and resulting in stronger urea-urea interactions. However, previous work reported by the Gale group demonstrated that this was not the case for a series of aliphatic mono-urea gelators with 4-nitrophenyl substituents directly adjacent to urea groups.[7] Whilst this study found, through DFT calculations, that the urea hydrogen atoms had a more positive electrostatic potential than an electron-donating derivative, the accessibility of the NO_2 group means that it can disrupt urea tape formation and any associated gelation. Furthermore, nitrophenyl substituents directly adjacent to urea functionalities cause $C\text{-}H_{(aryl)}\cdots O_{(urea)}$ interactions that essentially block the carbonyl acceptor from partaking in μ-tape synthons.[8] We are interested to see whether this result also applies to the 4,4-MDEP bis(urea) compounds and whether electron-withdrawing groups less capable of hydrogen bonding could enhance gelation via the increased acidity of the urea N-H.

2.3 Gel characterisation

2.3.1 Effect of R-group and solvent

The gelation behaviour of **2a-2g** were tested in a range of solvents spanning the polarity spectrum, initially at 1 % w/v on a 0.5 mL scale. Dissolution was aided by heating up to the boiling point of the solvent and samples were left to passively cool at ambient temperature. After 24 hours, the vials were inverted to qualitatively determine gel-like rheology (**Figure 2-1**). If the solvent was completely immobilised, it was considered to have gelled. A partial gel was classified where only a fraction of the solvent was immobilised. The gelation results are shown below (**Table 2-1**).

Table 2-1. Gel screen results of compounds 2a-g at 1 % w/v in the listed solvents. G^T = Translucent gel, G^C= clear/transparent gel, G^o = opaque gel, PG = partial gel, P = precipitate, S = solution, X = crystallisation

	2a	2b	2c	2d	2e	2f	2g
Nitrobenzene	G^{T*}	G^T	G^c	G^c	G^T	G^c	P
Chlorobenzene	S	G^T	G^T	P	P	G^T	P
1,2-Dichlorobenzene	S	G^T	G^T	G^T	G^T	G^T	P
Ethanol	P	G^o	P	P	P	P	IS
Methanol	PG/X*	P	P	IS	IS	IS	IS
THF	G^T	G^o	G^o	G^o	IS	P	P
DMF	S	G^T	G^T	P	P	P	P
Chloroform	P	G^o	P	IS	IS	P	P
Acetonitrile	P	G^o	G^T	P	P	P	P
1,4-dioxane	G^T	G^T	G^T	G^T	P	G^T	P
Toluene	P	G^T	G^T	G^T	P	G^T	P
Cyclohexane	P	P	IS	IS	IS	IS	IS
DMSO	P	G^T	G^T	G^T	P	G^T	P
Butan-2-one	G^o	G^o	G^o	P	IS	IS	P
Diethyl Ether	IS	IS	IS	IS	IS	IS	IS
DCM	P	G^o	P	IS	IS	IS	IS

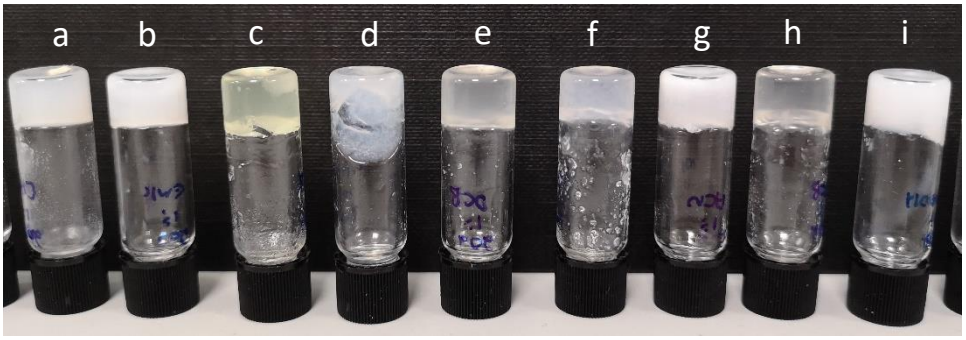

Figure 2-1. Gels of **2b** at 0.5 % w/v in **(a)** chlorobenzene, **(b)** butan-2-one, **(c)** nitrobenzene, **(d)** toluene, **(e)** 1,2-dichlorobeznene, **(f)** 1,4-dioxane, **(g)** acetonitrile, **(h)** DMSO and **(i)** ethanol.

Analogue **2b** (R = *n*-butyl) was the most versatile gelator, gelling 13 of the 16 tested solvents, including nitrobenzene, 1,4-dioxane, DMF and ethanol. The *t*-butyl derivative, **2a**, was far less versatile than **2b** only gelling nitrobenzene at 2 % w/v and THF, 1,4-dioxane and THF at 1 % w/v. Interestingly, **2b** also formed a partial gel in methanol at 1 % w/v, but when the concentration was increased to 2 % w/v homogenous gelation was not achieved, with miniscule crystalline needles forming concomitantly with a partial gel. This result supports the hypothesis that linear short alkyl chains are more versatile 4,4-MDEP-derived gelators than branched short alkyl chains.

Regarding the aromatic R-groups, analogue **2c** (R = benzyl) was the most versatile LMWGs, forming 10 gels. Analogues **2d** and **2f** each gelled 6 solvents. They mutually gelled nitrobenzene, 1,2-dichlorobenzene, 1,4-dioxane, DMSO and toluene, with **2d** also gelling THF, whilst **2f** gelled chlorobenzene. Compound **2e** (R = 4-fluorophenyl) was the least versatile gelator only gelling nitrobenzene and 1,2-dichlorobenzene, whilst compound **2g** (R= 4-nitrophenyl) was a non-gelator in all solvents tested. This evidence indicates that increasing the distance between urea functionality and aryl group improves gel versatility, whilst electron-withdrawing para-substituents reduce gelation capacity.

2.3.3 Rheological properties

In gels, the storage modulus (G') is an order of magnitude greater than the loss modulus (G") and remains constant as oscillatory shear is applied up to the yield stress of the gel.[9,10] Once the yield stress is exceeded, the gel breaks and the material flows. Here a representative gel of each analogue was investigated using frequency and stress sweep rheometry measurements. The 1,4-dioxane gels of compounds **2a-2d** and **2f** were used, whilst the sole 1,2-dichlorobenzene gel of **2e** was used for that compound. All gels were at 1 % w/v and were formed directly on the rheometer plate. Gelation took 30-60 mins to occur on the 2 mL scale, as opposed to a few minutes on the 0.5 mL scale which is consistent with previous reports of how vial type and gel volume can influence gelation times and behaviour.[11]

The frequency sweep measurements show that G' > G" by an order of magnitude for all gels, confirming their classifications as gels with all gels exhibiting a G' plateau of approximately 100,000 Pa (**Appendix 1**). Oscillatory stress sweep measurements were performed over 0.05-1000 Pa with a constant frequency of 1 Hz (**Figure 2-2**). The aliphatic R-groups **2a** and **2b** had higher yield stresses than the aromatic end groups. Interestingly, **2b** (R= *n*-butyl) was weaker than **2a** (R= *t*-butyl). Compound **2d** (R= phenyl) yielded weaker gels than **2c** (R= benzyl), whilst **2e** (R= 4-fluorophenyl) and **2f** (R= 4-chlorophenyl) were weaker than **2d**. These measurements are consistent with qualitative laboratory observations and ball-drop experiments (**Appendix 1**).

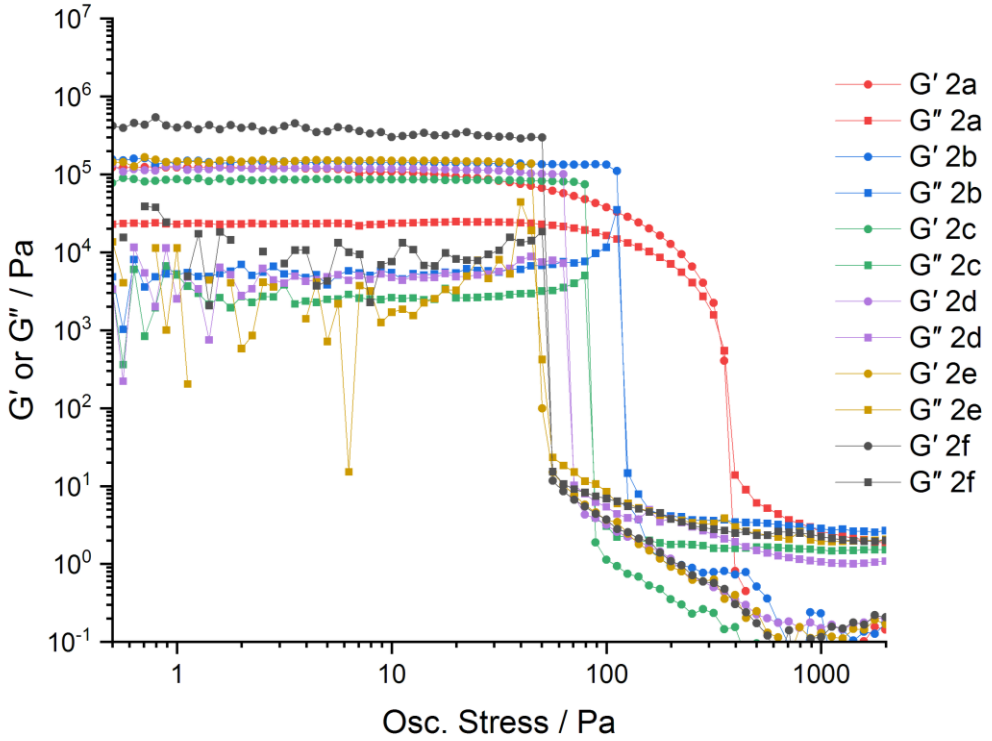

Figure 2-2. Stress-sweep measurements for 1 % w/v gels of **2a-2f**. The yield stress for each gel is defined as the point where G" exceeds G'. The solvent used was 1,4-dioxane for all gels, except **2e** where 1,2-dichlorobenzene was used instead due to a lack of gelation in 1,4-dioxane. Measurements were taken at 10 °C to minimize solvent evaporation.

2.3.2 Gel morphology

All gels comprise of a fibrous network with a large surface area and high surface tension capable of immobilising a fluid phase via capillary forces. However, the morphology of these fibres can be significantly different depending on many factors, including LMWG molecular structure and the solvent immobilised.[12–14] Drying down the gels often leaves the fibrous network intact, allowing fibres to be imaged on the nanoscale using scanning electron microscopy (SEM). It is worth noting that the drying process can induce changes in morphology,[15] however this method enables a quick and easy method to identify any differences between fibres formed by different LMWGs.

Analogue **2a** forms straight, long tape-like fibrils, approximately 500-800 nm in diameter (**Figure 2-3**). The fibrils aggregate to form thicker fibres. Interestingly, there is little difference observed between the fibres formed by **2b-2f**. These fibres entangle to form fibrous networks. Fibre diameters are typically 100-400 nm.

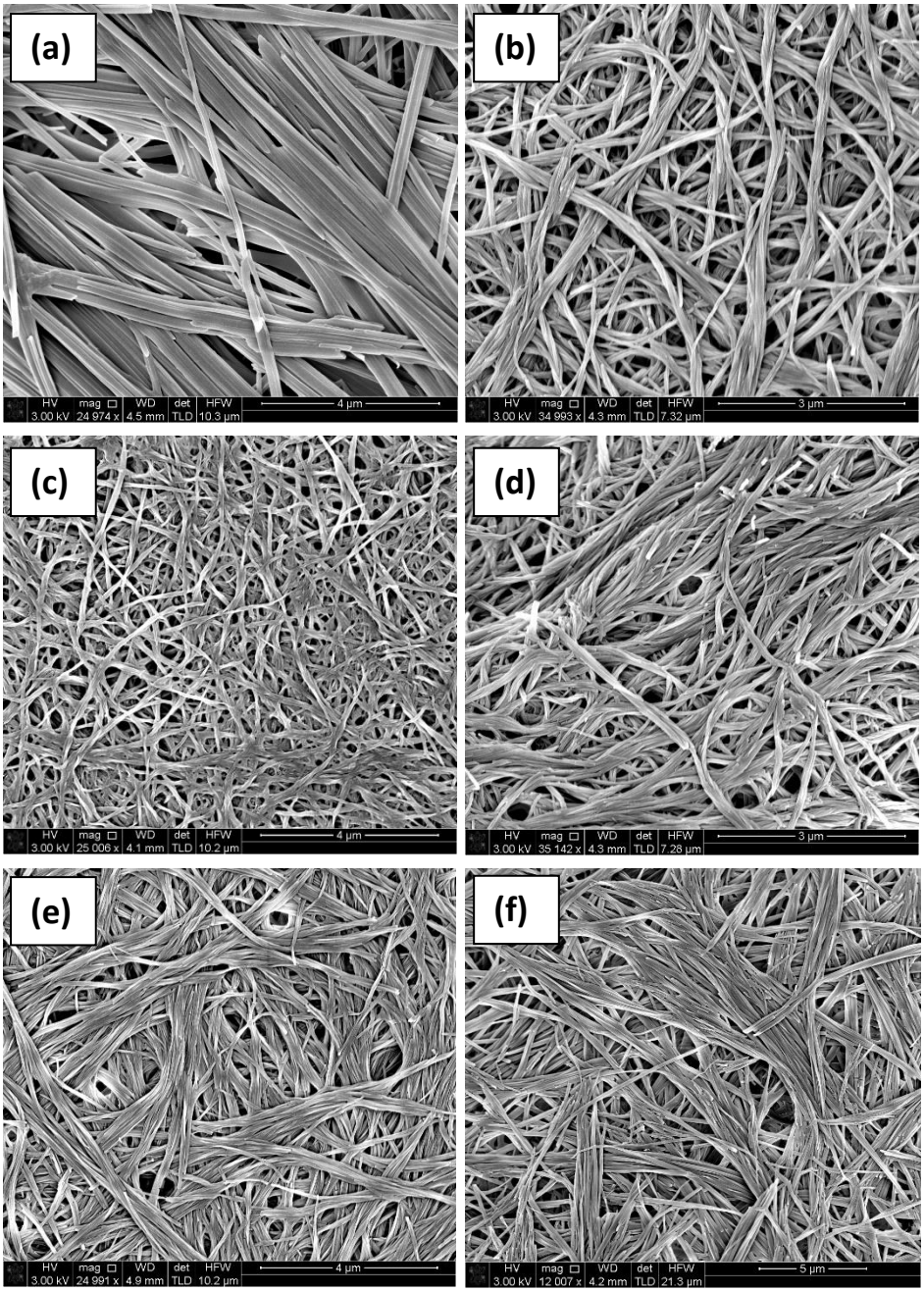

Figure 2-3. SEM images of xerogels of **(a) 2a**, **(b) 2b**, **(c) 2c, (d) 2d, (e) 2e** and **(f) 2f** . All xerogels were formed from 1 % w/v 1,4-dioxane gels, except for **2e** which was formed from a 1 % w/v 1,2-dichlorobenzene due to a lack of gelation in dioxane. Samples are coated with 2.5 nm platinum.

2.3.4 Discussion on gelation behaviour

The R-group has a significant impact on gelation behaviour. Comparing aliphatic analogues **2a** and **2b** reveals that the *t*-butyl analogue is far less versatile than the *n*-butyl analogue. Indeed, the *n*-butyl derivative was the most versatile gelator out of all the analogues tested, supporting the suggestion that linear aliphatic chains yield effective gelators,[16] likely due to their tendency to interact with solvents and neighbouring gelator molecules via van der Waals forces.[17,18]

The phenyl end group yielded a less versatile gelator than the benzyl derivative and gave weaker gels. This may be attributed with the delocalised nature of the aromatic ring resulting in a partial positive charge on the hydrogen atoms (Ar-**H**). This means that hydrogen in the ortho position relative to the urea group, can form a weak hydrogen bond with the electronegative urea oxygen atom to form a 6-membered ring, which is favourable as predicted by Etter's rules (**Figure 2-4**).[19] This is expected to weaken intermolecular urea α-tape interactions. This effect would be expected to be enhanced by electron-withdrawing groups, reducing the electron density of the aromatic ring and resulting in increased acidity of the aryl proton.[8] Displacing the aromatic ring by introducing a methylene functionality increases the distance between Ar-**H** and urea oxygen atom and preventing the formation of this weak hydrogen bond, resulting in stronger intermolecular hydrogen bonds between urea functionalities. The addition of the methylene functionalities and methyl groups can also increase the solubility of the gelator in organic solvents, which can increase gelator versatility.

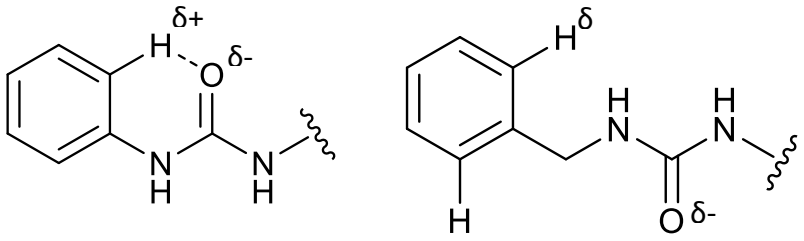

Figure 2-4. Chemical diagrams depicting **(a)** the weak intramolecular hydrogen bond between the phenyl proton and urea oxygen atom to form a 6-membered ring and **(b)** how the introducing the methylene unit between aryl and urea functionalities prevents this S(6) synthon forming.

The only non-gelator reported is **2g**; the 4-nitrophenyl derivative. The lack of gelation is likely partly due to the electron withdrawing effect of the nitro group, but also the presence of very accessible additional hydrogen bond acceptors that can disrupt self-

assembly via urea α-tape synthons, as discussed by Gale *et al.*[7] Interestingly, the previously reported analogue **2.1** (R= 2-nitrophenyl) is a gelator.[3] The nitro-group in the ortho position was predicted through CSP calculations to be involved in hydrogen bonding with urea N-H groups, but still enables the urea α-tape to form, promoting unidirectional assembly. The increased accessibility of the NO_2 functionality in *p*-nitrophenyl group means that hydrogen bonding involving the nitro substituent will significantly change the dimensionality of the self-assembly.

Interestingly, despite not being particularly versatile, the **2a** gels had the highest rheological yield stress which may be due to the thicker and more bundled fibres observed in the xerogel SEM micrographs compared to the other gelators. The *n*-butyl compound yielded the next most robust gels, followed by benzyl, phenyl and then the halogenated phenyl functionalities. The sequence in gel strength for **2b-2f** is similar to the gel versatility order and is likely due to the same reasons outlined above. Little difference was observed in the SEM images of these fibrous networks. All revealed cylindrical fibrils bundling to form thicker fibres. The diameters were similar for each of these analogues but smaller than those of **2a**. This indicates that these end groups had little influence over the fibre supramolecular architecture.

2.4 Crystallisation

2.4.1 Crystallisation procedures

Crystallisation of LMWGs is notoriously challenging due to the competitive nature of gelation and crystallisation. Indeed, gelation may be considered as a 'frustrated' crystallisation and often the task of crystallising LMWGs is a significant challenge.[28] Both gelation and crystallization occur under supersaturated conditions via the self-aggregation of molecules but differ in the directional nature of these aggregates, with crystallisation being multidirectional and gelation being unidimensional.

Here we investigated whether adjusting the conditions could encourage these 4,4-MDEP gelators to crystallise instead of gel. The general crystallisation strategy employed involved forming unsaturated solutions of gelators below the critical gel concentration and to steadily increase gelator concentration by either slow cooling the solution or slow evaporation of the solvent. This successfully yielded crystalline or

semi-crystalline material for **2a**, **2c**, **2d** and **2e** (**Figure 2-5**). The remaining compounds either formed partial gels, stable solutions, oils or amorphous powders. Attempts to optimise crystal growth conditions were made by lowering concentrations further and slowing the cooling or evaporation rate. The conditions used to grow the crystalline or semi-crystalline material in are shown below (**Table 2-2**). Representative examples of unsuccessful crystallisation conditions used are provided (**Appendix 1**).

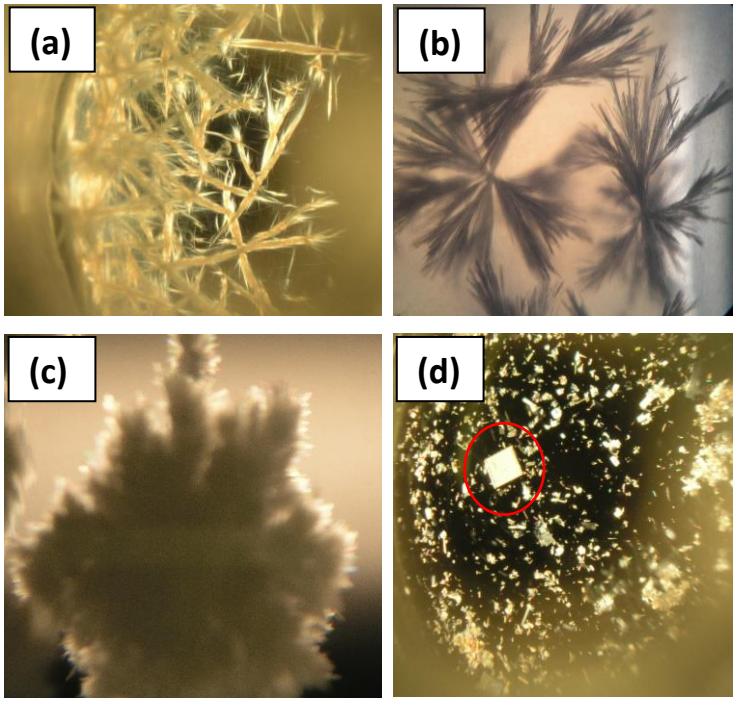

Figure 2-5. Optical microscopy images of semi-crystalline or crystalline material obtained of **(a) 2d** from 1,4-dioxane at 0.033 % w/v, **(b) 2e** from DMF at 0.05 % w/v and **(c) 2c** grown from a 0.05 % acetonitrile solution, slow cooled from 80 °C to 50 °C over 2 weeks. **(d)** The single crystal of **2a** (circled in red) grown from a 0.033 % w/v THF solution via slow evaporation at ambient temperature for 2 days, and then stored for a further 7 days undisturbed.

Table 2-2. The conditions used to grow the crystals and semi-crystalline material of **2c-e** pictured in Figure 5 Outcome abbreviations: X = crystalline or semi-crystalline aggregates unsuitable for SCXRD analysis.

Compound	Solvent	Procedure	Outcome
2c	Acetonitrile	2 mg **2c** was dissolved in 4 mL acetonitrile with heat. The vial was covered with pinpricked parafilm so solvent could slowly evaporate. After 5 days, aggregates of microcrystalline needles could be observed by eye.	X
2d	1,4-dioxane	2 mg **2d** was dissolved in 6 mL 1,4-dioxane with heat. The resulting solution was cooled from 98 °C to 50 °C over 2 weeks. Within this time, bundles of entangled semi-crystalline fibres formed.	X
2e	DMF	4 mg **2e** was dissolved in 8 mL DMF with heat and sonication. The solution was slowly cooled from 140 °C to 50 °C over 4 weeks. This yielded small, poor quality crystalline needles that were highly twinned and not suitable for SCXRD.	X

Further optimisation of the crystallisation conditions for **2c-2e** failed to yield single crystals suitable for SCXRD structure determination, despite the relative successes in obtaining poor quality crystalline material. Initially, similarly poor quality semi-crystalline material of **2a** was obtained from THF solutions. However, a methodical approach to adjust conditions each iteration to optimise crystal growth eventually yielded a single crystal of **2a** suitable for SCXRD analysis (**Table 2-3**).

Table 2-3. The method development used to grow a single crystal of **2a**. The first sentence (in bold) in each crystallisation procedure states how the method in each iteration differs from the previous. Outcomes: PG = partial gel, S = stable solution, X = crystalline powder, SC = single crystal.

Iteration	Crystallisation Procedure	Outcome
1	Compound **2a** (10 mg) was dissolved in THF (3 mL) with heat. The resulting sol was allowed to cool to ambient temperature. After 12 hours, the solvent was partially immobilised.	PG
2	**The concentration was decreased by half.** Compound **2a** (5 mg) was dissolved in THF (3 mL) with heat. The resulting sol was allowed to cool to ambient temperature. After 12 hours, a mixture of partial gel and small crystalline precipitate was observed.	PG and X
3	**The concentration was decreased significantly further.** Compound **2a** (2 mg) was dissolved in THF (7 mL). The resulting sol was allowed to cool to ambient temperature. After 1 week, the solution was still stable with no precipitate or gel observed.	S
4	**The concentration of the sol formed in iteration 3 was increased by slow evaporation.** The vial cap for the sol in iteration 3 was loosened and left undisturbed for 1 week. After this, around 2 mL of THF was left in the vial and a crystalline precipitate had formed.	X
5	**The rate of solvent evaporation was reduced.** Compound **2a** (2 mg) was dissolved in THF (7 mL). The resulting sol was allowed to cool to ambient temperature. The vial was then covered with parafilm instead of a cap. A single pinprick was put in the parafilm to allow solvent to slowly evaporate. After 5 days, approximately 2 mL THF had evaporated and a couple of small crystals just identifiable by eye had formed. The vial was left untouched for a further 2 days with solvent evaporation still enabled, during which time, mass nucleation occurred, and a lot of small poor-quality crystals were obtained.	X
6	**Solvent evaporation was restricted once the first crystalline seeds were observed by eye.** The rate of evaporation was reduced. Compound **2a** (2 mg) was dissolved in THF (7 mL). The resulting sol was allowed to cool to ambient temperature. The vial was then covered with parafilm. A single pinprick was put in the parafilm to allow solvent to slowly evaporate. After 5 days, approximately 2 mL THF had evaporate and a single small crystal just identifiable by eye had formed. The vial was then sealed with a cap, taking care to minimise movement of the vial. The vial was then left for a further 7 days, in which time the single crystal had grown to a sufficient size for SCXRD analysis. Additional small crystals had also formed in this time but had not disrupted the growth of the single crystal.	SC

This is the first reported crystal structure of a 4,4-MDEP bis(urea) gelator. The **2a** crystal was grown by dissolving 2 mg of **2a** in 7 mL of THF in a vial with heat. The vial was covered with parafilm with a single pinprick to enable slow evaporation of the solvent and stored at room temperature in a place where it could be visually inspected by eye without disturbing the vial. After 5 days, a small and but well-defined crystal at the bottom of the vial was observed. Approximately 2 mL of solvent had evaporated during this time. The vial was then carefully sealed to prevent any further loss of solvent and the crystal was left to grow over 7 days. This resulted in a single large crystalline block being obtained. Compound **2a** was purposefully designed to determine how steric hindrance directly adjacent to the urea affects self-assembly behaviour. It was anticipated that the steric hindrance could be sufficient to slow down unidirectional urea α-tape assembly and enable growth in multiple dimensions, i.e. crystallisation, to occur and this was the case here. The other compounds lack this steric hindrance and optimising conditions to achieve single crystal growth proved to be too challenging, with poor quality crystalline needles and threads typically obtained which are indicative of fast unidirectional self-assembly.

2.4.2 Analysis of the 2a single crystal structure

The **2a** single crystal was analysed by SCXRD using molybdenum radiation with an exposure time of 30 seconds per 1 ^{O} frame. The crystal was twinned, and the resulting structure was solved and refined by the author, using a twin law identified by Dr. Dmitri Yufit (*unpublished*).

Table 2-4. SCXRD data for the structure of **2a**.

	2a
Formula	$C_{31}H_{48}N_4O_2$
Formula weight	508.75
Crystal system	Monoclinic
Space group	$P2_1$
***a* / Å**	12.3139
***b* / Å**	26.1478
***c* / Å**	39.148
β / °	99.05
***V* / Å^3**	12448
Z* / *Z'	16 / 8
***D*$_{calc}$ / g cm^{-3}**	1.271
***R*$_{int}$**	0.0871
***R*$_1$ [*I* ≥ 2σ (*I*)]**	0.0439
***wR*$_2$ [all data]**	0.0964
Radiation Source	Mo

The structure shows **2a** adopts an extended conformation with representative torsion (**C**-**C**H2-**C**-**C**H) and dihedral angles between the two aromatic rings in the structure are 174.3 º and 86.28 º respectively. This is a relatively unusual conformation for methylene-linked aryl groups, with only 479 structures out of 7688 reported in the CSD having a torsion angle greater than 160 º. Most of these structures (n= 6083) have torsion angles between 45-135 º with a peak of 2052 structures around 90 º. The conformation is likely adopted for derivatives of 4,4-MDEP due to the steric hindrance generated by the ethyl groups on each aryl group. This dihedral angle results in each molecule forming two intermolecular $R_2^1(6)$ urea α-tape synthons orientated 85.8 º to one another. The N···O distances and N-H···O and N···C=O angles range between 2.8-2.9 Å, 145.8-149.7 º and 155.4-160.1 º.

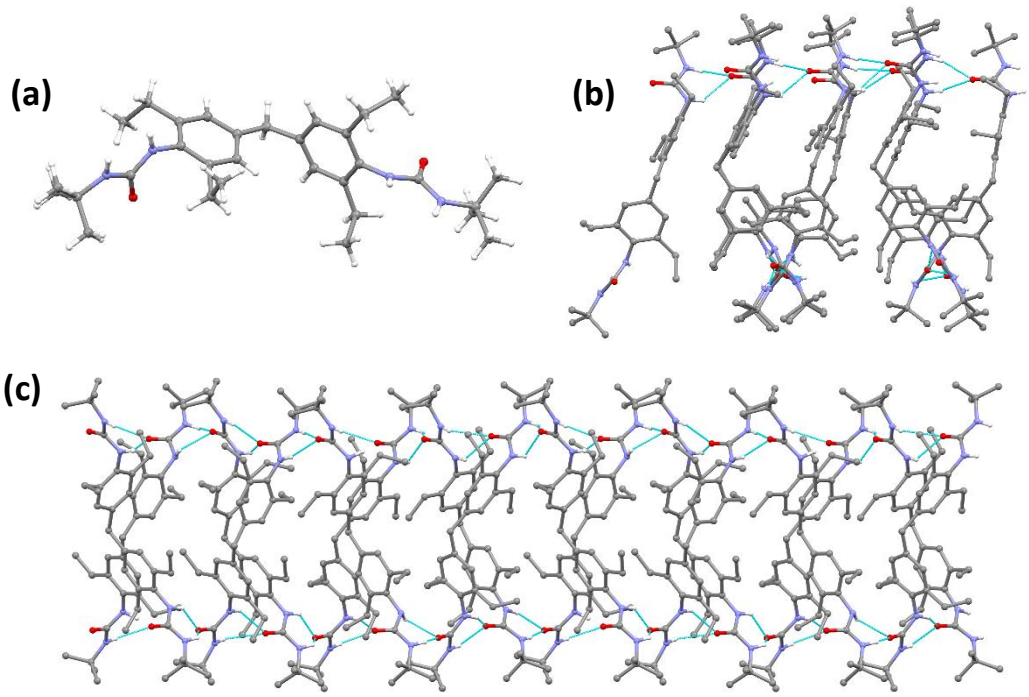

Figure 2-6. (a) Molecular conformation of **2a** determined by SCXRD. **(b)** Each molecule forms two $R_2^1(6)$ synthons with two independent molecules, with a dihedral angle of 85.6 º between the urea groups. **(c)** The view in the a-axis reveals molecules self-assemble to form 2D-sheets via infinite urea tapes.

The CSP calculations previously undertaken on the 2-nitrophenyl 4,4-MDEP analogue (**2.1**) revealed that such extended conformations of **2.1,** with the urea groups orientated anti-parallel, could give rise to gelation.[3] The calculations also revealed that the lowest energy conformers exhibit a folded conformation, with the end groups close together. However, higher energy conformers are often adopted in the solid-state to enable the formation of favourable intermolecular interactions. The crystal structure of **2a** reveals a conformation consistent with the CSP calculations of **2.1**,

however the relative orientation of the urea groups differs, with **2.1** forming anti-parallel urea tapes as opposed to the perpendicular urea tapes observed in **2a**. The perpendicular orientation observed in **2a** promotes self-assembly via hydrogen bonding in two dimensions, instead of the unidimensional assembly promoted by anti-parallel urea tapes. This may explain why **2a** is a less versatile gelator than the other 4,4-MDEP analogues, and why the **2a** xerogel fibres are thicker and more ribbon-like than the fine cylindrical fibres observed for the other compounds.

2.4.3 Cause of the high Z' value

The **2a** structure exhibits eight molecules in the asymmetric unit (*Z'*=8) which is an unusual and high value.[20] The SCXRD data was collected at 120 K and the high *Z'* here can likely be attributed to 'frozen out' disorder of the spacer ethyl groups, due to reduced molecular motion. The ethyl groups are free to rotate and three distinct relative orientations of the ethyl groups can be observed in the structure (**Figure 2-7**). The ethyl functionalities can be in an axial (up or down) conformation, where the CH_3 group is above or below the plane of the aromatic ring respectively, or an equatorial conformation, where both CH_2 and CH_3 functionalities sit in the plane of the aromatic ring. The three conformations observed of the ethyl groups on each ring are $axial_{(up)}$-$axial_{(up)}$, $axial_{(up)}$-$axial_{(down)}$ and axial-equatorial.

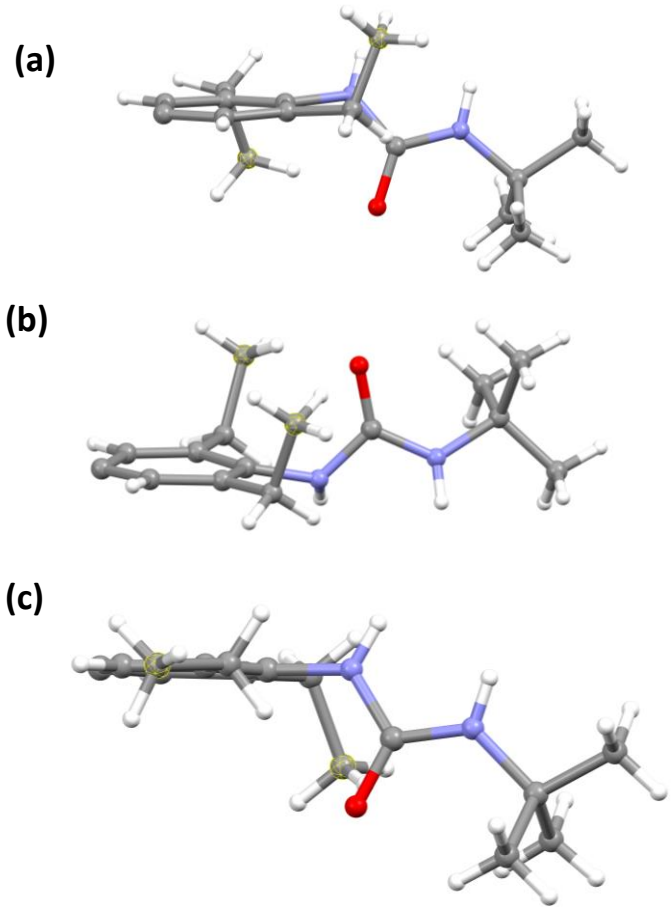

Figure 2-7. The distinct conformations of the ethyl groups on the 4,4-MDEP spacer observed in the **2a** crystal structure. **(a)** axial$_{(up)}$-axial$_{(down)}$ where the ethyl CH_3 groups are orientated in opposite directions above and below the plane of the aryl group. **(b)** Axial$_{(up)}$-axial$_{(up)}$, where both CH_3 groups are orientated in the same direction above the plane of the aryl group. **(c)** axial-equatorial, where one CH_3 group is in the plane of the aryl group, whilst the other is above or below the plane of the ring. The CH_3 groups in the ethyl functionalities are highlighted for clarity. These conformations are likely frozen out at the low collection temperature (120 K) and contribute to the high Z' value of the structure.

Seeding crystallisations were used to successfully grow 100 mg of crystalline **2a** from methanol, with the XRPD patterns of this bulk crystalline material broadly matching the calculated XRPD pattern for the single crystal. The ^{13}C CPMAS-NMR spectrum of the crystal form collected at ambient temperature reveals sharp, intense and well-defined signals which is indicative of the crystalline nature of the material. The spectrum reveals no duplicated or multiplicated peaks indicating that the asymmetric unit only contains one molecule at ambient temperature (**Figure 2-8**). Signals at 143.8 ppm and 50.0 ppm are strong singlets with a slight shoulder, which may indicate the presence of another polymorphic form. The experiment was repeated with interrupted decoupling which should suppress signals from CH_2 and CH functionalities in a fully rigid system. Indeed, the signal for the methylene CH_2 between the spacer aryl rings at

42.2 ppm is completely suppressed in this latter experiment, indicating that this conformation for the 4,4-MDEP aryl rings is rigid in the solid-state. The peaks at 24.9 and 25.9 ppm correspond to CH_2 functionalities from the ethyl groups and decreases in intensity but are not fully suppressed, indicating the groups are mobile at ambient conditions.

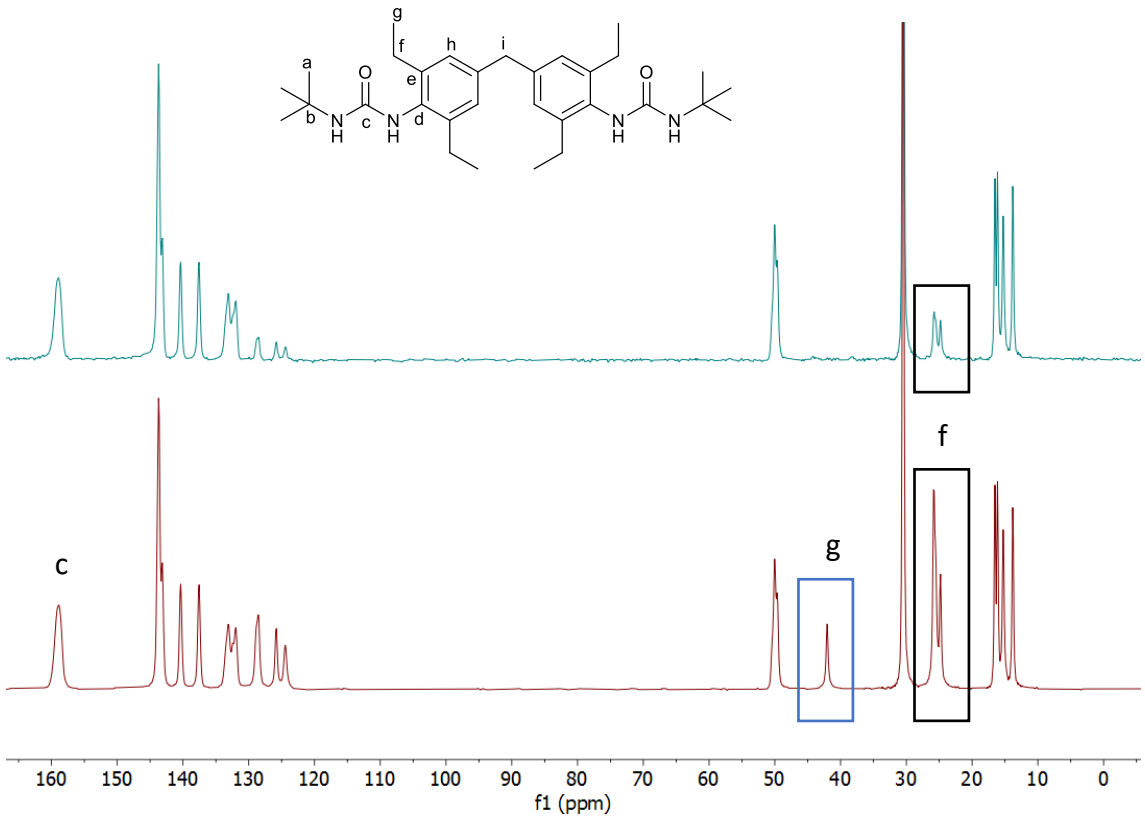

Figure 2-8. Solid-state ^{13}C CP-MAS NMR (100.63 MHz) spectra of **2a** with constant decoupling (bottom – in red) and interrupted decoupling (top – in green). The spectrum indicates a low Z' with most signals generally well-defined singlets. The signal at 42.2 ppm (blue box) corresponds to the spacer methylene unit and is fully suppressed in the interrupted decoupling spectrum, indicating the conformation is rigid. The signals at 25 ppm (black box) correspond to the ethyl $\underline{C}H_2$ and are not fully suppressed in the interrupted decoupling experiment, indicating some degree of mobility of these functionalities at ambient temperature.

Differential scanning calorimetry of the crystal form from -80 °C to 350 °C was undertaken to determine whether there are any changes in solid form as a function of temperature, but no transition are evident and the material exhibits a sole endothermic peak at 276 °C (**Figure 2-9**) assigned to the melting transition. The DSC equipment used had a temperature limit of -80 °C and probing transitions below this temperature via DSC could not be undertaken. Whilst this result does not rule out a form transition below this temperature, it does rule out a transition between -80 °C and 350 °C which further supports that the high *Z'* value is a consequence of the low collection temperature 'freezing-out' the disorder.

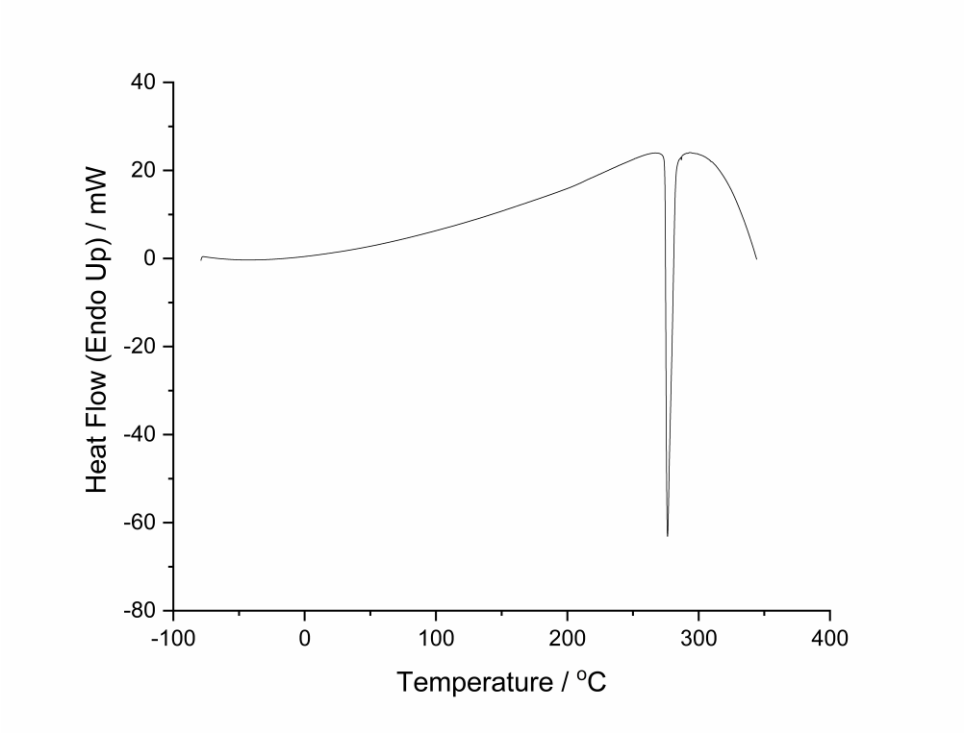

Figure 2-9. DSC thermogram of **2a**, showing no polymorphic phase transitions between -80 °C and 350 °C and a single melt point at 276 °C.

Regrettably, unit cell measurements and full SCXRD data collection at ambient temperature were not undertaken prior to the single crystal being utilised in destructive testing, such as DSC. Attempts to regrow another single crystal were unsuccessful.

2.4.4 Molecular packing in gel and crystalline state

A comparison between the experimental diffraction patterns of the **2a** bulk crystalline material obtained by seeding crystallisations from methanol and the **2a** 1,4-dioxane xerogel are essentially identical, meaning the same molecular packing is present in both form. It should be noted that gel fibres are often polymorphic[21–24] and changes in molecular packing can be induced upon drying down of the gel network.[25] Indeed, here the xerogel sample was prepared by drying the 1,4-dioxane xerogel at 50 °C over 5 days and the sample has a crystalline appearance upon retrieval and hence a solid form transition cannot be ruled out.

When comparing the calculated XRPD pattern and the experimental patterns, some expected discrepancies between the peak intensities can be observed, due to the crystallite orientation, and in some of the peak positions due to slight differences in

lattice parameters, possible a result of the difference in collection temperature and hence a slight change in unit cell dimensions. However, the comparison shows the patterns to have some similarities, indicating that similar molecular conformations and packing arrangements are present in all three phases.

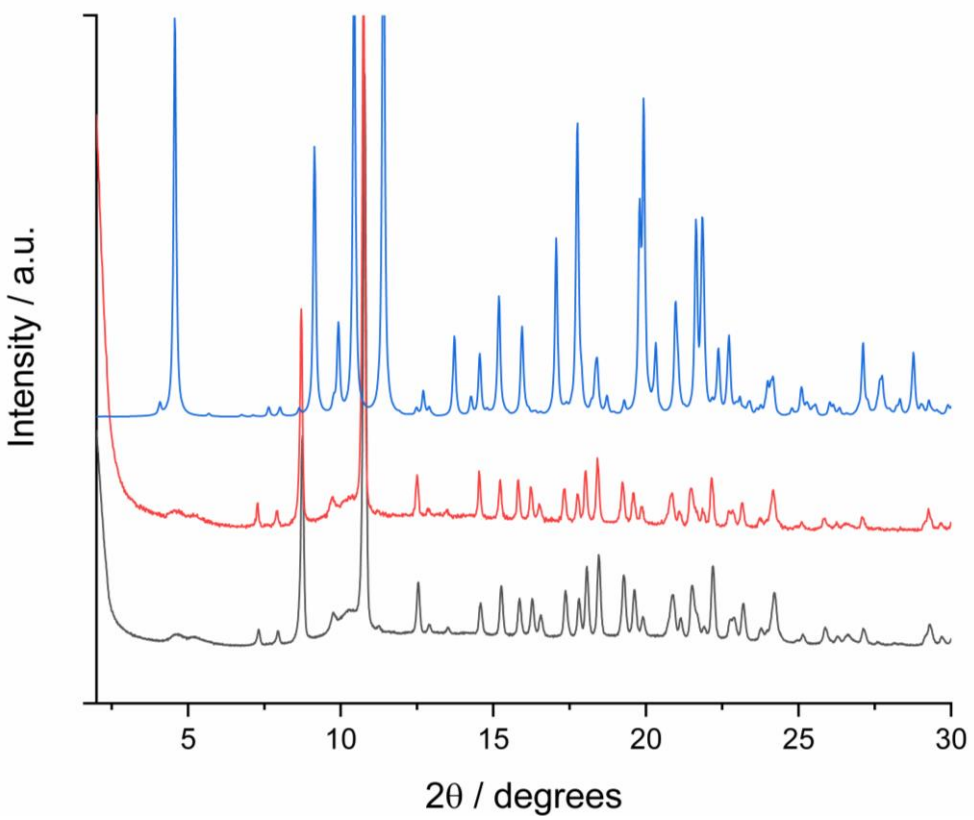

Figure 2-10. XRPD pattern calculated from the single crystal structure (in blue) and the experimental XRPD patterns for the bulk crystalline material obtained from seeding crystallisations (in red) and the **2a** 1,4-dioxane xerogel (in black). The xerogel and experimental crystal pattern are a perfect match, although the appearance and high crystallinity of the xerogel specimen may indicate crystallisation has occurred upon drying and this pattern may not accurately represent packing in the gel phase. Both experimental patterns have broad similarities with the calculated pattern, indicating molecular packing is similar in all three phases. Slight discrepencies between the calculated and experimental packings patterns are likely due to slight shifts in unit cell dimensions due to the difference in collection temperature.

2.5 Conclusions

A series of 4,4-MDEP-derived bis(urea) LMWGs were synthesised and their gelation capacity investigated. The series of compounds were generally effective LMWGs, which is consistent with previous observations regarding 4,4-MDEP bis(urea) derivatives. Changes in R-group were found to influence the gelation potential significantly, with the branched t-butyl group yielding a far less versatile gelator than the n-butyl derivative. Phenyl end groups were less versatile than benzyl end groups, likely due to reducing the effect of weak intramolecular hydrogen bonds between Ar-H

and urea oxygen atoms. The 4-nitrophenyl derivative was the only reported non-gelator, likely due to competitive hydrogen bonding afforded by the readily accessible NO_2 group, which restricting unidirectional α-tape formation.

The rheological analysis of the gels confirms their gel nature, with G' plateaus an order of magnitude greater than G" for all gels. Gel strength was determined by stress-sweep measurements and shows that aliphatic R groups were stronger than their aromatic counterparts. Interestingly, the branched *t*-butyl end group yielded stronger gels than the *n*-butyl end group. The strength of gels formed by aromatic derivatives were all slightly weaker than the alkyl compounds. Gels of the benzyl gelator exhibit a high yield stress than the phenyl gelator likely due to the anticipated intramolecular Ar-H$\cdots O_{(urea)}$ hydrogen bond in the latter. Electron-withdrawing *p*-substituents on the phenyl functionality further lowered the yield stress, which may be due to an increased acidity in the ortho Ar-H protons, resulting in strong intramolecular S(6) hydrogen bonds with the urea carbonyl.

Attempts to grow single crystals of all gelators were made by lowering the concentration of gelators to below their associated CGC to slow down the self-assembly process and encourage multidirectional growth. Only one single crystal was successfully grown, but the method also yielded crystalline/semi-crystalline material for **2c**, **2d** and **2e**, and further optimisation of conditions may yield more single crystals. The solved and refined **2a** crystal structure reveals that the molecules adopt and extended conformations with a relatively uncommon torsion angle (**C**-**C**H_2-**C**-**C**H) of 174.3 º and dihedral angle of 86.28 º between the two spacer aryl rings. Each molecule engages in two urea α-tapes that form perpendicular to one another, resulting in the formation of 2D-sheets. The extended molecular conformation and intermolecular hydrogen bonding observed in the structure is broadly consistent with the CSP calculations previously reported of a 4,4-MDEP 2-nitrophenyl gelator. However, in the CSP calculations for **2.1** the urea groups were anticipated to be in an antiparallel arrangement, whilst in the **2a** experimental structure the urea tapes exhibit a dihedral angle between 85.1-87.2 º. This may explain the less versatile gelation behaviour of **2a** compared with other 4,4-MDEP compounds and explain the thicker and flatter nature of the fibrous xerogel aggregates.

The structure exhibits 8 molecules in the asymmetric unit and this can be possibly attributed to frozen out disorder, due to the low XRD collection temperature, resulting in three distinct conformers of the spacer ethyl groups being observed in the structure. There is no disorder in the structure. This was confirmed by ss-NMR spectroscopy through ^{13}C CPMAS experiments. The NMR data was collected at ambient temperature and the spectrum reveals only one signal for most of the carbon environments, which is indicative of a single molecule in the asymmetric unit. Duplicated/split peaks would indicate Z' > 1.[20,26] Interrupted decoupling demonstrates that the signal corresponding to the ethyl CH_2 functionalities are not completely suppressed, indicating there is some degree of molecular motion. Meanwhile, the signal for the methylene spacer CH_2 is completely suppressed, indicating the core spacer conformation is rigid. DSC measurements from -80 ^oC to 350 ^oC only reveals a single melt point at 276 ^oC, with not polymorphic form transitions identifiable, which further supports the high Z' is due to frozen out disorder, although it should be noted that a transition below this temperature cannot be ruled out. Regrettably, the single crystal was not analysed via SCXRD at ambient temperature, which could further confirm whether the high Z' is due to frozen out disorder of the ethyl functionalities.

Finally, XRPD analysis of the xerogel, bulk crystalline material and calculated SCXRD were broadly a good match, indicating similar molecular packing arrangements in all three forms. However, the high crystallinity of the dried down xerogel may indicate a form change during the drying process and, whilst comparing XRPD patterns of xerogels to crystalline forms can provide some insight to packing tendencies, a degree of caution needs to be applied when claiming this is an accurate representation of the gel phase.[15] The findings in this study have significantly influenced the design of supramolecular gelators in the following chapters, with phenyl derivatives being avoided where possible and benzyl functionalities typically utilised instead.

2.6 Experimental Details

Synthesis details and characterisation of compounds presented in this chapter (**2a-2g**) are provided below. Please refer to Chapter 6– General Experimental for additional experimental details.

2.6.1 Synthesis of gelators

General Synthesis Procedure

All bis(urea) compounds in this chapter 2 were synthesised by similar synthetic procedures. Tetraethyl-4,4'-methylenediphenyl isocyanate (0.500 g, 1.38 mmol) was dissolved in a vial with chloroform (7 mL) or THF (7 mL) at ambient temperature with stirring. This was followed by the addition of 2.1 molar equivalents (2.90 mmol) of the desired primary amine. Details of the amine used in synthesis of each compound are provided for each compound below. For compounds **2a-2c**, the reaction mixture was stirred at room temperature for 2 to 4 hours, with white precipitates formed within minutes of stirring. For compounds **2d-g**, triethylamine (313 mg, 3.10 mmol) was also added to the reaction mixture before heating under reflux for up to 12 hours. Precipitates typically formed within 2 hours of reflux. For all compounds, the reaction mixture was filtered to obtain the crude precipitate before further purification steps.

Purification of compounds **2a-f** was achieved by washing the precipitate with dichloromethane (3 x 10 mL) and drying under vacuum in a drying pistol at 110 ^{o}C. Purification of the **2g** was achieved by triturating the precipitate with 15 mL DMF for 12 hours. The precipitate was then filtered and washed with copious amounts of water (150 mL), followed by washing with diethyl ether (3 x 10 mL). The solid was then dried under vacuum in a drying pistol at 110 ^{o}C for 24 hours.

2.6.2 Characterisation of Compounds

Compound 2a

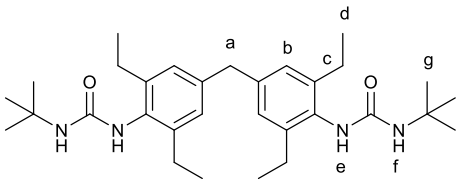

Primary amine used for synthesis: tert-butylamine

Solvent used: THF

Compound **2a** was obtained as a white solid (599 mg, 1.18 mmol, 88.7 % yield). **^{1}H NMR** (400 MHz, DMSO-[d6]): δ = 7.09 (s, 2H, *e*) 6.91 (s, 4H, *b*), 4.50 (s, 2H, *f*) 3.80 (s, 2H, *a*). 2.49-2.55 (m, *c* – overlaps with DMSO peak), 1.26 (s, 18H, *g*) 1.07 (t, 12H, J = 7.6

Hz, *d*). **m/z (ES$^+$-MS)** 509.4 [M+H], 531.4 [M+Na]. **Elemental analysis** calculated for $C_{31}H_{48}N_4O_2$ (%): C, 73.19; H, 9.51; N, 11.01. Found (%): C, 72.93; H, 9.38; N, 10.76.

Compound 2b

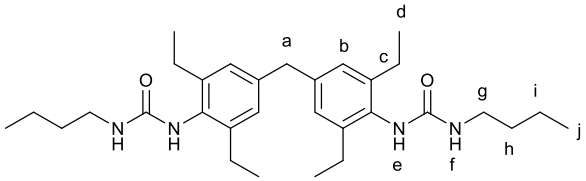

Primary amine used for synthesis: n-butylamine

Solvent used: THF

Compound **2b** was obtained as a white solid (638 mg, 1.26 mmol, 91.3 %). **^{1}H NMR** (400 MHz, DMSO-[d6]): δ = 7.23 (broad-s, 2H, *e*) 6.87 (s, 4H, *b*), 5.33 (t, *J* = 5.7 Hz, 2H, *f*), 3.69 (s, 2H, *a*), 2.92 (dt, J = 6.3, 5.7 Hz, 4H, *g*), 2.49-2.55 (m, *c* – overlaps with DMSO peak), 1.38-1.18 (m, 8H, *h i*) 1.07 (t, 12H, J = 7.6 Hz, *d)*, 0.91-0.73 (m, 6H, *j*). **m/z (ES$^+$-MS)** 509.4 [M+H], 531.4 [M+Na]. **Elemental analysis** calculated for $C_{31}H_{48}N_4O_2$ (%): C, 73.19; H, 9.51; N, 11.01. Found (%): C, 72.89; H, 9.26; N, 10.81.

Compound 2c

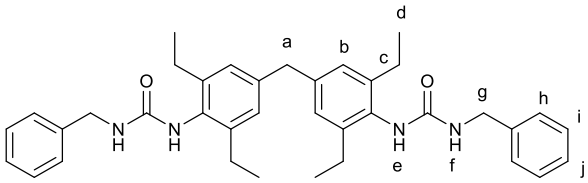

Primary amine used for synthesis: Benzylamine

Solvent used: Chloroform

Compound **2c** was obtained as a white solid (669 mg, 1.16 mmol, 84 % yield). **^{1}H NMR** (400 MHz, DMSO-[d6]): δ = 7.40 (s, 2H,*e*) 7.22-7.41 (m, 10H, *h i j*), 6.95 (s, 4H, *b*), 6.88 (s, 2H, *f*), 4.25 (d, 4H, J = 5.8 Hz, *g*), 3.80 (s, 2H, *a*). 2.49-2.55 (m, *c* – overlaps with DMSO peak), 1.12 (t, 12H, J = 7.6 Hz, *d*). **m/z (ES$^+$-MS)** 577.4 [M+H], 599.3 [M+Na]. **Elemental analysis** calculated for $C_{37}H_{44}N_4O_2$ (%): C, 77.05; H, 7.69; N, 9.71. Found (%): C, 77.05; H, 7.67; N, 9.66.

Compound 2d

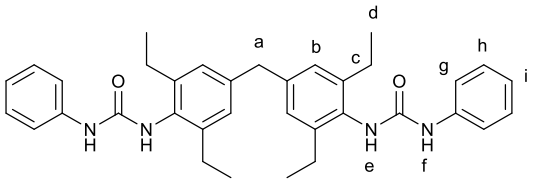

Primary amine used for synthesis: Aniline

Solvent used for synthesis: Chloroform

Compound **2d** was obtained as a white solid (537 mg, 0.98 mmol, 71 % yield). **^{1}H NMR** (400 MHz, DMSO-[d6]): δ = 8.74 (broad-s, 2H, *f*) 7.56 (s, 2H, *e*), 7.44 (d, 4H, J=7.7 Hz, *g*), 7.25 (m, 4H, *h*), 7.01 (s, 4H, *b*), 6.92 (m, 2H, *i*), 3.86 (s, 2H, *a*). 2.49-2.55 (m, *c* – overlaps with DMSO peak), 1.12 (t, 12H, J = 7.5 Hz, *d*). **m/z (ES$^+$-MS)** 571.3 [M+Na], 587.3 [M+K]. **Elemental analysis** calculated for $C_{35}H_{40}N_4O_2$ (%): C, 76.61; H, 7.35; N, 10.21. Found (%): C, 76.56; H, 7.38; N, 10.20.

Compound 2e

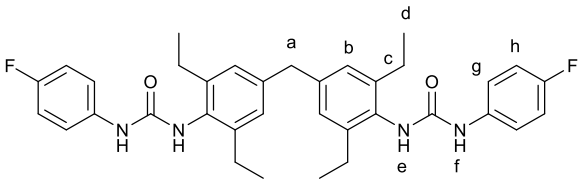

Primary amine used for synthesis: 4-fluoroaniline

Solvent used: Chloroform

Compound **2e** was obtained as a white solid (524 mg, 0.90 mmol, 65 % yield). **^{1}H NMR** (400 MHz, DMSO-[d6]): δ = 8.76 (broad-s, 2H, *f*) 7.54 (s, 2H, *e*), 7.43 (d, J = 8.4 Hz, 4H, *h*), 7.29 (d, 4H, J = 8.4 Hz, *g*), 6.99 (s, 4H, *b*), 3.85 (s, 2H, *a*). 2.49-2.55 (m, *c* – overlaps with DMSO peak), 1.10 (t, 12H, J = 7.6 Hz, *d*). **m/z (ES$^+$-MS)** 585.3 [M+H], 607.3 [M+Na]. **Elemental analysis** calculated for $C_{35}H_{38}N_4O_2F_2$ (%): C, 71.90; H, 6.55; N, 9.58. Found (%): C, 71.81; H, 6.71; N, 9.64.

Compound 2f

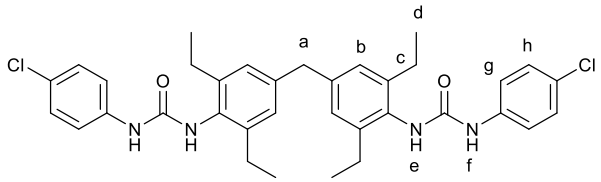

Primary amine used for synthesis: 4-chloroaniline

Solvent used: Chloroform

Compound **2f** was obtained as a white solid (639 mg, 1.04 mmol, 75 % yield). **^{1}H NMR** (400 MHz, DMSO-[d6]): δ = 8.89 (broad-s, 2H, *f*) 7.61 (s, 2H, *e*), 7.46 (d, 4H, J = 8.8 Hz, *h*), 7.28 (d, 4H, J = 8.8 Hz, *g*), 7.00 (s, 4H, *b*), 3.86 (s, 2H, *a*). 2.49-2.55 (m, *c* – overlaps with DMSO peak), 1.11 (t, 12H, J = 7.6 Hz, *d*). **m/z (ES$^+$-MS)** 617.2 [M+H], 639.2 [M+Na]. **Elemental analysis** calculated for $C_{35}H_{38}N_4O_2Cl_2$ (%): C, 68.07; H, 6.20; N, 9.07. Found (%): C, 67.83; H, 6.35; N, 9.13.

Compound 2g

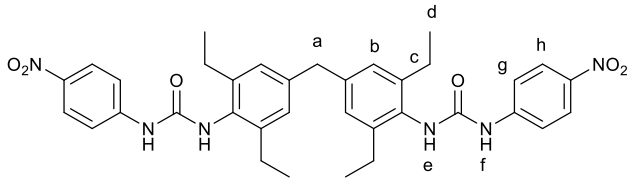

Primary amine used for synthesis: 4-nitroaniline

Solvent used for synthesis: Chloroform

Compound **2g** was obtained as a white solid (520 mg, 0.81 mmol, 59 % yield). **^{1}H NMR** (400 MHz, DMSO-[d6]): δ = 9.58 (broad-s, 2H, *f*) 8.17 (d, 4H, J = 9.3 Hz, *h*), 7.86 (broad-s, 2H, *e*), 7.67 (d, 4H, J = 9.3 Hz, *g*), 7.03 (s, 4H, *b*), 3.88 (s, 2H, *a*). 2.49-2.55 (m, *c* – overlaps with DMSO peak), 1.12 (t, 12H, J = 7.6 Hz, *d*). **m/z (ES$^+$-MS)** 639.3 [M+H], 661.3 [M+Na]. **Elemental analysis** calculated for $C_{35}H_{38}N_6O_6$ (%): C, 65.82; H, 6.00; N, 13.16. Found (%): C, 66.00; H, 5.89; N, 13.30.

2.7 References

1 S. R. Kennedy, C. D. Jones, D. S. Yufit, C. E. Nicholson, S. J. Cooper and J. W. Steed, *CrystEngComm*, 2018, **20**, 1390–1398.

2 A. Cayuela, S. R. Kennedy, M. L. Soriano, C. D. Jones, M. Valcárcel and J. W. Steed, *Chem. Sci.*, 2015, **6**, 6139–6146.

3 J. A. Foster, K. K. Damodaran, A. Maurin, G. M. Day, H. P. G. Thompson, G. J. Cameron, J. C. Bernal and J. W. Steed, *Chem. Sci.*, 2017, **8**, 78–84.

4 P. Brocorens, M. Linares, C. Guyard-Duhayon, R. Guillot, B. Andrioletti, D. Suhr, B. Isare, R. Lazzaroni and L. Bouteiller, *J. Phys. Chem. B*, 2013, **117**, 5379–5386.

5 P. Byrne, D. R. Turner, G. O. Lloyd, N. Clarke and J. W. Steed, *Cryst. Growth Des.*, 2008, **8**, 3335–3344.

6 J. Cui, Z. Shen and X. Wan, *Langmuir*, 2010, **26**, 97–103.

7 F. Piana, D. H. Case, S. M. Ramalhete, G. Pileio, M. Facciotti, G. M. Day, Y. Z. Khimyak, J. Angulo, R. C. D. Brown and P. A. Gale, *Soft Matter*, 2016, **12**, 4034–4043.

8 L. S. Reddy, S. Basavoju, V. R. Vangala and A. Nangia, *Cryst. Growth Des.*, 2006, **6**, 161–173.

9 P. Terech, D. Pasquier, V. Bordas and C. Rossat, *Langmuir*, 2000, **16**, 4485–4494.

10 G. Yu, X. Yan, C. Han and F. Huang, *Chem. Soc. Rev.*, 2013, **42**, 6697–6722.

11 S. R. Raghavan and B. H. Cipriano, in *Molecular Gels*, eds. R. G. Weiss and P. Terech, Springer, 2006.

12 W. Weng, Z. Li, A. M. Jamieson and S. J. Rowan, *Macromolecules*, 2009, **42**, 236–246.

13 S. Bartocci, I. Morbioli, M. Maggini and M. Mba, *J. Pept. Sci.*, 2015, **21**, 871–878.

14 K. Y. Kim, M. Ok, J. Kim, S. H. Jung, M. L. Seo and J. H. Jung, *Gels*, 2020, **6**, 16.

15 L. L. E. Mears, E. R. Draper, A. M. Castilla, H. Su, Zhuola, B. Dietrich, M. C. Nolan, G. N. Smith, J. Doutch, S. Rogers, R. Akhtar, H. Cui and D. J. Adams, *Biomacromolecules*, 2017, **18**, 3531–3540.

16 A. Dawn, M. Mirzamani, C. D. Jones, D. S. Yufit, S. Qian, J. W. Steed and H. Kumari, *Soft Matter*, 2018, **14**, 9489.

17 Y. Lan, M. G. Corradini, R. G. Weiss, S. R. Raghavan and M. A. Rogers, *Chem. Soc. Rev.*, 2015, **44**, 6035–6058.

18 D. J. Abdallah and R. G. Weiss, *Langmuir*, 2000, **16**, 352–355.

19 M. C. Etter, *Acc. Chem. Res.*, 1990, **23**, 120–126.

20 K. M. Steed and J. W. Steed, *Chem. Rev.*, 2015, **115**, 2895–2933.

21 X. Huang, S. R. Raghavan, P. Terech and R. G. Weiss, *J. Am. Chem. Soc.*, 2006, **128**, 15341–15352.

22 V. A. Mallia, P. D. Butler, B. Sarkar, K. T. Holman and R. G. Weiss, *J. Am. Chem. Soc.*, 2011, **133**, 15045–15054.

23 J. Van Esch, F. Schoonbeek, M. De Loos, H. Kooijman, A. L. Spek, R. M. Kellogg and B. L. Feringa, *Chem. - A Eur. J.*, 1999, **5**, 937–950.

24 S. Panja and D. J. Adams, *Chem. Commun.*, 2019, **55**, 10154–10157.

25 B. Bai, Z. Li, H. Wang, M. Li, Y. Ozaki and J. Wei, *R. Soc. Open Sci.*, 2018, **5**, 170492.

26 A. Nangia, *J. Indian Inst. Sci.*, 2007, 87, 133–147.

27 H. J. Knolker, T. Braxmeier and G. Schlechtingen, *Angew. Chem. Int. Ed. Engl.*, 1995, **34**, 2497–2500.

28 A. D. Martin, J. P. Wojciechowski, M. M. Bhadbhade and P. Thordarson, *Langmuir*, 2016, **32**, 2245-2250

Chapter 3 - API-mimetic gels for pharmaceutical crystallisations

3.1 Introduction

Previous work by the Steed group showed that molecular gels that contain moieties mimicking a crystallisation substrate can sometimes enable control over the crystallisation outcomes, including the polymorphic form and crystal habit obtained.[1,2] This was arguably best demonstrated by the crystallisation of the highly-polymorphic pharmaceutical precursor, ROY, where API-mimicking toluene gels typically crystallised a metastable red form, whilst generic toluene gels and toluene solution crystallisations always yielded the thermodynamically stable yellow form.[2] However, this phenomenon remains relatively untested and requires further exploration to determine how versatile and effective this method is for controlling the crystallisation outcomes and potentially identifying novel crystalline forms or producing typically elusive forms.

In this study, an API-mimicking approach is applied to two AstraZeneca API compounds, AZD-2281 and AZD-6140, to further explore the effect API-mimicking gels can have on the crystallisation outcomes. Both APIs are formulated as crystalline forms in solid-dose delivery systems and exhibit polymorphism. Both also contain chemical functionalities that can readily be incorporated into bis(urea) LMWG structures. A 'toolbox' of bis(urea) molecular gelators with end groups mimicking distinct substructures within the API molecules have been synthesised and their gelation properties investigated. The resulting gels are used as part of a solid-state screening process to identify whether crystallisation outcomes could be influenced and controlled. Preliminary work on a further approach to synthesise molecular gels with the whole API molecules appended on the end, via employing the well-documented reversible covalent bond formation between boronic acids and 1,2-diols, is also presented.

3.2 Known Crystal forms of AZD-2281 and AZD-6140

3.2.1 AZD-2281

AZD-2281, also known as olaparib, is a poly-ADP ribose polymerase (PARP) inhibitor currently licensed as an anti-cancer agent used primarily in ovarian cancer,[3,4] and has shown promising results in clinical trials against breast[5] and prostate cancers.[6] It has numerous known crystal forms denoted A-L. Form A is the form that crystallises most readily and is a kinetically stable anhydrous form under ambient conditions. It is the form that is used in the final formulation. Forms B-K are various solvated forms which could not be used for formulation due to the limitations of incorporating organic solvents in pharmaceutical products. Many of these solvates are isostructural. Meanwhile, anhydrous form L is of interest as it is the thermodynamically stable form under ambient conditions. However, it only crystallised later into product development via sublimation experiments using a cooling gradient.

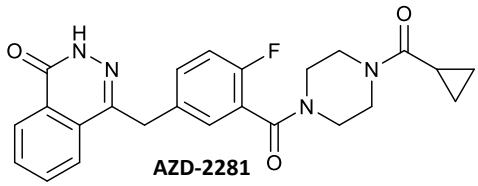

AZD-2281

Table 3-1. Space groups and unit cell values for AZD-2281 forms A, L and two isostructural solvate forms.

	Space Group	a	b	c	α	β	γ	Cell Volume
Form A	$P2_1/n$	20.32	8.18	24.8	90	95.5	90	4118.4
Form L	$P2_1/n$	22.99	8.09	11.86	90	111.5	90	2055.8
DCM Solvate	$P2_1/n$	10.41	9.14	24.48	90	97.2	90	2314.5
Methanol Solvate	$P2_1/n$	10.42	8.92	25.00	90	98.1	90	2303.9

Polymorphs can represent intellectual property opportunities and can significantly impact physicochemical properties; thus, the late identification of polymorphs can be detrimental to pharmaceutical companies from both a commercial and pharmacovigilance perspective. Indeed, concerns were raised by the European Medicines Agency regarding the risk of polymorph transformations from form A to form L in the final formulation and further stability data was requested to address this risk prior to issuance of a European marketing authorisation.[7] The transition from form A to form L is actually extremely slow, with the former being stable under ambient conditions over the shelf-life of the product. However, the later discovery of form L

demonstrates the need for thorough crystallisation screening procedures that use as many techniques as possible. Within this content supramolecular gel media offer an additional screening method.

3.2.2 AZD-6140

AZD-6140, also known as ticagrelor, is a novel antiplatelet drug used as an alternative to aspirin in patients at risk of cardiac disease. It has a low solubility and poor bioavailability (30-40 %) and is classified by the Biopharmaceutics Classification System as a class IV drug.[8] It has four patented anhydrous polymorphic forms, referred to as forms I-IV, and numerous pseudopolymorphs.[9] All the anhydrous forms exhibit enantiotropic relationships with one another, with Form III being the thermodynamically stable form between 0 °C to 40 °C, and form I being the thermodynamically stable form above 60 °C.[10]

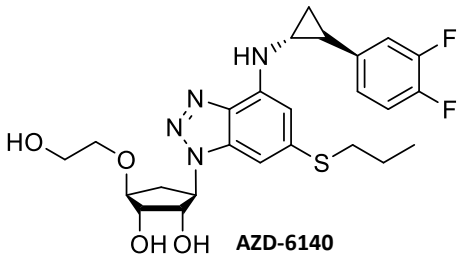

AZD-6140

Crystal structures of form I (JEMWIK) and II (JEMWIK01) are published in the CSD, in addition to a DMSO solvate (JEMWOQ). In form II, a two-dimensional hydrogen bond network is formed by a mixture of ring and chain motifs via O–H···O and N–H···N hydrogen bonds (**Figure 3-1**).[11] A study by Borjarska *et al.* reports that in form I F···H/H···F interactions and F···F contacts, in addition to π···π interactions, are more prominent than strong O··· H/H···O hydrogen bonding and play a critical role in stabilising this form.[12] The form I structure reveals AZD-6140 molecules packing in a head to tail arrangement with adenine functionalities stacked via π···π intermolecular interactions.

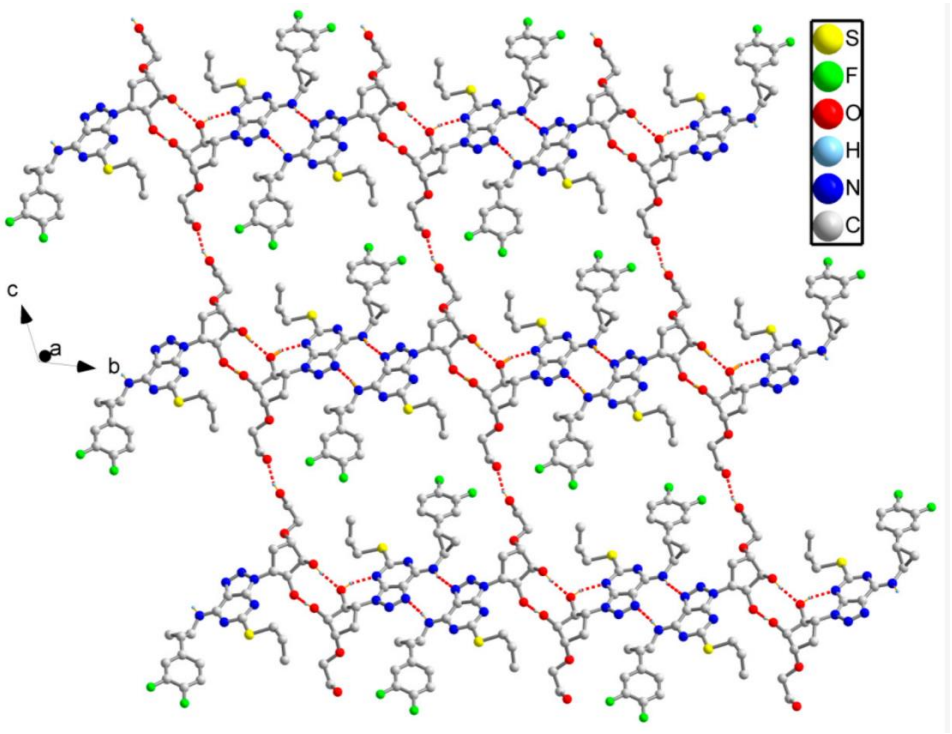

Figure 3-1. Images of the two-dimensional hydrogen bonding network observed in form II of AZD-6140. Adapted from reference 11.

3.3 API-mimetic LMWG design

Two spacer groups (**3.1** and **3.2**) are used as the core for all the gelators in this study, due to their tendency to yield effective bis(urea) LMWGs. In AZD-2281 the mono-fluorinated phenylene ring, piperazine functionality and cyclic amide were selected as API-mimicking functionalities that could be introduced to LMWGs. Meanwhile, the 3,4-difluorophenyl and adenine-like functionalities in AZD-6140 were chosen for mimicking structural motifs. Benzyl-derivatives of the fluorinated aromatic functionalities were used, due to the observations in chapter 2 that gelation behaviour is significantly reduced by aromatic substituents directly adjacent to urea functionalities. In addition to the API-mimetic gelators, a selection of generic gelators bearing limited to no resemblance to the target API molecules were utilised for control gel-phase experiments.

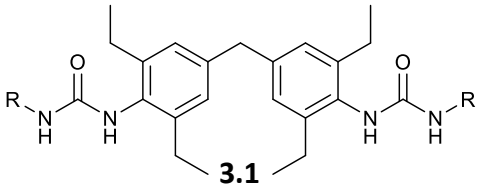

3.1

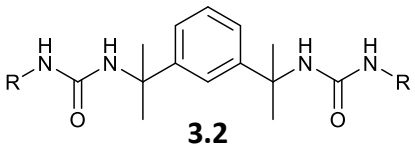

3.2

AZD-2281 mimetic functionalities:

R =

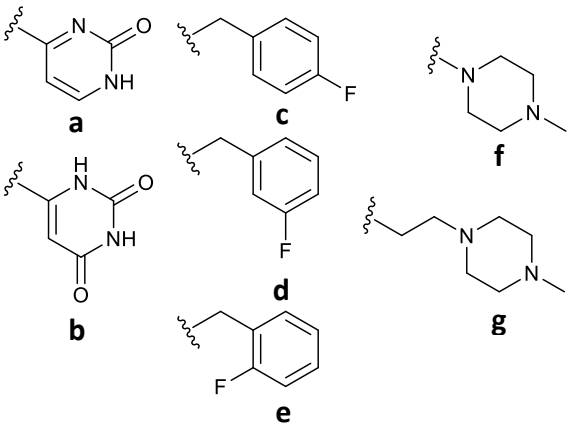

a **b** **c** **d** **e** **f** **g**

AZD-6140 mimetic functionalities:

R =

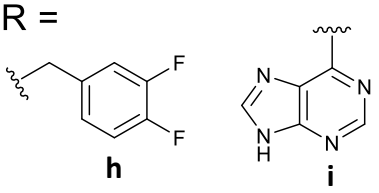

h **i**

'Generic' gelators for non-mimetic crystallisations:

R =

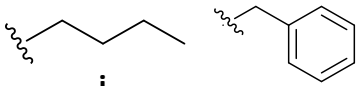

j **k**

Compounds **3.1a-k** and **3.2a-k** were all synthesised by reacting primary amino-derivatives of the R-group (2.1 molar eq.) with the diisocyanato-derivative of the spacer groups (1 molar eq.). Most of these reactions could be completed at ambient temperature in chloroform with precipitates forming within minutes, which could then be filtered and purified as required. Typical yields were from 74 % to 90 %. Synthesis under reflux and using dry conditions had little impact on the purity and yield of reaction. The exceptions to this procedure were the cytosine derivatives (**3.1a** and **3.2a**), uracil derivatives (**3.1b** and **3.2b**) and adenine derivatives (**3.1i** and **3.2i**) which were synthesised in a pyridine suspension under reflux due to the poor solubility of these products in organic solvents and instability of isocyanates in water. Yields ranged between 36 % to 68 % for these all compounds synthesised via reflux in pyridine. All compounds were characterised via ^{1}H-NMR spectroscopy, mass spectrometry and elemental analysis. Two-dimensional NMR methods were also employed to aid the characterisation of some compounds.

3.4 Gelation behaviour of API-mimetic bis(urea) compounds

All mimetic-gelators were screened for gelation behaviour in a diverse selection of 50 organic solvents and water, by attempting to dissolve the gelator in the solvent of choice via heating and allowing to cool to room temperature. Gelation was

qualitatively determined through inversion tests, with representative of gels further characterised through frequency-sweep and stress-sweep rheometry experiments. SEM imaging of the xerogels was also undertaken to confirm that formation of fibrous networks. All gels could be returned to sol state by the addition of tetrabutylammonium acetate (0.5-2 molar equivalents). Some single crystals of gelators were also obtained through the gelation screening and SCXRD data was collected, with the resulting structures providing insight to the gelator conformation and supramolecular interactions.

3.4.1 Cytosine, uracil and adenine derivatives

The bis(urea)s derived from cytosine, uracil and adenine are all insoluble in all tested organic solvents and water and are therefore non-gelators. Even when aliquots of DMSO are added to each suspension to encourage dissolution no gels form. Additional cytosine and uracil bis(urea)s derived from a hexylene spacer (**3.3a** and **3.3b**), which typically produces more soluble bis(urea) compounds, were also synthesised to try to improve the solubility profile in organic solvents and water. However, **3.3a** and **3.3b** are also essentially insoluble in the other solvents tested, except DMSO, benzyl alcohol and nitrobenzene in which dissolution can be achieved with heat. Stable solutions or precipitates form within minutes of cooling to ambient temperature. Therefore, these compounds could not be utilised for API-mimetic gel-phase crystallisations.

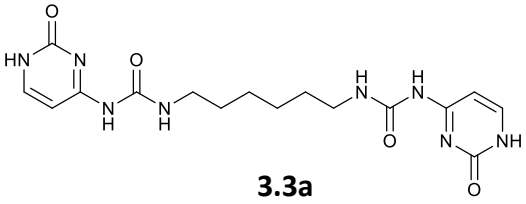

3.3a

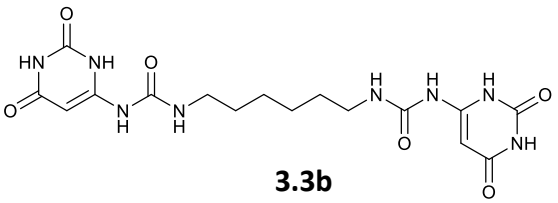

3.3b

3.4.2 Fluorobenzyl derivatives

The gelation versatility and effective of mono-fluorobenzyl gelators significantly varied based on the substitution position of the fluorine atom (**Table 3-2**). As expected, the **3.1**-spacer yielded more versatile gelators than the corresponding **3.2** derivatives. The *p*-fluorobenzyl gelators (**3.1c** and **3.2c**) are more versatile gelators than the corresponding *m*-fluorobenzyl and *o*-fluorobenzyl derivatives. This is particularly significant for the **3.2**-derivatives with **3.2c** gelling 12 solvents, whilst **3.2e** (*o*-

fluorobenzyl) gels 5 solvents and **3.2d** (*m*-fluorobenzyl) is a non-gelator in all solvents tested, typically crystallising or forming viscous liquids rather than gelling even when concentrations are increased up to 5 % w/v.

Table 3-2. Gel screening results in a selection of solvents used for AZD-2281 and AZD-6140 solid-state screening. The **3.1** derivatives were tested at 1 % w/v, whilst **3.2** derivatives were tested at 2 % w/v due to their higher solubility. G^o= opaque gel, G^T= translucent gel, Ppt = precipitate, X = crystallisation, VL = viscous liquid.

	3.1c	**3.1d**	**3.1e**	**3.1h**	**3.2c**	**3.2d**	**3.2e**	**3.2h**
Acetone	G^o	G^o	G^o	PG	G^T	X	Ppt	Ppt
Acetonitrile	G^T	G^T	G^o	G^T	G^T	X	G^T	X
Chloroform	G^T	PG	G^T	Ppt	G^T	Ppt	Ppt	Ppt
Chlorobenzene	G^T	G^T	G^T	VL	G^T	VL	G^T	G^T
DCM	G^T	Ppt	G^T	VL	PG	Ppt	PG	Ppt
1,4-Dioxane	G^T	G^T	G^T	G^T	PG	X	Ppt	X
Ethanol	G^T	PG	G^o	Ppt	X	X	X	X
Ethyl acetate	G^o	G^T	G^T	VL	G^T	Ppt	Ppt	G^T
Nitrobenzene	G^T	G^T	G^T	G^T	G^T	VL	G^T	G^T
Propan-2-ol	G^T	PG	PG	Ppt	X	X	X	X
THF	G^T	G^T	G^T	G^T	Ppt	X	Ppt	X
Toluene	G^T	PG	G^o	Ppt	G^T	Ppt	G^T	G^T
Water	IS	IS	IS	IS	IS	IS	IS	IS

The gel screening procedure also yielded single crystals of **3.2c-e** and **3.2h**, which could be analysed by SCXRD. The structures all exhibit intermolecular urea tape synthons (**Figure 3-2**). Interestingly, in the structures for **3.2d**, **3.2e** and **3.2h** the urea tapes are antiparallel, whereas the urea tapes are parallel in **3.2c**. Previous work by the Steed group has demonstrated that anti-parallel urea tapes typically yield more versatile and effective gelators,[19] however in this case the most versatile gelator of the three gelators is the one which forms parallel α-tapes.

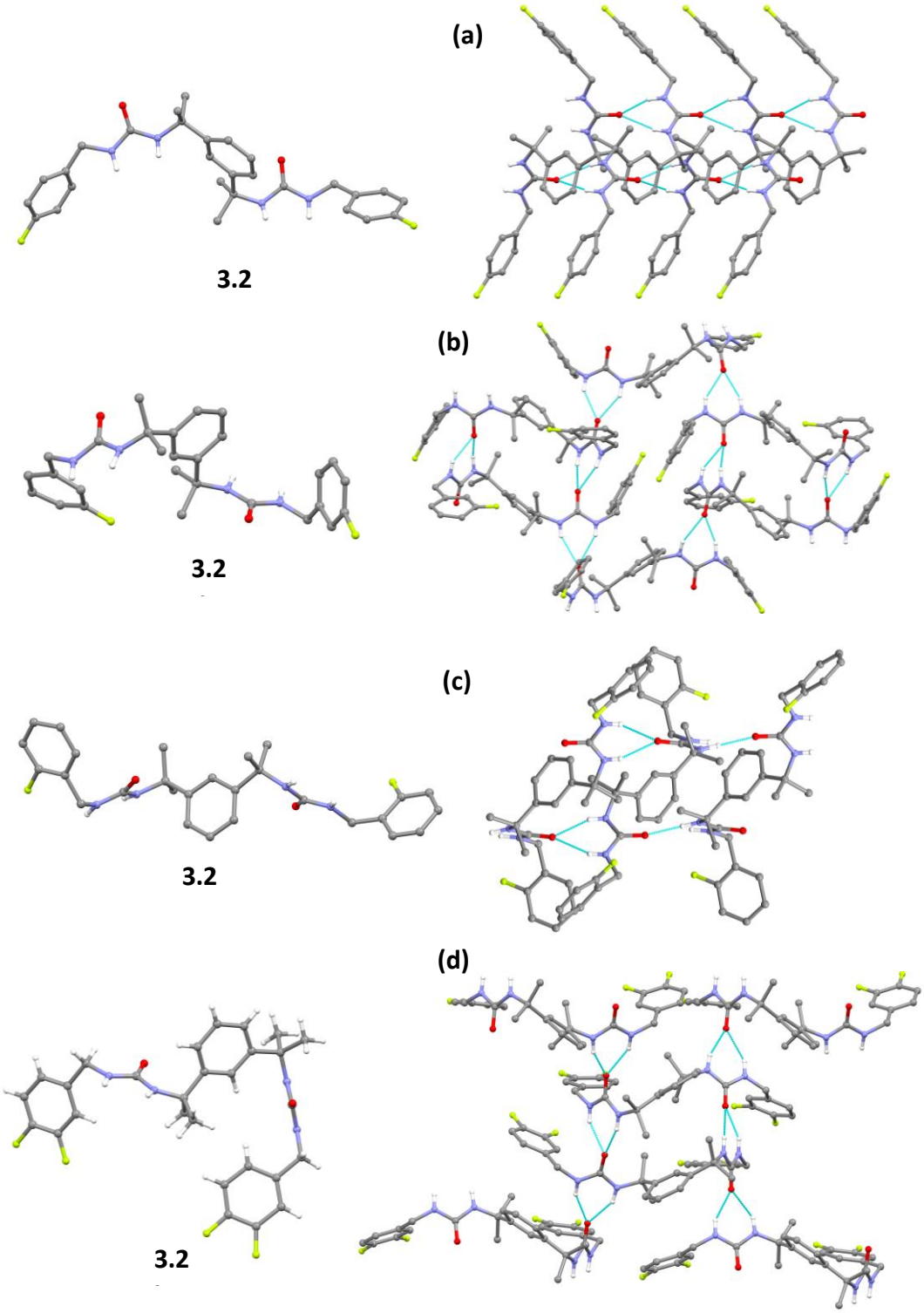

Figure 3-2. Urea tape synthons in crystal structures of **(a) 3.2c**, **(b) 3.2d**, **(c) 3.2e** and **(d) 3.2h**. The urea groups are in a parallel orientation in **3.2c**, which is the most versatile LMWG, whilst the urea groups are all arranged anti-parallel in **3.2d**, **3.2e** and **3.2h**.

The experimental XRPD patterns of the xerogels and crystal phase of **3.2c** are a good match. This raises the possibility that similar molecular packing could be exhibited in both the xerogel and crystal forms, and intermolecular parallel α-tape synthons may potentially be present in both forms (**Figure 3-3**). However, it is important to note that a transition from gel to crystal during the drying down process to form the xerogels cannot be excluded[13] and further techniques, such as fibre diffraction or computational modelling are required to confirm this. Indeed, the SEM images of the xerogel do exhibit two distinct architectures: large blocks/tapes and fine fibres (**Figure 3-4**). Microscopy imaging of all other xerogels examined revealed fine fibrous networks (**Appendix 2**).

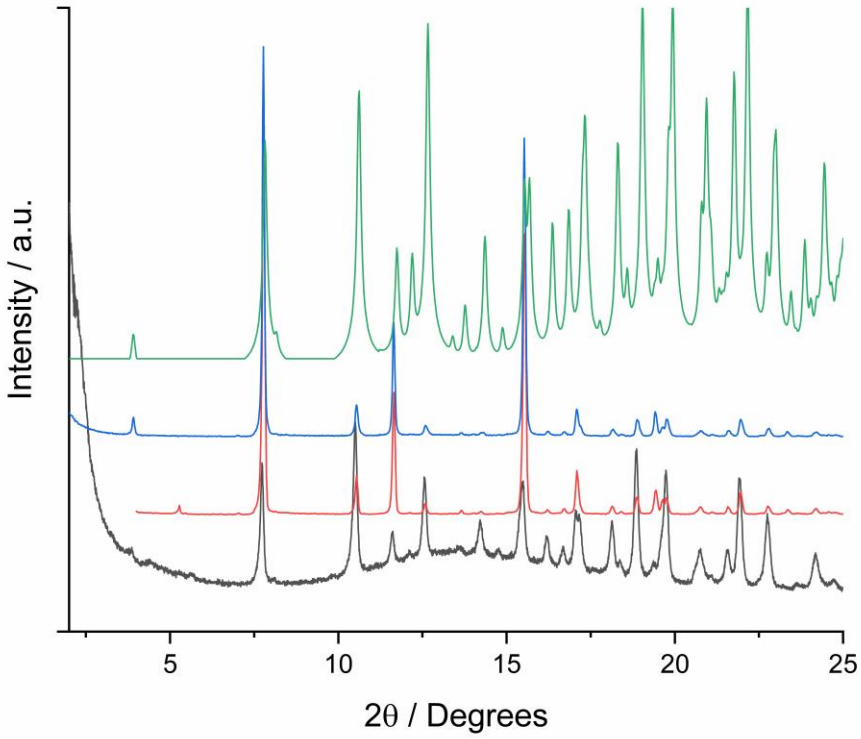

Figure 3-3. The calculated XRPD pattern from SCXRD data for **3.2c** at 120 K (in green) closely matches the experimental XRPD patterns (under ambient conditions) of the **3.2c** crystals (in blue), nitrobenzene xerogel (in red) and acetonitrile xerogel (in black). This indicates that the same molecular packing arrangement may be in the gel and crystal phases, which would mean gelation is driven by parallel urea tape synthon formation. However, a phase transition upon drying the gel phase cannot be ruled out. Significant preferred orientation can be observed in the XRPD patterns of the **3.2c** crystals and nitrobenzene xerogel.

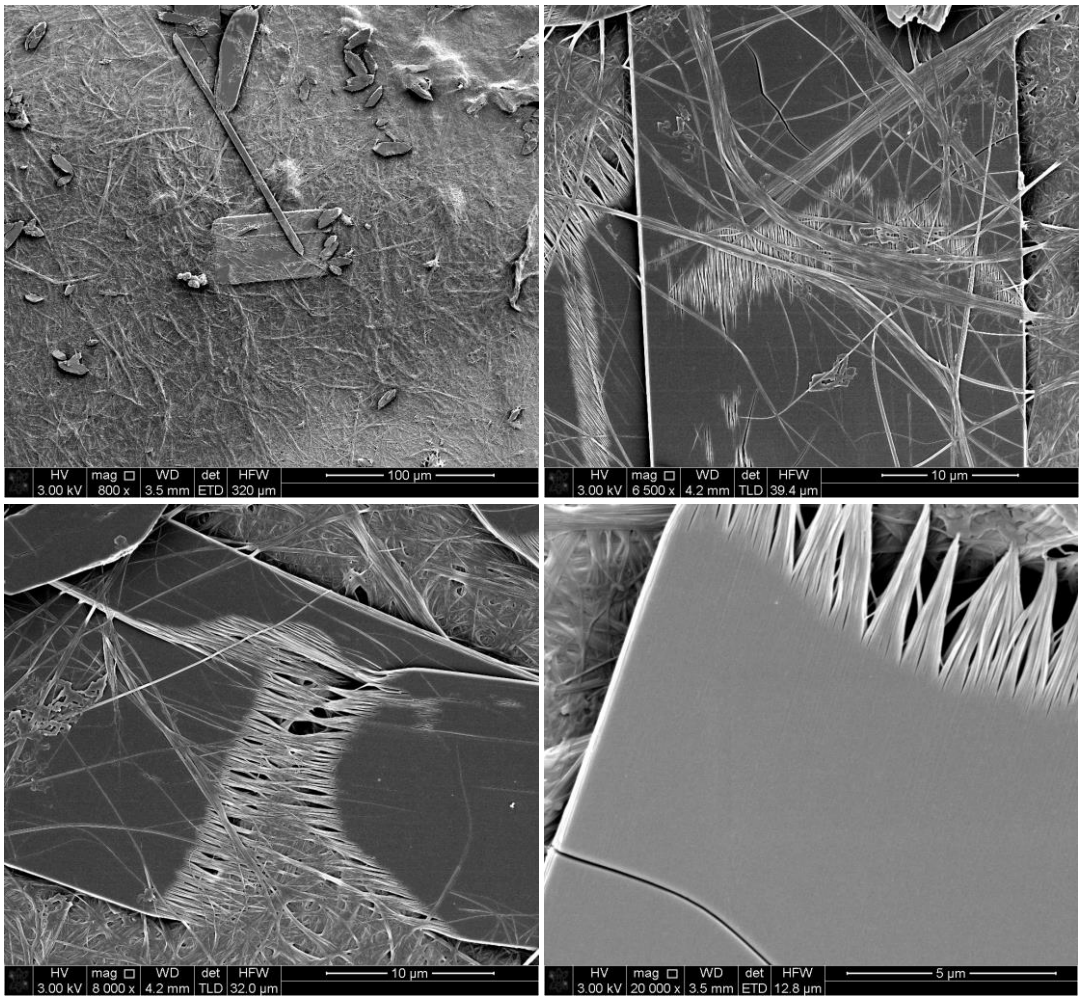

Figure 3-4. SEM images of the **3.2c** nitrobenzene xerogel revealing a mixture of fine fibres and larger block and rod type architectures. These block and rod architectures exhibit fibrous regions, which may be indicative of a potential phase transition from gel upon drying.

3.4.3 Piperazine Derivatives

Compounds **3.1f** and **3.2f** are both non-gelators in all solvents tested, whilst **3.1g** and **3.2g** are relatively versatile LWMGs (**Table 3-3**).

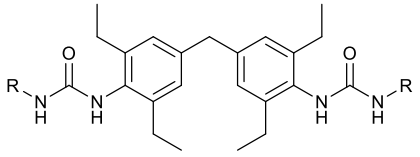

3.1

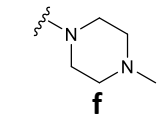

f

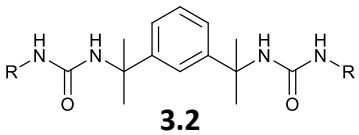

3.2

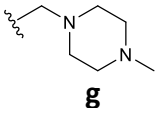

g

Table 3-3. Gel screening results for compounds **3.1f-g** and **3.2f-g**. The gel screen reveals **3.1f** and **3.2f** to both be non-gelators, whilst **3.1g** and **3.2g** did exhibit some gel behaviour in the solvents tested.

	3.1f	**3.2f**	**3.1g**	**3.2g**
Acetone	IS	Ppt	Ppt	Ppt
Acetonitrile	Ppt	X	G^T	X
Chloroform	IS	Ppt	IS	PG
Chlorobenzene	Ppt	Ppt	G^T	G^T
DCM	IS	Ppt	IS	Ppt
1,3-dichlorobenzene	Ppt	X	G^T	G^T
1,4-Dioxane	Ppt	Ppt	G^T	G^T
Ethanol	IS	S	IS	Ppt
Ethyl acetate	IS	Ppt	IS	Ppt
Nitrobenzene	Ppt	S	G^T	G^T
Propan-2-ol	Ppt	S	G^T	S
THF	Ppt	Ppt	G^T	G^T
Toluene	IS	Ppt	Ppt	Ppt
Water	IS	IS	IS	IS

A single crystal of **3.2f** was grown from 1,3-dichlorobenzene. The crystal diffracted poorly and SCXRD data has low associate reliability. However, the structure provides some valuable insights to the molecular assembly behaviour and reveals that both urea groups adopt an *anti-syn* conformation and form intermolecular $R_2^2(12)$ synthons via dimeric $N–H_{(urea)}\cdots N_{(piperazine)}$, as opposed to urea α-tapes (**Figure 3-5**). This likely explains the lack of gelation observed for these compounds. Introducing an ethylene linker between urea and piperazine group means that the intermolecular $R_2^2(12)$ synthons cannot be formed by molecules of **3.1g** and **3.2g**. This potentially enables the urea functionalities to form the infinite tape synthons associated with versatile gelation behaviour but attempts to grow single crystals of **3.1g** and **3.2g** for SCXRD analysis to test this theory were unsuccessful. SEM imaging was used to compare the

precipitate from nitrobenzene for **3.1f** and **3.2f** with the nitrobenzene xerogels of **3.1g** and **3.2g**. The microscopy images of the precipitates reveal large plank and needle architectures for **3.1f** and **3.2f**, as opposed to the network of fine fibres observed for the **3.1g** and **3.2g** xerogels (**Figure 3-6**).

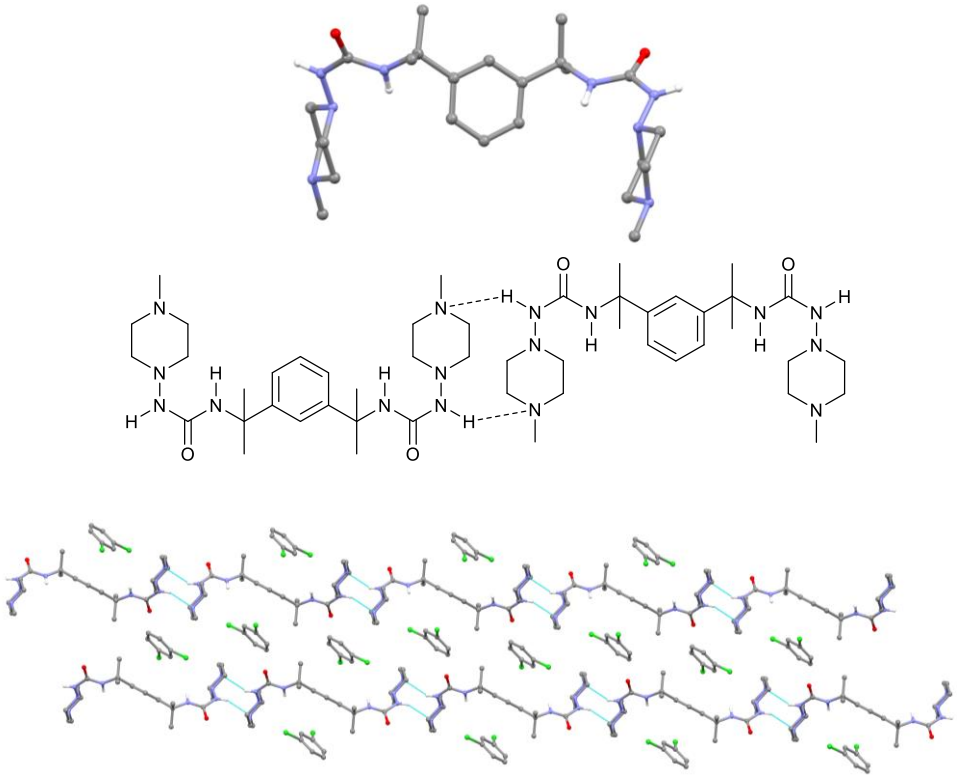

Figure 3-5. (a) The single crystal structure of **3.2f** reveals both urea groups are in the anti-syn conformation. **(b)** The molecules form intermolecular $R_2^2(12)$ synthons via dimeric N-$H_{(urea)}\cdots N_{(piperazine)}$ hydrogen bonds. **(c)** The molecules form chains via these interactions with alternating layers of **3.2f** and 1,3-dichlorobenzene molecules.

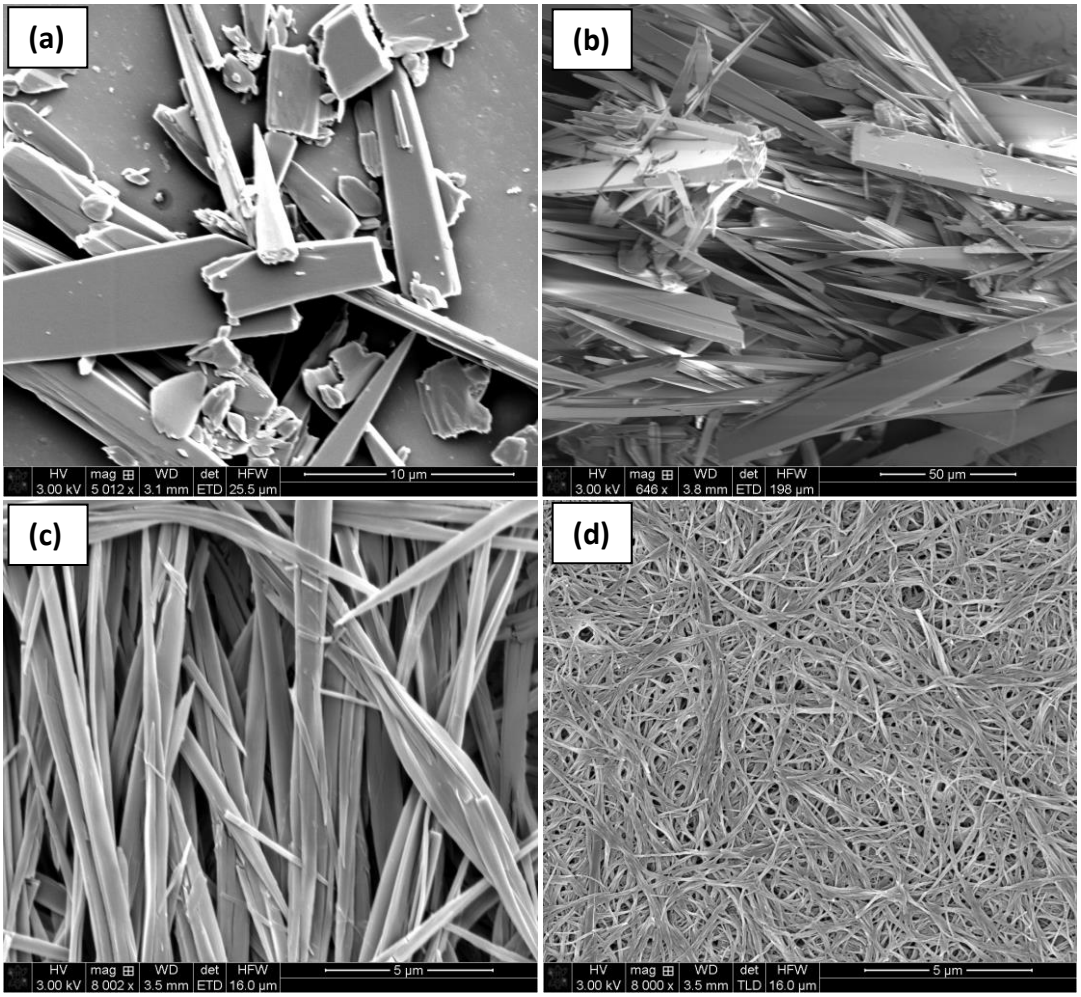

Figure 3-6. SEM images of the precipitate obtained from nitrobenzene for **(a) 3.1f** and **(b) 3.2f**. SEM images of the nitrobenzene xerogels of **(c) 3.1g** and **(d) 3.2g**. The $R_2^2(12)$ synthons observed in the **3.2f** crystal structre likely restricts α-tape assembly and promotes crystallisation over gelation.The addition of an ethylene unit between urea and piperazine end groups in **3.1g** and **3.2g** prevents the formation of $R_2^2(12)$ synthons and potentially enables α-tape assembly resulting in the formation of gel fibres.

3.5 Solid-form screening of APIs

3.5.1 Solid-form screening of AZD-2281

An solid-state screening in solution and LMWG media was undertaken for AZD-2281. Crystallisation under the conditions tested primarily yield either the kinetically stable form A or solvate forms. Single crystals of a nitrobenzene solvate was obtained that have not previously been reported. This nitrobenzene solvate was produced from both solution phase and gel-phase crystallisations, with the gels producing larger and well-defined crystalline blocks. This new form is essentially isostructural with known solvates (**Figure 3-7**). In these all these AZD-2281 solvates, the API molecules form

$R_2^2(8)$ dimers via hydrogen bonds between cyclic amide functionalities and the structures reveal pores which contain disordered solvent molecules (**Appendix 2**). The nitrobenzene solvate will never be viable for use in active formulations due to the harmful nature of nitrobenzene.

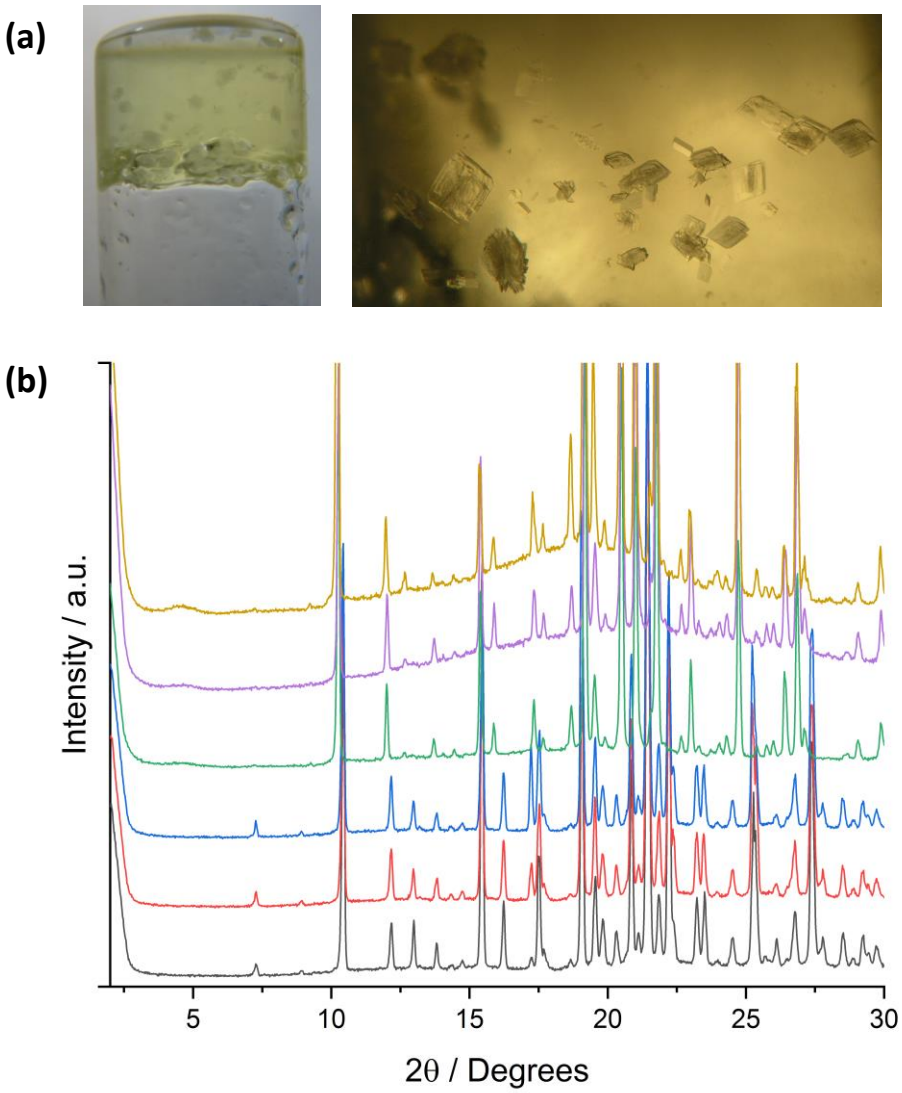

Figure 3-7. (a) Crystals of the AZD-2281 nitrobenzene solvate in a 1 % w/v gel of **3.1c**. **(b)** XRPD patterns of the AZD-2281 DCM solvate obtained from DCM solution (yellow), and DCM gels of **3.1c** (purple) and **3.1e** (green). XRPD patterns of the nitrobenzene solvate obtained from nitrobenzene solution (blue) and nitrobenzene solution API-mimetic gels **3.2c** (red) and **3.1g** (black). The similarities between the patterns of the DCM and nitrobenzene solvates can be seen, particularly at lower angles.

The anhydrous form A of AZD2281 was obtained from solutions of acetonitrile, chlorobenzene and 1,4-dioxane. Crystallisations in gels of these same solvents using API-mimetic **3.1c**, **3.2e** and **3.1g**, in addition to generic gelator **3.1k** also resulted in

form A being obtained (**Figure 3-8**). The fact that the thermodynamically stable form L did not crystallise from any solution or gel-phased crystallisation without seeds of form L being present is consistent with previous crystallisation conditions and experiments utilised. Form L has previously only been obtained via sublimation, seeding with crystals of form L and/or by stirring slurries of form A over days to weeks.[14] Gelator concentrations between 0.3-3 % w/v and AZD2281 concentrations between 2-25 % w/v were utilised in experiments as gelator-substrate interactions, which may ultimately impact crystallisation outcomes, can be dependent upon the molar ratio on the components.[15] However, form A or the solvated forms were obtained regardless of the concentrations used.

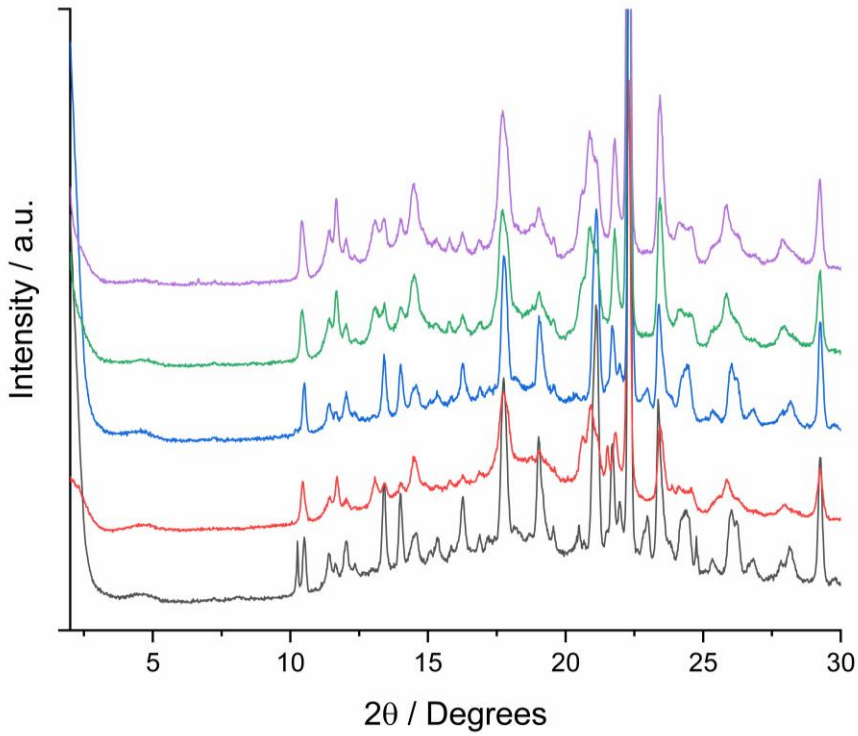

Figure 3-8. XRPD patterns of AZD-2281 anhydrous form A obtained from acetonitrile solution (black) and the following API-mimetic gels: 1 % w/v acetonitrile gel of **3.1c** (in red), 2 % w/v chlorobenzene gel of **3.2e** (in blue) and 0.5 % w/v 1,4-dioxane gel of **3.1g** (in green). Form A also crystallised from a 2 % w/v acetonitrile gel of generic **3.2k** (in purple).

3.5.2 Solid-form Screening of AZD-6140

Crystallisation procedures outlined in the AZD-6140 Polymorph patent[9] were carried out and forms I and II were obtained by following these procedures (**Table 3-4**). Forms III and IV proved elusive when following the procedures described in the patent, including some variation of the reported conditions, and these forms were not obtained. The AZD-6140 material provided by AstraZeneca was form II, which is

kinetically stable under ambient conditions. Form I was obtained exclusively from melt-cooling cycles.

Table 3-4. Crystallisation procedures to replicate the procedures outlined in the AZD-6140 polymorph patent.[9] The form that the procedure yielded according to the patent is reported, along with the form obtained experimentally experiments in this study. Only forms I and II were yielded, with reported forms III and IV proving to be elusive. Forms were confirmed via XRPD and DSC.

Crystallisation Procedure Outlined in Patent [9]	Form Reported in Patent	Form Obtained Experimentally
AZD-6140 (3 mg) was heated and cooled using a hot-stage microscope in the following manner: 35 to 143 to 35 to 148 to 35 to 148 to 350 °C.	Form I	Form I
AZD-6140 (10 mg) was dissolved in 200 µL of ethanol in a warm water bath (up to 60 °C). The solution then was left to cool slowly in the water bath from 60 °C to ambient temperature.	Form II and Form III (mixture)	Form II
AZD-6140 (45 mg) was dissolved in 150 µL of chloroform in a warm water bath (up to 50 °C). The resulting solution was left to crystallise overnight and dried under nitrogen.	Form II	Form II
AZD-6140 (10 mg) was dissolved in 0.12 mL acetonitrile via warming in water bath (up to 60 °C). The solution then was left to cool slowly in the water bath from 60 °C to ambient temperature. The resulting crystals were dried under nitrogen.	Form IV	Form II

A broader crystallisation screening procedure using multiple solvents and gels of **3.1h** and **3.2h** was also completed. The crystalline material from all experiments was obtained as either a powder or fine crystalline needles and was analysed by XRPD (**Figure 3-9**) and IR spectroscopy to determine the crystal form. Unit cell measurements were also obtained from single crystals. Form II crystallised from all solution and gel-phase crystallisation conditions tested (**Table 3-5**). Again, a wide range of gelator and API concentrations were utilised in these experiments but form II was obtained from all crystallisations regardless. Therefore, the API-mimetic 3,4-difluorobenzyl gelators failed to influence the crystallisation outcome regardless of solvent or API/gel concentrations. Crystallisations with the mono-fluorobenzyl gelators and the generic control gels also exclusively yielded II.

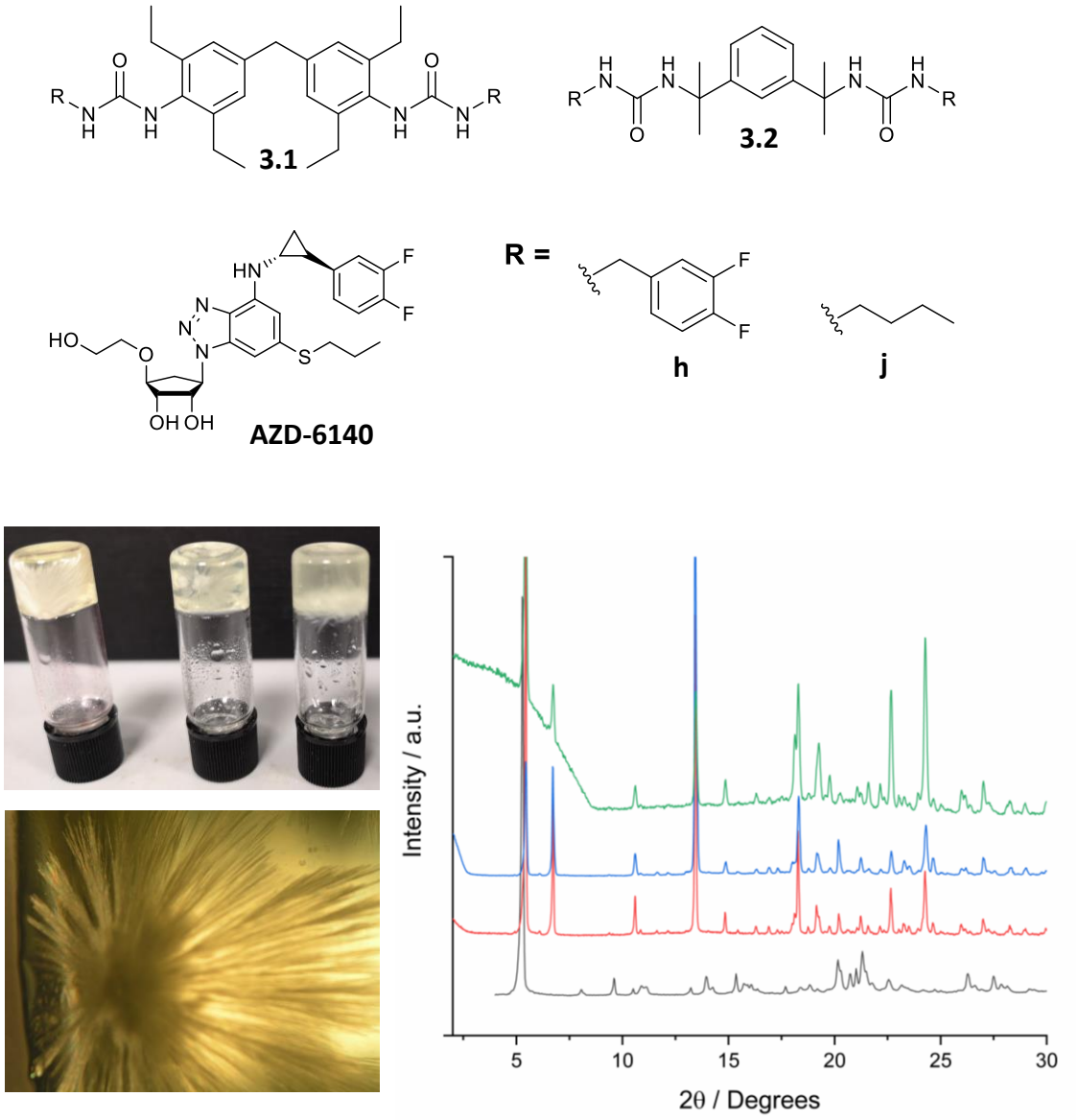

Figure 3-9. (a) Photograph of AZD-6140 crystals obtained in nitrobenzene gels of API-mimetic **3.1h** and **3.2h**, and control gel **3.1j** (left to right). **(b)** A close-up image to show the crystalline needles of form II of AZD-6140 obtained from a nitrobenzene gel of **3.2h**. **(c)** XRPD patterns of AZD-6140 form I crystallised from melt-cooling cycles (black) and form II of AZD6140 crystallised from an acetonitrile **3.1h** gel (red), a nitrobenzene **3.2h** gel (in blue) and nitrobenzene solution (green). Form II was obtained from all solution phase and gel-phase crystallisations, regardless of concentrations and conditions utilised. Generic control gels also yielded form II.

Table 3-5. A selection of the results of crystallisation screening using API-mimetic gelators **3.1h** and **3.2h**. All crystallisations yielded form II of AZD-6140, which is kinetically stable at ambient conditions. The solution-phase and generic gels using the same solvents and drug loading concentrations yielded the same crystallisation outcomes, meaning the API-mimetic gels had no influence on crystallisation outcomes.

Gelator	Solvent	Gel conc. / % (w/v)	Drug loading / mg	Crystallisation outcome from gel	Crystallisation outcome from solution
3.1h	Acetonitrile	0.5	10	Form II	Form II
3.1h	Chloroform	0.3	10	Form II	Form II
3.1h	Chloroform/Ethyl acetate (1:1)	0.3	10	Form II	Form II
3.1h	Nitrobenzene	0.5	10	Form II	Form II
3.2h	Nitrobenzene	1	10	Form II	Form II
3.2h	Toluene	1	10	Form II	Form II
3.2h	Ethyl Acetate	1	10	Form II	Form II
3.2h	IPA	1	25	Form II	Form II

3.7 Using boronic acid gelators for 'full API-mimicking'

Due to the unsuccessful attempts to influence crystallisation with partially-mimetic gelators, attempts were made to synthesise bis(urea) gelators with the full AZD-6140 molecule appended. This approach utilises the well-documented reversible covalent bond formation between boronic acids and 1,2- and 1,3-diols, which have been advantageous in many other applications.[16–18] The 1,2-diol functionality present in AZD-6140 allows the formation of a reversible covalent bond between a LMWG containing a boronic acid functionality and this could result in gel fibres with the full AZD-6140 structure presenting at the surface, providing a full molecule template site for nucleation to occur (**Figure 3-10**).

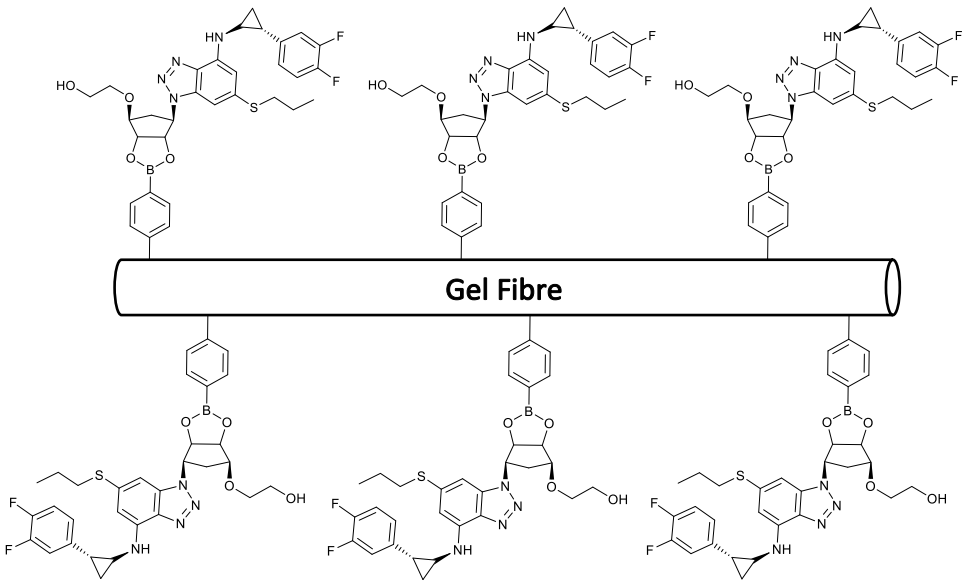

Figure 3-10. Proposed reversible covalent bond formation between the AZD-6140 1,2-diol and LMWG phenylboronic acid functionalities to yield fibres with the full AZD-6140 structure at the surface.

Attempts to synthesise gelators with the two previously utilised spacer groups (**3.1** and **3.2**) and ortho, meta and para-substituted amino phenylboronic acids were undertaken. Initial iterations involved THF or chloroform at room temperature and under reflux with the unprotected boronic acids result in an insoluble brown residue likely due to the isocyanate reacting indiscriminately with the hydroxyl and amine functionalities. Thus, the boronic acids were protected using pinacol and the reactions repeated in THF under reflux to yield pinacol protected boronic acid bis(urea) compounds. To deprotect the acid functionalities, the pinacol-protected products were suspended in a THF-Water mixture (4:1) with $NaIO_4$ and hydrochloric acid and heated at 60 ^oC for 5 hours. The **3.2** derivatives were then purified via trituration with DMF and washing with copious amounts of water and diethyl ether. However, attempts to purify the compounds of type **3.1** via this method failed, with trace amounts of impurities still being present. The negligible solubility of these **3.1**-derivatives at ambient temperatures and tendency to gel or precipitate within seconds to minutes of dissolution with heat made column purifications challenging. Thus the **3.1**-derivatives were preliminary screened for gelation behaviour with trace impurities present to offer insights into whether pursuing the purified product was worthwhile. Crystallizations were not attempted with the impure **3.1**-derivatives and further work should develop the synthetic process to yield pure compounds before they are utilised in crystallisation screening.

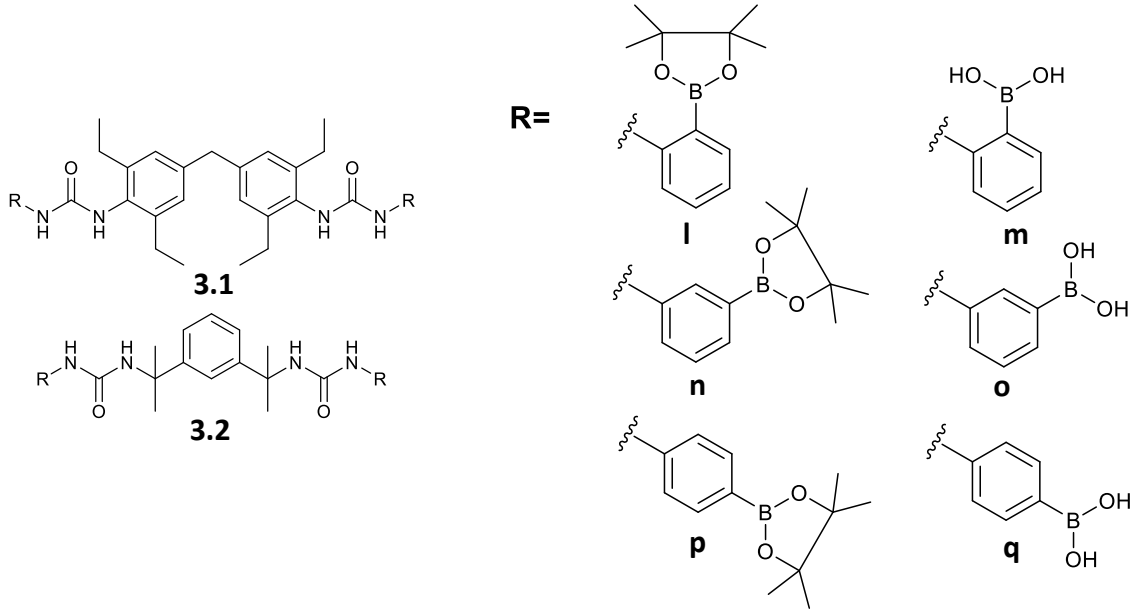

Gel screens of the **3.1** and **3.2** phenylboronic bis(urea) derivatives, both pinacol protected and free acid, were undertaken in solvents from which AZD-6140 crystallises (**Table 3-6**). Whilst impurities are present, homogenous dissolution of the **3.1** compounds was achieved in a selection of solvents and gels form indicating the purified compounds may also form gels. Gelation occurs within a matter of seconds to minutes. The phenylboronic bis(ureas) derived from linker **3.1** were seemingly more versatile gelators those derived from linker **3.2**, which is consistent with previous observations of these two linker groups in LWMG bis(urea) compounds. Generally, the gelation behaviour of the corresponding pinacol-protected and free boronic acid compounds were similar. For both **3.1** and **3.2** derivatives, the *para*-substituted phenyl boronic acid functionalities yielded the most versatile gelators, followed by the *meta*-substituted derivatives. The free and pinacol-protected ortho-phenylboronic acid compounds were non-gelators, likely due the proximity of the boronic acid and urea functionalities. This possibly results in intramolecular hydrogen bonds forming between the boronic oxygen atom and the urea hydrogen atom adjacent to the phenyl boronic functionalities, restricting the formation of intermolecular urea α-tapes. Additionally, steric hindrance generated by the pinacol group in compounds **3.1l** and **3.2l** likely restrict urea tape assembly. Again, a selection of gels of purified **3.2n-q** were characterised through rheological stress-sweep and frequency-sweep experiments to confirm their gel-like behaviour.

Table 3-6. Gel screen results of free and pinacol protected boronic acid gelators **3.1l-q** and **3.2l-q**. Gels were formed by dissolving the gelator in solvent via heat and allowing the resulting sol to cool to ambient temperature. The **3.1** compounds were tested at gelator concentrations of 1 % (w/v) and the **3.2** compounds at 2 % (w/v). Impurities are present in the **3.1** derivatives and may affect the gelation behaviour. G^o = opaque gel, G^T= translucent gel, PG = partial gel, IS = insoluble, Ppt = precipitate and S = stable solution.

Solvent	3.1l	3.1m	3.1n	3.1o	3.1p	3.1q	3.2l	3.2m	3.2n	3.2o	3.2p	3.2q
Acetonitrile	Ppt	Ppt	PG	PG	G^T	G^T	S	S	G^o	PG	G^T	G^T
Benzyl Alcohol	Ppt	Ppt	G^T	G^T	G^T	G^T	S	S	PG	PG	G^T	G^T
Chlorobenzene	Ppt	Ppt	G^T	G^T	G^T	Ppt	S	S	Ppt	Ppt	G^T	Ppt
Chloroform	Ppt	Ppt	Ppt	IS	Ppt	IS	Ppt	Ppt	Ppt	Ppt	Ppt	Ppt
Ethanol	IS	IS	IS	IS	IS	IS	S	S	Ppt	S	Ppt	S
DMF	Ppt	Ppt	Ppt	Ppt	G^T	G^T	Ppt	Ppt	Ppt	Ppt	Ppt	Ppt
DMSO	Ppt	Ppt	Ppt	PG	PG	PG	S	S	S	S	S	S
Nitrobenzene	Ppt	Ppt	G^T	G^T	G^T	G^T	S	S	G^T	G^T	G^T	G^T
Nitromethane	IS	IS	IS	IS	IS	IS	Ppt	Ppt	Ppt	Ppt	Ppt	Ppt
Toluene	Ppt	Ppt	Ppt	Ppt	G^T	G^T	Ppt	Ppt	Ppt	Ppt	Ppt	Ppt

Due to time constraints, only a limited crystallisation screening of AZD-6140, using only gels of **3.2p** and **3.2q,** was undertaken. Solutions of AZD-6140 were gelled by dissolving the gelator using heating (up to the boiling point of the tested solvent) and allowing to cool to room temperature. Only nitrobenzene, benzyl alcohol and acetonitrile were used in the gel screen and all crystallisation outcomes yielded the form II of AZD-6140 (**Table 3-7**).

Table 3-7. Representative crystallisation conditions and forms of AZD-6140 obtained from free boronic acid gels (**3.2q**) and pinacol protected boronic acid gels (**3.2p**). Form III was obtained from all solution and gel-phase crystallisations.

Gelator	Solvent	Gel conc. / % (w/v)	Drug loading / mg	Crystallisation outcome from gel	Crystallisation outcome from solution
3.2p	Nitrobenzene	0.5	10	Form II	Form II
3.2p	Benzyl alcohol	1	15	Form II	Form II
3.2p	Acetonitrile	1	10	Form II	Form II
3.2q	Nitrobenzene	0.5	10	Form II	Form II
3.2q	Benzyl alcohol	1	15	Form II	Form II
3.2q	Acetonitrile	1	10	Form II	Form II

3.8 Conclusions

LMWGs containing functionalities present in AZD-6140 and AZD-2281 were synthesised and their gelation behaviour investigated. Mono-fluorobenzyl compounds were found to be relatively versatile and effective gelators, whilst the 3,4-difluorobenzyl compounds were slightly less versatile. Crystal structures of these

fluorobenzyl compounds reveal urea α-tape synthons which are often considered a driver for gelation behaviour. For the piperazine-derived compounds, introducing a ethylene spacer between urea and piperazine functionalities is critical in order for gelation behaviour to be observed. This is likely due to the disruption of $R_2^2(12)$ motifs which are exhibited in the crystal structure of the **3.2f** 1,3-dichlorobenzene solvate, which possibly enables urea α-tape assembly. Cytosine and uracil bis(urea) compounds proved to have poor solubility and are non-gelators.

An extensive solid-state screen was completed including crystallisation from solution, generic supramolecular gels and API-mimetic gels. Solution and gel-phase crystallisations yielded the same crystal forms in all cases, meaning the API-mimetic gels failed to influence the crystallisation outcomes of AZD-2281 or AZD-6140. This was the result regardless of the concentrations of gelator and API used, despite a wide range being tested.

Bis(ureas) with either free or pinacol-protected phenylboronic acid end groups were synthesised, although further work to purify the **3.1**-derivatives is required. These compounds show promising gelation behaviour The protected boronic acid could be deprotected via stirring with acid and $NaIO_4$ under ambient temperature, with the rate of deprotection increased by heat. The impure **3.1**-derived meta and para-substituted phenyl boronic acid gelators exhibit gelation behaviour, whilst the ortho-substituted derivative yielded no gels, which is hypothesised to be due to the close proximity of boronic acid functionalities to urea groups in these ortho-compounds. An abridged crystallisation screening in pinacol protected and free boronic acid gelators crystallised form II of AZD-6140.

3.9 Future work

Future work should focus on completing the boronic acid gel work, including work to improve the yields obtained through deprotection reactions and the purification of the **3.1**-derivatives, which exhibit promising gelation behaviour. If pure gelators can be obtained, then a crystallisation screen of AZD-6140, or other 1,2- or 1,3-diols could be completed with both pinacol protected and free boronic acid gelators to see if full-molecule API-mimicking can influence the crystallisation outcomes. The free boronic acid gelators could also be utilised in two approaches. Firstly, by forming the reversible

covalent bond between the diol compound and boronic acid first in solution before inducing gelation. Secondly, by using the free-boronic acid gelators to gel a solution of AZD-6140.

Furthermore, crystallisation screen with the API-mimetic gels could be completed at different temperatures. This could be particularly useful for AZD-6140 where the forms all exhibit enantiotropic relationships with one another. Investigating whether the mimetic gelators can influence the crystallisation outcomes at the different reported transition points would be beneficial.

3.10 Experimental Details

Synthesis details and characterisation for compounds **3.1a-q** and **3.2a-q,** in addition to details of the crystallisation screening procedures presented in this chapter, are provided below. Please refer to Chapter 6– General Experimental for additional experimental details.

3.10.1 Synthetic Procedures

Synthesis of cytosine, uracil and adenine derivatives:

Bis(ureas) derived from cytosine, uracil and adenine were synthesised by the addition of tetraethyl-4,4'-methylenediphenyl isocyanate (500 mg, 1.38 mmol) or 1,3-bis(1-isocyanato-1-methylethyl)benzene (337 mg, 1.38 mmol) or hexamethylene diisocyanate (232 mg, 1.380 mmol) to a stirred suspension of cytosine, adenine or uracil (2.90 mmol) in pyridine (20 cm^3) under dry conditions at 115 ^oC. The suspension was then heated under reflex for 24 hours. After this, the suspension was filtered under suction and the precipitate triturated in DMF (15 cm^3) for 24 hours. The product was then filtered under suction and washed with hot water (150 cm^3) followed by diethyl ether (3 x 15 cm^3). The solid was then dried in a drying pistol at 110 ^oC for 24 to 48 hours. This process yielded the following compounds: **3.1a, 3.1b, 3.1i, 3.2a, 3.2b, 3.2i, 3.3a** and **3.3b**.

Synthesis of fluorobenzyl and piperazine derivatives:

Bis(ureas) derived from fluorobenzyl or piperazine compounds were synthesised by the addition of tetraethyl-4,4'-methylenediphenyl isocyanate (500 mg, 1.38 mmol) or 1,3-bis(1-isocyanato-1-methylethyl)benzene (337 mg, 1.38 mmol) to a stirred solution of the necessary amine in chloroform (15 cm^3) under air at ambient temperature. The resulting solution was stirred for up to 18 hours to yield a precipitate. The precipitate

was filtered under suction and washed with chloroform (3 x 10 cm^3) and dried in a drying pistol at 110 ^oC. The procedure yielded the following compounds: **3.1c-h** and **3.2c-h.** Generic gelators **3.1j, 3.1k, 3.2j** and **3.2k** were also synthesised via this procedure.

Synthesis of boronic acid derivatives:

The boronic acid derivatives in this work were synthesised by the addition of tetraethyl-4,4'-methylenediphenyl isocyanate (500 mg, 1.38 mmol) or 1,3-bis(1-isocyanato-1-methylethyl)benzene (337 mg, 1.38 mmol) to a stirred solution of the necessary aminophenylboronic acid pinacol ester in THF (15 cm^3) at under dry conditions at 60 ^oC. The resulting solution was heated under reflux for 18 hours to yield a pale cream solid which was isolated via filtration under suction. The **3.1** compounds were then dried in a drying pistol at 110 ^oc. For the **3.2** compounds, the solid can be purified by the trituration in DMF (15 cm^3) for 18 hours, before being washed with hot water (150 cm^3) and diethyl ether (3 x 15 cm^3). The resulting solid was dried in a drying pistol at 110 ^oC. This procedure yielded pinacol protected boronic acid compounds: **3.1l**, **3.1n**, **3.1p**, **3.2l**, **3.2n** and **3.2p**.

To deprotect the boronic acid functionalities, sodium periodate (278 mg, 1.3 mmol) and 2M aqueous hydrochloric acid (10 cm^3) were added to a stirred suspension of the necessary pinacol-protected bis(urea) compound (0.439 mmol) in a THF-water mixture (4:1, 15 cm^3 total). The resulting suspension was heated at 60 ^oC for 5 hours. The reaction mixture was then cooled and filtered under suction to obtain a pale cream precipitate. The solid was triturated in DMF (15 cm^3) for 18 hours, before being washed with water (150 cm^3), then 0.5 M hydrochloric acid aqueous solution (15 cm^3) and diethyl ether (3 x 15 cm^3), then dried in a drying pistol at 110 ^oC. This was sufficient to purify the **3.2** compounds, but impurities remained for the **3.1** compounds. This procedure yielded: **3.1m**, **3.1o**, **3.1q**, **3.2m**, **3.2o** and **3.2q**.

3.10.2 Compound Characterisation

Compound 3.1a

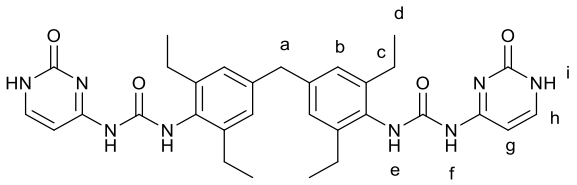

Compound **3.1a** was obtained as a white solid (476 mg, 0.81 mmol, 59 % yield). **1H NMR (400 MHz, DMSO-[d6]): δ =** 11.41 (broad-s, 2H, *i*), 10.22 (broad-s, 2H, *f*), 7.74 (d, 2H, J = 7.0 Hz, *h*), 7.03 (s, 4H, *b*), 6.39 (s, 2H, *e*), 5.58 (d, 2H, J = 7.0 Hz, *g*), 3.96 (s, 2H, *a*), 2.49-2.55 (m, *c* – overlaps with DMSO peak), 1.13 (t, 12H, J = 7.6 Hz, *d*). **[ES+-MS]:** 607.3 [M+Na]. **Elemental analysis** calculated for $C_{31}H_{36}N_8O_4$ (%): C, 63.68; H, 6.21; N, 19.17. Found (%): C, 63.82; H, 6.32; N, 19.01.

Compound 3.2a

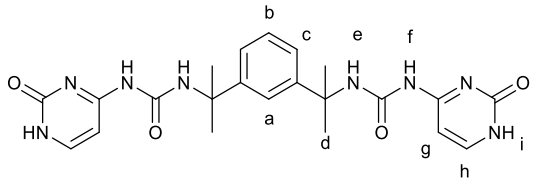

Compound **3.2a** was obtained as a white solid (431 mg, 0.93 mmol, 67 % yield). **1H NMR (400 MHz, DMSO-[d6]): δ =** 11.38 (broad-s, 2H, *i*), 10.18 (broad-s, 2H, *f*), 7.57 (d, 2H, J = 7.0 Hz, *h*), 7.37 (t, 1H, J = 2.0 Hz, *a*), 7.29-7.12 (m, 3H, *b c*) 6.11 (s, 2H, *e*), 5.67 (d, 2H, J = 7.0 Hz, *g*), 1.58 (s, 12H, d). **[ES+-MS]:** 467.2 [M+H], 489.2 [M+Na]. **Elemental analysis** calculated for $C_{22}H_{26}N_8O_4$ (%): C, 56.64; H, 5.62; N, 24.02. Found (%): C, 56.70; H, 5.52; N, 24.21.

Compound 3.3a

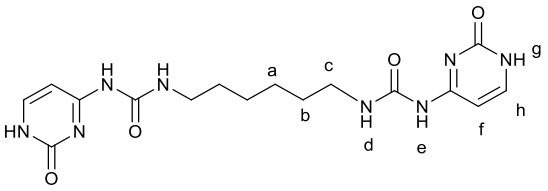

Compound **3.3a** was obtained as a white solid (275 mg, 0.76 mmol, 55 % yield). **^{1}H NMR** (400 MHz, DMSO-[d6]): δ = 9.80 (broad-s, 2H, *g*), 9.07 (broad-s, 2H, *e*), 7.65 (d, 2H, J = 7.0 Hz, *h*), 6.15 (t, 2H, J = 6.1 Hz, *d*), 5.53 (d, 2H, J = 7.0 Hz, *f*) 3.22-3.18 (m, 4H, *c*), 1.59-1.48 (m, 8H, *a b*). **[ES+-MS]:** 391.2 [M+H], 413.2 [M+Na]. **Elemental analysis** calculated for $C_{16}H_{22}N_8O_4$ (%): C, 49.22; H, 5.68; N, 28.70. Found (%): C, 49.11; H, 5.74; N, 28.63.

Compound 3.1b

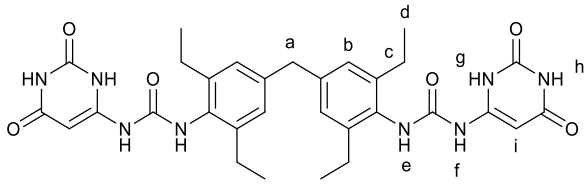

Compound **3.1b** was obtained as a yellow solid (391 mg, 0.64 mmol, 46 % yield). **1H NMR (400 MHz, DMSO-[d6]): δ =** 11.01 (s, 2H, *h*), 10.81 (broad-s, 2H, *g*), 7.92 (s, 2H, *f*), 7.46 (s, 2H, i), 7.03 (s, 4H, *b*), 6.89 (s, 2H, *e*), 3.96 (s, 2H, *a*), 2.49-2.55 (m, *c* – overlaps with DMSO peak), 1.13 (t, 12H, J = 7.6 Hz, *d*). **[ES+-MS]:** 617.3 [M+H], 639.3 [M+Na]. **Elemental analysis** calculated for $C_{31}H_{36}N_8O_6$ (%): C, 60.38; H, 5.88; N, 18.17. Found (%): C, 60.04; H, 6.11; N, 18.01.

Compound 3.2b

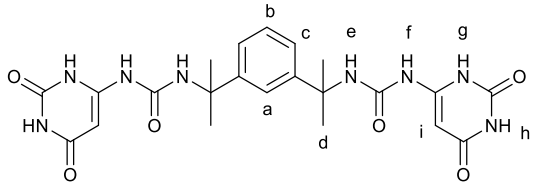

Compound **3.2b** was obtained as a yellow solid (427 mg, 0.86 mmol, 62 % yield). **1H NMR (400 MHz, DMSO-[d6]): δ =** 11.03 (s, 2H, *h*), 10.76 (broad-s, 2H, *g*), 7.98 (s, 2H, *f*), 7.47 (s, 2H, *i*), 7.37 (t, 1H, J = 2.0 Hz, *a*), 7.31-7.16 (m, 3H, *b c*), 6.33 (s, 2H, *e*), 1.58 (s,

12H, *d*). **[ES+-MS]:** 521.2 [M+Na], 537.2 [M+K]. **Elemental analysis** calculated for $C_{22}H_{26}N_8O_6$ (%): C, 53.01; H, 5.26; N, 22.48. Found (%): C, 52.81; H, 5.38; N, 22.53.

Compound 3.3b

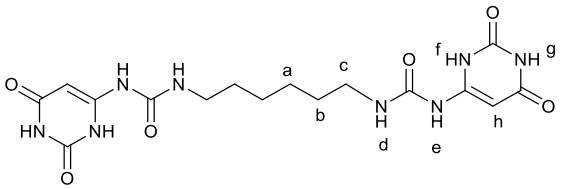

Compound **3.3b** was obtained as a yellow solid (285 mg, 0.68 mmol, 49 % yield). **^{1}H NMR (400 MHz, DMSO-[d6]): δ =** 11.01 (broad-s, 2H, *g*), 10.76 (broad-s, 2H, *f*), 7.54 (s, 2H, *e*), 7.47 (s, 2H, *h*), 6.08 (t, 2H, J = 6.1 Hz, *d*), 3.21-3.17 (m, 4H, *c*), 1.54-1.45 (m, 8H, *a b*). **[ES+-MS]:** 423.2 [M+H], 461.1 [M+K]. **Elemental analysis** calculated for $C_{16}H_{22}N_8O_6$ (%): C, 45.50; H, 5.25; N, 26.53. Found (%): C, 45.29; H, 5.49; N, 26.24.

Compound 3.1c

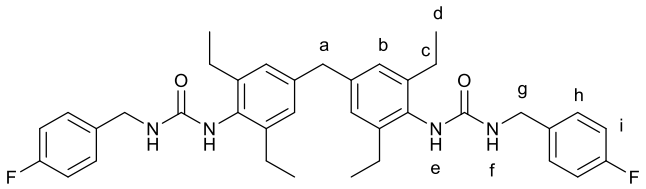

Compound **3.1c** was obtained as a white solid (753 mg, 1.23 mmol, 89 % yield). **^{1}H NMR (600 MHz, DMSO-d_6) δ =** 7.43-7.35 (m, 4H, *i*), 7.22-7.18 (m, 4H, *h*), 7.12 (s, 2H, *e*), 7.03 (s, 4H, *b*), 5.22 (t, 2H, J = 6.0 Hz, *f*), 4.43 (d, 4H, J = 6.0 Hz, *g*), 3.96 (s, 2H, *a*), 2.55-2.49 (m, *c* – overlaps with DMSO peak), 1.12 (t, 12H, J = 7.1 Hz, *d*). **m/z [ES$^+$-MS]:** 613.3 [M+H], 635.3 [M+Na]. **Elemental analysis** calculated for $C_{37}H_{42}F_2N_4O_2$ (%): C, 72.52; H, 6.91; F, 6.20; N, 9.14. Found (%): C, 72.45; H, 6.89; N, 9.13.

Compound 3.2c

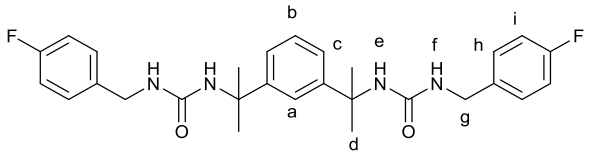

Compound **3.2c** was obtained as a white solid (567 mg, 1.15 mmol, 83 % yield) **^{1}H NMR (600 MHz, DMSO-d_6) δ =** 7.37 (t, 1H, J = 1.9 Hz, *a*), 7.28-7.24 (m, 4H, *i*), 7.20-7.16 (m, 3H, *b c*), 7.14-7.10 (m, 4H, *h*), 6.33 (s, 2H, *e*), 6.22 (t, 2H, J= 6.1 Hz, *f*), 4.14 (d, 4H, J= 6.1 Hz, *g*), 1.53 (s, 12H, *d*). **m/z [ES$^+$-MS]:** 495.2 [M+H], 533.2 [M+K]. **Elemental analysis** calculated for $C_{28}H_{32}F_2N_4O_2$ (%): C, 68.00; H, 6.52; N, 11.33. Found (%): C, 67.99; H, 6.62; N, 11.29.

Compound 3.1d

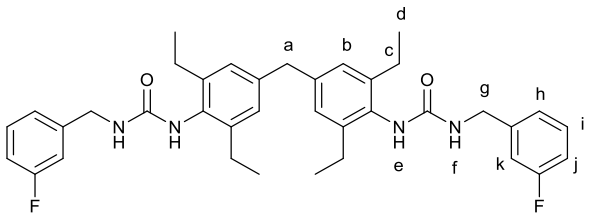

Compound **3.1d** was obtained as a white solid (719 mg, 1.17 mmol, 85 % yield). **1H NMR (700 MHz, DMSO-[d6]): δ =** 7.42 (s, 2H, *e*), 7.30-7.26 (m, 2H, *j*), 7.16-7.09 (m, 6H, Ar-H), 6.94 (s, 4H, Ar-H), 6.24 (t, 2H, J = 6.0 Hz, *f*), 4.14 (s, 2H, *g*), 3.80 (d, 4H, J = 6.0 Hz, *a*), 2.49-2.55 (m, *c* – overlaps with DMSO peak), 1.11 (t, 12H, J = 7.0 Hz, *d*). **[ES+-MS]:** 613.3 [M+H], 651.2 [M+K]. $C_{37}H_{42}F_2N_4O_2$ (%): C, 72.52; H, 6.91; F, 6.20; N, 9.14. Found (%): C, 72.51; H, 6.93; N, 9.11.

Compound 3.2d

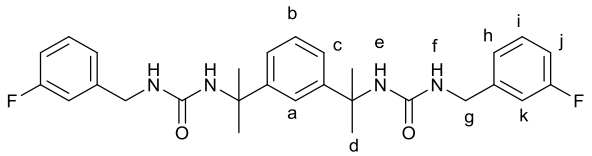

Compound **3.2d** was obtained as a white solid (573 mg, 1.16 mmol, 84 % yield). **1H NMR (700 MHz, DMSO-[d6]): δ =** 7.35 (t, 1H, J = 1.9 Hz, *a*), 7.31-7.28 (m, 2H, *j*), 7.16-7.13 (m, 3H, *b c*), 7.04-6.98 (m, 6H, *h i k*), 6.34 (s, 2H, *e*), 6.29 (t, 2H, J = 6.0 Hz, *f*), 4.16

(d, 4H, J = 6.0 Hz, *g*), 1.50 (s, 12H, *d*). **[ES+-MS]:** 495.2 [M+H], 517.2 [M+Na]. **Elemental analysis** calculated for $C_{28}H_{32}F_2N_4O_2$ (%): C, 68.00; H, 6.52; N, 11.33. Found (%): C, 68.00; H, 6.53; N, 11.35.

Compound 3.1e

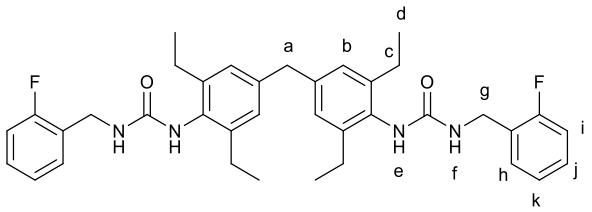

Compound **3.1e** was obtained as a white solid (660 mg, 1.08 mmol, 78 % yield). **1H NMR (700 MHz, DMSO-[d6]): δ =** 7.52 (s, 2H, *e*), 7.31-7.24 (m, 4H, *i k*), 7.16-7.09 (m, 4H, *h j*), 6.99 (s, 4H, *b*), 6.18 (t, 2H, J = 6.0 Hz, *f*), 4.10 (d, 4H, J = 6.0 Hz, *g*), 3.96 (s, 2H, *a*), 2.49-2.55 (m, *c* – overlaps with DMSO peak), 1.08 (t, 12H, J = 7.1 Hz, *d*). **[ES+-MS]:** 613.34 [M+Na], 635.32 [M+Na]. $C_{37}H_{42}F_2N_4O_2$ (%): C, 72.52; H, 6.91; F, 6.20; N, 9.14. Found (%): C, 72.39; H, 6.97; N, 9.17.

Compound 3.2e

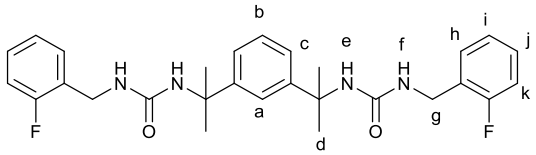

Compound **3.2e** was obtained as a white solid (519 mg, 1.05 mmol, 76 % yield). **1H NMR (700 MHz, DMSO-[d6]): δ =** 7.38 (t, 1H, J = 1.9 Hz, *a*), 7.28-7.23 (m, 4H, *i k*), 7.16-7.09 (m, 7H, b c h j), 6.33 (s, 2H, *e*), 6.25 (t, 2H, J = 6.0 Hz, *f*), 4.18 (d, 4H, J = 6.0 Hz, *g*), 1.59 (s, 12H, *d*). **[ES+-MS]:** 495.2 [M+H], 517.2 [M+Na]. **Elemental analysis** calculated for $C_{28}H_{32}F_2N_4O_2$ (%): C, 68.00; H, 6.52; N, 11.33. Found (%): C, 67.94; H, 6.58; N, 11.35.

Compound 3.1f

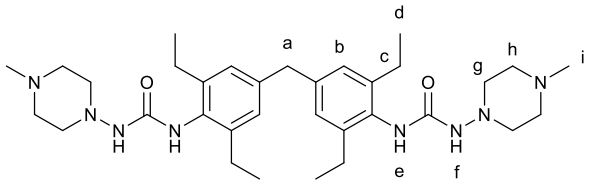

Compound **3.1f** was obtained as a white solid (638 mg, 1.08 mmol, 78 % yield). **1H NMR (700 MHz, DMSO-[d6]): δ =** 7.84 (s, 2H, *f*), 7.43 (s, 2H, *e*), 6.93 (s, 4H, *b*), 3.84 (s, 2H, *a*), 2.98-2.61 (broad-s, 16H, *g h*), 2.49-2.55 (m, *c* – overlaps with DMSO peak), 2.17 (s, 6H, *i*), 1.08 (t, 12H, *d*). **[ES+-MS]:** 593.4 [M+H], 615.4 [M+Na]. **Elemental analysis** calculated for $C_{33}H_{52}N_8O_2$ (%): C, 66.86; H, 8.84; N, 18.90. Found (%): C, 66.76; H, 8.98; N, 18.76.

Compound 3.2f

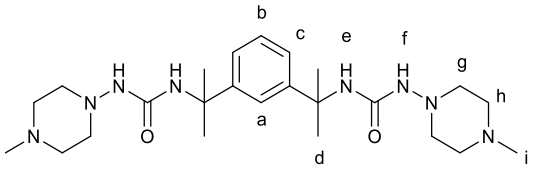

Compound **3.2f** was obtained as a white solid (471 mg, 0.99 mmol, 72 % yield). **1H NMR (700 MHz, DMSO-[d6]): δ =** 7.37 (t, 1H, J = 1.9 Hz, *a*), 7.28-7.15 (m, 3H, *b c*), 7.10 (s, 2H, *f*), 6.46 (s, 2H, *e*), 2.89-2.59 (broad-s, 16H, *g h*) 2.17 (s, 6H, *i*) 1.54 (s, 12H, *d*). **[ES+-MS]:** 475.3 [M+H], 497.3 [M+Na]. **Elemental analysis** calculated for $C_{24}H_{42}N_8O_2$ (%): C, 60.73; H, 8.92; N, 23.61. Found (%): C, 60.59; H, 9.00; N, 23.54.

Compound 3.1g

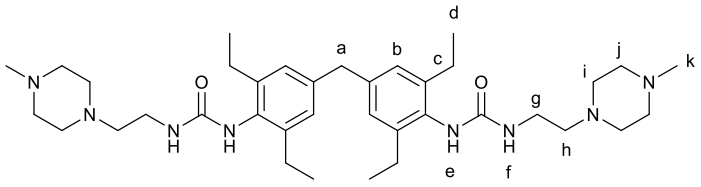

Compound **3.1g** was obtained as a white solid (726 mg, 1.12 mmol, 81 % yield). **1H NMR (700 MHz, DMSO-[d6]): δ =** 7.41 (s, 2H, *e*), 6.93 (s, 4H, *b*), 5.89 (t, 2H, J = 6.0 Hz, *f*), 3.82 (s, 2H, *b*), 3.15-3.10 (q, 4H, J = 6.1 Hz, *g*), 2.49-2.55 (m, *c* – overlaps with DMSO

peak), 2.46-2.32 (broad-s, 16H, *i j*), 2.14 (s, 6H, *k*), 1.08 (t, 12H, *d*). **[ES+-MS]:** 649.5 [M+H], 671.5 [M+Na]. **Elemental analysis** calculated for $C_{37}H_{60}N_8O_2$ (%): C, 68.48; H, 9.32; N, 17.27. Found (%): C, 68.21; H, 9.51; N, 17.20.

Compound 3.2g

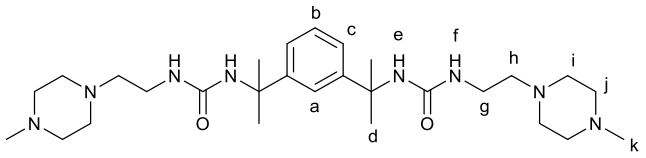

Compound **3.2g** was obtained as a white solid (600 mg, 1.13 mmol, 82 % yield). **1H NMR (700 MHz, DMSO-[d6]): δ =** 7.39 (t, 1H, J = 1.9 Hz, *a*), 7.20-7.12 (m, 3H, *b c*), 6.37 (s, 2H, *e*), 5.72 (t, 2H, J = 5.8 Hz, *f*), 3.05-3.01 (q, 4H, J = 6.1 Hz, *g*), 2.53-2.35 (broad-s, *i j* – overlaps with DMSO peak), 2.28-2.24 (t, 4H, J = 6.4 Hz, *h*), 2.15 (s, 6H, *k*), 1.51 (s, 12H, *d*). **[ES+-MS]:** 531.4 [M+H], 569.4 [M+K]. **Elemental analysis** calculated for $C_{28}H_{50}N_8O_2$ (%): C, 63.36; H, 9.50; N, 21.11. Found (%): C, 63.33; H, 9.60; N, 21.08.

Compound 3.1h

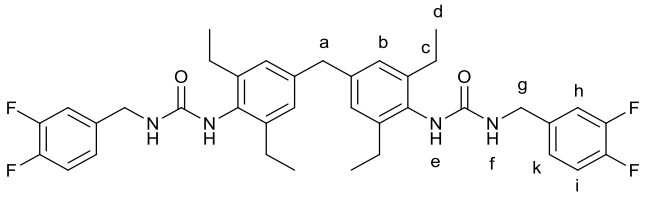

Compound **3.1h** was obtained as a white solid (671 mg, 1.04 mmol, 75 % yield) **^{1}H NMR (700 MHz, DMSO-[d6]): δ =** 7.40-7.35 (m, 2H, *i*), 7.23-7.18 (m, 2H, *k*) , 7.05-7.00 (m, 6H, *b h*), 5.11 (t, 2H, J = 6.0 Hz, *f*), 4.43 (s, 2H, *g*), 3.90 (s, 2H, *a*), 2.17 (m, *c* – overlaps with DMSO peak), 1.04 (t, J = 7.62 Hz, 12H, *d*). **m/z (ES$^+$-MS):** 649.3 [M+H], 671.3 [M+Na]. **Elemental analysis** calculated for $C_{37}H_{40}F_4N_4O_2$ (%): C, 68.50; H, 6.22; F, 11.71; N, 8.64. Found (%): C, 68.33; H, 6.16; F, 11.61; N, 8.58.

Compound 3.2h

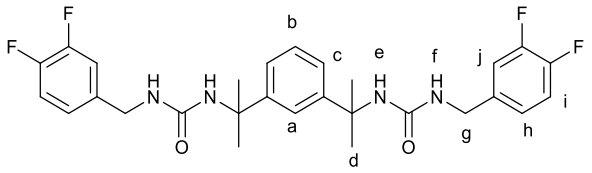

Compound **3.2h** was obtained as a white solid (571 mg, 1.08 mmol, 78% yield). **^{1}H NMR (700 MHz, DMSO-[d6]): δ =** 7.38-7.31 (m, 3H, *a j*), 7.22-7.12 (m, 5H, *b c i*), 7.05-7.00 (m, 2H, *h*), 6.39 (s, 2H, *e*), 6.31 (t, J = 6.2 Hz, 2H, *f*), 4.10 (d, J= 6.1 Hz, 4H, *g*) 1.51 (s, 12H, *d*). **m/z [ES$^+$-MS]** 531.2 [M+H], 553.4 [M+Na]. **Elemental analysis** calculated for $C_{28}H_{30}F_4N_4O_2$ (%): C, 63.39; H, 7.70; F, 14.32; N, 10.56. Found (%): C, 63.30; H, 7.73; F, 14.30; N, 10.52.

Compound 3.1i

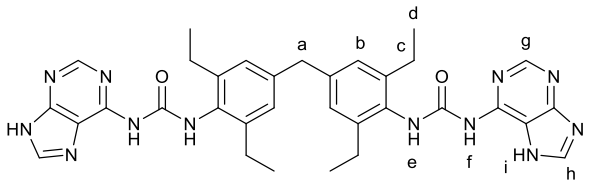

Compound **3.1i** was obtained as a white solid (559 mg, 0.88 mmol, 64 % yield). **1H NMR (400 MHz, DMSO-[d6]): δ =** 12.82 (broad-s, 2H, *i*), 8.31 (broad-s, 2H, *f*), 8.13 (s, 2H, *g*), 8.10 (s, 2H, *h*), 6.52 (s, 2H, *e*), 3.69 (s, 2H, *a*) 2.49-2.55 (m, *c* – overlaps with DMSO peak), 1.13 (t, 12H, J = 7.6 Hz, *d*). **[ES+-MS]:** 655.3 [M+Na]. **Elemental analysis** calculated for $C_{33}H_{36}N_{12}O_2$ (%): C, 62.64; H, 5.74; N, 26.56. Found (%): C, 62.49; H, 5.99; N, 26.21.

Compound 3.2i

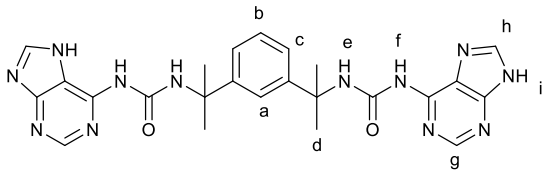

Compound **3.2i** was obtained as a white solid (376 mg, 0.73 mmol, 53 % yield). **1H NMR (400 MHz, DMSO-[d6]): δ =** 12.81 (broad-s, 2H, *i*), 8.21 (s, 2H, *g*), 8.13 (s, 2H, *h*), 8.11 (s, 2H, N-C<u>H</u>-N), 7.37 (t, 1H, J = 2.0 Hz, Ar-H), 7.29-7.12 (m, 3H, Ar-H), 6.16 (s, 2H, $C(CH_3)_2$-N<u>H</u>), 1.58 (s, 12H, C-(C<u>H</u>$_3$)$_2$). **[ES+-MS]:** 537.2 [M+Na]. **Elemental analysis**

calculated for $C_{24}H_{26}N_{12}O_2$ (%): C, 56.02; H, 5.09; N, 32.67. Found (%): C, 55.79; H, 5.32; N, 32.31

Compound 3.1j

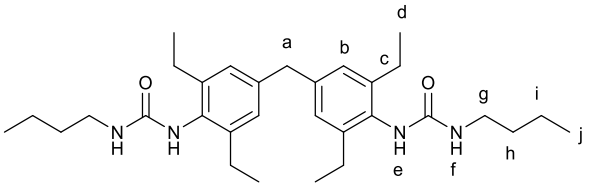

Compound **3.1j** was obtained as a white solid (638 mg, 1.26 mmol, 91.3 %). **^{1}H NMR** (400 MHz, DMSO-[d6]): δ = 7.23 (broad-s, 2H, *e*) 6.87 (s, 4H, *b*), 5.33 (t, *J* = 5.7 Hz, 2H, *f*), 3.69 (s, 2H, *a*), 2.92 (dt, J = 6.3, 5.7 Hz, 4H, *g*), 2.49-2.55 (m, *c* – overlaps with DMSO peak), 1.38-1.18 (m, 8H, *h i*) 1.07 (t, 12H, J = 7.6 Hz, *d)*, 0.91-0.73 (m, 6H, *j*). **m/z (ES$^+$-MS)** 509.4 [M+H], 531.4 [M+Na]. **Elemental analysis** calculated for $C_{31}H_{48}N_4O_2$ (%): C, 73.19; H, 9.51; N, 11.01. Found (%): C, 72.89; H, 9.26; N, 10.81.

Compound 3.2j

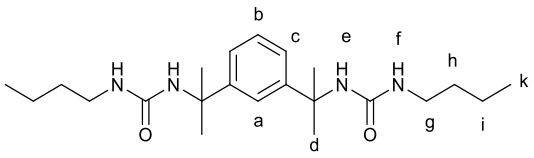

Compound **3.2j** was obtained as a white solid (491 mg, 1.26 mmol, 91% yield), **^{1}H NMR** (400 MHz, DMSO-[d6]): 7.33 (t, *J* = 1.8 Hz, 1H, *a*), 7.20 – 7.08 (m, 3H, *b c*), 6.12 (s, 2H, *e*), 5.75 (t, *J* = 5.7 Hz, 2H, *f*), 2.92 (dt, *J* = 6.3, 5.7 Hz, 4H, *g*), 1.51 (s, 12H, *d*), 1.38 – 1.18 (m, 8H, *h i*), 0.95 – 0.73 (m, 6H, *k*). **m/z (ES$^+$-MS)** 413.8 [M+Na]. **Elemental analysis** calculated for $C_{31}H_{48}N_4O_2$ (%): C 67.66, H 9.81, N 14.35; Found (%) C 67.45, H 9.75, N 14.31.

Compound 3.1k

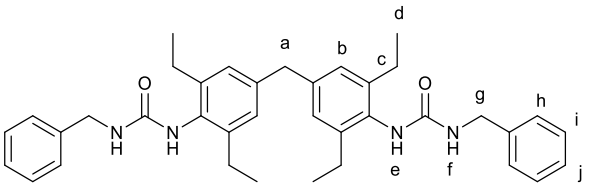

Compound **3.1k** was obtained as a white solid (669 mg, 1.16 mmol, 84 % yield). **^{1}H NMR** (400 MHz, DMSO-[d6]): δ = 7.40 (s, 2H,*e*) 7.22-7.41 (m, 10H, *h i j*), 6.95 (s, 4H, *b*), 6.88 (s, 2H, *f*), 4.25 (d, 4H, J = 5.8 Hz, *g*), 3.80 (s, 2H, *a*). 2.49-2.55 (m, *c* – overlaps with DMSO peak), 1.12 (t, 12H, J = 7.6 Hz, *d*). **m/z (ES$^+$-MS)** 577.4 [M+H], 599.3 [M+Na]. **Elemental analysis** calculated for $C_{37}H_{44}N_4O_2$ (%): C, 77.05; H, 7.69; N, 9.71. Found (%): C, 77.05; H, 7.67; N, 9.66.

Compound 3.2k

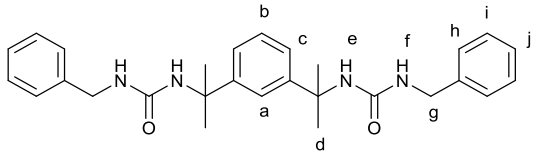

Compound **3.2k** was obtained as a white solid (468 mg, 1.02 mmol, 74 % yield), **^{1}H NMR (400 MHz, DMSO-[d6]): δ =** 7.40 (t, *J* = 1.9 Hz, 1H, *a*), 7.35 – 7.26 (m, 4H, *i*), 7.26 – 7.14 (m, 9H, *b c h j*), 6.32 (s, 2H, *e*), 6.27 (t, *J* = 6.0 Hz, 2H, *f*), 4.16 (d, *J* = 5.9 Hz, 4H, *g*), 1.55 (s, 12H, *d*). **m/z (ES$^+$-MS)** 481.7 [M+Na]. **Elemental analysis** calculated for $C_{28}H_{34}N_4O_2$ (%): C, 73.33; H, 7.47; N, 12.22; Found (%) C, 73.24; H, 7.46; N, 12.22.

Compound 3.1l

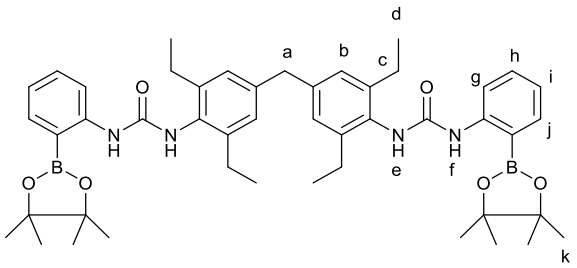

Compound **3.1l** was obtained as a cream solid (784 mg, 0.98 mmol, 71 % yield - impure). **^{1}H NMR (400 MHz, DMSO-[d6]): δ =** 9.34 (broad-s, 2H, *f*), 7.61 (s, 2H, *e*), 7.39-7.31 (m, 2H, Ar-H), 7.18-7.14 (td, 2H, J = 7.6, 1.6 Hz, *h*), 7.01 (s, 6H, Ar-H including *b*), 3.86 (s, 2H, *a*), 2.49-2.55 (m, *c* – overlaps with DMSO peak), 1.28 (s, 24 H, *k*), 1.12 (t, 12H, J = 7.6 Hz, *d*).

Compound 3.2l

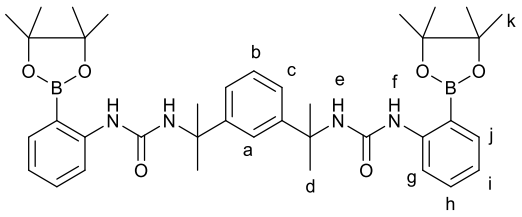

Compound **3.2l** was obtained as a cream solid (603 mg, 0.88 mmol, 64 % yield). **^{1}H NMR (400 MHz, DMSO-[d6]): δ** = 9.22 (broad-s, 2H, *f*), 7.42 (t, 1H, J = 2.1 Hz, *a*), 7.34-7.30 (td, 2H, J = 7.6, 1.6 Hz, *h*), 7.23-7.19 (m, 3H, *b c*), 7.03-6.94 (m, 6H, *g i j*), 6.39 (s, 2H, *e*), 1.51 (s, 12H, *d*), 1.28 (s, 24 H, *k*). **m/z (ES$^+$-MS)** 683.4 [M+H], 705.4 [M+Na]. **Elemental analysis** calculated for $C_{39}H_{53}B_2N_4O_6$ (%): C, 66.88; H, 7.68; N, 8.21; Found (%) C, 66.59; H, 7.83; N, 7.98.

Compound 3.1m

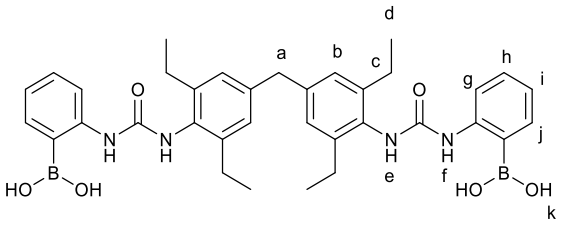

Compound **3.1m** was obtained as a cream solid. (143 mg, 0.22 mmol, 51 % yield - impure). **^{1}H NMR (400 MHz, DMSO-[d6]): δ =** 9.34 (broad-s, 2H, *f*), 7.61 (s, 2H, *e*), 7.99 (broad-s, 4H, *k*), 7.39-7.31 (m, 2H, Ar-H), 7.18-7.14 (td, 2H, J = 7.6, 1.6 Hz, *h*), 7.01 (s, 6H, Ar-H including *b*), 3.86 (s, 2H, *a*), 2.49-2.55 (m, *c* – overlaps with DMSO peak), 1.12 (t, 12H, J = 7.6 Hz, *d*).

Compound 3.2m

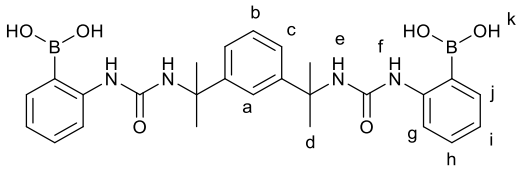

Compound **3.2m** was obtained as a cream solid (98 mg, 0.19 mmol, 43 % yield). **^{1}H NMR (400 MHz, DMSO-[d6]): δ =** 9. (broad-s, 2H, *f*), 7.87 (broad-s, 4H, *k*), 7.42 (t, 1H, J = 2.1 Hz, *a*), 7.34-7.30 (td, 2H, J = 7.6, 1.6 Hz, *h*), 7.23-7.19 (m, 3H, *b c*), 7.03-6.94 (m, 6H, *g i j*), 6.39 (s, 2H, *e*), 1.59 (s, 12H, *d*). **m/z (ES$^+$-MS)** 541.2 [M+Na]. **Elemental analysis** calculated for $C_{26}H_{32}B_2N_4O_6$ (%): C, 60.27; H, 6.22; N, 10.81. Found (%): C, 60.00; H, 6.19; N,10.52.

Compound 3.1n

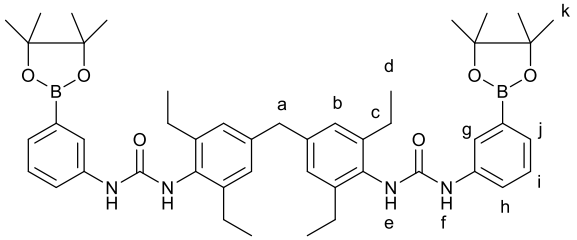

Compound **3.1n** was obtained as a cream solid (851 mg, 1.06 mmol, 77 % yield - impure). **^{1}H NMR (400 MHz, DMSO-[d6]): δ =** 8.81 (s, 2H, *e*), 7.85 (s, 2H, *f*), 7.55-7.44 (m, 4H, Ar-H), 7.28-7.22 (m, 4H, Ar-H), 7.01 (s, 4H, *b*), 3.86 (s, 2H, *a*). 2.49-2.55 (m, *c* – overlaps with DMSO peak), 1.28 (s, 24 H, *k*), 1.12 (t, 12H, J = 7.6 Hz, *d*).

Compound 3.2n

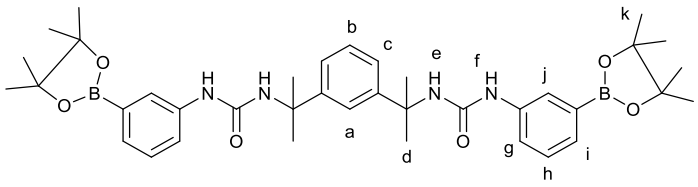

Compound **3.2n** was obtained as a cream solid (659 mg, 0.97 mmol, 70 % yield). **NMR (400 MHz, DMSO-[d6]): δ =** 8.56 (s, 2H, e), 7.61-7.53 (m, 4H, *Ar-H*), 7.40 (t, 1H, J = 2.0 Hz, *a*), 7.22-7.12 (m, 7H, *Ar-H, b c*), 6.43 (s, 2H, *e*), 1.50 (s, 12H, *d*), 1.28 (s, 24 H, *k*). **m/z (ES$^+$-MS)** 683.4 [M+H], 705.4 [M+Na]. **Elemental analysis** calculated for $C_{39}H_{53}B_2N_4O_6$ (%): C, 66.88; H, 7.68; N, 8.21; Found (%) C, 66.61; H, 7.76; N, 8.00.

Compound 3.1o

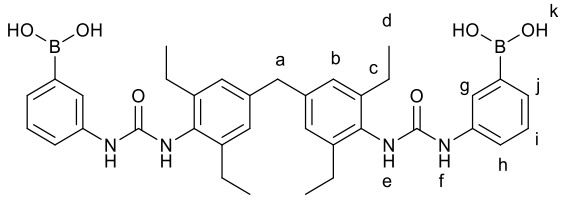

Compound **3.1o** was obtained as a cream solid (170 mg, 0.27 mmol, 61 % yield - impure). **^{1}H NMR (400 MHz, DMSO-[d6]): δ =** 8.81 (s, 2H, *f*), 8.01 (broad-s, 4H, *k*), 7.85 (s, 2H, *e*), 7.55-7.44 (m, 4H, Ar-H), 7.28-7.22 (m, 4H, Ar-H), 7.01 (s, 4H, *b*), 3.86 (s, 2H, *a*). 2.49-2.55 (m, *c* – overlaps with DMSO peak), 1.12 (t, 12H, J = 7.6 Hz, *d*).

Compound 3.2o

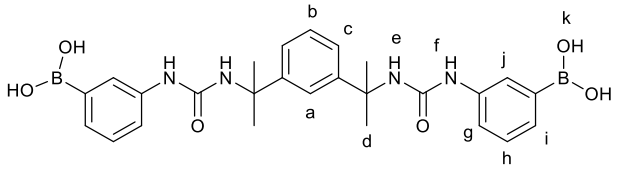

Compound **3.2o** was obtained as a cream solid (123 mg, 0.24 mmol, 54 % yield). **^{1}H NMR (400 MHz, DMSO-[d6]): δ =** 8.67 (broad-s, 2H, *f*), 7.98 (broad-s, 4H, *k*), 7.61-7.53 (m, 4H, *Ar-H*), 7.40 (t, 1H, J = 2.0 Hz, *a*), 7.22-7.12 (m, 7H, *Ar-H, b c*), 6.43 (s, 2H, *e*), 1.50 (s, 12H, *d*). **m/z (ES$^+$-MS)** 557.2 [M+K]. **Elemental analysis** calculated for $C_{26}H_{32}B_2N_4O_6$ (%): C, 60.27; H, 6.22; N, 10.81. Found (%): C, 60.11; H, 6.41; N,10.72.

Compound 3.1p

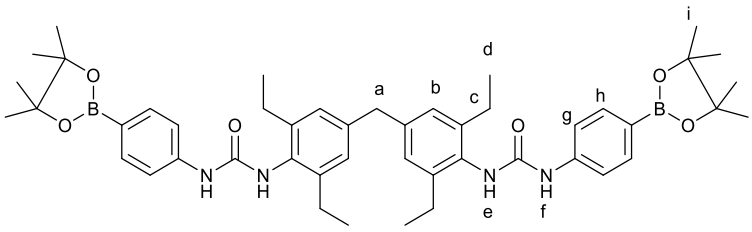

Compound **3.1p** was obtained as a cream solid (773 mg, 0.97 mmol, 70 % yield - impure). **^{1}H NMR (400 MHz, DMSO-[d6]): δ =** 8.97 (s, 2H, *f*), 7.63 (s, 2H, *e*), 7.55 (d, 4H, J = 8.4 Hz, *h*) 7.44 (d, 4H, J = 8.4 Hz, *g*), 7.01 (s, 4H, *b*), 3.86 (s, 2H, *a*). 2.49-2.55 (m, *c* – overlaps with DMSO peak), 1.28 (s, 24 H, *i*), 1.12 (t, 12H, J = 7.6 Hz, *d*)

Compound 3.2p

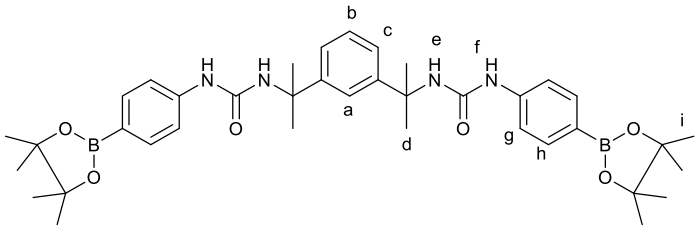

Compound **3.2p** was obtained as a cream solid (584 mg, 0.86 mmol, 62 % yield). **^{1}H NMR (400 MHz, DMSO-[d6]): δ =** 8.38 (s, 2H, *f*), 7.50 (d, 4H, J = 8.1 Hz, *h*), 7.42 (t, J = 2.0 Hz, *a*), 7.33 (d, 4H, J = 8.4 Hz, *g*), 7.25-7.18 (m, 3H, *b c*), 6.63 (s, 2H, *e*), 1.51 (s, 12H, *d*), 1.28 (s, 24 H, *i*). **m/z (ES$^+$-MS)** 683.4 [M+H], 705.4 [M+Na]. **Elemental analysis** calculated for $C_{39}H_{53}B_2N_4O_6$ (%): C, 66.88; H, 7.68; N, 8.21; Found (%) C, 66.59; H, 7.83; N, 7.98.

Compound 3.1q

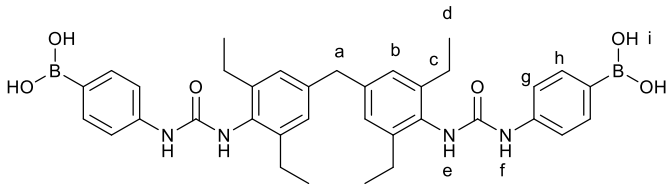

Compound **3.1q** was obtained as a cream solid (179 mg, 0.28 mmol, 64 % yield - impure). **^{1}H NMR (400 MHz, DMSO-[d6]): δ =** 8.97 (s, 2H, *f*), 7.97 (broad-s, 4H, *i*), 7.65 (s, 2H, *e*), 7.55 (d, 4H, J = 8.4 Hz, *h*), 7.45 (d, 4H, J = 8.4 Hz, *g*), 7.01 (s, 4H, *b*), 6.91 (s, 2H, *e*), 3.86 (s, 2H, *a*). 2.49-2.55 (m, *c* – overlaps with DMSO peak), 1.12 (t, 12H, J = 7.6 Hz, *d*).

Compound 3.2q

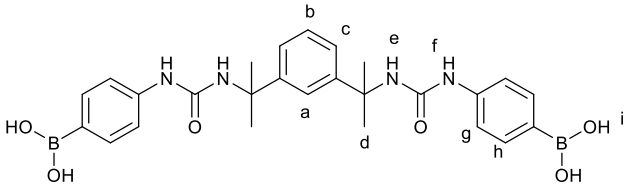

Compound **3.2q** was obtained as a cream solid (125 mg, 0.24 mmol, 55 % yield). **^{1}H NMR (400 MHz, DMSO-[d6]): δ =** 8.58 (s, 2H, *f*), 7.91 (broad-s, 4H, *i*), 7.50 (d, 4H, J = 8.1 Hz, *h*), 7.42 (t, J = 2.0 Hz, *a*), 7.33 (d, 4H, J = 8.4 Hz, *g*), 7.25-7.18 (m, 3H, *b c*), 6.39

(s, 2H, *e*), 1.51 (s, 12H, *d*). **m/z (ES$^+$-MS)** 557.2 [M+K]. **Elemental analysis** calculated for $C_{26}H_{32}B_2N_4O_6$ (%): C, 60.27; H, 6.22; N, 10.81. Found (%): C, 59.95; H, 6.51; N,10.62.

3.10.3 Crystallization of gelators

Single crystals of **3.2c**, **3.2d**, **3.2e** and **3.2h** were obtained during the gel screening process, where 10 mg of the respective compound was dissolved in 0.5 mL of a selected solvent with heat. The solution was allowed to cool and left undisturbed at ambient temperature for a number of days, after which time single crystals had grown. A poorly diffracting single crystal of **3.2f** was also grown from 1,3-dichlorobenzene by reducing the concentration to 2.5 mg per 0.5 mL. Conditions are for each table are summarised below (**Table 3-8**).

Table 3-8. *Summary of Crystallisation conditions which yielded single crystals of gelators* ***3.2c****,* ***3.2d****,* ***3.2e****,* ***3.2f*** *and* ***3.2h****.*

Compound	Solvent	Concentration (% w/v)	Outcome
2c	Ethanol	2	Anhydrous form
2d	Acetonitrile	2	Anhydrous form
2e	1-Propanol	2	Anhydrous form
2f	1,3-dichlorobenzene	0.5	1,3-dichlorobenzene disolvate
2h	THF	2	THF disolvate

3.10.4 Crystallisation conditions for AZD-2281

Table 3-9. Crystallisation outcomes when using gels of API-mimetic **3.1c-e**, **3.2c** and **3.2e** as crystallisation media for AZD-2281. All the experiments were undertaken on a 0.5 mL scale and repeated up to 3 times, consistently yielded the kinetically stable form A of AZD-2281 (confirmed by XRPD) or the isostructural solvate form. All solution phase crystallisations also yielded form A or the isostructural solvates. Polymorphic form was determined via IR, XRPD or SCXRD unit cell measurements.

Gelator	Solvent	Gel concentration / % w/v	Drug loading / mg	Crystallisation outcome
3.1c	Nitrobenzene	1	10	Solvate
		1	25	Solvate
	1,4-dioxane	0.5	10	Form A
		1	10	Form A
	Chloroform	0.5	10	Form A
		1	10	Form A
	Acetonitrile	0.5	15	Form A
		1	15	Form A
	DCM	0.5	10	Solvate
		1	10	Solvate
	Propan-1-ol	0.5	25	Form A
		1	25	Form A
3.2c	Acetonitrile	1	15	Form A
		2	15	Form A
	Nitrobenzene	2	10	Solvate
		2	25	Solvate
3.1d	1,4-dioxane	0.5	10	Form A
		1	10	Form A
	Nitrobenzene	0.5	10	Solvate
		1	10	Solvate
	Acetonitrile	0.5	15	Form A
		1	15	Form A
3.1e	Nitrobenzene	0.5	10	Solvate
		1	10	Solvate
	DCM	0.5	10	Solvate
		1	10	Solvate
	1,4-dioxane	0.5	10	Form A
		1	10	Form A
	Chlorobenzene	0.5	25	Form A
		1	25	Form A
3.2e	Nitrobenzene	1	10	Solvate
		2	10	Solvate
	Acetonitrile	1	15	Form A
		2	15	Form A

Table 3-10. Crystallisation outcomes when using gels of API-mimetic **3.1g** and **3.2g** as crystallisation media for AZD-2281. All the experiments were undertaken on a 0.5 mL scale and repeated up to 3 times, consistently obtaining the kinetically stable form A of AZD-2281 (confirmed by XRPD) or the isostructural solvate form. All solution phase crystallisations also yielded form A or the isostructural solvates. Polymorphic form was determined via IR, XRPD or SCXRD unit cell measurements.

Gelator	Solvent	Gel concentration / % w/v	Drug loading / mg	Crystallisation outcome
3.1g	1,4-dioxane	0.5	10	Form A
		1	10	Form A
	Nitrobenzene	0.5	10	Solvate
		1	10	Solvate
	Acetonitrile	0.5	15	Form A
		1	15	Form A
	Chlorobenzene	0.5	25	Form A
		1	25	Form A
3.2g	Nitrobenzene	2	10	Solvate
		2	25	Solvate
	1,4-dioxane	1	10	Form A
		2	10	Form A
	Chlorobenzene	1	25	Form A
		2	25	Form A

3.10.5 Crystallography Data

Gelator crystal structures:

	3.2c	**3.2d**	**3.2e**	**3.2f**	**3.2h**
Formula	$C_{28}H_{32}F_4N_4O_2$	$C_{28}H_{32}F_2N_4O_2$	$C_{28}H_{32}F_4N_4O_2$	$C_{24}H_{42}N_8O_2.$ $2(C_6H_2Cl_2)$	$C_{28}H_{30}F_4N_4O_2$ $2(C_4H_8O)$
Formula weight	638.72	494.50	494.50	768.65	530.47
Crystal system	Orthorhombic	Monoclinic	Monoclinic	Monoclinic	Orthorhombic
Space group	Pbca	C 2/c	P 2_1/c	C 2/c	Fdd2
***a* / Å**	12.330(2)	23.5744(10)	9.5545(4)	29.528(6)	29.258(6)
***b* / Å**	9.1455(16)	19.5612(8)	11.0786(5)	7.6482(17)	34.472(7)
***c* / Å**	45.180(8)	23.2674(9)	24.4767(11)	19.745(4)	13.186(3)
β / °	90	97.214(2)	93.371	119.373(11)	90
***V* / Å^3**	5094.68	10644.7	2586.39	3816.04	13299.1
Z* / *Z'	8 / 1	16 / 2	4 / 1	4 / 0.5	16 / 1
***D*$_{calc}$ / g cm^{-3}**	1.290	1.257	1.190	1.315	1.223
***R*$_{int}$**	0.0711	0.0758	0.0772	0.0855	0.0812
***R*$_1$ [*I* ≥ 2σ (*I*)]**	0.0692	0.0616	0.0601	0.0865	0.0721
***wR*$_2$ [all data]**	0.1727	0.1693	0.1616	0.2018	0.1932
Goodness of fit	1.077	1.019	1.115	1.298	1.102
Radiation Source	Mo	Mo	Mo	Synchrotron	Mo

API crystal structure:

	AZD-2281 (Nitrobenzene Solvate)
Formula	$C_{24}H_{23}FN_4O_3$
Formula weight	434.46
Crystal system	Monoclinic
Space group	P 2_1/n
***a* / Å**	10.5245(5)
***b* / Å**	9.1669(5)
***c* / Å**	24.6982(13)
β / °	98.873(2)
***V* / Å^3**	2354.3
Z / Z'	4 / 1
***D*$_{calc}$ / g cm^{-3}**	1.226
***R*$_{int}$**	5.76
***R*$_1$ [*I* ≥ 2σ (*I*)]**	4.69
***wR*$_2$ [all data]**	7.66
Goodness of fit	1.056
Radiation Source	Mo

3.11 References

1 A. Dawn, K. S. Andrew, D. S. Yufit, Y. Hong, J. P. Reddy, C. D. Jones, J. A. Aguilar and J. W. Steed, *Cryst. Growth Des.*, 2015, **15**, 4591–4599.

2 J. A. Foster, K. K. Damodaran, A. Maurin, G. M. Day, H. P. G. Thompson, G. J. Cameron, J. C. Bernal and J. W. Steed, *Chem. Sci.*, 2017, **8**, 78–84.

3 National Institute for Clinical Excellence (NICE), *Olaparib for maintenance treatment of relapsed, platinum-sensitive ovarian, fallopian tube and peritoneal cancer*. https://www.nice.org.uk/guidance/TA620 (accessed 20.10.2021)

4 National Institute for Clinical Excellence (NICE), *Olaparib for maintenance treatment of BRCA mutation- positive advanced ovarian , fallopian tube or peritoneal cancer after response to first- chemotherapy*. https://www.nice.org.uk/guidance/TA598 (accessed 20.10.2021)

5 M. E. Robson, N. Tung, P. Conte, S. A. Im, E. Senkus, B. Xu, N. Masuda, S. Delaloge, W. Li, A. Armstrong, W. Wu, C. Goessl, S. Runswick and S. M. Domchek, *Ann. Oncol.*, 2019, **30**, 558–566.

6 C. H. Marshall, A. O. Sokolova, A. L. McNatty, H. H. Cheng, M. A. Eisenberger, A. H. Bryce, M. T. Schweizer and E. S. Antonarakis, *Eur. Urol.*, 2019, **76**, 452–458.

7 Committee for Medicinal Products for Human Use (CHMP) - European Medicines Agency (EMA), *European Public Assessment Report - Olaparib*. https://www.ema.europa.eu/en/documents/assessment-report/lynparza-epar-public-assessment-report_en.pdf (accessed 20.10.2021)

8 P. K. K. Ramesh, B. Chandra Shekar, *Indo Am. J. Pharm. Res.*, 2015, **5**, 3850–3858.

9 AstraZeneca AB, US Pat., 7 265 124 B2, 2007.

10 L. M. Belca, A. Ručigaj, D. Teslič and M. Krajnc, *Ultrason. Sonochem.*, 2019, **58**, 104642.

11 Y. Ren, J. Shen, K. X. Yu, C. U. Phan, G. X. Chen, J. Y. Liu, X. Hu and J. Y. Feng, *Crystals*, 2019, **9**, 556.

12 J. Bojarska, M. Remko, A. Fruziński and W. Maniukiewicz, *J. Mol. Struct.*, 2018, **1154**, 290–300.

13 L. L. E. Mears, E. R. Draper, A. M. Castilla, H. Su, Zhuola, B. Dietrich, M. C. Nolan, G. N. Smith, J. Doutch, S. Rogers, R. Akhtar, H. Cui and D. J. Adams, *Biomacromolecules*, 2017, **18**, 3531–3540.

14 Kudos Pharmaceuticals Limited, US Pat., 8 183 369 B2, 2012.

15 A. Dawn, M. Mirzamani, C. D. Jones, D. S. Yufit, S. Qian, J. W. Steed and H. Kumari, *Soft Matter*, 2018, **14**, 9489.

16 S. D. Bull, M. G. Davidson, J. M. H. Van Den Elsen, J. S. Fossey, A. T. A. Jenkins, Y. B. Jiang, Y. Kubo, F. Marken, K. Sakurai, J. Zhao and T. D. James, *Acc. Chem. Res.*, 2013, **46**, 312–326.

17 Y. Egawa, R. Miki and T. Seki, *Materials (Basel).*, 2014, **7**, 1201–1220.

18 N. A. Siddiqui, N. Billa, C. J. Roberts and Y. A. Osei, *Pharmaceutics*, 2016, **8**, 30.

19 M. O. M. Piepenbrock, G. O. Lloyd, N. Clarke and J. W. Steed, *Chem. Commun.*, 2008, **110,** 2644-2646

Chapter 4 - The crystallisation of bis(*acyl*-semicarbazides): effects of spacer group and molecular chirality

4.1 Background

As discussed in the previous chapters, discoveries of novel LMWGs and gelation functionalities have frequently relied upon serendipity or making structural modifications to known gelators, often via altering terminal groups whilst preserving the gelation functionality to limit the risk of interrupting gel-promoting supramolecular motifs. However, sometimes these slight modifications can result in a loss of gelation or yield gels with unfavourable properties that are unfit for purpose. This highlights the need for LMWG engineers to catalogue as many effective gelation functionalities and LMWG spacer groups to increase the possibility of developing LMWGs with appropriate properties that can be utilised in the desired applications. Whilst LMWG literature has grown aggressively since the early 2000s, there remain some promising functionalities that have rarely been reported in LMWG structures. The acyl-semicarbazide linkage is one such functionality is underexplored as a potential gelation functionality. Acyl-semicarbazides can be made cheaply and easily via reactions between hydrazides and isocyanates, yielding amidourea functionalities with a high local density of hydrogen bond donors and acceptors. In theory, these acyl-semicarbazides could form at least three hydrogen bonding synthons linked with promoting versatile gelation behaviour (**Figure 4-1**). They could resemble amide gelators that typically form amide to amide C(4) hydrogen bonding motifs, urea gelators that form $R_2^1(6)$ α-tapes and hydrazide gelators that form $R_2^2(10)$ synthons. This hydrogen bonding capacity makes their supramolecular self-assembly behaviour potentially very interesting and could theoretically yield highly versatile and effective LMWGs. Whilst acyl-semicarbazides have previously been utilised in a few supramolecular applications, including anion binding[1,2] and self-assembly via molecular recognition,[3–5] the number of reported acyl-semicarbazide gelators are very limited in comparison to other LMWG classes.

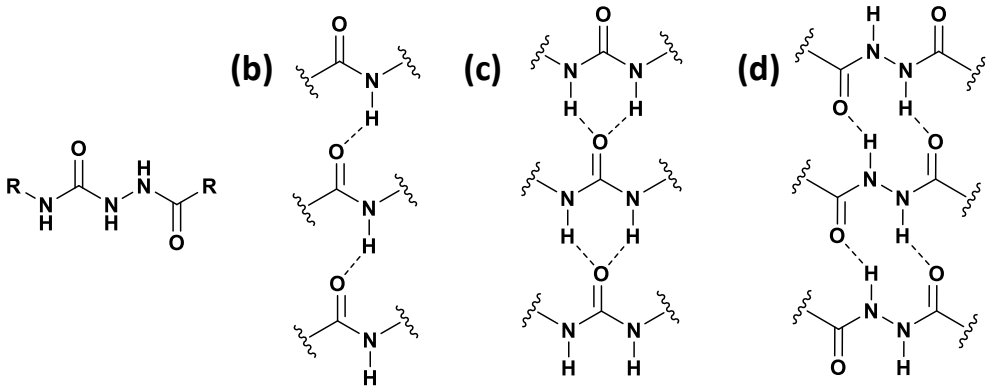

Figure 4-1. Chemical diagrams of **(a)** the acyl-semicarbazide linker and **(b)** C(4) motifs between amides, **(c)** $R_2^1(6)$ α-tapes between urea groups and **(d)** $R_2^2(10)$ motifs in hydrazide-based gelators, representing three well-documented gel-promoting synthons that can theoretically be formed by acyl-semicarbazide compounds.

As discussed in chapter 2, understanding the supramolecular interactions dictating self-assembly behaviour is essential for effective LMWG design and enables an understanding of how and why specific stimuli, structural functionalities and additives may affect the gelation behaviour. However, in the few existing studies reporting *acyl*-semicarbazide LMWGs, there has been sparse experimental data pinpointing the supramolecular synthons that promote gelation. The Zentel group reported the first example of mono-acyl-semicarbazide gelators in 2005 and have since reported a selection of structurally related compounds as effective gelators, highlighting the potential gelation capabilities of acyl-semicarbazides.[6–9] They have only reported one crystal structure of an acyl-semicarbazide gelator (**4a**), which revealed the urea functionality to be in the syn-anti conformation, as opposed to being the syn-syn conformer associated with α-tape assembly. Instead, the structure exhibits a $R_4^4(20)$ motif (**Figure 4-2**) with hydrogen bonds forming between N–H_c···O_a and between NH_a···O_b. Gel formation was attributed to this supramolecular motif by comparison of the IR spectra of the gel and crystal forms, with very little difference in the peaks assigned to N–H and C=O stretches, indicating similar hydrogen bond motifs in both phases.

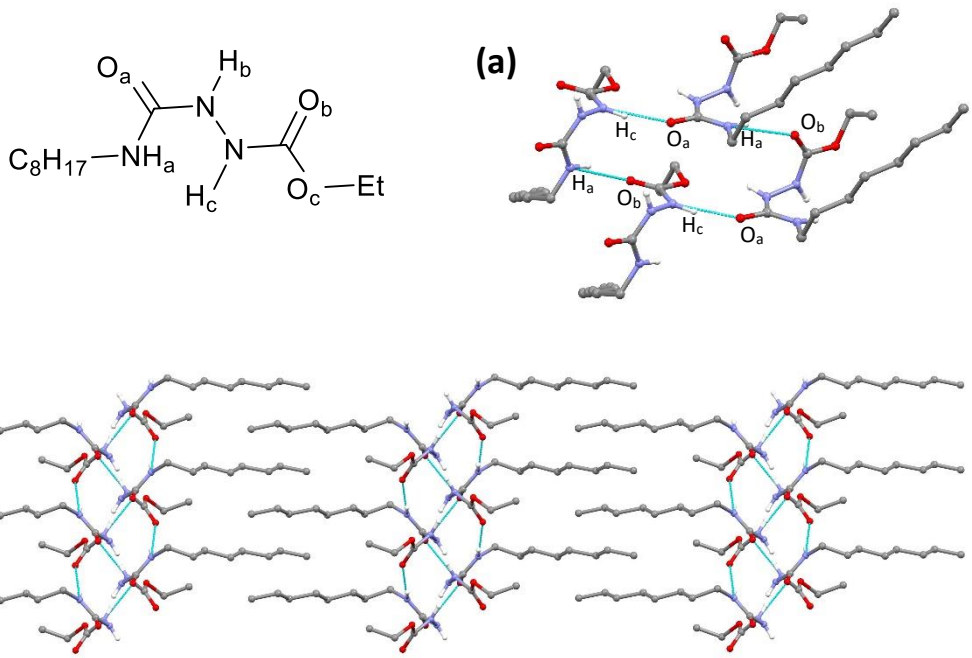

Figure 4-2. An acyl-semicarbazide LMWG (**4a**), reported by the Zentel group (ref. 6), crystallised to reveal **(a)** R_4^4 (20) synthons, with hydrogen bonds N–Hc···Oa=C and NHa···Ob=C, which was attributed to gelation in mono-acyl-semicarbazide compounds (CSD refcode, XAYSUL). **(b)** The packing in this structure reveals a 'head to tail' arrangement, with a hydrophilic core of hydrogen bond acyl-semicarbazide groups forming an infinite ribbon, and hydrophobic alkyl groups protruding to the side.

Most of the *acyl*-semicarbazide gelling agents identified in the literature are bis(acyl-semicarbazide), with the majority coming from recent studies by the Palanisamy group.[10–13] In their earliest example of bis(*acyl*-semicarbazide) gelation, the group demonstrated that bis(*acyl*-semicarbazide) LMWGs derived from a 2,4-toluene diisocyanate spacer and a fatty acid terminal groups yielded gelators that gel a wide variety of solvents, including cyclohexane, butanol, toluene and 1,4-dioxane. Hydrogen bonding between the *acyl*-semicarbazide groups and aromatic stacking of the 1-methyl-2,4-phenylene spacer functionalities were attributed with gel formation via IR spectroscopy, but no supramolecular motifs were proposed. A later study by the group demonstrated that isophorone-derived bis(*acyl*-semicarbazide) fatty acid gelators, with core structure **4b**, were able to gel a range of solvents at 2.5-3 % w/v. In this work they combined experimental IR data with computational models to pinpoint noncovalent interactions responsible for fibril formation, identifying infinite tapes of alternating $S_2^2(10)$ and R_2^2 (10) synthons between the amide and urea groups as the key supramolecular motifs (**Figure 4-3**).[11] Interestingly, the models reveal the two urea groups in each molecule adopting two different conformations, with one *syn-syn* and one *anti-syn* conformer. They have since utilised the *acyl*-semicarbazide functionality

in a series of supramolecular polymers that also display versatile gelation behaviour.[14,15]

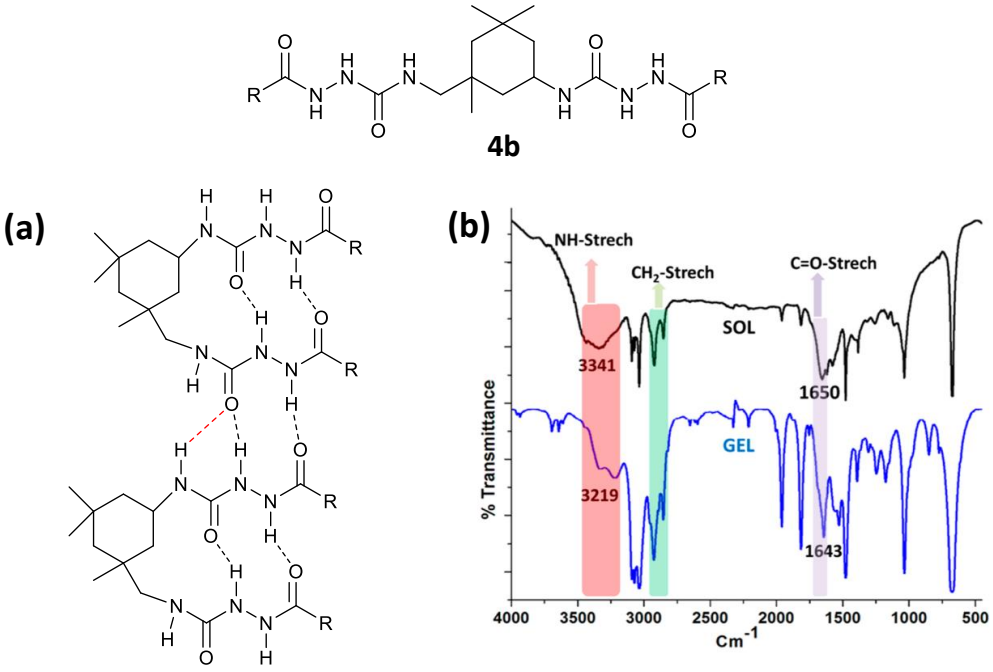

Figure 4-3. The Palanisamy group reported a range of isophorone-spaced bis(acyl-semicarbazides) with generic structure (**4b**). **(b)** Computational calculations identified alternating $S_2^2(10)$ and $R_2^2(10)$ between amide and urea groups as the key supramolecular interactions driving gelation. The $NH_{(urea)}\cdots O_{(urea)}$ intermolecular interaction shown in red is a weak stabilising interaction. **(c)** IR spectra of both the gel and solution phases at 30 mg/mL in benzene. In the solution phase, bands at 3341, 1650 and 1577 are characteristic of the non-hydrogen bonded N–H stretching, C=O (amide 1) and N–H (amide 2) frequencies. In the gel phase, all these bands broaden and shift to a lower wavenumber, confirming intermolecular hydrogen bonding between the amide functionalities in the gel phase. Adapted from Ref. 11.

Li et al have previously reported bis(*acyl*-semicarbazide) **1** that exclusively gel alcohols.[16] They suggested that mechanism of gelation for this system is via a two-step pathway with spherical aggregates initially forming and presenting as a cloudy emulsion, before evolving into gel fibres; a transition that can be accelerated by sonication. The FTIR spectra of both the spherical aggregates and fibres implicate hydrogen bonding between N–H and C=O groups as key but these interactions are stronger in the fibre phase, thus implicating hydrogen bonding between the acyl-semicarbazide functionalities as the driving force for the sol-gel transition. However, the study presented no data or speculation on the specific underlying hydrogen-bonding motifs responsible for gelation.

Chu and Chen reported a bis(*acyl*-semicarbazide) (**4c**) as an organogelator in a wide range of solvents, with minimum gelation concentrations as low as 0.19 % w/v, further

highlighting the potential application of bis(*acyl*-semicarbazides) as effective gelling agents.[17] This study employed ^{1}H-NMR experiments and density functional theory (DFT) calculations to propose that the molecules initially assemble into homoduplexes via four $R_2^1(6)$ synthons between urea N–H and amide carbonyl functionalities, with the duplexes stacking into 2D lamellar structures via π-π interactions (**Figure 4-4**). This mechanism of gelation and supramolecular motif differs from the previous examples discussed and further demonstrates the potential diversity of gelation mechanisms of acyl-semicarbazide compounds.

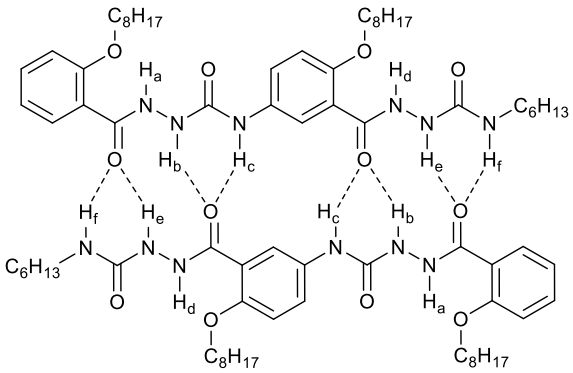

Figure 4-4. Homoduplex assembly of bis(acyl-semicarbazide) **4c**; a super organogelator reported by Chu and Chen. π- π stacking is attributed with the formation of 2D-lamellae and the resulting gel.[17]

A final example of a known bis(*acyl*-semicarbazide) LMWG comes from previous work by the Steed group, who reported a versatile bis(*acyl*-semicarbazide) gelator derived from the tuberculosis drug Isoniazid and the diphenylmethane derived spacer reviewed in chapter 2.[18] Pyridyl groups are often found to inhibit gelation of bis(urea) LMWGs due to their tendency to form finite pyridyl-urea hydrogen bonds, which disrupt α-tape assembly,[19,20] yet this compound demonstrated versatile gelation behaviour, forming gels in 19 organic solvents. The gels were utilised in a drug-mimetic approach to crystallise isoniazid, but no attempt was made to identify the supramolecular motifs responsible for gelation.

This same study also reported numerous crystal structures of a bis(acyl-semicarbazide) (**4d**) derived from isoniazid and a 1,3-bis(1-isocyanato-1-methylethyl) benzene spacer group. Many crystal structures of the polymorphic non-gelator were obtained and provide insight into the potential supramolecular interactions that dictate the self-assembly of bis(*acyl*-semicarbazides). In the non-solvated crystal form, the molecules are shown to form intermolecular $R_2^2(10)$ synthons via amide NH and urea carbonyl

hydrogen bonds. Similar $R_2^2(10)$ synthons are attributed to the gelation of many hydrazide based gelators due to their tendency to form infinite tapes, but in this case, gelation is likely not observed due to an $R_2^1(6)$ motif between urea NH and pyridyl groups, which truncates fibre formation.

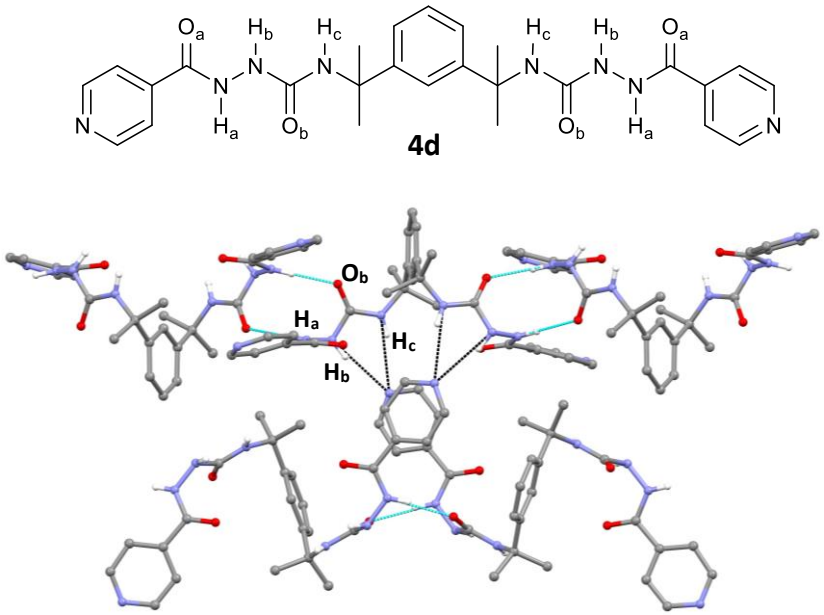

Figure 4-5. Molecular packing in the non-solvated form of **4d** (first reported in ref. 8). Dimeric $R_2^2(10)$ interactions form between amide NH_a and urea O_b (shown in light blue), but these are truncated by $R_2^1(6)$ motif (in black) between urea $NH_{b\text{-}c}$ and pyridyl nitrogen atoms.

Three of the five solvated **4d** structures reveal $S_2^1(6)$ motifs between one pair of urea NH and an amide carbonyl, whilst one urea NH from the other group form an S-motif with the other amide carbonyl (**Figure 4-6**). These three structures all differ in how NH_b hydrogen bonds, which is shown to form finite hydrogen bonds with the carbonyl oxygen atom of cyclohexanone in the cyclohexanone solvate and with a pyridyl end group in a neighbouring molecule in the 2-ethylpyridine solvate and a $D_2^2(4)$ motif, via $NH_{(urea)}\cdots O\text{-}H_{(propan\text{-}2\text{-}ol)}\cdots N_{(pyridyl)}$ interactions, in the propan-2-ol solvate. In the cyclohexanone and 2-ethylpyridine structures, the solid network is a lamellar assembly driven by $R_2^2(10)$ synthons between $NH_{(amide)}$ and urea carbonyl functionalities. This results in alternating intramolecular-intermolecular interactions, which bear resemblance to the synthons that **4b** is predicted to form. In the propan-2-ol solvate, lamellar assembly via intermolecular $R_3^3(12)$ motifs that are essentially the $R_2^2(10)$ with one of the $NH_{(amide)}\cdots O{=}C_{(urea)}$ interactions propagated by a propan-2-ol acceptor and donor.

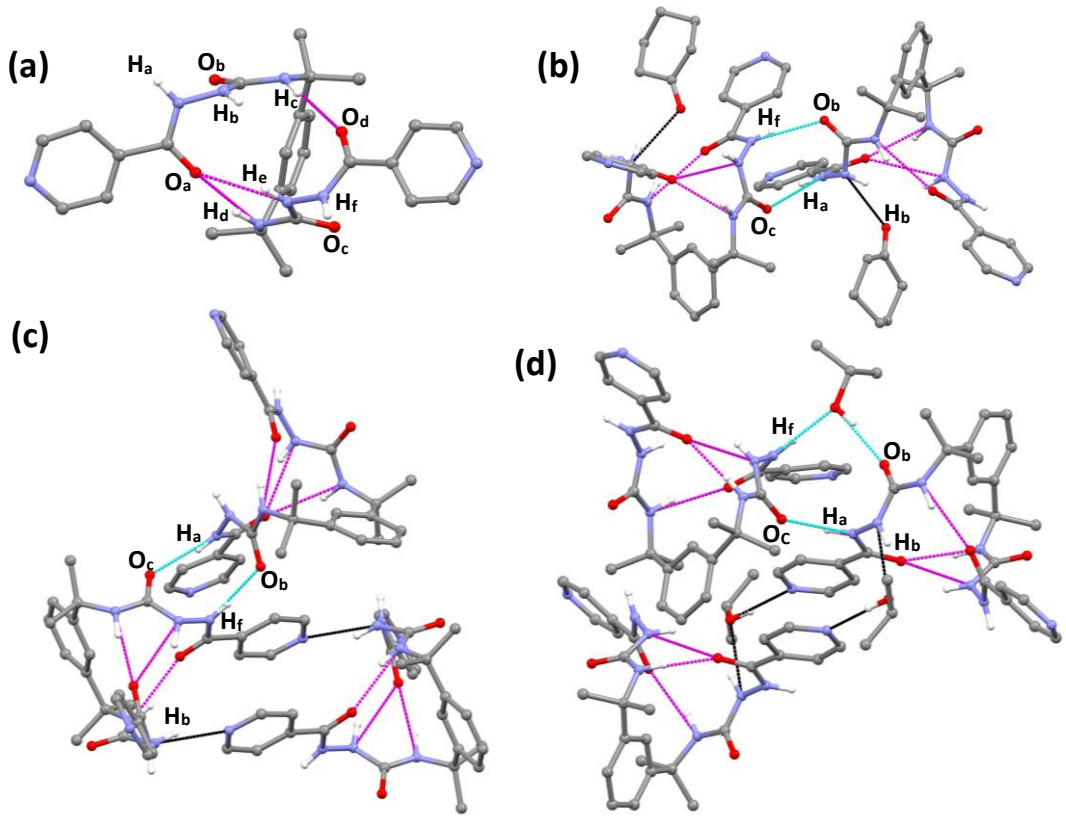

Figure 4-6. (a) The conformation of **4d** in the propan-2-ol solvate with labelled hydrogen bond donors and acceptors. The conformation reveals intramolecular hydrogen bonds (in pink) between $H_c\cdots O_d$ and $H_{d/e}\cdots O_a$. Identical intramolecular hydrogen bonds are observed in the cyclohexanone and 2-ethylpyridine solvates. Intermolecular $R_2^2(10)$ synthons (in light blue), formed via $NH_a\cdots O_c$ and $NH_f\cdots O_b$ hydrogen bonds, are exhibited in **(b)** the cyclohexanone solvate and **(c)** the 2-ethylpyridine solvate. In **(d)** the propan-2-ol solvate this synthon is propagated by a 2-propanol molecule to form a $R_3^3(12)$ motif (in light blue). In each structure H_b forms a finite hydrogen bond (in black) with cyclohexanone **(b)**, a pyridyl end group **(c)** or propan-2-ol **(d)**.

A search of the CSD for further structures containing acyl-semicarbazide functionalities returned 10 additional results. The corresponding studies cover a range of contexts which can be grouped into biological[21,22] or supramolecular applications[1,3,4,23,24] or simply structural reports.[25–27] However, none report gelation of the acyl-semicarbazides studied. These structures provide valuable insight into the self-assembly behaviour and can be grouped into three broad categories based on the intermolecular interactions exhibited. The first set are structures exhibiting $R_2^2(10)$ motifs, as observed in the structures for **4d** and attributed with the gelation of **4b**. Two additional structures reported in the CSD fit this category. The first of these structures (CSD refcode **FUZQEX**) shows an acyl-semicarbazide molecule with an additional carbonyl directly adjacent to the urea functionality via an N–C(O) covalent bond.[22] The urea group adopts a syn-anti conformation to facilitate an S(6) motif between this additional carbonyl oxygen atom ($C{=}O_a$) and urea NH_b. Molecules interact with one

neighbouring molecule via dimeric $R_2^2(10)$ motifs via $NH_c\cdots O_b$ hydrogen bonds, and with another adjacent molecule via dimeric $R_2^2(14)$ synthons formed via $NH_a\cdots O_c$ interactions. These ring motifs alternate infinitely throughout the structure and promote the formation of lamellae along the a-axis. The second of these structures (CSD refcode **IGUNAZ**) was reported by Zhao and colleagues in 2003 in which the molecules assemble via $R_2^2(10)$ motifs between urea NH and amide carbonyl oxygen atoms, instead of between amide NH and urea carbonyl oxygen atoms. The two urea NH interact with amide carbonyls from two distinct molecules which results in a zipper forming via hydrogen bonds (**Figure 4-8**). The structure displays the highly favourable S(6) motifs between NH_{amide} and alkoxy groups,[28] which have been shown to drive dimer assembly of *acyl*-semicarbazides by rigidifying the molecular backbone and reducing the likelihood of unidirectional $R_2^2(10)$ infinite tapes forming and any consequential gelation.

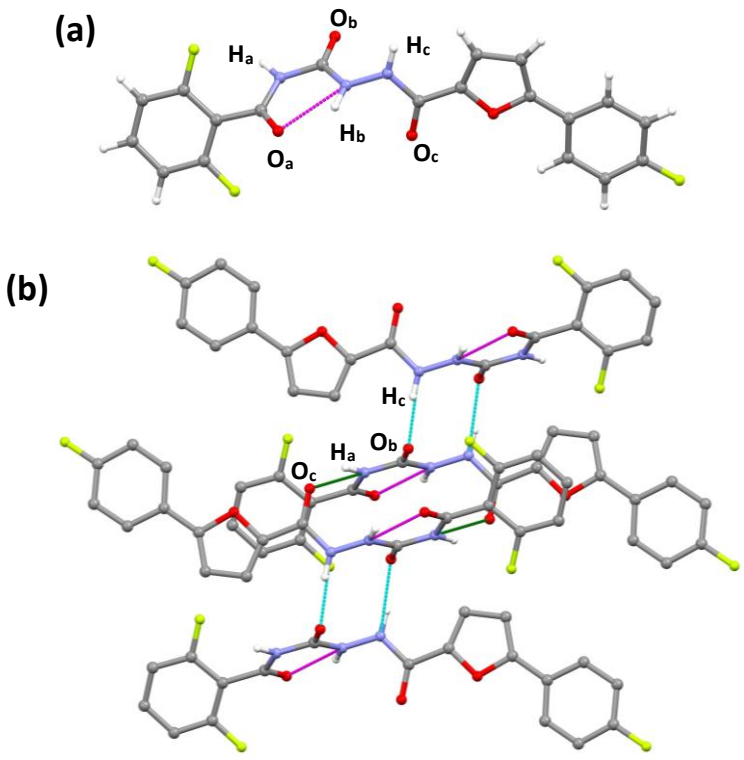

Figure 4-7. (a) Image of the molecules in CSD ref code FUZQEX (first reported in ref. 22) with relevant hydrogen bond donors and acceptors labelled. An S(6) motif forms NH_b and $C{=}O_a$ directly (shown in pink). **(b)** The structure reveals alternating $R_2^2(10)$ synthons (in light blue) and $R_2^2(14)$ synthons (in green), which drive lamellar growth along the a-axis.

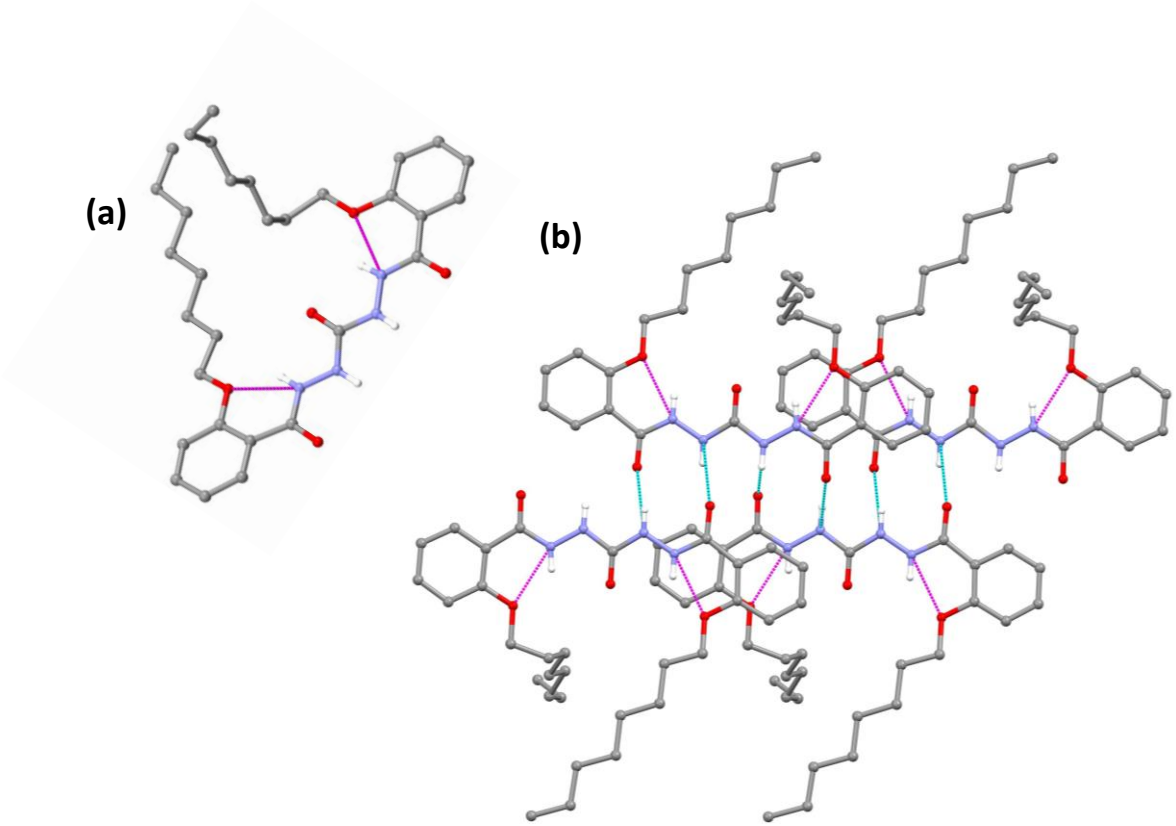

Figure 4-8. (a) Image of the acyl-semicarbazide in CSD ref code IGUNAZ (first reported in ref. 28). **(b)** $R_2^2(10)$ motifs between urea NH and amide carbonyl oxygen atoms (in light blue), form a supramolecular zipper with alkoxy groups protruding to the sides. The amide-alkoxyl S(6) motif forms (in pink) with the long aliphatic chain generating steric hindrance preventing hydrogen bonds to the urea carbonyl.

The second grouping of structures all exhibit $R_2^1(6)$ urea tape motifs which are often considered responsible for the versatile gelation behaviour of urea LMWGs (**Figure 4-9**). Whilst all these structures reveal infinite urea tape synthons, the interactions that the amide groups form are diverse. In CSD structure **UGIWOX** the urea and amide groups are coplanar, with the latter forming $NH_{(amide)}\cdots O{=}C_{(amide)}$ infinite chain motifs that are orientated anti-parallel to the α-tape. The molecules in **NUQFIP** also form infinite C(4) amide-amide interactions, but these form perpendicular to the α-tape plane between molecules in adjacent urea stacks. Similarly, **XAYSOF** shows hydrogen bonds forming perpendicular to the urea tape via dimeric $R_2^2(10)$ motifs between amide NH groups and the urea oxygen atoms. Finally, in **PEJKIZ** steric hindrance from the spacer aryl groups inhibits hydrogen bond formation by the amide functionalities. The diversity in the amide groups interactions may greatly influence the directionality of self-assembly and consequentially play a key role in determining the gelation potential of acyl-semicarbazides.

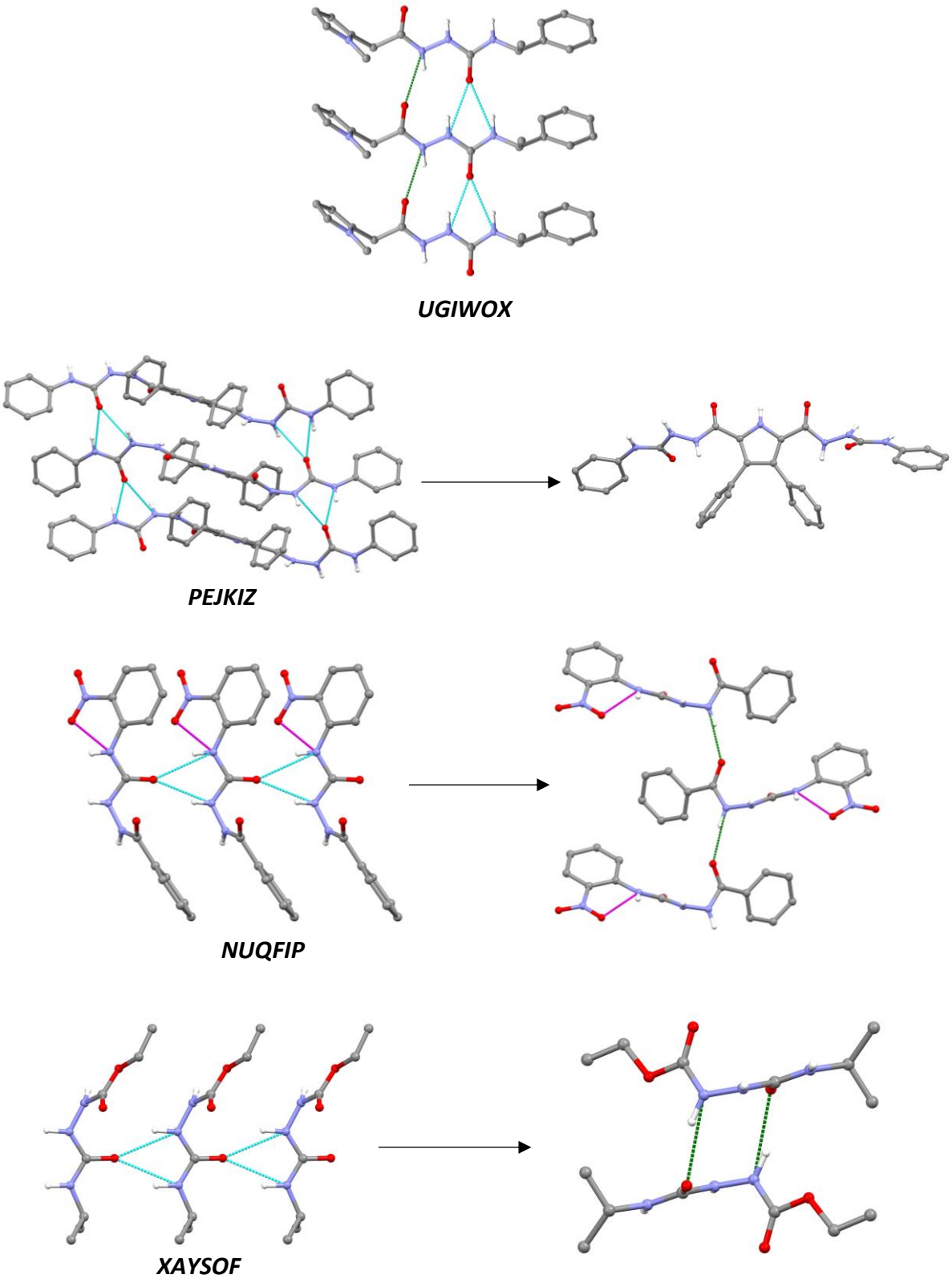

Figure 4-9. Images of $R_2^1(6)$ urea-urea α-tape motifs (in blue) in acyl-semicarbazide structures reported in the CSD, with the associated CSD refcode below each image. The amide group hydrogen bond behaviour is distinct in each structure. Intermolecular C(4) synthons between amide groups (in green) are present in **NUQFIP** and **UGIWOX**, and form perpendicular and parallel to the urea tape in each structure respectively. In **XAYSOF**, amide NH and urea oxygen atoms interact to form dimeric $R_2^2(10)$ synthons (in green) perpendicular to the urea tape. Steric hindrance generated by the spacer aryl groups in **PEJKIZ** inhibits amide group hydrogen bond formation. Intramolecular S(6) motifs (in pink) are also observed in NUQFIP between urea NH and NO_2 functionalities.

The final grouping of structures reveals molecules forming molecular duplexes via two $R_2^1(6)$ synthons between urea NH and amide carbonyl oxygen atoms. Two *acyl*-semicarbazide structures exhibit this assembly behaviour (CSD refcodes ULIXOD and BIDRUD) and were both reported in the same study by Chen and colleagues (**Figure 4-10**).[3] They demonstrated how the *acyl*-semicarbazide unit is self-complementary and that this dimer assembly was also adopted by longer asymmetric bis(*acyl*-semicarbazides*)* via ^{1}H-NMR and ESI-MS experiments. The finite nature of these interactions is discouraging when regarding gelation behaviour driven by hydrogen bonding, but it is worth noting that organogelator **4c** was predicted to induce gelation via $R_2^1(6)$ urea-amide duplex assembly and subsequent π-π stacking of adjacent duplexes.

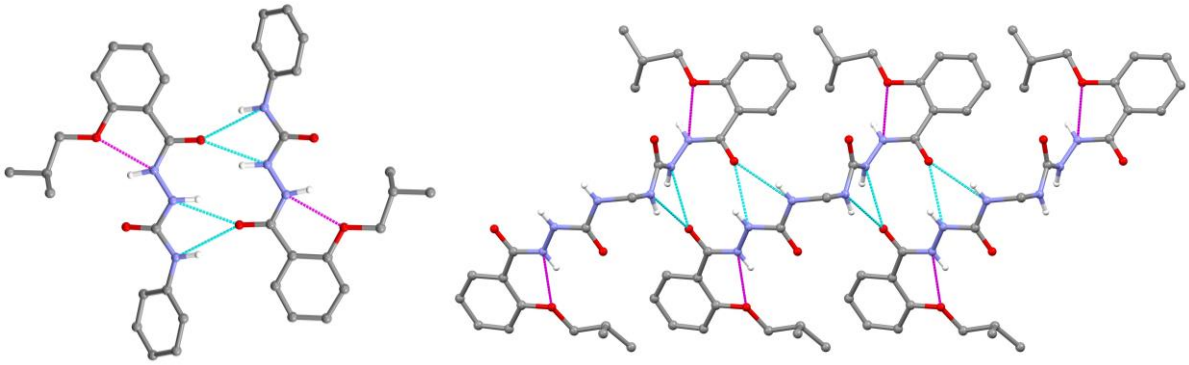

ULIXOD ***BIDRUD***

Figure 4-10. Images of antiparallel dimeric $R_2^1(6)$ synthons formed via $NH_{(urea)}\cdots O{=}C_{(amide)}$ interactions (in light blue) in acyl-semicarbazide structures CSD ref code ULIXOD and BIDRUD. Both structures show intramolecular S(6) motifs (in pink) forming between amide NH and alkoxy functionalities.

The two-remaining acyl-semicarbazide structures reported in the CSD do not fit into any of these groupings due to the role of additional hydrogen bond functionalities within the molecules. Maguire *et al.* reported the structure of a mono-acyl-semicarbazide derived from isoniazid and phenyl isocyanate (CSD refcode ILEWON).[29] The structure contains molecules assembling via intermolecular $R_2^2(12)$ synthons formed by hydrogen bonds between one urea NH and urea carbonyl oxygen atom and an amide NH and amide carbonyl oxygen atom (**Figure 4-11**). This is closely related to the urea-tape assembly with synergistic amide C(4) synthons identified in UGIWOX, yet the structure serves as another example of how pyridyl functionalities can disrupt ideal urea tape formation, with the unaccounted for urea NH_b forming a finite hydrogen bond with the nitrogen atom of a pyridyl end group. The molecule in the final structure

(CSD refcode ZINCEG) is comprised of an acyl-semicarbazide with an additional amide functionality, which forms an S(10) motif between C=O_c and NH_a (**Figure 4-12**). Intermolecular hydrogen bonds between $NH_b\cdots O_c$ and $NH_c\cdots O_b$ result in $R_2^2(12)$ synthons being exhibited as a unidirectional ribbon through the crystal lattice. Whilst the additional amide functionality plays a key role in this self-assembly behaviour, it is conceivable that bis(acyl-semicarbazides) may be able to form the same or similar interactions interactions.

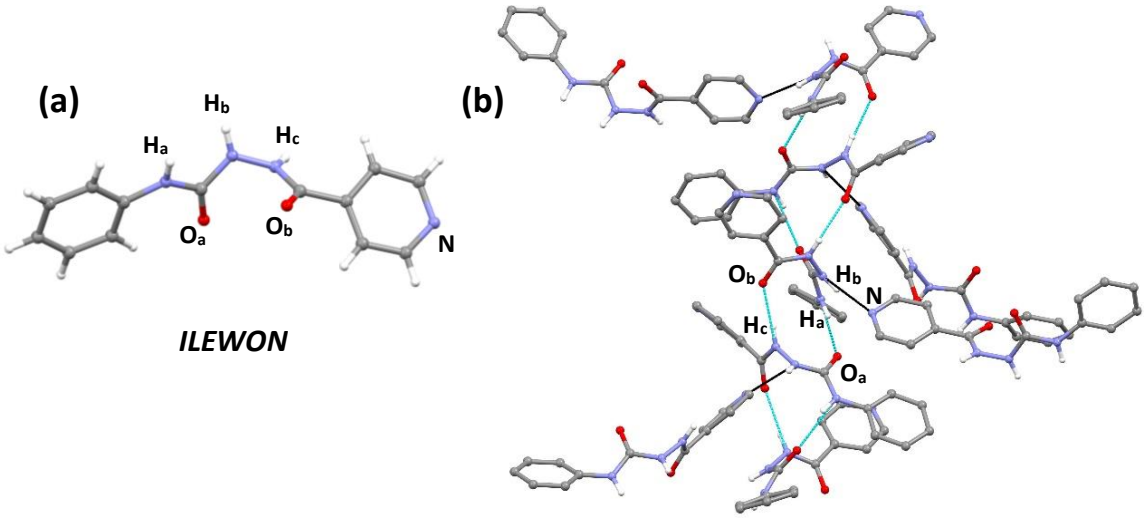

Figure 4-11. (a) Image of the molecule in CSD ref code ILEWON (ref. 29) with key hydrogen bond donors and acceptors labelled. **(b)** $R_2^2(12)$ synthons form via $NH_a\cdots O_a$ and $NH_c\cdots O_b$ hydrogen bonds (in light blue). These form infinite ribbons in one dimension, however molecular assembly is multidirectional, due to $NH_b\cdots N_{pyridyl}$ interactions, which interrupt urea tape formation and any potential fibre formation.

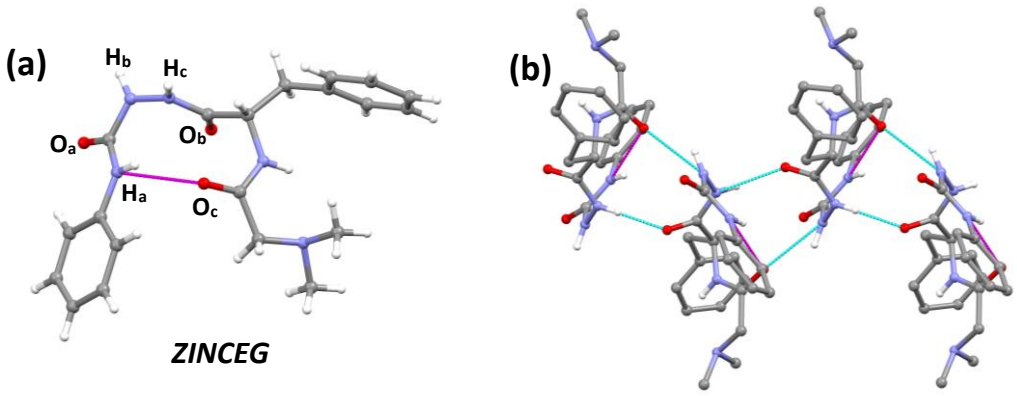

Figure 4-12. (a) Image of the acyl-semicarbazide in CSD refcode ZINCEG, exhibiting an S(10) hydrogen bond motif between urea NH_a and amide C=O_c (in pink). **(b)** Molecules assemble via $R_2^2(12)$ synthons formed from $NH_b\cdots O_c$ and $NH_c\cdots O_b$ hydrogen bonds (in light blue). This forms an infinite unidirectional ribbon through the structure. Despite the role of the additional amide functionality in these interactions, the interactions could be adopted by bis(acyl-semicarbazide) compounds.

It is worth noting that none of the limited bis(*acyl*-semicarbazide) gelation or crystallisation studies directly examine how the spacer group nature and the distance between the two *acyl*-semicarbazide linkages affect self-assembly and the supramolecular motifs that form. Additionally, the effect that molecular chirality has on the supramolecular motifs and self-assembly of bis(*acyl*-semicarbazides) has also not been reported. As discussed in chapter 1, molecular chirality is typically linked with more effective and versatile gelation behaviour as it reduces the symmetry of the molecular building blocks, promoting the likelihood of anisotropic aggregation. Previous studies have demonstrated that mixing opposite enantiomers of LMWGs can tailor gel and fibre properties to improve suitability for applications,[30] whilst molecular and/or supramolecular chirality in gel systems can be desirable and potentially have many useful applications, such as chiral recognition or resolution.[31–33] Understanding the trends and effects could enable LMWG engineers to design novel bis(*acyl*-semicarbazide) gelators with properties fit for these applications.

The current study presents a range of novel bis(*acyl*-semicarbazides) and explores their crystallisation and self-assembly behaviour via SCXRD analysis. By growing single crystals, the molecular conformation, packing arrangements and supramolecular motifs dictating self-assembly could be identified, including any infinite hydrogen bonding synthons that may be attributed with any gelation behaviour. The bis(*acyl*-semicarbazides) described in this work are symmetrical and were designed so that the effect that different spacer groups and molecular chirality have on the lattice arrangements and supramolecular motifs could be examined. To achieve this both aliphatic and aromatic spacer groups were utilised, with the impact that aliphatic chain length and aromatic substitution positions have on self-assembly behaviour being explored. Achiral benzyl and chiral 1-phenylethyl end groups were employed with each spacer group to probe how molecular chirality affects the hydrogen bonding synthons and molecular packing. Both R,R and S,S enantiomers of the 1-phenylethyl terminated compounds were synthesised and crystallisations of the racemic mixture of the enantiomers were undertaken to explore how this impacts the molecular packing. It was anticipated that understanding how these factors affect molecular packing and supramolecular motifs would provide rational understanding on how gelation and fibre properties are affected by these factors, with the gelation behaviour and applications of all compounds being discussed in chapter 5.

4.2 Results and Discussion

4.2.1 Synthesis and Characterisation

Bis(*acyl*-semicarbazide) compounds were prepared by reacting oxalyl dihydrazide (**4.1**), malonic dihydrazide (**4.2**), succinic dihydrazide (**4.3**), adipic dihydrazide (**4.4**), isophthalic dihydrazide (**4.5**) or terephthalic dihydrazide (**4.6**) with excess benzyl isocyanate, (R)-(+)-α-methylbenzyl isocyanate or (S)-(+)-α-methylbenzyl isocyanate. Purification was generally achieved by washing with copious amounts of hot water, followed by a diethyl ether wash and drying in a drying pistol at 110 ^{o}C for 24 to 48 hours. All products were obtained with high yields between 83-98 %. Racemic mixtures of the 1-phenylethyl terminated enantiomers (**Rac**) were also produced by mixing equimolar amounts of the purified R,R and S,S bis(acyl-semicarbazides).

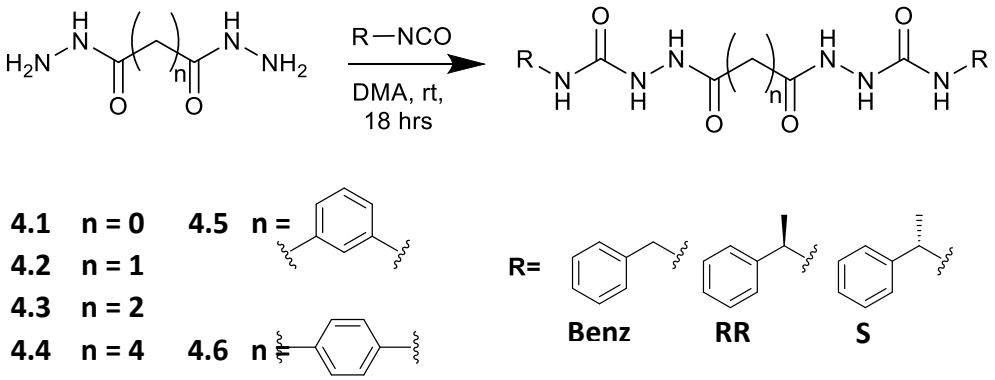

Scheme 4-1. The simple one-step synthesis of bis(acyl-semicarbazides) 4.1-4.6$_{Benz}$, 4.1-4.6$_{RR}$ and **4.1-4.6$_{SS}$.**

It is well known that amide bonds can exhibit restricted rotation resulting in slow interconversion between different molecular conformations, since the nitrogen lone pair of electrons are delocalised over the carbonyl group, affording the C–N bond a degree of double bond character. This generates a large rotational barrier of approximately 54-84 kJ mol^{-1} between the *cis* and *trans* conformations and results in amide bond rotation occurring within the proton magnetic resonance time scale, enabling consequential conformational features to be detected in the ^{1}H-NMR spectra as two or more sets of resonances.[34] This is observed in the spectra for all the bis(*acyl*-semicarbazides) prepared in this work and is observed as the presence of two sets of signals corresponding to major and two minor conformers (**Figure 4-13**). The spectra were assigned through ^{1}H-^{1}H COSY, ^{1}H-^{13}C HMBC and ^{1}H-^{13}C HSQC experiments. The

COSY spectra show the protons giving rise to signal NH_a and NH_b are coupled and bound to adjacent N atoms, whilst the HMBC experiments shows that the signals NH_b and NH_c are exclusively coupled to the same carbon atom which corresponds to the urea carbonyl, and NH_a is coupled to a separate carbon atom, assigned as the amide carbonyl. Some of the minor signals are overlapped with major signals, but many are baseline separated and can be reliably integrated. The resulting integration reveals two sets of minor peaks in each spectrum for the aliphatic-spacer compounds. The three conformers arise due to the major (M) or minor (m) forms of the two amide groups, giving isomers MM, Mm and mm. The proportions of the three isomers are approximately 90:9:1. To confirm the conformational nature of these features, 2D Rotating frame nuclear Overhauser effect spectroscopy (ROESY) NMR and variable temperature (VT)-NMR were employed.

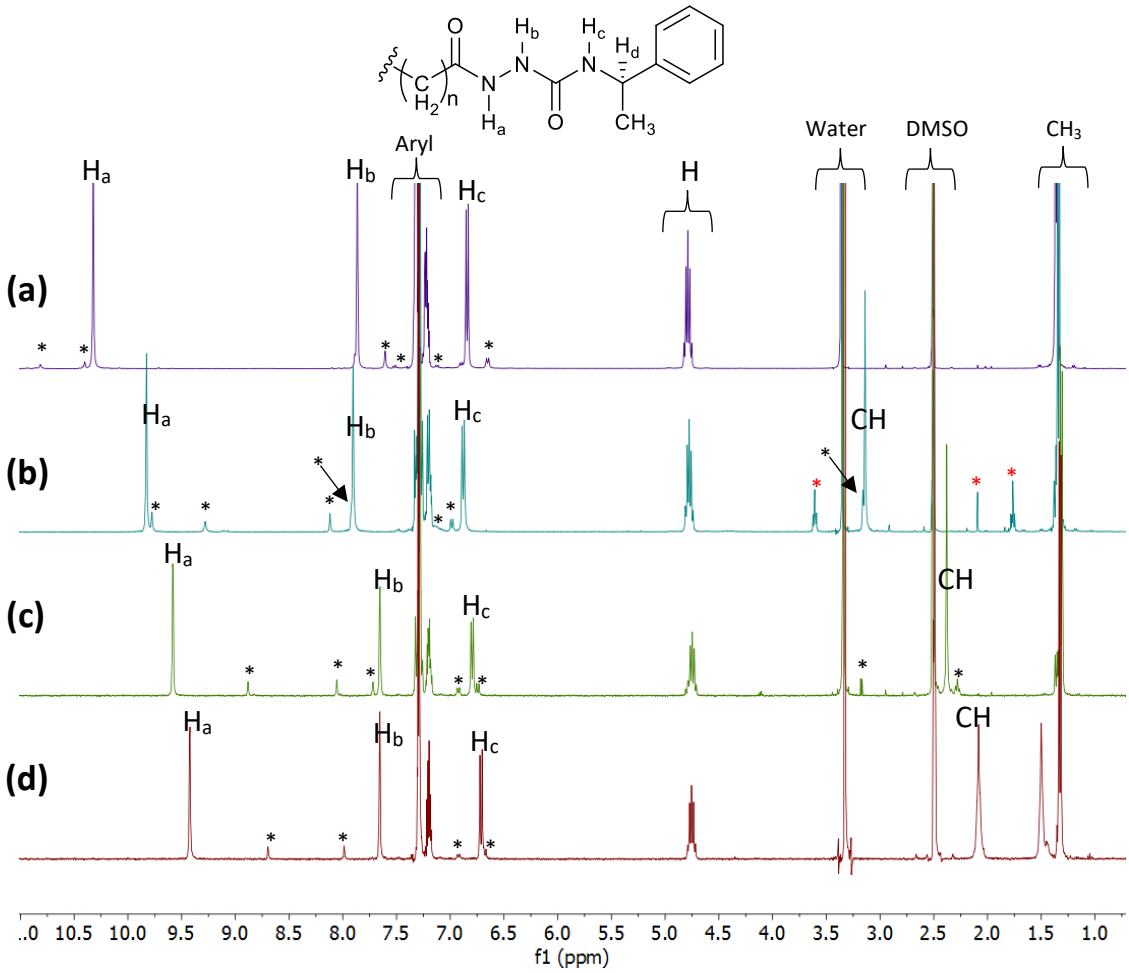

Figure 4-13. Stacked ^{1}H-NMR spectra of **4.1**$_{RR}$ (a), **4.2**$_{RR}$ (b), **4.3**$_{RR}$ (c) and **4.4**$_{RR}$ (d), presenting low intensity peaks 5-10 % the integral of major peaks, which are highlighted by a black asterisk. Black arrows are used to show minor features overlapping with major signals. Even lower intensity peaks are present in the spectra but not identifiable in the figure. Nearly identical minor signals are also present in the spectra for benzyl-terminated bis(acyl-semicarbazides). Peaks denoted by a red asterisk correspond to residual DMA.

2D ROESY experiments enabled the spatial proximity of ^{1}H nuclei to be assessed, with cross-peaks arising where protons are within 4 Å of each other, due to the nuclear Overhauser effect (NOE).[35] NOE detection is often challenging for compounds of an intermediate molecular weight (400-600 g mol^{-1}). This is because NOEs arise when two interacting nuclei relax each other via one of two pathways. The W_2 pathway gives rise to positive NOEs and occurs when the spins of two nuclei switch between two well separated energy levels. Meanwhile, relaxation via the W_0 pathway involves no net change in nuclear spin between two close energy levels and generates negative NOEs. Whilst the W_2 pathway is stimulated by the higher-frequency tumbling of small molecules (M_w < 400), the W_0 pathway is stimulated by the lower-frequency tumbling of larger molecules (M_w > 600-700. Molecules with an intermediate molecular weight stimulate both positive and negative relaxation pathways to similar extents, which results in negligible NOE signals. The intermediate molecular weights of the compounds in this study, coupled with the low signal-to-noise ratio of the minor signals and the restriction of using d_6-DMSO for adequate solubility, meant that the more commonly utilised NOESY sequence failed to detect NOEs for the minor signals. ROESY uses an alternative pulse sequence to acquire the NMR data than NOESY experiments and is often better for detecting NOEs for intermediate size molecules, despite a lower signal to noise ratio and the tendency to yield more artefacts in the spectra.[36] The ROESY experiments detected NOEs for major signals and the minor signals with 5-10 % integral of major peaks, but failed to detect any NOEs for the set of lower intensity signals.

The ROESY spectrum of **4.2$_{RR}$** is shown below as a representative example. The spectrum has been split into four segments for clarity and the low intensity signals for which NOEs were detected are labelled numerically (**Figure 4-14** and **Figure 4-15**). The spectrum indicates that the high-field CH_d, methyl and some aryl protons are all within 4 Å of each other, whilst NH_c is also within a 4 Å radius of the methyl and CH_d protons. NOEs are detected between NH_a, NH_b and NH_c, with the intensity of the NOEs between NH_b and the other two NH protons being greater than for the NOEs between NH_a and NH_c, which should be expected based on their covalent connectivity. NOEs are also detected between low intensity signals 6, 5 and 2 and between 7, 4 and 3 which implies that this molecular conformation is asymmetric. An NOE is identified between peak 1, which is partially overlapped by the CH_2 peak at 3.15 ppm, and minor peaks 6

and 7. Thus, signals 6 and 7 correspond to NH_a in a less abundant isomeric form, given the proximity of 6 and 7 to the major NH_a signal and the coupling between a peak in the CH_2 region. The fact that both these signals couple to the same low intensity CH_2 signal supports the asymmetrical nature of the less favourable molecular conformation, thus correspond to a Mm conformer. Signals 5 and 4 correspond to NH_b, 2 and 3 to NH_c, and 1 to CH_2 in this Mm conformer. The NOE between CH_d and NH_c, and also between CH_d and 2, further confirms that the low intensity peaks are signals from the same compound as the dominant signals (**Figure 4-16**). This pattern of NOEs being detected between the separate sets of low and high intensity signals, and between the minor NH_c and major CH_d signals are observed for all the 1-phenylethyl aliphatic-spaced bis(*acyl*-semicarbazides), whilst the same pattern is also observed in the spectra for the aliphatic-spaced benzyl-terminated compounds, with NOEs observed between signal 2 and the dominant signal for the benzyl methylene protons. Indeed, this is also the case in all the aliphatic-spaced bis(acyl-semicarbazide) spectra.

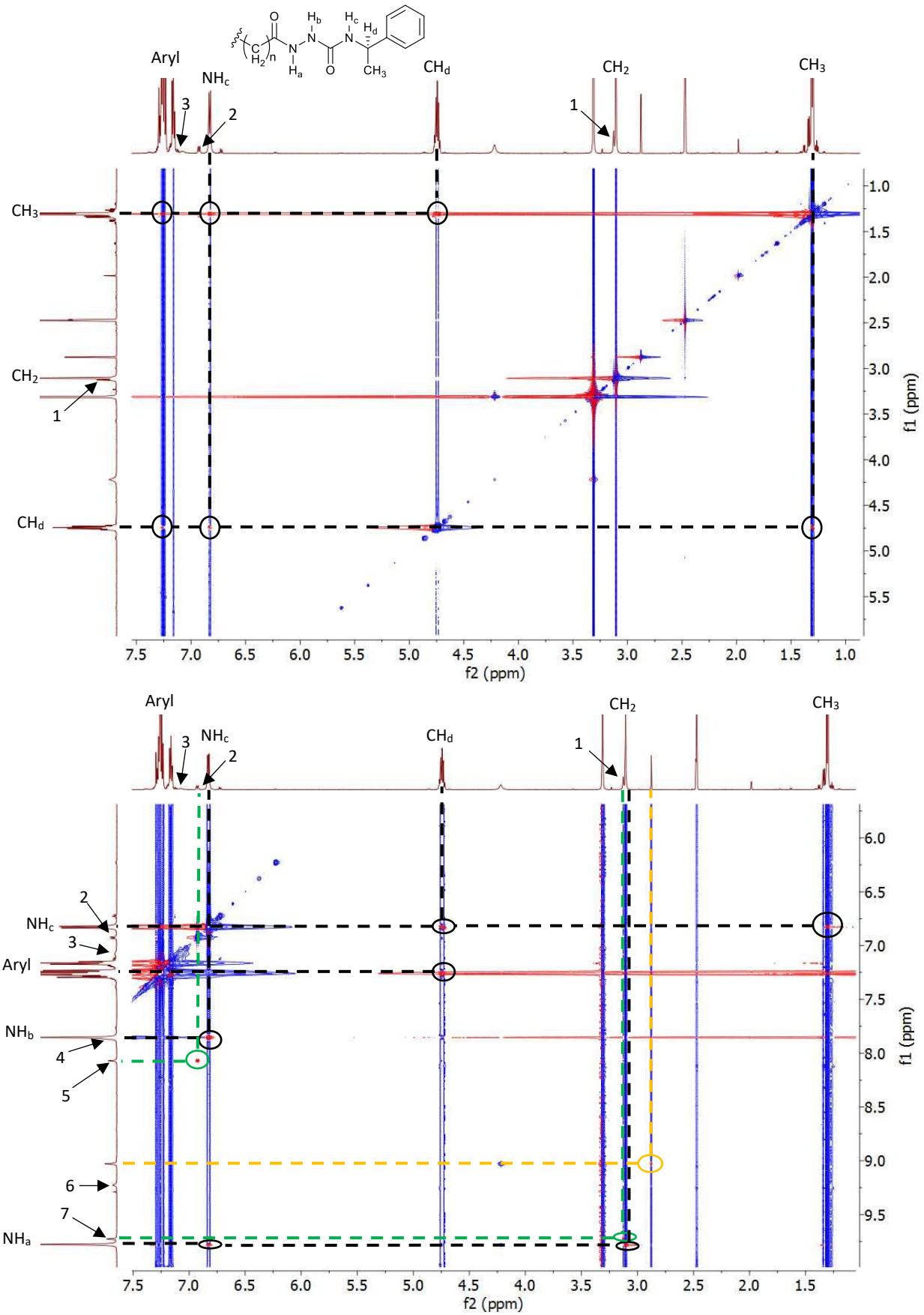

Figure 4-14. Rotating Overhauser effect spectroscopy (ROESY) pattern in d_6-DMSO at 25 °C of **4.2$_{RR}$** identifying NOEs when protons with chemical shift between 1-7.5 ppm are irradiated (horizontal axis) with observed nuclei between **(a)** 1-5.5ppm and **(b)** 6.0-10ppm (vertical axis). All NOEs are shown as red contours and are circled for clarity. Black circles highlight NOEs that arise between two dominant nuclei and green circles highlight NOEs that arise between two minor nuclei. The yellow circle highlights a NOE arising from an impurity of malonic acid dihydrazide that disappears after further purification.

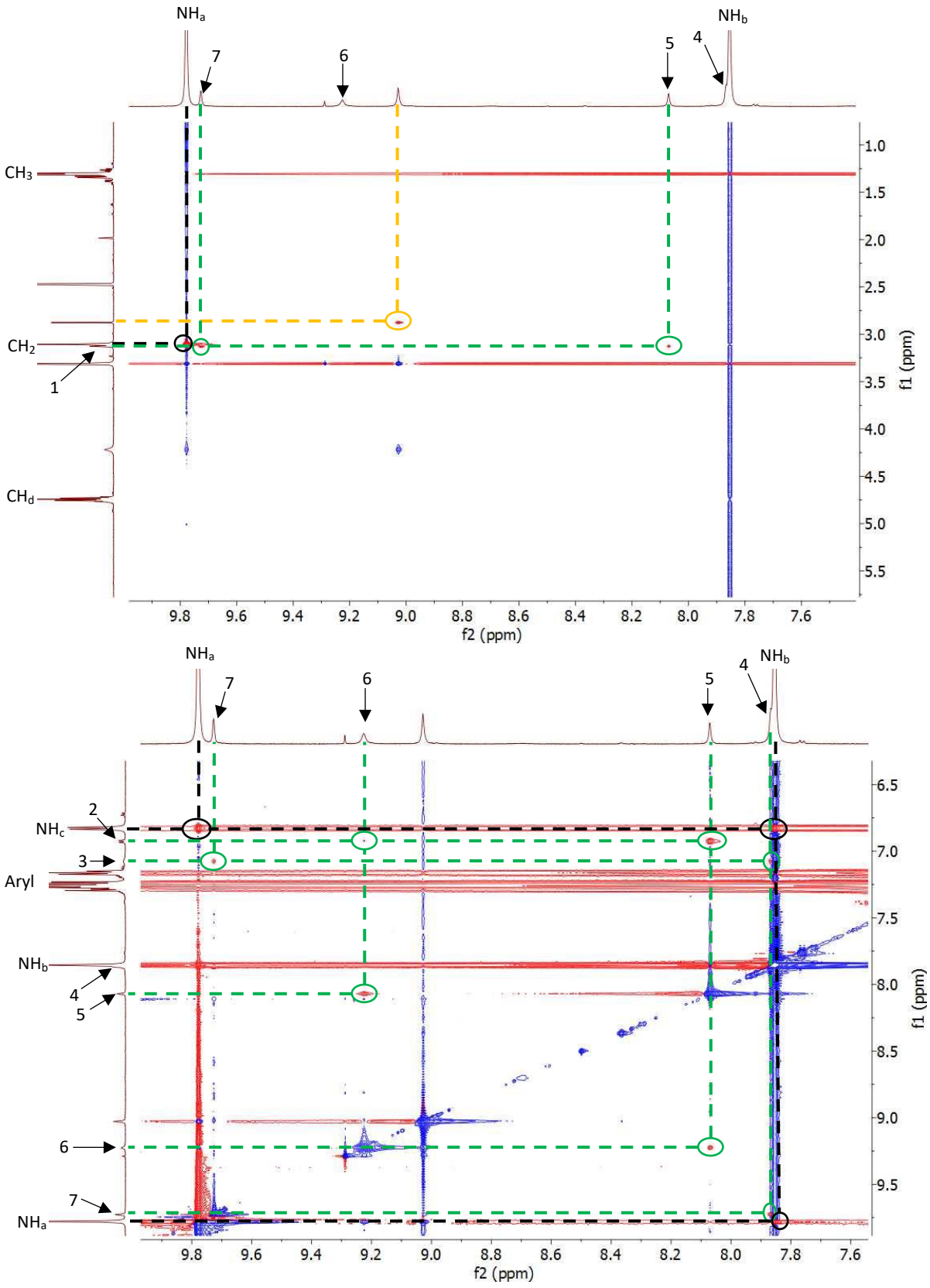

Figure 4-15. ROSEY-NMR spectra of **4.2RR** identifying NOEs when protons with chemical shift between 7.5-10 are irradiated. The same colour scheme is applied where NOEs corresponding to the dominant conformation are circled in black, whilst NOEs arising from minor conformations or impurity are circled in green and yellow respectively. **(a)** NOEs arise between the major NH_a peak and major CH_2 peak, whilst the minor NHa and CH_2 peaks are also in close proximity. The minor conformation of CH_2 also forms an NOE with the minor NH_b conformer, but the major NH_b isn't close enough to the CH_2 to produce an NOE when in the dominant conformation. **(b)** NOEs form between the minor conformations of: NH

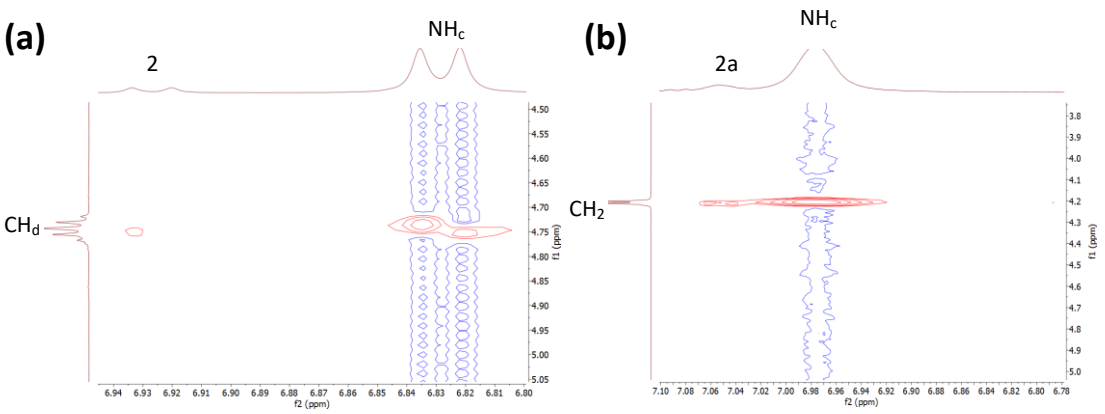

Figure 4-16. (a) Close up of the NOEs between NH_c and CH_d and signal 2 and CH_d in the **4.2$_{RR}$** ROESY spectrum. **(b)** An NOE also presents between NH_c and the terminal methylene unit in **4.2$_{Benz}$**, and between low intensity signal 2a and the spacer methylene unit. These features confirm that the set of low intensity signals correspond to a less abundant isomer.

Variable temperature NMR experiments demonstrates that most of the minor peaks coalesce with major peaks when the ^{1}H-NMR spectra is collected at 90 ^{o}C (**Figure 4-18**). This is because the higher temperature accelerates molecular motion and overcomes the barrier to bond rotation. Some of the more significant low intensity features persist in the high temperature spectra for compounds derived from **4.1** and **4.2**, demonstrating that the barrier between interconversion is higher for these shorter spacers. This is likely due to the proximity of the amide carbonyls in these compounds, generating an additional electrostatic repulsion barrier between the amide oxygen atoms. The major NH peaks also shift upfield by 0.1-0.3 ppm at the higher acquisition temperature, which arises from a reduction in hydrogen bonding at higher temperatures.[37]

The fact that different conformers in solution can be observed via ^{1}H-NMR spectroscopy raises the possibility of multiple conformations being adopted in the solid-state which could significantly impact upon the dominant supramolecular synthons and packing arrangements. Superficially, the *trans* conformers of amide and urea groups would be anticipated to be the most stable and predominant form in all compounds, whilst the cis-cis isomers would be anticipated to be the least energetically favourable with intermediate cis-trans conformers lying in between the two extremes. However, alternative cis-cis or a combination of cis-trans isomers may be relatively stable if they allow favourable intra or intermolecular hydrogen bonding.

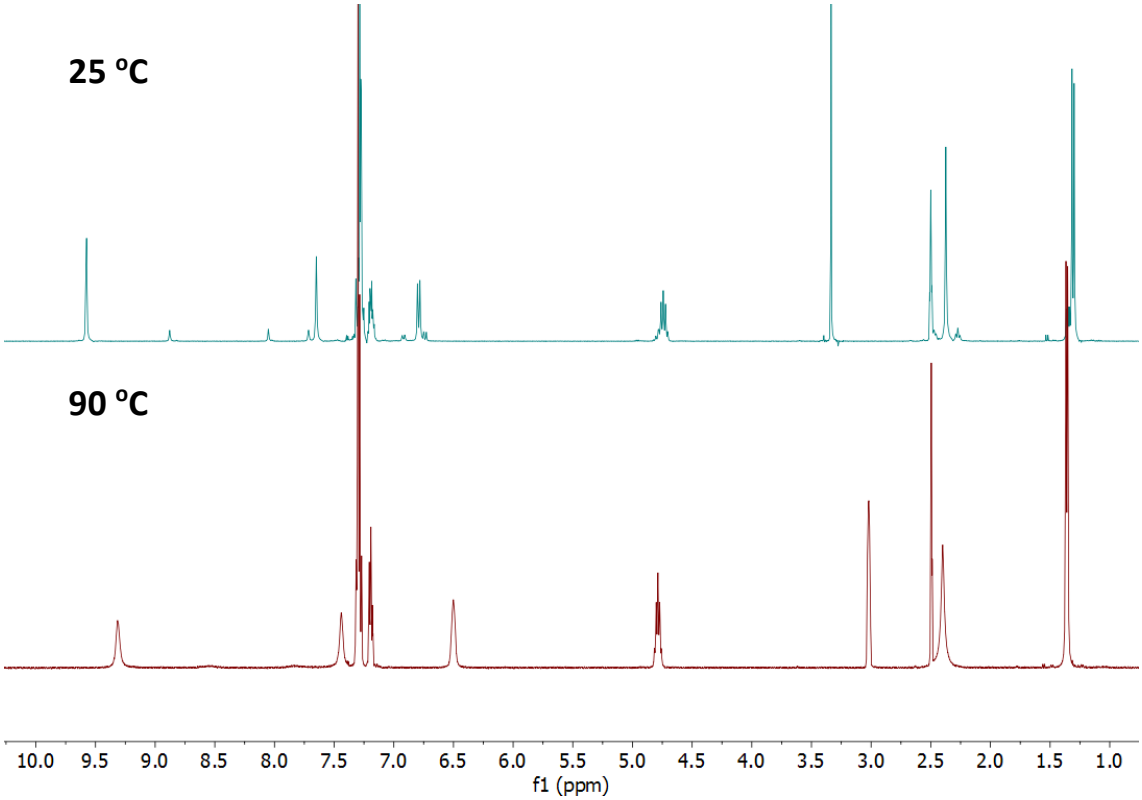

Figure 4-17. ^{1}H-NMR spectra of **4.3$_{RR}$** collected at 25 °C and 90 °C. The minor signals broaden and coalesce with major signals at the higher acquisition temperature, which is a common feature of signals arising due to minor conformational species.

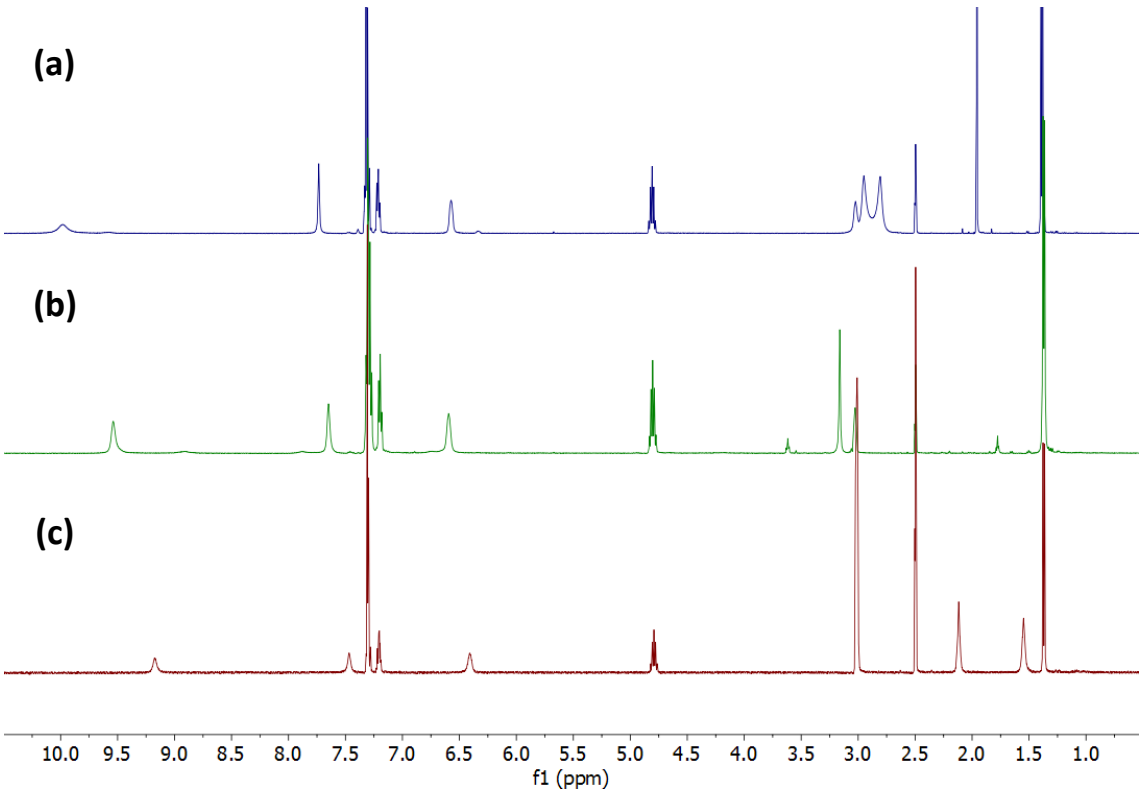

Figure 4-18. ^{1}H-NMR spectra of **(a) 4.1$_{RR}$**, **(b) 4.2$_{RR}$** and **(c) 4.4$_{RR}$** collected at 90 °C show that most of the minor features have also broadened or coalesced with major peaks in these spectra. A few minor signals are still visible in (a) and (b) indicating a higher barrier to rotation around the amide groups in these compounds.

4.2.2 Crystallisation Procedures

SCXRD is the gold-standard technique for experimentally determining the 3D molecular structure and conformation adopted by a molecule, in addition to identifying supramolecular synthons and packing behaviour. This work largely focuses on the growth and characterisation of single crystals of the bis(*acyl*-semicarbazides). The crystallisation screening was extensive due to the possibility of polymorphic forms that may be afforded by the high abundance of hydrogen bond donors and acceptors and the distinct conformations identified in the ^{1}H-NMR characterisation of the compounds. A series of procedures were employed to optimise crystal growth conditions and obtain single crystals suitable for SCXRD analysis. The procedures outlined were also used to grow racemic crystals comprising of both the R,R and S,S enantiomer to see how this mixing may affect the molecular packing behaviours.

The solubility of the compounds was determined in a range of solvents spanning the polarity spectrum by heating 5 mg in 0.5 mL suspensions. Most of the compounds dissolved upon heating in methanol, ethanol, propan-2-ol, benzyl alcohol, pyridine, DMSO, acetonitrile, toluene, nitromethane, 2-ethylpyridine and 3-picoline. For the crystallisation screening, supersaturated solutions were created by adjusting the substrate concentration so that the solid compound partially dissolved at room temperature but formed a homogenous solution upon heating. Supersaturated solutions were then left undisturbed for two weeks. This procedure was undertaken for all solvents in which supersaturated solutions formed. If no crystals or precipitate were observed after 8 weeks, multiple methods (described below) were employed in parallel to gradually increase the extent of supersaturation. These procedures were carried out at a range of concentrations and conditions to fine-tune the degree of supersaturation, with the aim to be close to the critical point of nucleation to facilitate growth of high-quality single crystals.

Initially, one sample of each saturated solution was stored at 4^{o}C for 2 weeks and another stored at -20^{o}C, as lower temperatures typically reduce substrate solubility. The second method was slow evaporation of all the saturated solutions over 2 days to 2 weeks at room temperature. The slow evaporation experiments were repeated at 40^{o}C if the solvent volume had not diminished significantly after 2 weeks. If the evaporation was rapid, the experiment was repeated with the vial tightly sealed with

pinpricked parafilm or foil to slow the evaporation rate. The final three methods employed to increase the extent of supersaturation all involve decreasing compound solubility by anti-solvent addition. The first way this was done was by using water as an antisolvent, or hexane if the solvent was water immiscible. The antisolvent was added in 25 µL aliquots every 2 minutes until the solution turned slightly translucent, at which point the solution was reheated until transparent and left undisturbed over days to weeks. Vapour diffusion experiments were also utilised, with several different solvent-anti-solvent combinations being employed, typically based on successful combinations from other studies[38] and on combinations with an intermediate to slow diffusion rate.[39] If a precipitate or low-quality crystal formed within hours, the experiment was repeated with a foil or parafilm lid with pinpoint holes covering the inner solvent vial to slow down the vapour diffusion process. The third antisolvent method involved layering a saturated DMSO solution of compound with octane, where 0.5 mL of the DMSO solution was pipetted into a glass NMR tube and was layered with a further 0.1-0.3 mL of DMSO and then 0.3-0.5 mL octane. The additional layer of DMSO was incorporated to form a buffer zone between the solvent and anti-solvent, which should slow down crystallisation as described by Spingler et al.[38]

Additional steps were taken if poor-quality crystals or a crystalline powder formed from any of the procedures already outlined. Firstly, the experimental conditions yielding the poor crystals was repeated at lower concentrations, with each iteration typically using a solution 0.05-0.1 % w/v lower in concentration to fine-tune conditions. Furthermore, the poor-quality crystalline material was used to seed a range of supersaturated solutions of the same compound. Only a small amount of seed was introduced to each solution via the tip of a needle. Finally, poor-quality crystals were re-dissolved in the mother liquor by heating, with the resulting solutions then slowly cooled from either 120 ^{o}C or from 5 ^{o}C below the solvent boiling point (whichever was lower) to 50^{o}C over 4 weeks in an automated laboratory oven. The cooling rate employed was 1-3 ^{o}C per day, which enabled the solubility of the compound to slowly decrease and for the solution to be stored at a temperature where the supersaturation is close to the critical nucleation concentration for a few days, resulting in the growth of a small number of single crystals. The procedures outlined resulted in numerous single crystals being obtained, with the successful crystallisation procedures outlined below (**Table 4-1.**Details of the successful

procedures used to grow single crystals of bis(acyl-semicarbazide) compounds.**Table 4-1**).

Table 4-1. Details of the successful procedures used to grow single crystals of bis(acyl-semicarbazide) compounds.

Compound	Solvent	Crystallisation Procedure	Crystal Habit
4.1$_{RR}$	Methanol	2 mg of **4.1$_{RR}$** was dissolved in 0.5 mL methanol with heat and passively cooled to room temp. Slow evaporation over 24 hours resulted in single crystals of a **4.1$_{RR}$** methanol disolvate.	Needle
4.2$_{Benz}$	Pyridine	2.5 mg **4.2$_{Benz}$** was dissolved in 3 mL of pyridine with heat. This was passively cooled to room temp, then placed in the fridge at 8 ^{o}C and left undisturbed for 2 weeks, yielding large single crystals of a **4.2$_{Benz}$** pyridine disolvate.	Needle
4.2$_{RR}$	Ethanol:H_2O	5 mg of **4.2$_{RR}$** was dissolved in 1 mL ethanol. Water was added in 50 µL aliquots until the solution turned translucent (0.8 mL total). The solution was then heated at 75 ^{o}C until turned transparent, before being cooled slowly from 75 ^{o}C to 50 ^{o}C over 10 days. This yielded crystalline needles which were identified to be an ethanol solvate of **4.2$_{RR}$**.	Needle
4.3$_{SS}$	1:1 Methanol:H_2O	**1)** 20 mg **4.3$_{SS}$** dissolved in 0.5 mL DMSO at room temperature and pipetted into a glass NMR tube. The solution was layered with 0.1 mL DMSO and 0.4 mL octane. The layered solution was left for 4 days and yielded very small crystalline needles. **Then;** **2)** 3 mg of **4.3$_{SS}$** was dissolved in 1 mL of a 1:1 MeOH:H_2O solution with heat, cooled to room temperature, seeded with a needle-tip of crystals from **1)** and left undisturbed for 2 weeks to yield single crystals of an anhydrous form of **4.3$_{SS}$**.	Plate
4.4$_{RR}$	Ethanol	**1)** 50 mg of **4.4$_{RR}$** was dissolved in 3 mL methanol with heat; a crystalline precipitate formed within 2 hours at -20 ^{o}C. **Then;** **2)** 3 mg of **4.4$_{RR}$** was dissolved in 1 mL ethanol with heat, cooled to room temperature, seeded with a needle-tip of crystals from **1)** and left undisturbed for one week to yield crystalline needles of an ethanol solvate of **4.4$_{RR}$**.	Needle
4.4$_{SS}$	Methanol	**1)** 50 mg of **4.4$_{SS}$** was dissolved in 4 mL methanol with heat; a crystalline precipitate formed within 2 days of cooling to room temperature. **Then;** **2)** 3 mg of **4.4$_{RR}$** was dissolved in 1 mL methanol with heat, cooled to room temperature, seeded with a needle-tip of crystals from **1)** and left undisturbed for one week to yield crystalline needles of a methanol solvate of **4.4$_{SS}$**.	Needle
4.5$_{RR}$	Ethanol	2.5 mg **4.5$_{RR}$** was dissolved in 0.5 mL ethanol. A vapour diffusion experiment with 2 mL diethyl ether as antisolvent was set up, with a foil lid with a pin-point hole pierced in it tightly covering the solvent vial to slow down the diffusion process. Crystals of an ethanol solvate of **4.5$_{RR}$** grew over 3 days.	Block
4.6$_{SS}$	Benzyl alcohol	5 mg of **4.6$_{SS}$** was dissolved in 0.5 mL benzyl alcohol with heat and slowly cooled from 120 ^{o}C to 50 ^{o}C over 2 weeks after which time two large hexagonal crystals had formed. Crystals were stored at room temperature in the mother liquor thereafter and were identified as a **4.6$_{SS}$** benzyl alcohol solvate with a high Z' value.	Hexagonal
4.1$_{Rac}$	Ethanol	**1)** 5 mg of a 1:1 **4.1$_{SS}$** and **4.1$_{RR}$** mixture was formed and dissolved in 1 mL methanol with heat; a crystalline precipitate formed within minutes of cooling to room temperature. **Then;** **2)** 1 mg of a 1:1 **4.1$_{RR}$** and **4.1$_{SS}$** mixture was formed and dissolved in 2 mL EtOH with heat, cooled to room temperature, seeded with a needle-tip of crystalline precipitate from **1)** and left undisturbed for 1 week to yield single crystals of anhydrous **4.1$_{Rac}$**.	Needle

4.2$_{Rac}$	Acetonitrile (stable)	1.5 mg of 1:1 **4.1$_{SS}$** and **4.1$_{RR}$** was dissolved in 2 mL with heat and slowly cooled from 80 °C to 50 °C over 5 days in which time needle and plate crystals formed. Crystals were stored at room temperature in the mother liquor thereafter. The needle crystals were a stable acetonitrile solvate of **4.2$_{Rac}$**.	Needle
	Acetonitrile (metastable)	Crystallised concomitantly with the stable **4.2$_{Rac}$** form.	Plate
4.3$_{Rac}$	Methanol	2.5 mg of a 1:1 **4.3$_{SS}$** and **4.3$_{RR}$** mixture was formed and dissolved in 3 mL methanol with heat. The solution was cooled to room temp and slow evaporation facilitated over 12 hours to yield single crystals of a **4.3$_{Rac}$** methanol solvate.	Plate
	Pyridine:H_2O	2 mg of a 1:1 **4.3$_{SS}$** and **4.3$_{RR}$** mixture was formed and dissolved in 1mL of pyridine with heat. The solution was then cooled to room temp and 1.5 mL water was added in 50 µL aliquots over one hour. The resulting solution was left undisturbed for 1 week, in which time crystals of a **4.3$_{Rac}$** dihydrate had grown.	Plate

What is striking about the successful crystallisation conditions are the low compound masses required to form supersaturated solutions of the bis(*acyl*-semicarbazides), particularly for the achiral compounds. This was due to their low solubility in most organic solvents, and their tendency to rapidly gel or precipitate even when soluble. The slightly higher relative solubility of the chiral compounds was anticipated, as both methylation and introducing chirality tend to increase solubility.[40,41] This is due to chirality disrupting molecular planarity, thus decreasing the efficiency of molecular packing and typically resulting in a lower crystal stability, while bulky methyl groups can cause steric hindrance that reduces packing efficiency and intermolecular hydrogen bond favourability, particularly when positioned in proximity of hydrogen bond moieties. Racemic solutions of the R,R and S,S enantiomers tended to yield crystalline powders at low concentrations and more fine-tuning of conditions were required to optimise crystal growth compared with enantiomerically pure forms. The exception to this tendency were the compounds derived from the succinic acid derived spacer (**4.3**), where the racemic form crystallised at the first attempt from methanol solutions via slow evaporation and also from pyridine/water antisolvent addition experiments, whilst single crystals of the enantiomerically pure **4.3$_{RR}$/4.3$_{SS}$** proved far more challenging to obtain.

There are a few notable cases where promising crystalline material was obtained but growing single crystals suitable for SCXRD were unsuccessful despite many attempts to optimise crystal growth conditions. Compound **4.1$_{Benz}$** crystallises as minuscule but well-defined block crystals when dissolved at concentrations as low as 1 mg in 3 mL in ethylene glycol. Crystalline needles formed from **4.4$_{Rac}$** solutions in methanol at

concentrations above 2 mg in 3 mL, but the crystalline aggregates were relatively small but seemed suitable for data collection via a synchrotron radiation source. However, the crystals diffracted poorly, and suitable diffraction data was not obtained. Miniscule needles of **4.3$_{RR}$** were also obtained by dissolving 20 mg in 200 µL of DMSO via sonication and layering the resulting sol with either octane but were too small for data collection. Finally, very fine crystalline needles of **4.5$_{Benz}$** were also obtained by dissolution in methanol, nitromethane or pyridine at concentrations between 0.1-0.5 % w/v, but again were an inadequate size or quality for SCXRD experiments. Attempts to optimise the crystallisation conditions for all these compounds, via the procedures outlined, failed to yield better quality crystals.

4.2.3 General analysis of *bis*(acyl-semicarbazide) crystal structures

All crystal structures were analysed with the primary aim to identify key hydrogen bond motifs dictating the self-assembly directionality and packing arrangements. Hydrogen bonding synthons were classified using the nomenclature proposed by Etter, Bernstein and coworkers.[42] Any potential π-π interactions were also identified due to their relatively strong nature, which could significantly influence self-assembly behaviour and may be particularly influential in the packing differences between enantiomerically pure and racemic forms. The directionality of major supramolecular interactions was documented to understand potential gelator and non-gelator behaviour, with infinite unidirectional motifs being a key feature in driving fibre formation, whilst forming a multidimensional hydrogen bond networks is indicative of non-gelator behaviour. Comparisons between the synthons and molecular packing in enantiomerically pure structures of the 1-phenyethyl terminated compounds and their racemic counterparts were made where possible. Only **4.2$_{Benz}$** was successfully crystallised of the achiral compounds but provides valuable insight into how the molecular packing and supramolecular interactions change in the absence of a methyl group. Hydrogen atoms have been hidden in all images of the crystal structures, except those involved in hydrogen bonding and those at chiral centres to enable identification of enantiomeric configuration.

Most of the crystals were weakly diffracting and required copper or synchrotron radiation sources. The quality of the diffraction data and reliability of the corresponding models were generally good with a few exceptions (**Table 4-2**). The

most notable of these was the metastable **4.2$_{Rac}$** acetonitrile solvate, which degraded within 2 minutes under synchrotron radiation. The corresponding structure was solved and refined using only the initial pre-scan runs, hence has a low data coverage and associated precision of the structure. The **4.6$_{RR}$** crystals had a well-defined hexagonal habit and had a size greater than 0.3 mm in three dimensions, which is adequate for SCXRD analysis. However, they diffracted weakly, and synchrotron radiation was required to attain useful diffraction data. Even then the absolute structure could not be reliably determined. The asymmetric unit contains six **4.6$_{RR}$** molecules and ten benzyl alcohol units with the disorder of the solvent molecules, in combination with the weak diffraction, likely contributing to the higher R_1 factor at 10.71 %. Finally, **4.2$_{RR}$** ethanol solvate structure also has a slightly higher R_1 value associated with it at 9.80 %. In this structure, the modelling of the **4.2$_{RR}$** molecules is well resolved but the absolute structure cannot be determined reliably due to the poor resolution of what appears to be a severely disordered ethanol molecule. However, these structures still provide a valuable insight to how these bis(*acyl*-semicarbazide) molecules behave, and some of the features in these structures are consistent with those exhibited in structures of the other bis(*acyl*-semicarbazides) with higher associated reliability.

Table 4-2. A summary of the crystallography data for the determined structures of the bis(acyl-semicarbazide) compounds. For solvates, the solvent abbreviation is provided in subscript after the compound code. MeOH = methanol, EtOH = ethanol, ACN = acetonitrile, Pyr = pyridine, BenzOH = benzyl alcohol, H_2O = water.

	4.1$_{RR\cdot MeOH}$	**4.1$_{Rac}$**	**4.2$_{RR\cdot EtOH}$**	**4.2$_{Rac\cdot ACN}$ (metastable)**
Formula	$C_{20}H_{24}N_6O_4$. CH_4O	$C_{20}H_{24}N_6O_4$	$C_{21}H_{26}N_6O_4$. $0.5(C_2H_6O)$	$C_{21}H_{26}N_6O_4$. $2(C_2H_3N)$
Formula weight	476.53	412.45	449.51	508.58
Crystal system	Monoclinic	Triclinic	Monoclinic	Monoclinic
Space group	$P2_1$	P-1	$P2_1$	$P2_1/c$
***a* / Å**	4.6107(3)	4.6640(7)	11.278(2)	18.450(6)
***b* / Å**	38.881(3)	12.9178(18)	4.5289(10)	9.1918(17)
***c* / Å**	6.9270(5)	17.612(2)	22.111(5)	17.257(3)
β / °	96.155(4)	87.667(3)	91.188(5)	109.148(12)
***V* / Å^3**	1234.64(15)	999.9(2)	1129.1(4)	2764.7(11)
Z* / *Z'	2 / 1	2 / 1	2 / 1	4 / 1
***D*$_{calc}$ / g cm^{-3}**	1.282	1.370	1.322	1.222
***R*$_{int}$**	0.0891	0.0545	0.2721	0.1235
***R*$_1$ [*I* ≥ 2σ (*I*)]**	0.0580	0.0672	0.0980	0.1584
***wR*$_2$ [all data]**	0.1470	0.2002	0.1897	0.4294
Goodness of fit	1.041	1.136	1.034	1.501
Radiation Source	Cu	Synchrotron	Synchrotron	Synchrotron
	4.2$_{Rac\cdot ACN}$ (stable)	**4.2$_{Benz\cdot Pyr}$**	**4.3$_{SS\cdot H2O/MeOH}$**	**4.3$_{Rac\cdot MeOH}$**
Formula	$C_{21}H_{26}N_6O_4$. $2(C_2H_3N)$	$C_{19}H_{22}N_6O_4$. $2(C_5H_5N)$	$C_{22}H_{28}N_6O_4$. CH_4O. H_2O	$C_{22}H_{28}N_6O_4$. CH_4O

Formula weight	508.58	556.61	490.56	472.54
Crystal system	Monoclinic	Monoclinic	Orthorhombic	Triclinic
Space group	C2/c	$P2_1/c$	$P2_12_12_1$	P-1
***a* / Å**	38.366(10)	31.9271(12)	7.0442(5)	7.6783(2)
***b* / Å**	4.5756(11)	9.1729(4)	9.2521(7)	12.6879(3)
***c* / Å**	15.248(4)	19.0229(7)	39.682(3)	13.4322(3)
β / °	99.235(7)	95.004(1)	90	77.5271(10)
***V* / Å^3**	2642.1(11)	5549.9(4)	2586.2(3)	1249.19(5)
Z* / *Z'	4 / 2	10 / 2	4 / 1	2 / 1
***D*$_{calc}$ / g cm^{-3}**	1.279	1.431	1.260	1.256
***R*$_{int}$**	0.0808	0.0953	0.0756	0.0413
***R*$_1$ [*I* ≥ 2σ (*I*)]**	0.0679	0.0667	0.0736	0.0375
***wR*$_2$ [all data]**	0.2036	0.1799	0.2060	0.1039
Goodness of fit	1.073	1.010	1.104	1.050
Radiation Source	Synchrotron	Mo	Synchrotron	Cu
	4.3$_{Rac\cdot H2O}$	**4.4$_{RR\cdot EtOH}$**	**4.4$_{SS\cdot MeOH}$**	**4.5$_{SS\cdot EtOH}$**
Formula	$C_{22}H_{28}N_6O_4$. H_2O	$C_{24}H_{32}N_6O_4$. $2(C_2H_6O)$	$C_{24}H_{32}N_6O_4$. $2(CH_4O)$	$C_{26}H_{28}N_6O_4$. C_2H_6O
Formula weight	458.52	560.69	532.64	534.61
Crystal system	Triclinic	Monoclinic	Monoclinic	Monoclinic
Space group	P-1	$P2_1$	$P2_1$	$P2_1$
***a* / Å**	7.6639(4)	8.2919(3)	8.2949(2)	12.9016(4)
***b* / Å**	12.9628(8)	11.3010(4)	11.1568(3)	14.9082(4)
***c* / Å**	12.9701(8)	16.6965(6)	31.5124(9)	14.5459(4)
β / °	74.054(4)	99.467(2)	92.6590(17)	93.7394(17)
***V* / Å^3**	1207.39(13)	1543.27(10)	2913.16(13)	791.80(14)
Z* / *Z'	2 / 1	2 / 1	4 / 2	4 / 2
***D*$_{calc}$ / g cm^{-3}**	1.261	1.207	1.214	1.272
***R*$_{int}$**	0.1027	0.0894	0.0776	0.0497
***R*$_1$ [*I* ≥ 2σ (*I*)]**	0.0536	0.0571	0.0490	0.0431
***wR*$_2$ [all data]**	0.1365	0.1464	0.1263	0.1058
Goodness of fit	1.006	1.038	1.214	1.011
Radiation Source	Cu	Cu	Cu	Cu

	4.6$_{RR\cdot BenzOH}$
Formula	$C_{26}H_{28}N_6O_4$). 1.66(C_7H_8O)
Formula weight	668.062
Crystal system	Trigonal
Space group	$P3_2$
***a* / Å**	25.693(3)
***b* / Å**	25.693(3)
***c* / Å**	29.576(3)
β / °	90°
***V* / Å^3**	16909(3)
Z* / *Z'	18 / 6
***D*$_{calc}$ / g cm^{-3}**	
***R*$_{int}$**	0.1823
***R*$_1$ [*I* ≥ 2σ (*I*)]**	0.1071
***wR*$_2$ [all data]**	0.2832
Goodness of fit	1.292
Radiation Source	Synchrotron

Pitucha et al. have previously reported that the *acyl*-semicarbazide functionality exists in several tautomeric forms due to the migration of protons from NH to the carbonyl

oxygen atoms, with the most stable tautomer typically being the keto-keto tautomer.[43] All the crystal structures in this study exclusively exhibit this keto-keto tautomer, with all the C=O bond lengths in each structure being 1.20-1.25 Å in length (**Table 4-3**), which is consistent with previously reported C=O bond lengths.[44] A bond length around 1.4 Å is typical for a Csp_3–OH bond and should be observed if any of the other tautomeric forms were present. Indeed, the Csp_3–OH bond lengths in alcohol units in the solvated bis(*acyl*-semicarbazide) structures are typically around 1.4 Å. All the structures also exhibit conjugation of the semicarbazide functionality, with representative N–N bond and C(O)–N bonds lengths of 1.390 Å and 1.340 Å respectively, which are an intermediate length between those of single and double N–N/C(O)–N bonds. This is further evidence of the partial double bond character responsible for the restricted rotation around the amide bonds. The exception to these findings is the metastable **4.2$_{Rac}$** acetonitrile solvate, where the bond lengths are less reliable due to the limited diffraction data.

Table 4-3. Tabulated bond lengths (Å) of C=O$_{a-d}$ in all the bis(acyl-semicarbazide) structures and Csp_3–OH lengths in incorporated solvent molecules. (a)-(j) is used to distinguish between molecules of the sa\me species where more than one is present in the asymmetric unit cell.

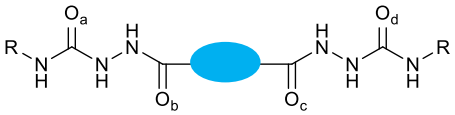

Structure	C=O$_a$	C=O$_b$	C=O$_c$	C=O$_d$	Solvent Csp_3–OH
4.1$_{RR•MeOH}$	1.245(9)	1.22(1)	1.23(1)	1.243(9)	(a) 1.43(1); (b) 1.435(9)
4.1$_{Rac}$	1.243(2)	1.214(2)	1.209(2)	1.238(2)	N/a
4.2$_{RR•EtOH}$	1.2577	1.2260	1.2466	1.2088	1.6747
4.2$_{RR•ACN}$	1.19(2)	1.17(2)	1.21(2)	1.27(2)	N/a
4.2$_{Rac•ACN}$	1.235(2)	1.227(2)	1.227(2)	1.235(2)	N/a
4.2$_{Benz•Pyr}$	(a) 1.233(2); (b) 1.234(2)	(a) 1.218(2); (b) 1.221(2)	(a) 1.220(2); (b) 1.220(2)	(a) 1.233(2); (b) 1.235(2)	N/a
4.3$_{SS•MeOH}$	1.235(3)	1.226(4)	1.224(4)	1.228(5)	1.450(7)
4.3$_{Rac•H2O}$	1.244(3)	1.232(3)	1.244(3)	1.241(3)	N/a
4.3$_{Rac•MeOH}$	1.238(2)	1.227(2)	1.235(2)	1.230(2)	1.413(2)
4.4$_{RR•MeOH}$	(a) 1.236(4); (b) 1.231(4)	(a) 1.239(4); (b) 1.237(4)	(a) 1.241(4); (b) 1.237(4)	(a) 1.227(4); (b) 1.231(4)	(a) 1.414(6); (b) 1.420(6); (a) 1.426(5); (b) 1.425(5)
4.4$_{SS•EtOH}$	1.231(6)	1.235(7)	1.234(7)	1.235(6)	(a) 1.418(6); (b) 1.44(1)
4.5$_{SS•EtOH}$	(a) 1.243(4); (b) 1.234(4)	(a) 1.225(4); (b) 1.232(4)	(a) 1.224(4); (b) 1.228(4)	(a) 1.234(4); (b) 1.246(4)	(a) 1.447(6); (b) 1.440(5)
4.6$_{RR•BnOH}$	(a) 1.2337 (b) 1.2370 (c) 1.2177 (d) 1.2340 (e) 1.2445 (f) 1.2337	(a) 1.2088 (b) 1.2265 (c) 1.2291 (d) 1.2485 (e) 1.2368 (f) 1.2567	(a) 1.2399 (b) 1.2523 (c) 1.2402 (d) 1.2438 (e) 1.2356 (f) 1.2237	(a) 1.2124 (b) 1.2214 (c) 1.2320 (d) 1.2878 (e) 1.2449 (f) 1.2180	(a) 1.4584; (b) 1.4111; (c) 1.4245; (d) 1.4169; (e) 1.3968; (f) 1.4424; (g) 1.4205; (h) 1.4703; (i) 1.4396; (j) 1.4326

4.2.4 Molecular conformations in the solid-state

The molecular conformation of the bis(acyl-semicarbazides) is largely dictated by the spacer group nature and flexibility. The amide groups were observed to be in the typically favourable *trans* conformation with a **C**(O)$_{amide}$-**N**-**N**-**C**(O)$_{urea}$ torsion angle between 60-90 ^{o} in all the structures reported here, which is consistent with the previous observations by Fusco *et al.*[45] This arrangement of the acyl-semicarbazide functionalities is adopted as it minimises repulsion of the nitrogen lone pairs. The rigid aromatic-spaced bis(acyl-semicarbazides) were observed in a single conformation, in which the amide groups lie planar to the central aromatic spacer with urea groups in the *anti-anti* conformation and orientated 85 ^{o} to the amide plane (**Figure 4-19**).

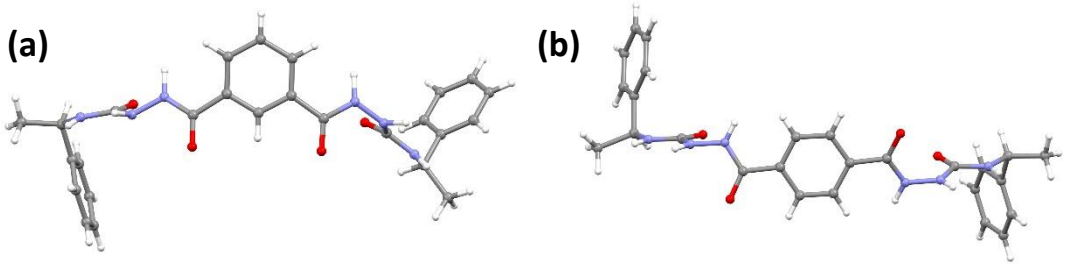

Figure 4-19. The molecular conformations of **(a)** isophthalic-spaced **4.5$_{RR}$** and **(b)** terephthalic-spaced **4.6$_{SS}$**. Both structures exhibit urea groups in the *anti-anti* conformation and orientated at 85 ^{o} to the adjacent amide group, which lie essentially planar to the aromatic ring.

The flexibility afforded by the aliphatic-spacers resulted in two types of conformation being observed for aliphatic-spaced bis(acyl-semicarbazides). The flexibility of these aliphatic-spaced compounds increases with the number of methylene units (n), with n=0 possessing a high rigid diamide core, whilst n=4 possess a relatively high degree of flexibility. It is known that flexible molecules do not necessarily adopt the global minimum conformation in the solid state and high energy conformations may be adopted if they significantly increase the accessible surface area for favourable intermolecular interactions to form.[46] One conformation observed is an extended conformation, whereby the hydrophilic core forms a linear chain with the hydrophobic end groups extending outwards at opposing ends of the molecule (**Figure 4-20**). This conformation is adopted by molecules in the structures of **4.1$_{RR}$**, **4.2$_{Benz}$**, **4.2$_{RR}$**, **4.4$_{RR}$**, **4.4$_{SS}$** and the stable **4.2$_{Rac}$** acetonitrile solvate. In these structures, both urea groups are in the *anti-anti* conformation with the relative orientation of urea groups being determined by number of methylene units in the spacer (n) with an odd-even effect observed. In molecules with no methylene spacer (n=0) or where n is even (n= 4), the

urea groups are oriented antiparallel to one another, whilst the urea groups are parallel where n is odd (n=1). It is worth noting the highly rigid nature of spacer **4.1** (n=0). Indeed, oxalyl dihydrazide (**4.1**) is highly polymorphic with five identified packing polymorphs with SCXRD structures all exhibiting the same all-*trans* conformation but distinct hydrogen bond synthons.[47–49] The rigidity of this core coupled with the preference for a **C**(O)$_{amide}$-**N**-**N**-**C**(O)$_{urea}$ torsion angle between 60-90 °[45] likely reduces the likelihood of conformational polymorphs of **4.1**-derived bis(acyl-semicarbazides). Meanwhile, the longer aliphatic spacers may be more likely to exhibit conformational polymorphism due to the flexible nature of aliphatic chains.

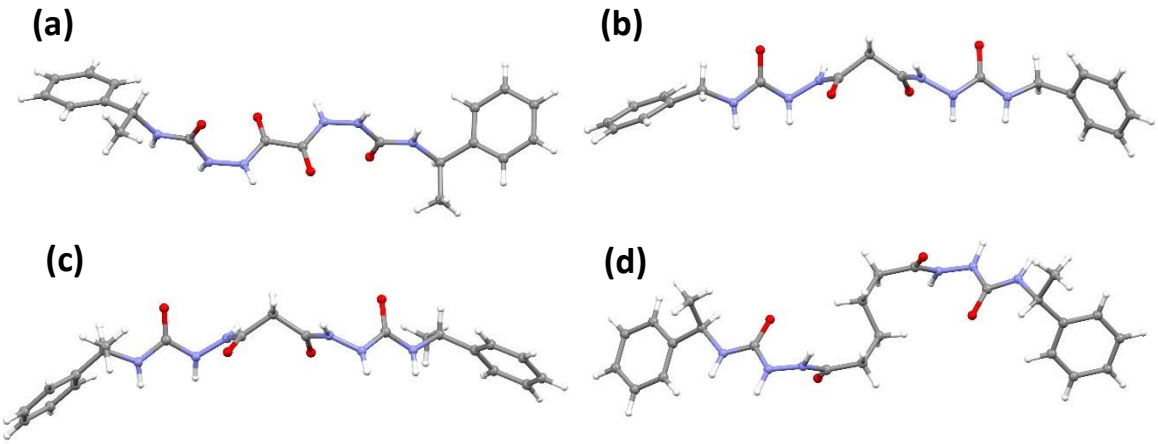

Figure 4-20. Extended molecular conformations in **(a) 4.1$_{RR}$** methanol solvate, **(b) 4.2$_{Benz}$** pyridine solvate, **(c) 4.2$_{RR}$** ethanol solvate and **(d) 4.4$_{SS}$** methanol solvate. Urea groups are orientated parallel to each other where the number of methylene spacers is odd (n=1), whilst they are antiparallel where n is even (n=0 or 4). Amide and urea groups are orientated between 60-90 ° to each other.

The second general conformation observed is a folded conformation, where an intramolecular hydrogen bond forms between the semicarbazide moieties and the two hydrophobic end groups are in proximity with each other, resulting in a single hydrophobic surface (**Figure 4-21**). This conformation was the only observed conformation adopted by **4.3$_{RR/SS}$** and was also observed in the metastable **4.2$_{Rac}$** acetonitrile solvate. Molecules in this conformation exhibit one urea group in the *anti-anti* conformation and the other in the *anti-syn* conformation. An intramolecular hydrogen bond between the *anti*-NH from the *anti-syn* urea and an amide carbonyl oxygen atom forms an S(9) and an S(10) motif in molecules derived from **4.2** and **4.3** respectively. The *anti-syn* urea conformation has rarely been observed in compounds with the **N**–**N**–**C**(O)–**N** covalent sequence. Indeed, a search of the CSD for structures

with a similar torsion angle for this atomic sequence found only two structures with similar torsion angles between 12-24 ° (CSD refcodes ZINCEG and XAYSUL), whilst 53 other structures had a torsion angle of 148-178 ° which is the typical range for the anti-anti urea conformer (**Figure 4-22**). Interestingly, the compound in XAYSUL was a relatively versatile gelator.

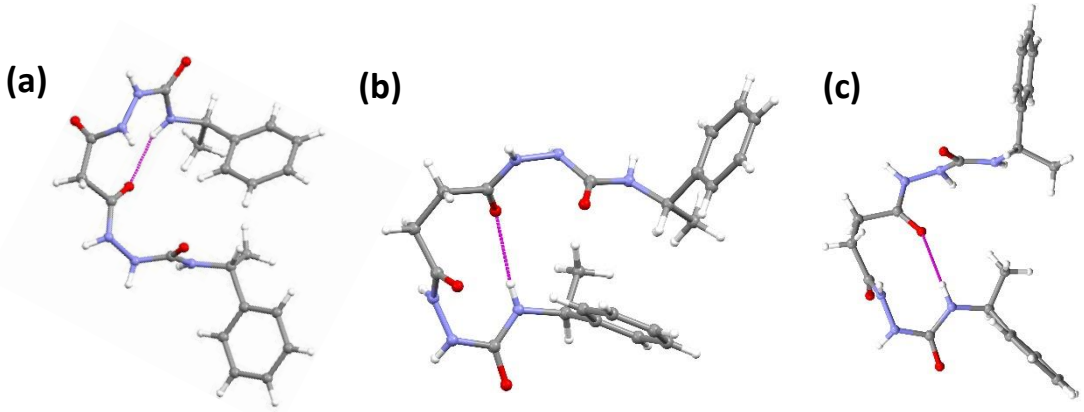

Figure 4-21. Molecular conformations in **(a)** the metastable acetonitrile solvate of **4.2Rac**, **(b)** solvate of **4.3$_{SS}$** and **(c)** hydrate of **4.3$_{Rac}$**. Molecules in these structures exhibit one *anti-anti* urea conformer and one *anti-syn* urea conformer. The bent conformations are facilitated by an S(9) and S(10) motif (in pink) between urea NH and amide carbonyl in compounds derived from **4.2** and **4.3** respectively.

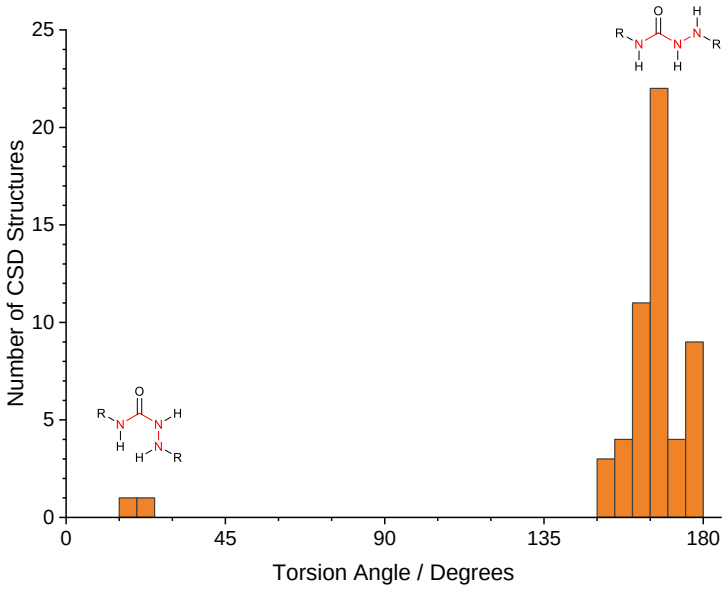

Figure 4-22. The N-N-C(O)-N torsion angles in all 55 CSD structures with this sequence of atoms. The majority have torsion angles between 150-180 ° and correspond to the *anti-anti* urea conformation. Only two previously reported structures have a torsion angle between 15-25 ° for this atom sequence, with both exhibiting an *anti-syn* urea. The relevant torsion angle is highlighted in red in the chemical diagrams.

The S(9) motif in **4.2$_{Rac}$** appears to be less favourable and was only observed in the highly metastable polymorph, with the extended conformation observed in stable **4.2$_{Rac}$** polymorph and homochiral **4.2$_{RR}$** structure. The two **4.2$_{Rac}$** acetonitrile disolvate polymorphs crystallised concomitantly, indicating that the folded conformation

observed in the metastable form is long-lived in solution and slowly converts to the stable extended conformation, possibly due to the restricted rotation around the acyl-semicarbazide functionalities. However, the S(10) motif adopted by derivatives of **4.3** appears to be more favourable and the folded conformer is exclusive in the three crystal structures containing **4.3$_{RR}$** or **4.3$_{SS}$** molecules. Indeed, the geometry of the intramolecular hydrogen bond is more favourable in **4.3$_{SS}$** than in molecules in the **4.2$_{Rac}$** structure, with respective angles of N-H···O 173 º and 156 º and C=O···N 137.4 º and 129.5 º, despite the interatomic distance between N···O being slightly longer due to the additional methylene spacer in **4.3** (N···O 3.13 Å and 2.88 Å in **4.3$_{SS}$** and **4.2$_{Rac}$** respectively). An S(10) motif was also identified in CSD structure ZINCEG, which is the only other crystal structure of a molecule where the amide oxygen atom is connected to a urea proton via 8 other atoms. This suggests that the folded conformation is stable in the solid-state for derivatives of **4.3**. The flexibility and length of the spacer core is key in enabling formation of this folded conformation. Compounds derived from spacer **4.1** (n=0) have a highly rigid diamide core and the extended rod conformation observed is anticipated to be highly favourable based on basic steric and electrostatic arguments. Meanwhile, the extended chain length of **4.4** increases the entropic penalty for intramolecular bond formation, meaning intermolecular interactions in the solid-state are more likely to overcome intramolecular hydrogen bonds.

Structures of acyl-semicarbazides with the identical spacers to those employed here have rarely been reported. However, one other acyl-semicarbazide structure reported in the CSD exhibits molecules with an identical adipic spacer group to **4.4** (CSD refcode FAVTOO). The adipic spacer in the **4.4$_{RR}$** structure and in FAVTOO adopts an extended anti-conformation with **C**H$_2$-**C**H$_2$-**C**H$_2$-**C**H$_2$ torsion angle of 175 º and 180 º respectively. However, the **C**(O)-**C**H$_2$-**C**H$_2$-**C**H$_2$ torsion angles differ between the two structures, with representative measurements of 66.13 º (*gauche*-conformation) and 178.34 º (*anti*-conformation) in **4.4$_{RR}$** and FAVTOO respectively. These slight differences in spacer conformation demonstrates how slight conformational adjustments of the central space group can be adopted to form more favourable intermolecular interactions, which may be influenced by the end group. This flexibility also increases the likelihood of conformational polymorphism.

A tenuous correlation between crystal habit and molecule conformation/packing behaviour is also observed here. Crystal forms exhibiting the linear conformations all crystallised with a needle habit, whilst crystals forms with the folded conformation all crystallised as plates. Sonication of supersaturated DMSO **4.3$_{RR}$** or **4.3$_{SS}$** solutions, prior to layering with octane, resulted in semi-crystalline needles growing within hours as opposed to crystalline plates. The PXRD pattern of the needles revealed very few diffraction peaks, however the peaks that were observed do not match the diffraction pattern for the plates (**Figure 4-23**). This indicates a different molecular packing arrangement in both crystalline forms which may be due to a conformational change induced by sonication breaking the intramolecular hydrogen bond, although this is speculative. Further attempts to isolate a single crystal of the needle form or obtain enough material of the crystalline plates for ss-NMR analysis to compare molecular conformations in each form were unsuccessful.

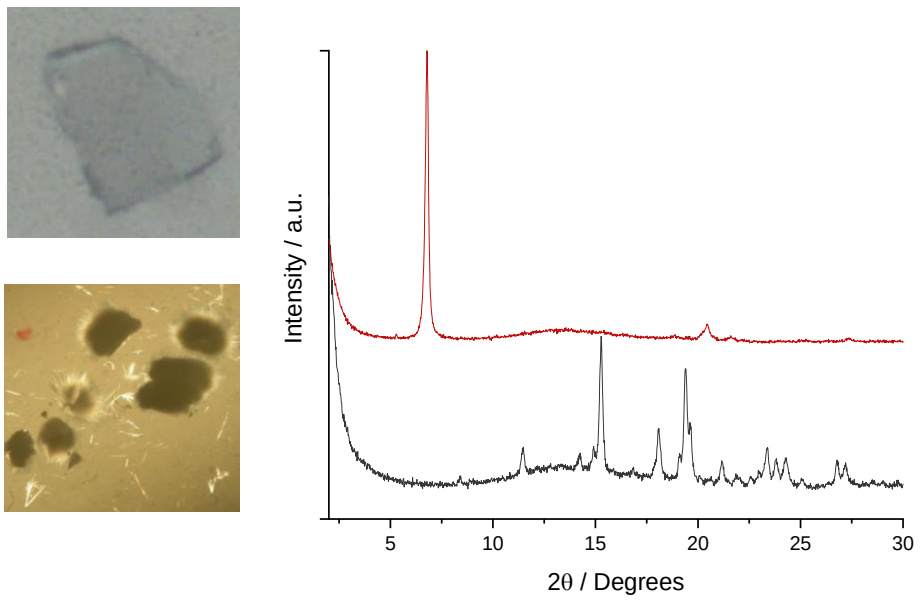

Figure 4-23. Optical microscopy photographs of the plates and semi-crystalline needles obtained of **4.3$_{SS}$** and **4.3$_{RR}$** respectively. PXRD patterns of the plates (black) and the semi-crystalline needles (red) are different. There are few diffraction peaks in the pattern of the needles, but the peaks at 6.7° and 20.4°are not present in the pattern for the plates. Meanwhile, none of the peaks in the pattern for the plates are observed in the corresponding needle pattern.

4.2.5 Assembly of extended aliphatic-spaced conformers

All the structures exhibiting aliphatic-spaced molecules in the linear conformation reveal molecules assembling via intermolecular $R_2^1(6)$ synthons between urea groups

(**Figure 4-24**). These interactions assemble into infinite unidirectional tapes throughout the lattice to form molecular stacks with hydrophobic end groups shielding a hydrophilic core, which is typical of amphiphile assembly. The $R_2^1(6)$ motifs in all **4.1**/**4.2** structures are symmetrical, with both N-H···O interactions having a near identical interatomic distance and geometry. In the **4.4$_{RR/SS}$** solvates, the urea tape is slightly different with one urea N-H forming a stronger hydrogen bond (N···O 2.80 Å, N-H···O 165 °) with the urea oxygen atom than the other urea N-H, which forms weaker hydrogen bonds with both urea and amide oxygen atoms (N···O$_{(urea)}$ 3.11 Å, N-H···O$_{(urea)}$ 134 °; N···O$_{(amide)}$ 3.13 Å, N-H···O$_{(amide)}$ 143 °). The odd-even spacer effect is observed with molecules derived from **4.2** (n=1) assembling via two parallel urea tapes, whilst those derived from **4.1** and **4.4** (n = 0 and 4 respectively) form antiparallel urea tapes. Interestingly, the urea stacks in racemic structures are homochiral with urea tapes forming exclusively between like enantiomers.

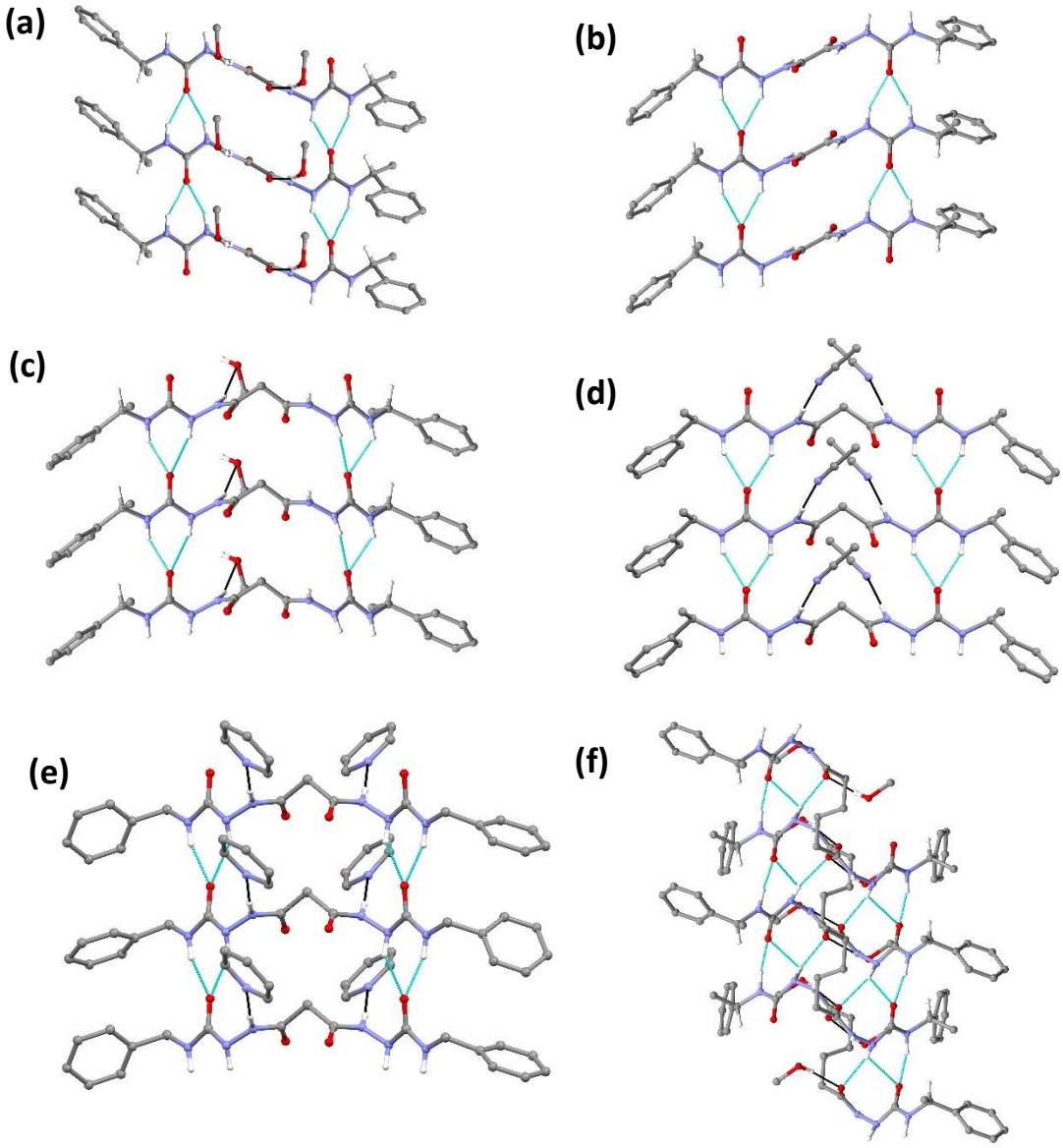

Figure 4-24. Urea tape synthons in **(a) 4.1$_{RR}$** methanol solvate, **(b) 4.1$_{Rac}$** anhydrous form, **(c) 4.2$_{RR}$** ethanol solvate, **(d) 4.2$_{Rac}$** stable acetonitrile solvate, **(e) 4.2$_{Benz}$** pyridine solvate and **(f) 4.4$_{SS}$** methanol solvate.

The amide groups in all these structures, except for the anhydrous **4.1$_{Rac}$** structure, form hydrogen bonds with solvent molecules (**Figure 4-25**). In the solvates of **4.1$_{RR}$** and **4.4$_{SS}$** the amide N-H forms $C_2^2(6)$ synthons via N–H···O–H···O(C) hydrogen bonds with alcohol hydroxyl groups. Meanwhile, finite N–H···N hydrogen bonds between amide N–H and nitrogen atoms in acetonitrile and pyridine are observed in the stable **4.2$_{Rac}$** and **4.2$_{Benz}$** solvates respectively. Due to the orientation of the amide groups, these interactions form perpendicular to the urea tape and result in solvent molecules entrapped between adjacent urea stacks. Both amide groups in each molecule form identical interactions in all these structures.

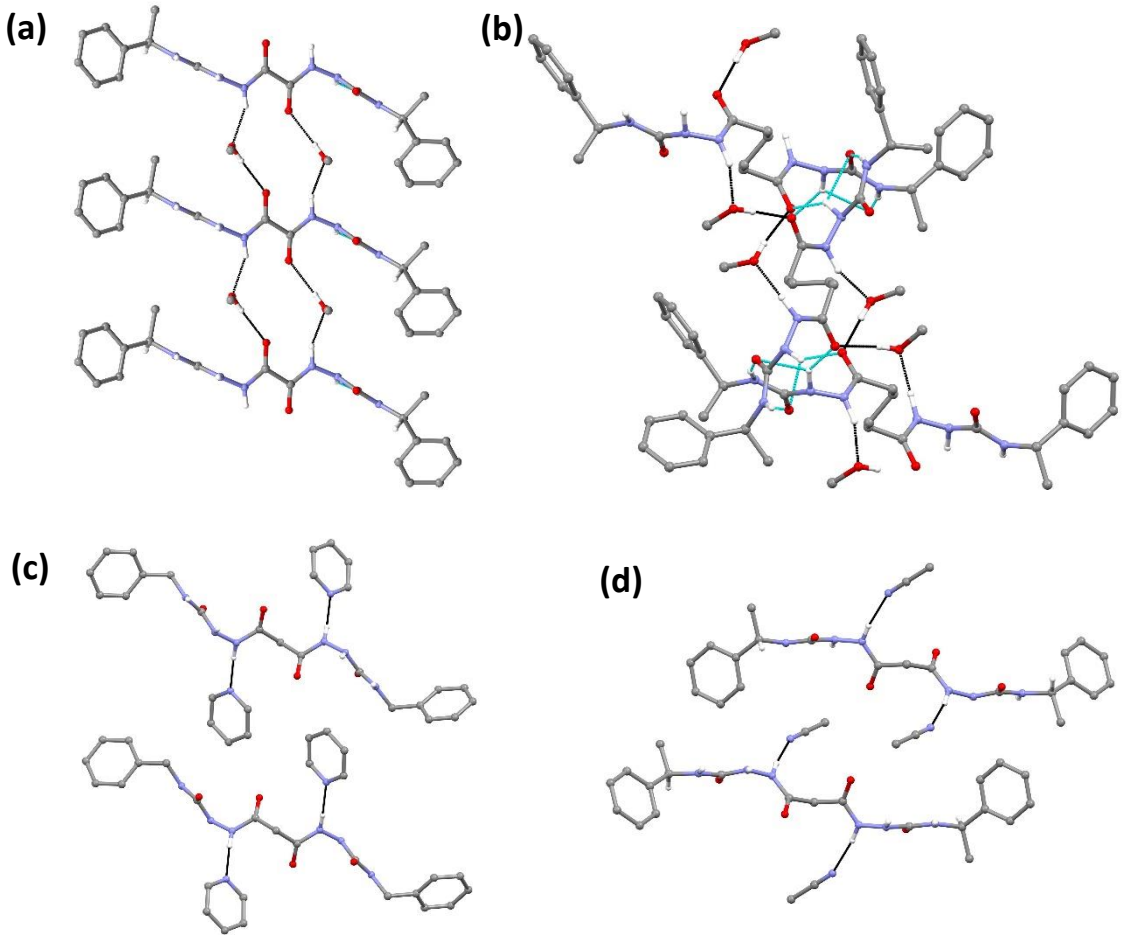

Figure 4-25. Infinite $C_2^2(6)$ synthons (in black) between bis(acyl-semicarbazide) amide functionalities and methanol in **(a) 4.1$_{RR}$** and **(b) 4.4$_{SS}$** methanol solvates. Finite N–H$_{(amide)}$···N$_{(solvent)}$ hydrogen bonds (in black) between **(c) 4.2$_{Benz}$** and pyridine, and **(d)** a **4.2$_{SS}$** molecule and acetonitrile in the stable **4.2$_{Rac}$** acetonitrile solvate. All structures are viewed in the axis of the urea tape.

The **4.2$_{RR}$** ethanol solvate also reveals finite hydrogen bonds between amide N-H and the ethanol oxygen atom, however only one amide NH proton per molecule interacts with ethanol. The other amide proton forms an intermolecular hydrogen bond with an amide oxygen atom from a molecule in an adjacent urea stack. These hydrogen bonds form $C_2^2(6)$ synthons that form a zipper between the two urea stacks (**Figure 4-26**). This results in ethanol molecules being entrapped between alternate urea stacks and is not observed in any of the previously reported structures in the CSD.

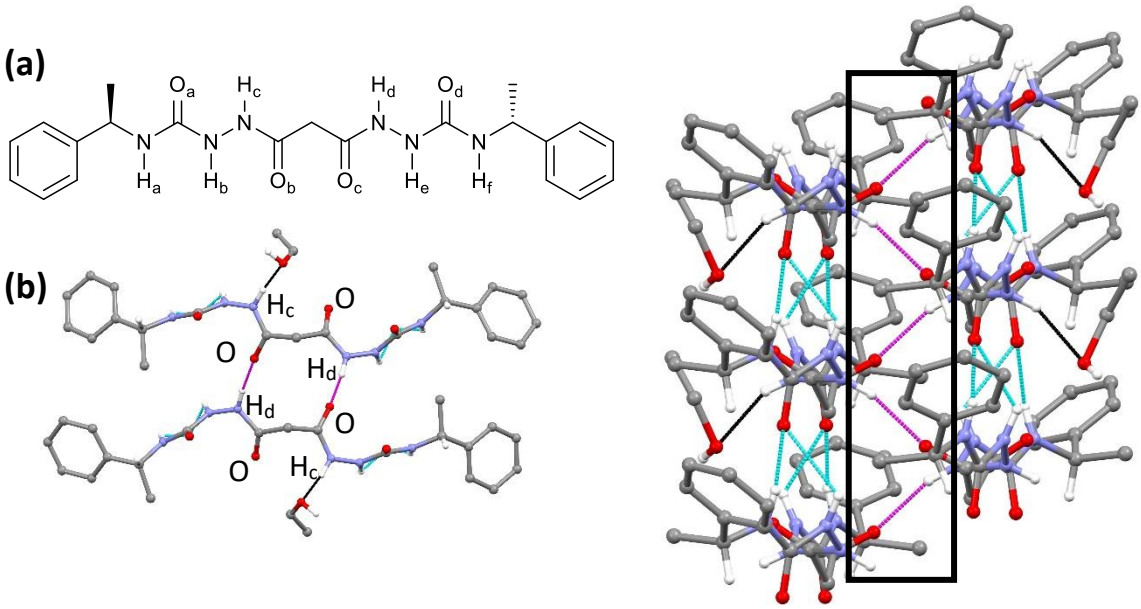

Figure 4-26. (a) Chemical diagram of **4.2$_{RR}$** with labelled hydrogen bond donors and acceptors. **(b)** The finite N–H$_c$···O$_{(EtOH)}$ hydrogen bond (in black) and N–H$_d$···O$_b$ hydrogen bond (in pink). **(c)** The N–H$_d$···O$_b$ hydrogen bonds are observed as $C_2^2(6)$ synthons (in pink) that form a supramolecular zipper between two adjacent urea stacks in the same direction as the urea tape (in light blue). These synthons form between every other urea-stack pair, with ethanol molecules lying between other adjacent urea stacks.

The anhydrous **4.1$_{Rac}$** structure exhibits significantly different amide hydrogen bonding to the other structures. Here the urea carbonyl oxygen is a trifurcated acceptor with $R_2^2(10)$ synthons forming via N–H$_{(amide)}$···O$_{(urea)}$ hydrogen bonds (N···O 3.17 Å, D-H···A 167 °), in addition to the urea tape (**Figure 4-27**). These are identical to interactions observed in CSD refcode XAYSOF, which was reported as a non-gelator in a gelation study. These interactions lie perpendicular to the urea tape and form exclusively between molecules of opposite enantiomeric form.

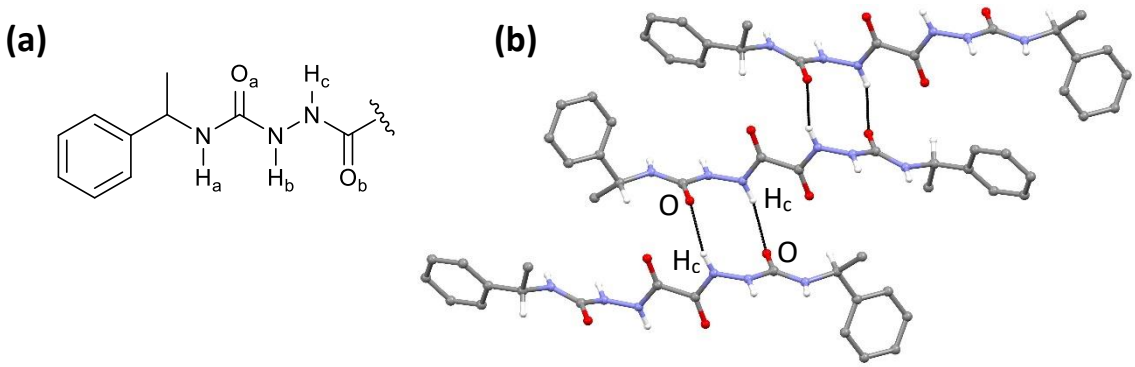

Figure 4-27. (a) Generic labelling scheme for bis(acyl-semicarbazides) where both halves of the molecules are involved in identical interactions. **(b)** Structure of **4.1$_{Rac}$** as viewed in the urea axis revealing $R_2^2(10)$ synthons (in black) forming between adjacent **4.1$_{RR}$** and **4.1$_{SS}$** molecules via N-H$_c$···O$_a$ hydrogen bonds.

4.2.6 Assembly of folded aliphatic-spaced conformers

When molecules adopt an anti-syn urea conformation, urea tape formation is less likely and alternative motifs typically form. This is the case with the aliphatic-spaced compounds that adopt the folded conformation. The structures of these compounds reveal molecules packing core to core to form bilayers (**Figure 4-28**). Like the urea stacks previously discussed, these lamellae all exhibit hydrophobic 1-phenylethyl end groups at the surface which protect a hydrophilic core of acyl-semicarbazide moieties. The hydrogen bond synthons driving these assemblies are different in each structure, but infinite chains or tapes are observed in 2-dimensions in each, which offers a slightly tenuous explanation for the 2D-plate morphology of these crystal forms.

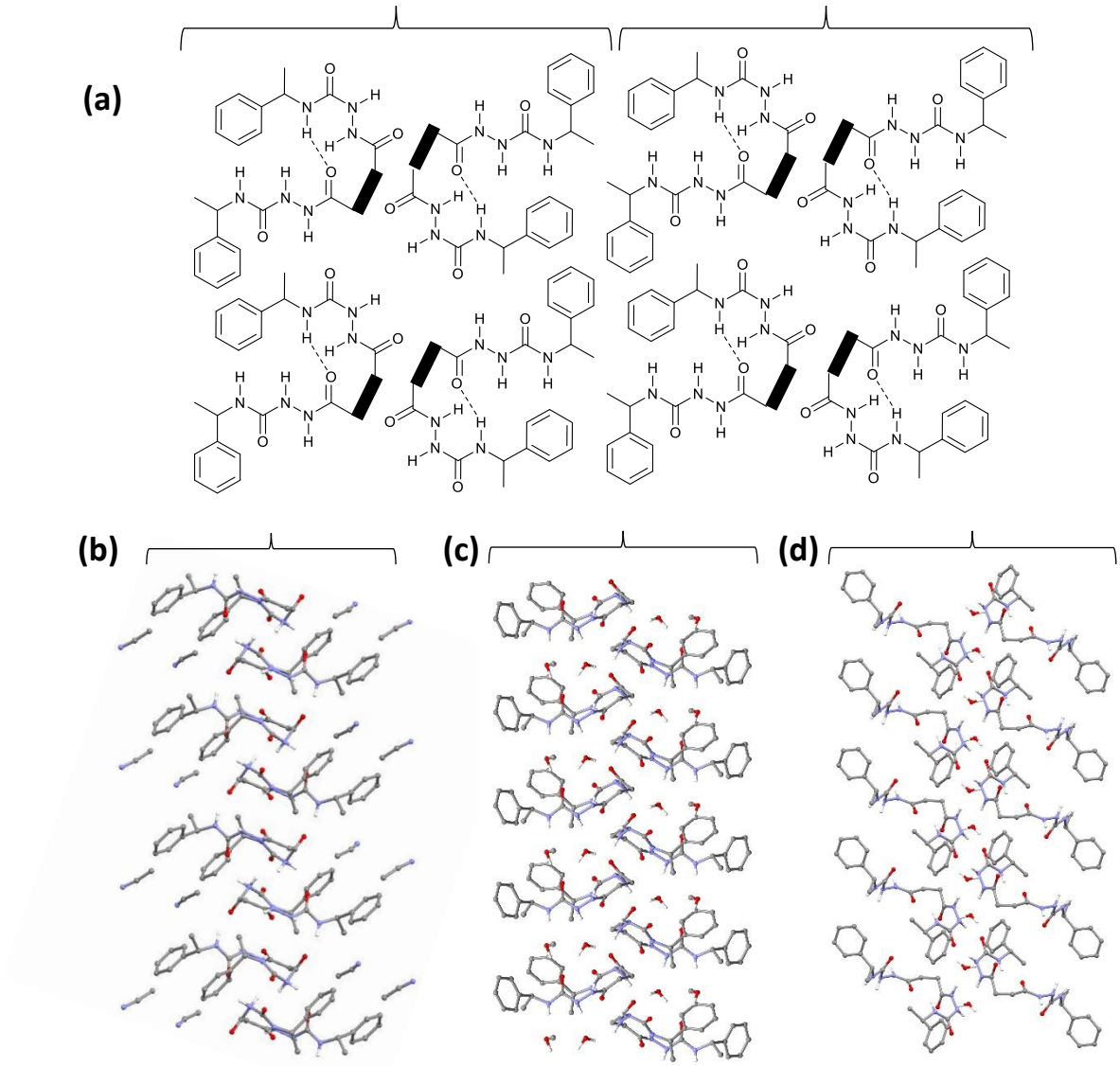

Figure 4-28. (a) A representation of the general molecular packing arrangement observed in all bis(acyl-semicarbazides) in the folded conformation. Spacer groups are represented by black bars. Molecules assemble core to core, with their aromatic end groups orientated in opposing directions to form lamellae with hydrophobic surfaces and a hydrophilic core. Images of these lamellae are shown in **(b)** the metastable **4.2$_{Rac}$** acetonitrile solvate, **(c) 4.3$_{SS}$** solvate and **(d) 4.3$_{Rac}$** hydrate. The intermolecular hydrogen bonding differs in each structure.

In the **4.3$_{SS}$** solvate, molecules pack together along the a-axis via $R_4^3(10)$ hydrogen bond motifs, which are essentially infinite α-tapes propagated by the hydrogen bond donors and acceptors in a water and methanol molecule (**Figure 4-29**). Furthermore, $R_2^2(12)$ synthons form via N-H$_c$···O$_b$ (N···O 2.86 Å, D-H···A 133°) and N-H$_b$···O$_c$ (N···O 2.88 Å, D-H···A 143 °) hydrogen bonds and present as an infinite twisted helix of hydrogen bonds with the same directionality as the $R_4^3(10)$ tape. The structure also exhibits intermolecular hydrogen bonds between amide NH$_d$ and urea O$_a$ (N···O 2.76 Å,

N-H···O 169 º), which results in infinite $C_2^2(8)$ synthons comprising of alternating intermolecular-intermolecular hydrogen bonds and drives assembly along the b-axis.

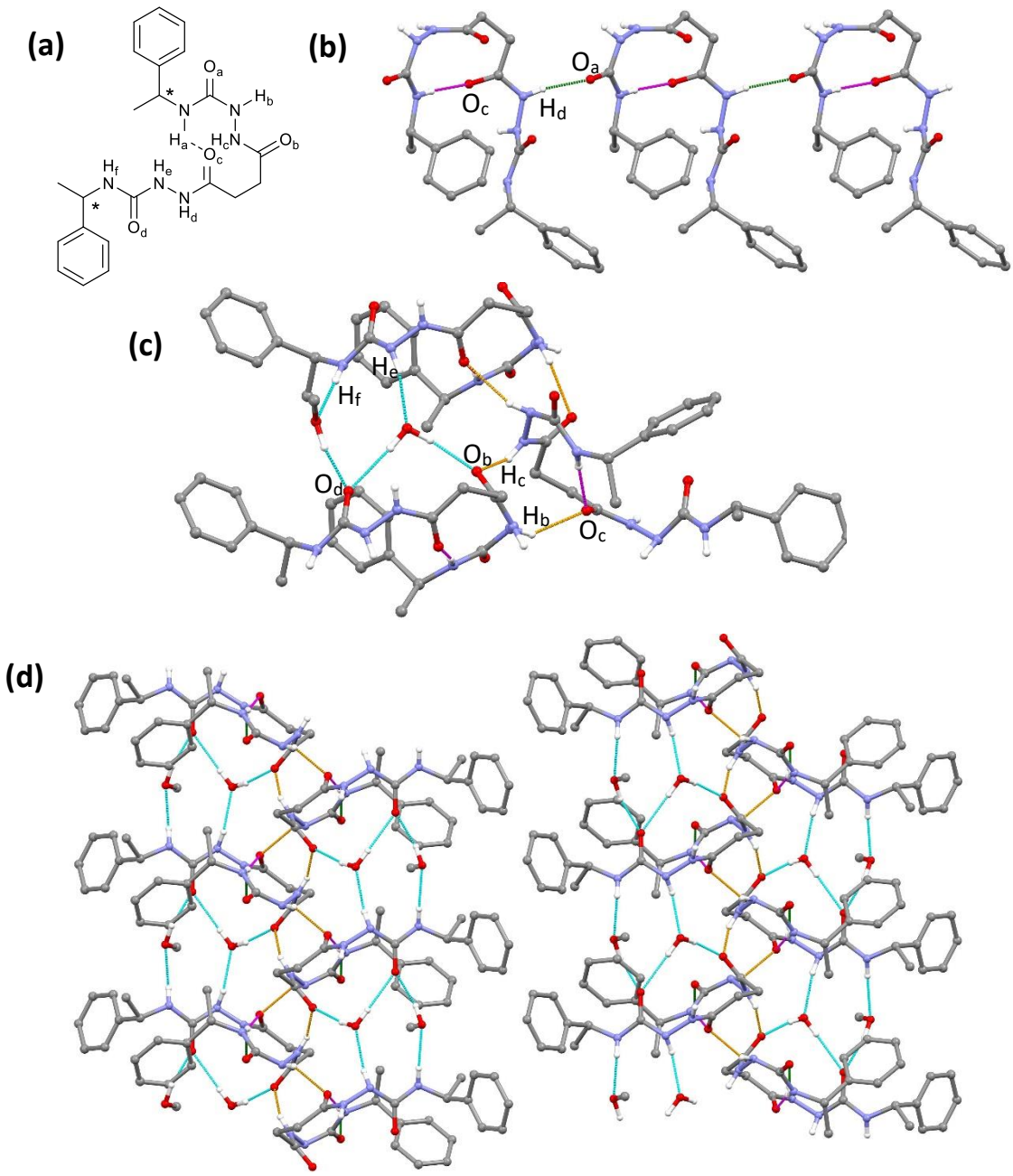

Figure 4-29. (a) Chemical diagram of **4.3$_{SS}$** with label hydrogen bond donors and acceptors. **(b)-(d)** images of the hydrogen bond motifs revealed in the crystal structure of **4.3$_{SS}$. (b)** Chains of alternating intra- and intermolecular hydrogen bonds (shown in pink and green respectively), promote assembly in the axis. **(c)** $R_4^3(10)$ (in blue) and $R_2^2(12)$ (in orange) hydrogen bond motifs are also present in the structure. **(d)** The two ring motifs form infinite tapes and twisted ribbons that promote assembly of lamellae in the a-axis.

The two **4.3$_{Rac}$** structures exhibiting near identical molecular packing and supramolecular synthons (**Figure 4-30**). In these structures, **4.3$_{SS}$** and **4.3$_{RR}$** molecules assemble into heterochiral dimers via two $R_2^2(11)$ synthons facilitated by N–H_f···O_b (N···O 2.95 Å, D-H···A 160 °) and N-H_e···O_c (N···O 2.93 Å, D-H···A 176 °) hydrogen bonds. Adjacent pairs of dimers assemble along the a-axis via $R_2^2(10)$ motifs, formed by NH_d···O_d interactions (N···O 2.83 Å, D-H···A 172 °). The combination of $R_2^2(11)$ and $R_2^2(10)$ alternate throughout the structure as infinite tapes in the *a*-axis to form lamellae. Assembly of these layers along the a-axis is further promoted by unidimensional $C_2^2(7)$ motifs, comprising of NH_c···$O_{MeOH/H2O}$ and $OH_{MeOH/H2O}$···O_a interactions that entrap solvent molecules between adjacent lamellae. Molecules in adjacent lamellae interact in the *b*-axis via dimeric $R_2^2(8)$ synthons consisting of two NH_b···O_a interactions (N···O 2.96 Å, D-H···A 171 °). There is no hydrogen bonding observed in the *c*-axis.

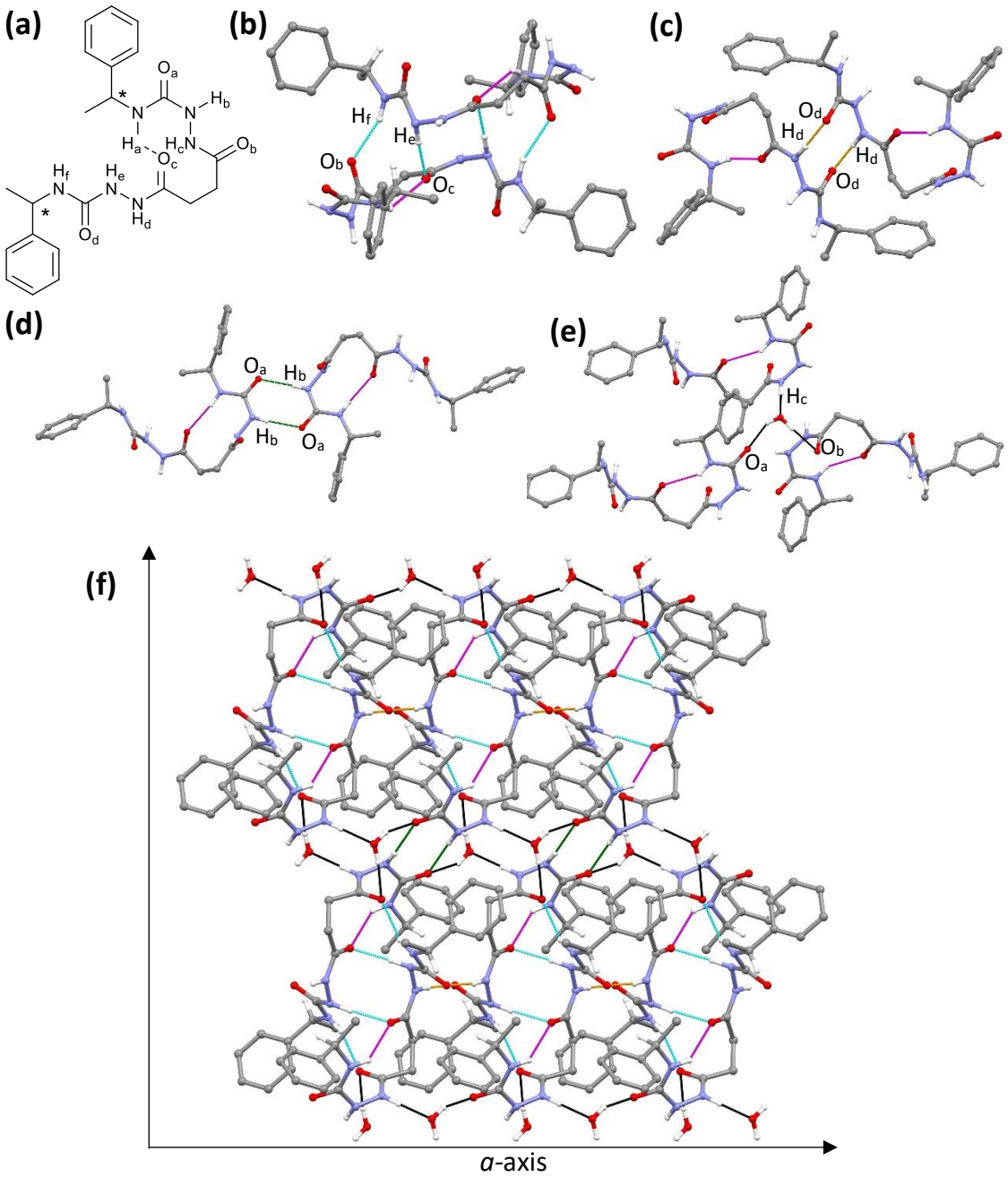

Figure 4-30. (a) Chemical diagram of **4.3$_{Rac}$** with labelled hydrogen bond donors and acceptors. **(b)** Two $R_2^2(11)$ motifs (in light blue) form heterochiral dimers via $NH_f\cdots O_b$ and $NH_e\cdots O_c$ interactions. **(c)** Another heterochiral dimer forms via $R_2^2(10)$ motifs (in orange) comprising of two $NH_d\cdots O_d$ hydrogen bonds. **(d)** $R_2^2(8)$ motifs (in orange) form heterochiral dimers form via $NH_b\cdots O_a$ hydrogen bonds. **(e)** Water molecules interact with three bis(acyl-semicarbazide) molecules, accepting a hydrogen bond from NH_c from one molecule and forming hydrogen bonds with O_a and O_b in two other molecules (all in black). **(f)** Viewing the lattice in the *c*-axis shows how the hydrogen bond synthons drive assembly in the *a*- and *b*-axis. There are no hydrogen bonds in the *c*-axis. The intramolecular S(10) hydrogen bond is shown in pink in each image.

In the metastable **4.2$_{Rac}$** acetonitrile solvate, $R_2^2(13)$ hydrogen bond motifs form between identical enantiomers, via $NH_c\cdots O_a$ and $NH_b\cdots O_d$ hydrogen bonds, to form homochiral molecular columns in the b-axis (**Figure 4-31**). These dimer pairs interact with molecules of the opposite enantiomeric form in the c-axis via $R_2^2(18)$ motifs formed via dimeric $N\text{-}H_f\cdots O_b$ interactions. This results in alternating homochiral columns of R,R and S,S molecules. Interestingly, the structure reveals large pores between columns filled with acetonitrile molecules that are incorporated into the structure via weak electrostatic interactions and no hydrogen bonds. This may explain the metastable nature of this form as any loss of this weakly bound solvent will result in large pores in the structure, which consequently could result in collapse of the lattice.

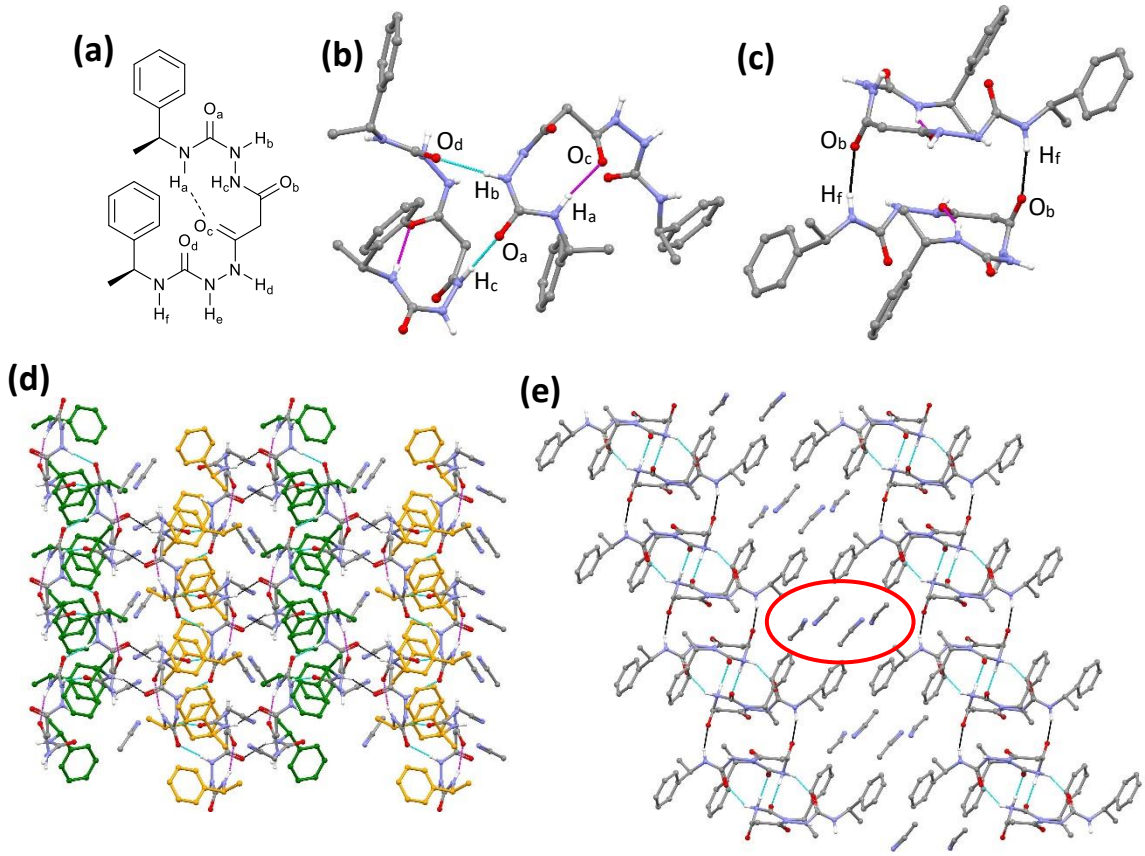

Figure 4-31. (a) Chemical diagram of **4.2$_{Rac}$** with labelled hydrogen bond donors and acceptors. **(b)** $R_2^2(13)$ motifs (in light blue) for between identical enantiomers and **(c)** $R_2^2(18)$ motifs synthons form between molecules of the opposite enantiomeric form. **(d)** These interactions result in alternating molecular homochiral columns of R,R and S,S enantiomers, with end groups coloured orange and green respectively for clarity. **(e)** This organisation of molecular columns forms pores filled with aceontiriles molecules, circled in red, that are stabilised via weak electrostatic interactions. The intramolecular S(9) hydrogen bond is shown in pink in each image.

4.2.7 Assembly of aromatic-spaced compounds

The crystal structures of aromatic-spaced **4.5$_{RR}$** and **4.6$_{SS}$** reveal that molecules self-assemble to form duplexes, driven by two $R_2^2(10)$ hydrogen bonding motifs formed from NH$_{(amide)}$···O=C$_{(urea)}$ interactions, and by π-π face-to-face interactions between the phenylene spacers, where the rings are planar and stacked with intermolecular distance between the aromatic ring centroids of 3.7 Å in both structures (**Figure 4-32**). Only one dimer pair and two ethanol units are present in the asymmetric cell of isophthalic-spaced **4.5$_{RR}$**, whilst terephthalic-spaced **4.6$_{SS}$** exhibits three dimers in the asymmetric cell, with each dimer distinguishable by the torsion angle of the 1-phenylethyl functionalities; many of which are disordered. At least ten benzyl alcohol units are also present in the asymmetric cell in this latter structure, with many being severely disordered which lowers the overall precision.

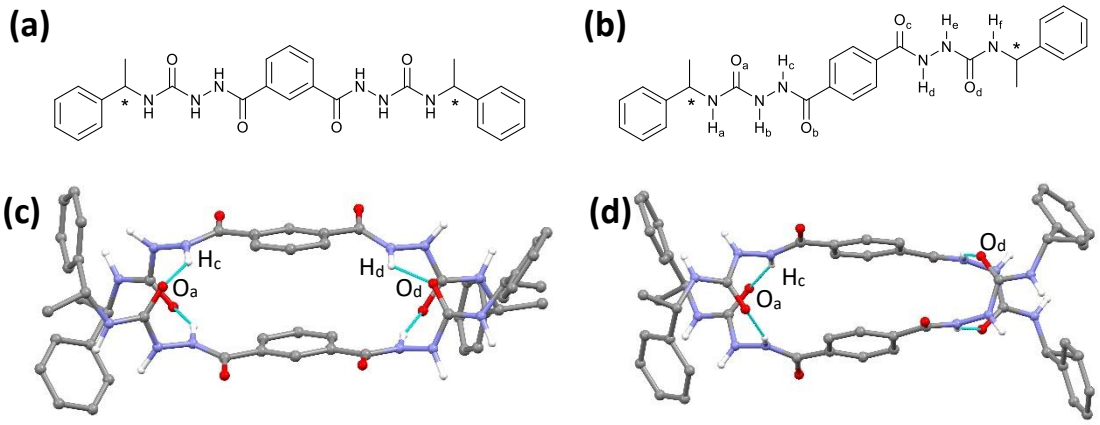

Figure 4-32. Chemical diagrams of **(a) 4.5$_{RR/SS}$** and **(b) 4.6$_{RR/SS}$** and images of molecular duplexes in the structures of **(c) 4.5$_{RR}$** and **(d) 4.6$_{SS}$**. $R_2^2(10)$ motifs, formed via N–H$_{(amide)}$ O$_{(urea)}$ interactions, and π-π stacking between the spacer phenylene groups stabilise dimer formation.

In the **4.5$_{RR}$** structure, molecules interact with molecules in an adjacent dimer via hydrogen bonding between urea NH and amide carbonyl oxygen atoms (**Figure 4-33**). This hydrogen bonding results in the assembly of sheet-like lamellae, stabilised by finite intermolecular face-to-face π-π interactions between two aryl end groups, with 4.118 Å between ring centroids and dihedral angle of 14.52°. Molecules in adjacent lamellae interact via and $C_3^3(8)$ hydrogen bond motifs, which form via NH$_{(urea)}$···O-H$_{(ethanol)}$···O-H$_{(ethanol)}$···O(C)$_{(urea)}$ hydrogen bonds and intermolecular edge-to-face π-π interactions between two aryl end groups (4.70 Å, 64°). Only one urea proton and carbonyl per molecule with the ethanol chain.

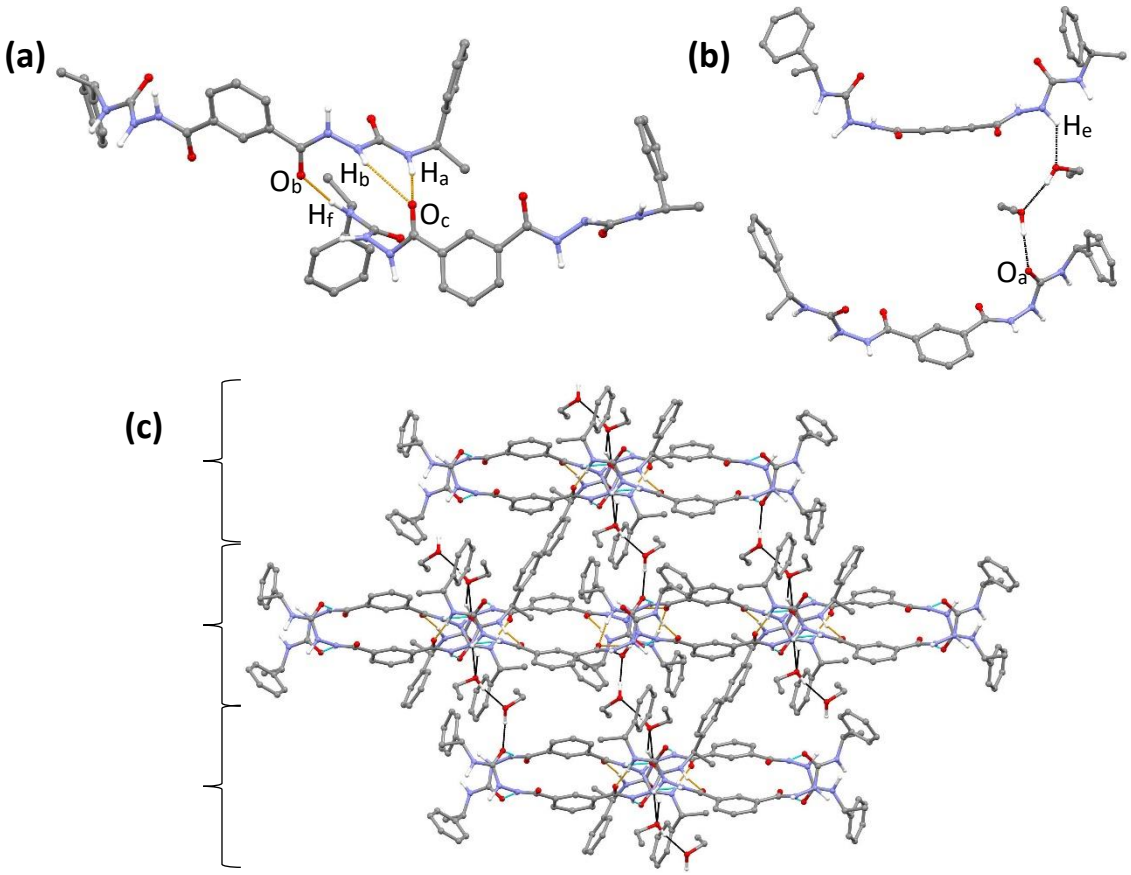

Figure 4-33. (a) Molecules in adjacent dimer pairs in **4.5$_{RR}$** interact via hydrogen bonds between urea NH and amide carbonyl oxygen atoms (in orange). **(b)** One urea NH in each molecules forms a $C_3^3(8)$ synthons (in black) with two ethanol molecules and a urea oxygen atom in a neighbouring molecule. **(c)** These interactions result in lamellae of dimers packing together, with molecules in adjacent layers interacting via the $C_3^3(7)$ hydrogen bond synthons and π-π interactions between 1-phenylethyl groups. The lamellae can be distinguished using the braces on the left hand side of the image.

The **4.6$_{SS}$** structure exhibits a high Z', with six **4.6$_{SS}$** molecules and ten benzyl alcohol units in the asymmetric unit (**Figure 4-34**). The compound crystallised in the trigonal space group $P3_1$ and the asymmetric unit contains three distinct dimers, referred to as dimer 1, 2 and 3. These dimers assemble via the same supramolecular interactions, but can be distinguished by slight differences in the conformations of their aromatic end groups and their interactions with benzyl alcohol molecules. Molecules in a dimer pair each interact with two molecules from the two other distinct dimers via $R_2^1(6)$ synthons or a single $NH_{(urea)}\cdots O(C)_{(amide)}$ hydrogen bond. This results in alternating dimer pairs along the *a* and *b* axes. The other urea NH in each molecule interacts with benzyl alcohol units, which form different lengths of solvent propagated hydrogen

bond chain synthons between molecules in different dimer pairs. These hydrogen bond synthons drive molecular assembly into a 3D porous network, with the pores filled with hydrogen-bonded benzyl alcohol units. This is significantly different from the 2D-sheet formation observed in **4.5$_{RR}$**, despite the similarities in initial dimer formation.

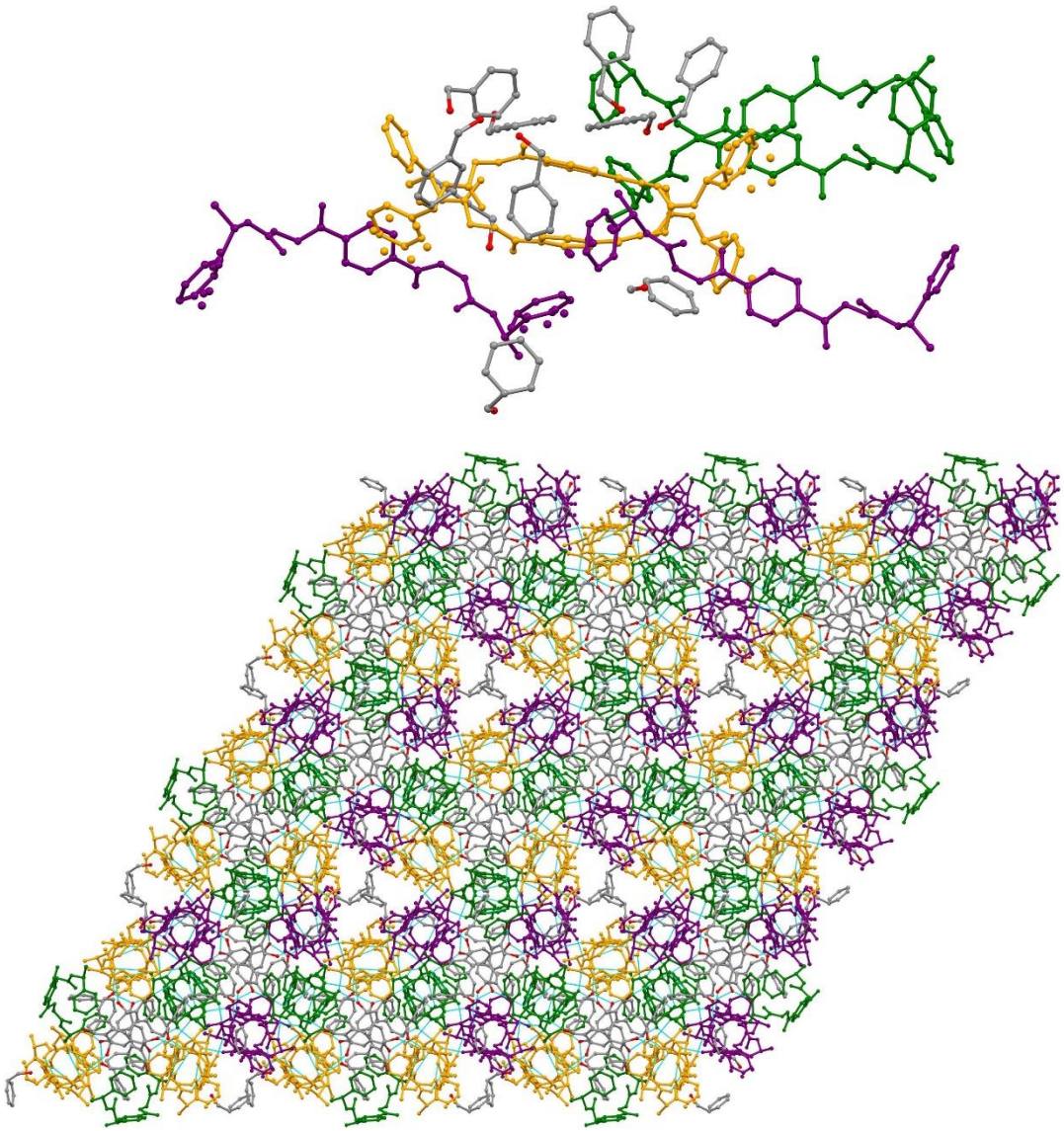

Figure 4-34. (a) An image of the **4.6$_{SS}$** asymmetric cell with three dimers coloured green, purple and orange based to distinguish. Ten benzyl alcohol units (coloured by atom) are present. **(b)** A 3x3x3 unit cell lattice of the **4.6$_{SS}$** showing how the distinct dimers pack together to form 3D pores filled with benzyl alcohol molecules.

Whilst no aromatic-spaced bis(acyl-semicarbazide) structures exhibiting duplex assembly have been reported in the CSD, the super organogelator reported by Chen and colleagues was predicted, via ^{1}H-NMR studies and DFT calculations, to initially assemble into homoduplexes via the same urea-amide hydrogen bonds observed in these crystal structures.[17] The homoduplexes were then hypothesised to stack to form 2D-lamellae, which is highly similar to the behaviour observed by **4.5$_{SS}$**.

4.2.8 Achiral vs homochiral vs racemic forms

The packing efficiency of crystalline forms can be evaluated by comparing calculated density values (**Table 4-4**). Wallach's rule states that racemic crystal forms are typically denser than homochiral forms as they can pack more efficiently.[50] This was true when comparing the calculated densities for racemic (ρ_{rac}) and homochiral ($\rho_{RR/SS}$) forms derived from spacer **4.1** (ρ_{rac} = 1.370 g cm^{-3}, ρ_{RR}= 1.282 g cm^{-3}) indicating that the presence of both enantiomers enables a more efficient molecular packing arrangement. Indeed, in the **4.1$_{Rac}$** structure, $R_2^2(10)$ form between opposite enantiomers so that homochiral urea stacks of opposite enantiomers alternate throughout the structure (**Figure 4-35**). Strong dimeric face-to-edge π-π interactions are formed between these aryl groups of opposite enantiomeric form with ring centroid distance and dihedral angles of 5.42 Å and 81 ° respectively. Meanwhile, there are no π-π interactions in **4.1$_{RR}$** due to the methyl group and homochirality sterically prevent with 1-phenylethyl positions stabilised via electrostatic interactions instead. The formation of these stronger π-π interactions likely drives the more efficient packing of alternating enantiomers.

Table 4-4. The calculated densities (g cm-3) for homochiral and racemic bis(acyl-semicarbazide) structures.

Structure	Calculated Density / g cm^{-3}
4.1$_{RR}$	1.282
4.1$_{Rac}$	1.370
4.2$_{RR}$	1.322
4.2$_{Rac}$ (stable)	1.279
4.2$_{Rac}$ (metastable)	1.222
4.3$_{SS}$	1.260
4.3$_{Rac}$.MeOH	1.256
4.3$_{Rac}$.H$_2$O	1.261

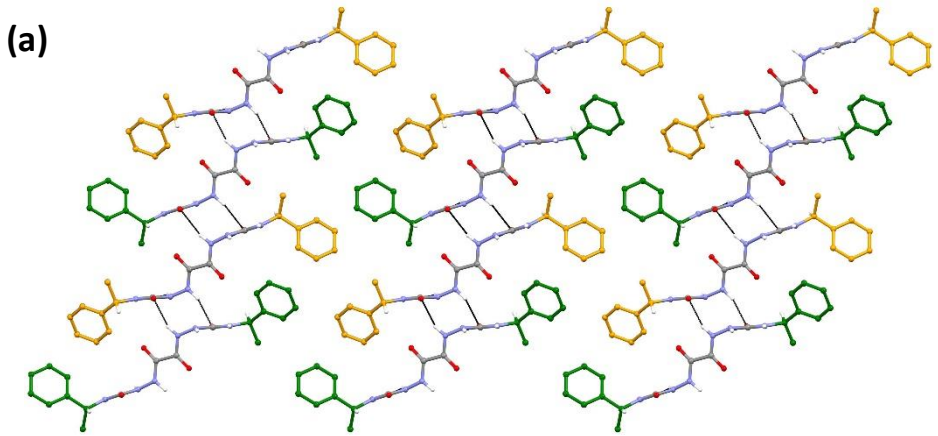

Figure 4-35. Packing of homochiral urea stacks in **4.1$_{Rac}$**. R-1-phenylethyl and S-1-phenyethly end groups are coloured green and yellow respectively to aid enantiomer identification. Dimeric face-to-edge π-π interactions form between the terminal aryl groups of opposite enantiomers.

However, Wallach's rule does not hold true for compounds derived from spacer **4.2,** with **4.2$_{RR}$** having a higher density (ρ_{RR}= 1.322 g cm^{-3}) than the stable and metastable **4.2$_{Rac}$** forms (ρ_{Rac} = 1.279 and 1.222 g cm^{-3}). The higher density of the stable **4.2$_{Rac}$** compared with the metastable form is further evidence of the more efficient packing and higher stability. Both **4.2$_{RR}$** and the stable **4.2$_{Rac}$** structure exhibit urea tape assembly with solvent molecules between urea stacks. The different solvent in each structure may account for the unexpected higher density for homochiral **4.1$_{RR}$** with larger ethanol molecules reducing the space in the crystal structure resulting in a denser structurer than compared with the acetonitrile **4.2$_{Rac}$** solvate.

The homochiral and racemic crystals of **4.3** derivatives were all remarkably similar in density, indicating that the end group chirality seemingly has little influence on overall packing efficiency. In addition to hydrogen bonding, molecules within lamellae in **4.3$_{SS}$** interact via intermolecular edge-to-face π-π interactions between adjacent aryl groups, with 5.096 Å between ring centroids and dihedral angles of 84.32°. Unlike in the structure of **4.3$_{SS}$**, continuous edge-to-face π-π interactions between lamellae along the c-axis are anticipated in the **4.3$_{Rac}$** methanol solvate, due to a dihedral angle of 75.31° and a distance between the aryl centroids of 4.91 Å.

Only one structure of an achiral benzyl-terminated bis(acyl-semicarbazide) was obtained in this study (**4.2$_{Benz}$**) but this provides some insight to differences in packing behaviour between the chiral and achiral molecules (**Figure 4-36**). Whilst the structure reveals an extended conformation and urea tape assembly consistent with **4.2$_{RR}$** and the stable form of **4.2$_{Rac}$**, the benzyl end groups are expected to enable a more efficient packing arrangements due to the absence of chirality and bulky methyl groups. Indeed, the calculated density of the **4.2$_{Benz}$** structure is 1.431 g cm^{-3} which is significantly higher than the **4.2$_{RR}$** structure (ρ = 1.322 g cm^{-3}) or stable **4.2$_{Rac}$** forms (ρ $_{stable}$=1.279 g cm^{-3}). In **4.2$_{Benz}$** the aromatic end groups from molecules in adjacent urea stacks, overlap with no defined space between adjacent urea stacks. Meanwhile, in **4.2$_{RR}$** and the stable **4.2$_{Rac}$** form, which both adopt a similar extended conformation, the urea stacks have a defined space between them.

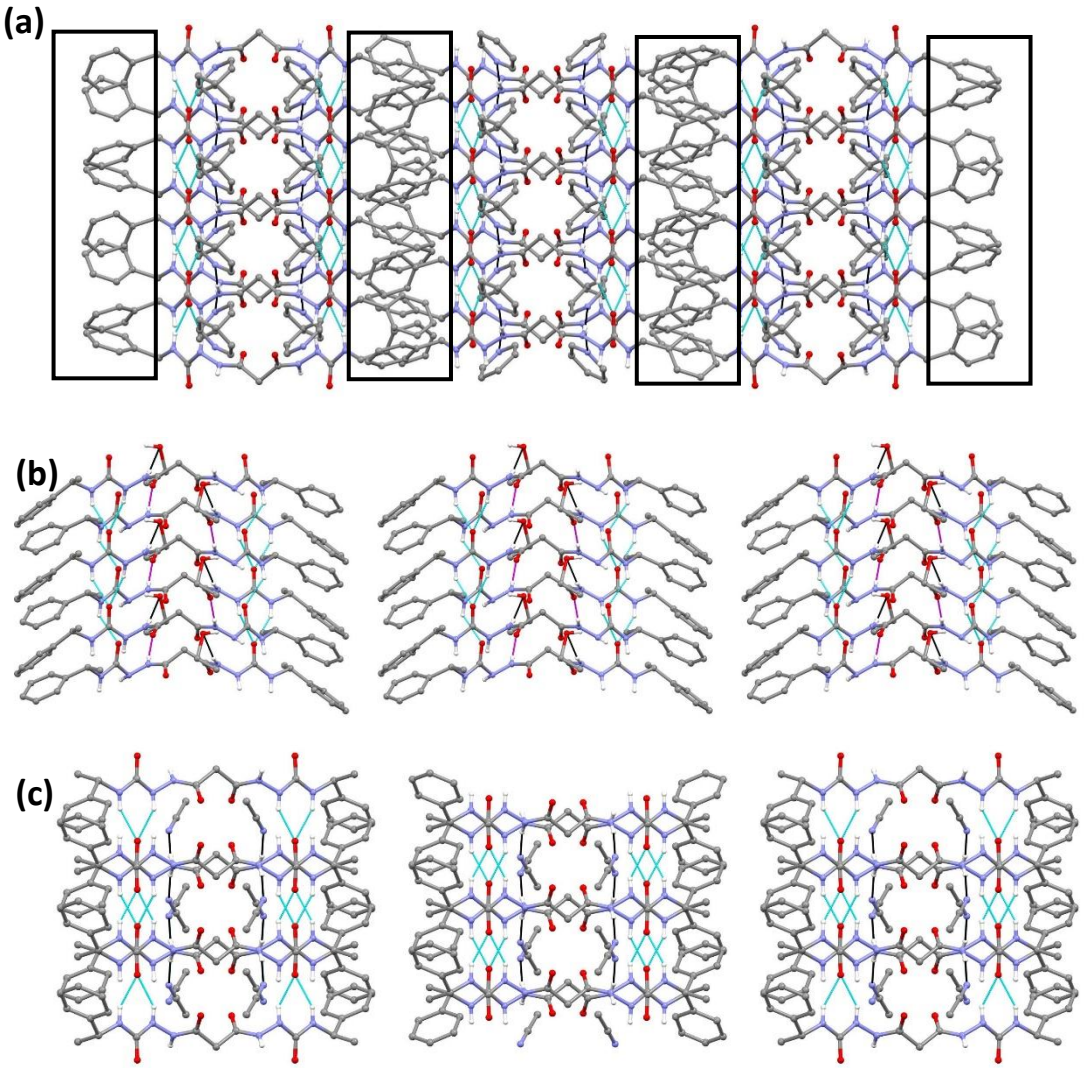

Figure 4-36. Images of 3 adjacent urea stacks in **(a) 4.2$_{Benz}$**, **(b) 4.2$_{RR}$** and **(c)** the stable **4.2$_{Rac}$** form. The benzyl end groups in **4.2$_{Benz}$** are much more much more intimately packed than the 1-phenylethyl groups in **4.2$_{RR}$** and **4.2$_{Rac}$**, which both have defined spaces between adjacent stacks.

4.3 Conclusions

A range of novel bis(acyl-semicarbazides) were synthesised and characterised from different dihydrazide spacer groups and achiral or chiral end groups. 2D-ROESY and variable temperature solution NMR experiments confirmed the presence of three conformers for each compound due to the restricted rotation around the amide bonds. A crystallisation screen of the compounds results in the growth of homochiral crystals for all the 1-phenylethyl terminated compounds and racemic crystals for derivatives of **4.1**, **4.2** and **4.3**. This included two conformational polymorphs of a **4.2$_{Rac}$** acetonitrile disolvate, with remarkably different radiation sensitivities despite the identical chemical composition. Only one crystal of an achiral benzyl end group compound was obtained.

The structures of aliphatic-spaced compounds revealed two types of conformation, both exhibiting the trans amide isomer. These are an extended conformation, adopted by derivatives of **4.1**, **4.2** and **4.4**, and a folded conformation adopted by derivatives of **4.3** and in a metastable form of **4.2$_{Rac}$**. The folded conformations exhibit both an *anti-anti* and an *anti-syn* urea group, which has rarely been observed in acyl-semicarbazide structures previously reported. The *anti*-NH forms an intramolecular hydrogen bond with the amide carbonyl oxygen atom in the other acyl-semicarbazide functionality. Two specific self-assembly behaviours were observed which were depended on conformation. The extended conformers assembled via unidirectional urea α-tape synthons, with amide functionalities generally forming hydrogen bonds with solvent molecules, resulting in solvent molecules entrapped between urea stacks. Meanwhile, the folded conformers assembled core-to-core to form lamellae with hydrophobic surfaces and a hydrophilic centre. The hydrogen bonding dictating this latter assembly was distinct in each structure and include several synthons not previously observed in acyl-semicarbazide structures.

Wallach's rule holds true for the **4.1** derivatives with the **4.1$_{Rac}$** crystal having a higher density than **4.1$_{RR}$**, with stronger interactions between aromatic end groups in the racemic form. Meanwhile, **4.2$_{Benz}$** was significantly denser than its corresponding 1-phenylethyl counterparts due to the absence of bulk methyl groups enabling bis(acyl-semicarbazides) to pack more efficiently. The **4.2$_{Rac}$** acetonitrile solvate showing an extended conformation had a higher density than its polymorph exhibiting the folded

conformation, which is indicative of the observed higher stability of the extended form. Minimal differences in density are observed for the homochiral and racemic crystal structures for 4.3 1-phenylethyl derivatives, with highly similar packing arranged observed and slight differences likely attributed to differences in solvent content.

Both aromatic-spaced 1-phenylethyl derivatives adopt a similar conformation with the amide moiety planar with the spacer aromatic ring, and molecules assemble to form homoduplexes via identical amide $N–H_{(urea)}\cdots O_{(amide)}$ hydrogen bonds. However, they differed in how these duplex building blocks assembled. The terephthalic derivative **4.6$_{RR}$** crystallised with a high Z' and three dimers and ten benzyl alcohol units in the asymmetric cell. These dimers pack together to form columnar pores, which are filled with a disordered network of hydrogen-bonded benzyl alcohol units. Meanwhile, molecules derived from isophthalic spacer **4.5** assembled to form 2D-sheets with ethanol units linking molecules in adjacent sheets together via hydrogen bond chains. Whilst no phenylene-spaced bis(acyl-semicarbazide) structures are reported in the CSD, this latter assembly is consistent with the predicted mechanism for gelation of a super organogelator reported by Chen and colleagues.

This understanding in molecular conformations, supramolecular synthons and packing behaviour provides a valuable foundation for understanding gelation behaviour exhibited by these compounds, especially any differences in gelation behaviour observed between homochiral and racemic systems.

4.4 Experimental Details

Synthesis details and characterisation for compounds presented in chapter 4. Please refer to Chapter 6– General Experimental for additional experimental details.

4.4.1 General synthetic method for compounds in Chapter 4

Bis(acyl-semicarbazide) compounds were all synthesised via the same generic method whereby 0.5 mmol of oxalyl (4.1), malonic (4.2), succinic (4.3), adipic (4.4), isophthalic

(4.5) or terephthalic (4.6) dihydrazide was suspended in 2 mL DMA at room temperature with stirring. 1.2 mmol of benzyl isocyanate (Benz), R-methylbenzyl isocyanate (RR) or S-methylbenzyl isocyanate (SS) was added and the resulting suspension was stirred at room temperature for 18 hours. The suspension was then filtered, and the precipitate washed with copious amounts of water and then diethyl ether. The precipitate was then dried in a drying pistol at 110 ^{o}C for 12-48 hours.

4.4.2 Compound characterisation

4.1$_{Benz}$: 2,2'-oxalylbis(N-1-benzyl)hydrazine-1-carboxamide), white powder; yield = 90 %. **^{1}H NMR** (400 MHz, DMSO-[d6]): δ = 10.35 (broad-s, 2H, NH-NH-CO-CO) 8.00 (s, 2H, NH-CO-NH-NH), 7.26 (m, 8H, Ar-H), 7.20 (m, 2H, Ar-H), 6.93 (broad-S, 2H, CH_2-NH-CO-NH), 4.22 (d, J = 6.00 Hz, 4H, Phe-CH_2-NH). **^{13}C NMR** (100 MHz, DMSO-[d6]): δ = 44.10, 126.99, 127.40, 128.56, 140.85, 157.98, 159.81. **m/z (ES^{+}-MS)** 385.16 [M+H], 407.14 [M+Na]. **Elemental analysis** calculated for $C_{18}H_{20}N_6O_4$ (%): C, 56.24; H, 5.24; N, 21.86. Found (%): C, 56.48; H, 5.43; N, 21.64.

4.1$_{RR}$: 2,2'-oxalylbis(N-((R, R)-1-phenylethyl)hydrazine-1-carboxamide), white powder; yield = 94 %. **^{1}H NMR** (400 MHz, DMSO-[d6]): δ = 10.27 (s, 2H, NH) 7.82 (s, 2H, NH), 7.29-7.25 (m, 8H, Ar-H), 7.19-7.17 (m, 2H, Ar-H), 6.78 (d, 2H, NH), 4.78-4.73 (p, J= 7.2 Hz, 2H, Phe-CH(CH_3)-NH), 1.32 (d, J= 7.01 Hz, 6H, CH_3). **^{13}C NMR** (100 MHz, DMSO-[d6]): δ = 24.32, 48.97, 126.34, 126.90, 128.58, 145.55, 157.04, 158.33, 159.61. **m/z (ES^{+}-MS)** 435.31 [M+Na], 413.2 [M+H]. **Elemental analysis** calculated for $C_{20}H_{24}N_6O_4$ (%): C, 58.24; H, 5.87; N, 20.38. Found (%): C, 58.11; H, 5.89; N, 20.20.

4.1$_{SS}$: 2,2'-oxalylbis(N-((S, S)-1-phenylethyl)hydrazine-1-carboxamide), white powder; yield = 93 %. **^{1}H NMR** (400 MHz, DMSO-[d6]): δ = 10.27 (broad-d, 2H, NH-NH-CO-CO) 7.82 (broad-d, 2H, NH-CO-NH-NH), 7.27 (m, 8H, Ar-H), 7.19-7.17 (d, J= 1.85 Hz, 4H, Ar-H), 6.78 (d, J= 8.17 Hz, 2H, CH-NH-CO), 4.78-4.73 (m, 2H, Phe-CH(CH_3)-NH), 1.32 (d, J= 7.01 Hz, 6H, CH-CH_3). **^{13}C NMR** (100 MHz, DMSO-[d6]): δ = 24.32, 48.97, 126.34, 126.90, 128.58, 145.55, 157.04, 158.33, 159.61. **m/z (ES^{+}-MS)** 435.31 [M+Na], 847.59 [2M+Na]. **Elemental analysis** calculated for $C_{20}H_{24}N_6O_4$ (%): C, 58.24; H, 5.87; N, 20.38. Found (%): C, 58.19; H, 5.91; N, 20.28.

4.2$_{Benz}$: 2,2'-malonylbis(N-1-benzyl)hydrazine-1-carboxamide), white powder; yield = 88 %. **^{1}H NMR** (400 MHz, DMSO-[d6]): δ = 9.75 (s, 2H, NH-NH-CO-CH_2), 7,99 (s,

2H, NH-CO-NH-NH), 7.25 (m, 4H, Ar-H), 7.22 (m, 4H, Ar-H), 7.18 (td, J = 7.0, 1.5 Hz, 2H, Ar-H), 6.98 (broad-s, 2H, CH_2-NH-CO-NH), 4.21 (d, J= 6.00 Hz, 4H, Phe-CH_2-NH), 4.11 (s, 2H, CO-CH_2-CO). **^{13}C NMR** (100 MHz, DMSO-[d6]): δ = 44.10, 126.95, 127.27, 128.56, 140.84, 158.42, 167.10. **m/z (ES$^+$-MS)** 421.16 [M+Na], 399.18 [M+H]. **Elemental analysis** calculated for $C_{19}H_{22}N_6O_4$ (%): C, 57.28; H, 5.57; N, 21.09. Found (%): C, 57.19; H, 5.78; N, 20.98.

4.2$_{RR}$: 2,2'-malonylbis(N-((R, R)-1-phenylethyl)hydrazine-1-carboxamide), white powder; yield = 91 %. **^{1}H NMR** (400 MHz, DMSO-[d6]): δ = 9.78 (broad-S, 2H, NH-NH-CO-CH_2), 7.85 (broad-s, 2H, NH-CO-NH-NH), 7.25 (m, 8H, Ar-H), 7.17 (m, 2H, Ar-H), 6.83 (d, 2H, J = 7.994 Hz, CH-NH-CO-NH), 4.74 (p, J= 7.2 Hz, 2H, Phe-CH-NH), 1.31 (d, J = 7.0 Hz, 6H, CH-CH_3). **^{13}C NMR** (100 MHz, DMSO-[d6]): δ = 24.48, 49.01, 126.21, 127.00, 128.54, 145.71, 157.44, 166.43, 167.09. **m/z (ES$^+$-MS)** 449.19 [M+Na], 427.21 [M+H]. **Elemental analysis** calculated for $C_{21}H_{26}N_6O_4$ (%): C, 59.14; H, 6.15; N, 19.71. Found (%): C, 58.89; H, 5.93; N, 19.90.

4.2$_{SS}$: 2,2'-malonylbis(N-((S, S)-1-phenylethyl)hydrazine-1-carboxamide), white powder; yield = 87 %. **^{1}H NMR** (400 MHz, DMSO-[d6]): δ = 9.78 (broad-S, 2H, NH-NH-CO-CH_2), 7.85 (broad-s, 2H, NH-CO-NH-NH), 7.25 (m, 8H, Ar-H), 7.17 (m, 2H, Ar-H), 6.83 (d, 2H, J = 7.994 Hz, CH-NH-CO-NH), 4.74 (p, J= 7.2 Hz, 2H, Phe-CH-NH), 1.31 (d, J = 7.0 Hz, 6H, CH-CH_3). **^{13}C NMR** (100 MHz, DMSO-[d6]): δ = 24.48, 49.01, 126.21, 127.00, 128.54, 145.71, 157.44, 166.43, 167.09. **m/z (ES$^+$-MS)** 449.19 [M+Na], 427.21 [M+H]. **Elemental analysis** calculated for $C_{21}H_{26}N_6O_4$ (%): C, 59.14; H, 6.15; N, 19.71. Found (%): C, 59.01; H, 5.91; N, 19.95.

4.3$_{Benz}$: 2,2'-succinylbis(N-1-benzyl)hydrazine-1-carboxamide): white powder; yield = 91 %. **^{1}H NMR** (400 MHz, DMSO-[d6]): δ = 9.56 (broad-s, 2H, NH-NH-CO-CH_2), 7.76 (broad-s, 2H, NH-CO-NH-NH), 7.24 (m, 8H, Ar-H), 7.18 (td, J = 7.00 Hz, 2H, Ar-H), 1.77 (broad-s, 2H, CH_2-NH-CO-NH), 4.18 (d, J = 6.16 Hz, 4H, Phe-CH_2-NH), 2.37 (s, 4H, NH-CO-CH_2). **^{13}C NMR** (100 MHz, DMSO [d6]): δ = 28.91, 44.01, 126.91, 127.31, 128.53, 141.01, 158.67, 172.02. **m/z (ES+-MS)** = 413.2 [M+H] **Elemental analysis** calculated for $C_{20}H_{24}N_6O_4$ (%): C, 58.24; H, 5.87; N, 20.38. Found (%): C, 58.00; H, 5.80; N, 20.56.

4.3$_{RR}$: 2,2'-succinylbis(N-((R,R)-1-phenylethyl)hydrazine-1-carboxamide): white powder; yield = 95 %. **^{1}H NMR** (100 MHz, DMSO-[d6]): δ = 1.31 (d, J = 8 Hz, 6 H, CH_3), 2.37 (s, 4H), 4.74 (m, 2 H, CH), 6.79 (d, J = 8 Hz, 2 H, NH), 7.19 (m, 2 H, Ar-H), 7.21 (m, 8

H, Ar-H), 7.65 (s, 2 H, NH), 9.57 (s, 2 H, NH). **^{13}C NMR** (100 MHz, DMSO [d6]): δ = 24.4, 28.9, 49.0, 126.3, 126.8, 128.5, 145.9, 157.7, 171.9. **m/z (ES$^+$-MS)** = 441 [M+H] **Elemental analysis** calculated for $C_{22}H_{28}N_6O_4$ (%): C, 59.99; H, 6.41; N, 19.08. Found (%): C, 60.18; H, 6.35; N, 18.92.

4.3$_{SS}$: 2,2'-succinylbis(N-((S,S)-1-phenylethyl)hydrazine-1-carboxamide): white powder; yield = 89 %. **^{1}H NMR** (400 MHz, DMSO-[d6]): δ = 1.31 (d, J = 8 Hz, 6 H), 2.28 (s, 4H), 4.75 (m, 2 H), 6.80 (d, J = 8 Hz, 2 H), 7.19 (m, 2 H), 7.28 (m, 8 H), 7.65 (s, 2 H), 9.58 (s, 2 H). **^{13}C NMR** (100 MHz, DMSO [d6]): δ = 24.4, 28.9, 49.0, 126.3, 126.8, 128.6, 145.9, 157.7, 171.9. **m/z (ES$^+$-MS)** = 463.21 [M+Na]. **Elemental analysis** calculated for $C_{22}H_{28}N_6O_4$ (%): C, 59.99; H, 6.41; N, 19.08. Found (%): C, 59.75; H, 6.33; N, 18.89.

4.4$_{Benz}$: 2,2'-adipicbis(N-1-benzyl)hydrazine-1-carboxamide): white powder; yield = 88 %. **^{1}H NMR** (400 MHz, DMSO-[d6]): δ = 9.44 (broad-s, 2H, NH-N<u>H</u>-CO-CH_2), 7.76 (broad-s, 2H, NH-CO-N<u>H</u>-NH), 7.22 (m, 12 H, Ar-H), 6.84 (broad-s, 2H, CH_2-N<u>H</u>-CO-NH), 4.20 (d, J = 6.1 Hz, 4H, Phe-C<u>H$_2$</u>-NH), 2.08 (d, J = 6.50 Hz, 4H, NH-CO-C<u>H$_2$</u>-CH_2), 1.50 (q, J = 4.5 Hz, 4H, (CO-CH_2-C<u>H$_2$</u>). **^{13}C NMR** (100 MHz, DMSO [d6]): δ = 24.86, 34.39, 44.17, 126.94, 127.36, 128.54, 140.99, 158.75, 172.52. **m/z (ES$^+$-MS)** = 441.23 [M+H]. **Elemental analysis** calculated for $C_{22}H_{28}N_6O_4$ (%): C, 59.99; H, 6.41; N, 19.08. Found (%): C, 60.11; H, 6.39; N, 19.21.

4.4$_{RR}$: 2,2'-adipicbis(N-((R,R)-1-phenylethyl)hydrazine-1-carboxamide): white powder; yield = 89 %. **^{1}H NMR** (400 MHz, DMSO-[d6]): δ = 1.33 (d, J = 4 Hz, 6 H), 1.51 (s, 4H), 2.08 (s, 4H), 4.77 (q, 2 H), 6.72 (d, J = 8 Hz, 2 H), 7.21 (m, 2 H), 7.30 (m, 8 H), 7.67 (s, 2 H), 9.43 (s, 2 H). **^{13}C NMR** (100 MHz, DMSO [d6]): δ = 24.4, 24.9, 34.3, 49.0, 126.3, 126.9, 128.6, 145.7, 157.8, 172.4. **m/z (ES$^+$-MS)** = 469 (M+H). **Elemental analysis** calculated for $C_{24}H_{32}N_6O_4$ (%): C, 61.52; H, 6.88; N, 17.94. Found (%): C, 61.46; H, 6.80; N, 17.79.

4.4$_{SS}$: 2,2'-adipicbis(N-((S,S)-1-phenylethyl)hydrazine-1-carboxamide): white powder; yield = 89 %. **^{1}H NMR** (400 MHz, DMSO-[d6]): δ = 1.33 (d, J = 4 Hz, 6 H), 1.51 (s, 4H), 2.09 (s, 4H), 4.77 (q, 2 H), 6.72 (d, J = 8 Hz, 2 H), 7.21 (m, 2 H), 7.30 (m, 8 H), 7.67 (s, 2 H), 9.43 (s, 2 H). **^{13}C NMR** (100 MHz, DMSO [d6]): δ = 24.4, 24.9, 34.3, 49.0, 126.3, 126.9, 128.6, 145.7, 157.8, 172.4. **m/z (ES$^+$-MS)** = 469 [M+H]. **Elemental analysis**

calculated for $C_{24}H_{32}N_6O_4$ (%): C, 61.52; H, 6.88; N, 17.94. Found (%): C, 61.33; H, 6.94; N, 18.10.

4.5$_{Benz}$: 1,5-Isophthalic-bis(N-1-benzyl)hydrazine-1-carboxamide): white powder; yield = 93 %. **^{1}H NMR** (400 MHz, DMSO-[d6]): δ = 10.24 (s, 2H, NH-CO-NH-NH), 8.41 (s, 1H, Ar-H), 8.04 (dd, J = 7.79, 1.76 Hz, 2H, Ar-H), 8.03 (broad-s, 2H, NH-CO-NH-NH), 7.57 (t, J = 7.77 Hz, 1H, Ar-H), 7.27 (m, 8H, Ar-H), 7.19 (tt, J = 6.58, 1.78 Hz, 2H, Ar-H), 7.08 (broad-s, 2H, CH_2-NH-CO), 4.24 (d, J = 6.1 Hz, 4H, Phe-CH_2(CH_3)-NH). **^{13}C NMR** (100 MHz, DMSO [d6]): δ = 44.09, 126.95, 127.36, 127.72, 128.55, 128.75, 130.92, 134.40, 141.03, 158.83, 166.38. **m/z (ES$^+$-MS)** 483.18 [M+Na], 943.37 [2M+Na]. **Elemental analysis** calculated for $C_{24}H_{24}N_6O_4$ (%): C, 62.60; H, 5.25; N, 18.25. Found (%): C, 62.43; H, 5.19; N, 17.97.

4.5$_{RR}$: 1,5-isophthalic-bis(N-(R, R)1-phenylethyl)hydrazine-1-carboxamide: white powder; yield = 85 % **^{1}H NMR** (400 MHz, DMSO-[d6]): δ = 10.20 (d, J = 2.27, 2H, NH-CO-NH-NH), 8.38 (t, J = 1.86, 1H, spacer Ar-H), 8.02 (dd, J = 7.77, 1.73 Hz, 2H, spacer Ar-H), 7.90 (d, J = 2.20, 2H, NH-CO-NH-NH), 7.57 (t, J = 7.78, 1H, spacer Ar-H), 7.30 (m, 8H, Ar-H), 7.18 (m, 2H, Ar-H), 6.89 (d, J = 8.21 Hz, 2H, CH-NH-CO-NH), 4.80 (p, J = 7.20, 2H, Phe-CH(CH_3)-NH), 1.34 (d, J = 7.02 Hz, 6H, CH-CH_3). **^{13}C NMR** (100 MHz, DMSO [d6]): δ = 24.31, 49.05, 126.34, 126.92, 127.57, 128.58, 128.85, 130.81, 134.40, 145.69, 157.87, 166.21. **m/z (ES$^+$-MS)** 489.22 [M+H], 999.43 [2M+Na]. **Elemental analysis** calculated for $C_{26}H_{28}N_6O_4$ (%): C, 64.92; H, 5.78; N, 17.20. Found (%): C, 64.78; H, 5.99; N, 17.34.

4.5$_{SS}$: 1,5-isophthalic-bis(N-(S, S)1-phenylethyl)hydrazine-1-carboxamide: white powder; yield = 89 %. **^{1}H NMR** (400 MHz, DMSO-[d6]): δ = 10.20 (d, J = 2.27, 2H, NH-CO-NH-NH), 8.38 (t, J = 1.86, 1H, spacer Ar-H), 8.02 (dd, J = 7.77, 1.73 Hz, 2H, spacer Ar-H), 7.90 (d, J = 2.20, 2H, NH-CO-NH-NH), 7.57 (t, J = 7.78, 1H, spacer Ar-H), 7.30 (m, 8H, Ar-H), 7.18 (m, 2H, Ar-H), 6.89 (d, J = 8.21 Hz, 2H, CH-NH-CO-NH), 4.80 (p, J = 7.20, 2H, Phe-CH(CH_3)-NH), 1.34 (d, J = 7.02 Hz, 6H, CH-CH_3). **^{13}C NMR** (100 MHz, DMSO [d6]): δ = 24.31, 49.05, 126.34, 126.92, 127.57, 128.58, 128.85, 130.81, 134.40, 145.69, 157.87, 166.21. **m/z (ES$^+$-MS)** 489.22 [M+H], 999.43 [2M+Na]. **Elemental analysis** calculated for $C_{26}H_{28}N_6O_4$ (%): C, 64.92; H, 5.78; N, 17.20. Found (%): C, 64.06; H, 5.83; N, 17.07.

4.6$_{Benz}$: 1,4-terephthalic-bis(N-1-benzyl)hydrazine-1-carboxamide): white powder; yield = 95 %. **^{1}H NMR** (400 MHz, DMSO-[d6]): δ = 10.28 (broad-s, 2H, NH-CO-NH-NH), 8.01 (broad-s, 2H, NH-CO-NH-NH), 7.96 (s, 4H, spacer Ar-H), 7.27 (m, 8H, Ar-H), 7.19 (td, J = 6.90, 4.30 Hz, 2H, Ar-H), 7.10 (broad-s, 2H, CH_2-NH-CO), 4.06 (d, J = 6.1 Hz, 4H, Phe-CH_2-NH). **^{13}C NMR** (100 MHz, DMSO [d6]): δ = 44.08, 126.95, 127.37, 127.99, 128.54, 135.84, 141.04, 158.83, 166.26. **m/z (ES$^+$-MS)** 483.18 [M+Na], 943.37 [2M+Na]. **Elemental analysis** calculated for $C_{24}H_{24}N_6O_4$ (%): C, 62.60; H, 5.25; N, 18.25. Found (%): C, 62.69; H, 5.51; N, 18.04.

4.6$_{RR}$: 1,4-terephthalic-bis(N-(R, R)-1-phenylethyl)hydrazine-1-carboxamide): white powder; yield = 95 %. **^{1}H NMR** (400 MHz, DMSO-[d6]): δ =10.23 (d, J= 2.12, 2H, NH-CO-NH-NH), 7.94 (s, 4H, spacer Ar-H), 7.88 (d, 2.07 Hz, 2H, NH-CO-NH-NH), 7.30 (m, 8H, Ar-H), 7.19 (m, 2H, Ar-H), 6.91 (d, J = 8.21 Hz, 2H, CH-NH-CO), 4.71 (p, J = 7.2, 2H, Phe-CH(CH_3)-NH), 1.34 (d,7.03 Hz, 6H, CH-CH_3). **^{13}C NMR** (100 MHz, DMSO [d6]): δ = 24.30, 49.06, 126.34, 126.92, 127.95, 128.57, 135.80, 145.69, 157.87, 166.06. **m/z (ES$^+$-MS)** 511.21 [M+Na], 489.23 [M+H]. **Elemental analysis** calculated for $C_{26}H_{28}N_6O_4$ (%): C, 64.92; H, 5.78; N, 17.20. Found (%): C, 64.79; H, 5.80; N, 17.32.

4.6$_{SS}$: 1,4-terephthalic-bis(N-(S, S)-1-phenylethyl)hydrazine-1-carboxamide): white powder; yield = 95 %. **^{1}H NMR** (400 MHz, DMSO-[d6]): δ = 10.23 (d, J= 2.12, 2H, NH-CO-NH-NH), 7.94 (s, 4H, spacer Ar-H), 7.88 (d, 2.07 Hz, 2H, NH-CO-NH-NH), 7.30 (m, 8H, Ar-H), 7.19 (m, 2H, Ar-H), 6.91 (d, J = 8.21 Hz, 2H, CH-NH-CO), 4.71 (p, J = 7.2, 2H, Phe-CH(CH_3)-NH), 1.34 (d,7.03 Hz, 6H, CH-CH_3). **^{13}C NMR** (100 MHz, DMSO [d6]): δ = 24.30, 49.06, 126.34, 126.92, 127.95, 128.57, 135.80, 145.69, 157.87, 166.06. **m/z (ES$^+$-MS)** 511.21 [M+Na], 489.23 [M+H]. **Elemental analysis** calculated for $C_{26}H_{28}N_6O_4$ (%): C, 64.92; H, 5.78; N, 17.20. Found (%): C, 64.69; H, 5.81, N, 17.04.

4.5 References

1 L. S. Evans, P. A. Gale, M. E. Light and R. Quesada, *New J. Chem.*, 2006, **30**, 1019–1025.

2 E. Quinlan, S. E. Matthews and T. Gunnlaugsson, *J. Org. Chem.*, 2007, **72**, 7497–7503.

3 W. J. Chu, Y. Yang and C. F. Chen, *Org. Lett.*, 2010, **12**, 3156–3159.

4 W. J. Chu, J. Chen, C. F. Chen, Y. Yang and Z. Shuai, *J. Org. Chem.*, 2012, **77**, 7815–7822.

5 W. J. Chu and C. F. Chen, *Tetrahedron*, 2012, **68**, 9200–9205.

6 P. Deindörfer, T. Geiger, D. Schollmeyer, J. H. Ye and R. Zentel, *J. Mater. Chem.*, 2006, **16**, 351–358.

7 P. Deindörfer, R. Davis and R. Zentel, *Soft Matter*, 2007, **3**, 1308–1311.

8 P. Deindörfer, A. Eremin, R. Stannarius, R. Davis and R. Zentel, *Soft Matter*, 2006, **2**, 693–698.

9 R. Meziane, M. Brehmer, U. Maschke and R. Zentel, *Soft Matter*, 2008, **4**, 1237–1241.

10 S. Baddi and A. Palanisamy, *Sensors Actuators, B Chem.*, 2017, **245**, 711–719.

11 S. Baddi, S. S. Madugula, D. S. Sarma, Y. Soujanya and A. Palanisamy, *Langmuir*, 2016, **32**, 889–899.

12 S. Baddi, K. Kamalakar, M. S. L. Karuna and A. Palanisamy, *J. Sol-Gel Sci. Technol.*, 2014, **71**, 372–379.

13 M. Himabindu and A. Palanisamy, *Gels*, 2017, **3**, 12.

14 S. Baddi and A. Palanisamy, *Eur. Polym. J.*, 2018, **99**, 90–101.

15 S. Baddi, R. R. Nayak and A. Palanisamy, *Polymer (Guildf).*, 2017, **114**, 199–208.

16 W. Li, X. Che, F. Chen, C. Zhang, T. Zhang, H. Wang, B. Bai and M. Li, *J. Phys. Chem. B*, 2017, **121**, 8795–8801.

17 W. J. Chu and C. F. Chen, *Chinese Sci. Bull.*, 2012, **57**, 4278–4283.

18 S. R. Kennedy, C. D. Jones, D. S. Yufit, C. E. Nicholson, S. J. Cooper and J. W. Steed, *CrystEngComm*, 2018, **20**, 1390–1398.

19 A. Dawn, K. S. Andrew, D. S. Yufit, Y. Hong, J. P. Reddy, C. D. Jones, J. A. Aguilar and J. W. Steed, *Cryst. Growth Des.*, 2015, **15**, 4591–4599.

20 P. Byrne, D. R. Turner, G. O. Lloyd, N. Clarke and J. W. Steed, *Cryst. Growth Des.*, 2008, **8**, 3335–3344.

21 X. S. Yan, K. Wu, Y. Yuan, Y. Zhan, J. H. Wang, Z. Li and Y. B. Jiang, *Chem. Commun.*, 2013, **49**, 8943–8945.

22 Z. Cui, Y. Ling, B. Li, Y. Li, C. Rui, J. Cui, Y. Shi and X. Yang, *Molecules*, 2010, **15**, 4267–4282.

23 Z. Wei, J. H. Yang, J. Zhou, F. Xu, M. Zrínyi, P. H. Dussault, Y. Osada and Y. M. Chen, *Chem. Soc. Rev.*, 2014, **43**, 8114–8131.

24 X. Zhao, X. Z. Wang, X. K. Jiang, Y. Q. Chen, Z. T. Li and G. J. Chen, *J. Am. Chem. Soc.*, 2003, **125**, 15128–15139.

25 P. B. Pansuriya, C. Patel, H. B. Friedrich and G. E. M. Maguire, *Zeitschrift fur Krist. - New Cryst. Struct.*, 2016, **231**, 649–652.

26 M. Pitucha, Z. Rzaczynska and L. Mazur, *Japan Soc. Anal. Chem.*, 2009, **25**, 67–68.

27 T. Sun, G. C. Li, J. Li and F. L. Yang, *Acta Crystallogr. Sect. E Struct. Reports*

Online, 2010, **66**, 515–519.

28 M. C. Etter, *Acc. Chem. Res.*, 1990, **23**, 120–126.

29 P. B. Pansuriya, C. Patel, H. B. Friedrich and G. E. M. Maguire, *Zeitschrift fur Krist. - New Cryst. Struct.*, 2016, **231**, 649–652.

30 W. Edwards and D. K. Smith, *J. Am. Chem. Soc.*, 2014, **136**, 1116–1124.

31 L. Zhang, Q. Jin and M. Liu, *Chem. Asian. J.*, 2016, **11**, 2642.

32 T. Noguchi, B. Roy, D. Yoshihara, J. Sakamoto, T. Yamamoto and S. Shinkai, *Angew. Chem. Int. Ed.*, 2017, **56**, 12518.

33 X. Duan, Y. Fu, J. Zhang and W. Li, *Prog. Chem. Beijing*, 2013, **25**, 1272–1282.

34 J. Zhang and M. W. Germann, *Biopolymers*, 2011, **95**, 755–762.

35 D. Williams and I. Fleming, in *Spectroscopic Methods in Organic Chemistry*, ed. C. Watson, McGraw-Hill Education, Maidenhead, 6th edn., 2008, p. 120.

36 L. R. Brown and B. T. Farmer II, in *Methods in Enzymology*, eds. N. J. Oppenheimer and T. I. James, Academic Press, New York, 1989, vol. 176, Part, pp. 199–216.

37 N. J. Baxter and M. P. Williamson, *J. Biomol. NMR*, 1997, **9**, 359–369.

38 B. Spingler, S. Schnidrig, T. Todorova and F. Wild, *CrystEngComm*, 2012, **14**, 751–757.

39 M. J. Wen, M. T. Jackson and C. M. Garner, *Dalt. Trans.*, 2019, **48**, 11575–11582.

40 M. A. Walker, *Bioorganic Med. Chem. Lett.*, 2017, **27**, 5100–5108.

41 M. Ishikawa and Y. Hashimoto, *J. Med. Chem.*, 2011, **54**, 1539–1554.

42 J. Bernstein, R. E. Davis, L. Shimoni and N. -L Chang, *Angew. Chem. Int. Ed. Engl.*, 1995, **34**, 1555–1573.

43 M. Pitucha, K. Sobotka-Polska, R. Keller, A. Pachuta-Stec, E. Mendyk and A. A. Kaczor, *J. Mol. Struct.*, 2016, **1104**, 24–32.

44 F. H. Allen, O. Kennard, D. G. Watson, L. Brammer, A. G. Orpen and R. Taylor, *J. Chem. Soc. Perkin Trans. 2*, 1987, 1–19.

45 R. Centore, M. Causà, F. Cerciello, F. Capone and S. Fusco, *CrystEngComm*, 2014, **16**, 9168–9175.

46 H. P. G. Thompson and G. M. Day, *Chem. Sci.*, 2014, **5**, 3173–3182.

47 S. Ahn, F. Guo, B. M. Kariuki and K. D. M. Harris, *J. Am. Chem. Soc.*, 2006, **128**, 8441–8452.

48 S. Wen and G. J. O. Beran, *J. Chem. Theory Comput.*, 2012, **8**, 2698–2705.

49 D. Presti, A. Pedone, M. C. Menziani, B. Civalleri and L. Maschio, *CrystEngComm*, 2014, **16**, 102.

50 C. P. Brock, W. B. Schweizer and J. D. Dunitz, *J. Am. Chem. Soc.*, 1991, **113**, 9811–9820.

Chapter 5 - Gelation of bis(acyl-semicarbazides) and applications as crystallisation media

5.1 Introduction

This work follows on from chapter 4 and describes the gelation behaviour of bis(acyl-semicarbazides) derived from spacers **4.1**-**4.6**, and their application as crystallisation media. The self-assembly behaviour of all the compounds, including racemic mixtures of the R,R and S,S enantiomers, was tested in solvents spanning the polarity spectrum, to thoroughly characterise their effectiveness and versatility as molecular gels. XRPD, IR spectroscopy and DSC were utilised to compare the molecular packing and supramolecular interactions in the crystalline and xerogel phases to determine whether the supramolecular synthons identified in the crystal structures are also observed in the fibrous phases. The minimum gelation concentration and rheometric behaviour for a selection of gels were experimentally determined, whilst scanning electron microscopy was utilised to examine the supramolecular aggregates, to identify how spacer group, molecular chirality and racemic mixtures impact architectures on the supramolecular scale. A key property of supramolecular gels with regards to their use as crystallisation media is their reversible nature, thus the sensitivity of the gels to anion addition were also probed. Once fully characterised, an assortment of these gels was utilised as crystallisation media for a range of substrates, including API-salts, racemic drug mixtures and polymorphic compounds. It was hoped that the use of these gels as crystallisation media may influence the crystallisation outcomes compared to solution crystallisations and include attempts to facilitate API-mimetic and enantiomer-selective crystallisations.

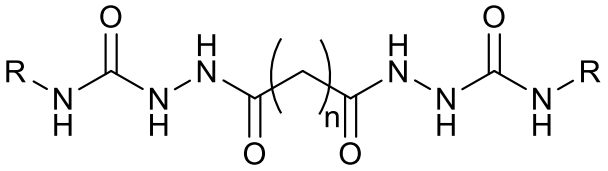

4.1 **n = 0**
4.2 **n = 1**
4.3 **n = 2**
4.4 **n = 4**

4.5 **n =**

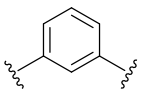

4.6 **n =**

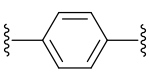

R=

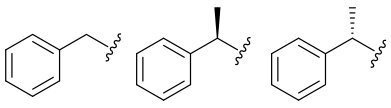

Benz **RR** **S**

5.2 Gel Characterisation

5.2.1 Gelation behaviour of aliphatic-spaced compounds

The gelation behaviour of the achiral benzyl-terminated and chiral 1-phenylethyl-terminated bis(*acyl*-semicarbazides) were compared (**Table 5-1**). The compounds were initially tested for gelation behaviour by forming 1% (w/v) solutions in solvents ranging the polarity spectrum and heating up to the boiling point of the solvent to facilitate dissolution. The resulting solutions were left to cool to room temperature and the vials were inverted after 24 hours to see whether any gel-like rheological behaviour was displayed. A partial gel result was determined where some gel-like rheology was exhibited but the full volume of solvent was not immobilised. On rare occasions, some of the compounds formed an opaque 'sponge-like' state that did not flow when inverted but allowed the entrapped solvent to slowly drip out. This result was not considered to meet the definition of a gel due to the failure to completely immobilize the solvent and was recorded as a precipitate. This ensured that the gel determination criteria by eye were as rigorous as possible. If no gel had formed after 48 hours, the sample was reheated to dissolve any precipitate and allowed cool to room temperature before being sonicated for 10-30 seconds in an ultrasound water bath. All gels were stable for months at 1 % w/v and gel formation occurred within minutes to 2 hours in most solvents for all compounds on a 0.5 mL scale, with sonication after dissolution for 3 to 15 seconds increasing the rate of gel formation. Most gels formed by were transparent or translucent (**Figure 5-1**), which is an useful trait for use as crystallisation media. Where insolubility was encountered, small aliquots of DMSO (10-100 µL) were added to the suspensions to aid dissolution, but this still resulted in no gelation in all cases, with crystalline precipitates or stable solutions forming instead.

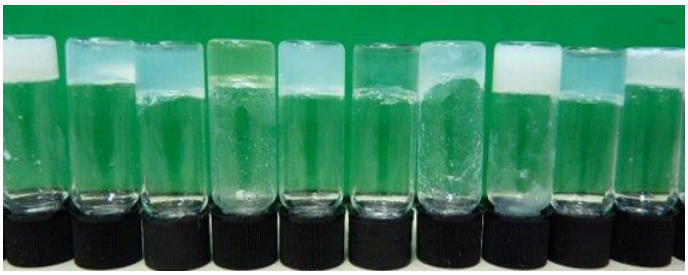

Figure 5-1. Photograph showing a selection of the 1% (w/v) gels formed by dissolving **4.1$_{SS}$** in different solvents, (left to right) 2-butanone, 1-pentanol, cyclohexanone, 1,3-dichlorobenzene, chlorobenzene, 1,4-dioxane, acetonitrile, acetone, ethanol and methanol.

Table 5-1. The full gel screening results of aliphatic-spaced bis(acyl-semicarbazides), derived from spacers **4.1-4.4** and the benzyl (**Benz**) and R-1-phenylethyl (**R,R**) end groups, at 1% w/v in a range of solvents. The RR and SS enantiomorphs exhibited identical gelation behaviour for each spacer. Results for 1:1 racemic mixtures of the R,R and S,S enantiomers (**Rac**) are also shown. IS = insoluble, X = crystallisation, P = precipitation, VL = viscous liquid, S= soluble, PG = partial gel G^{o}= opaque gel, G^{T}= translucent gel, G^{C}= transparent/clear gel. An asterisk indicates where sonication was required for gelation to occur. $^{\Delta}$ indicates a result at 2 % w/v.

	4.1			**4.2**			**4.3**			**4.4**		
	Benz	**R,R**	**Rac**	**Benz**	**R,R**	**Rac**	**Benz**	**R,R**	**Rac**	**Benz**	**R,R**	**Rac**
Acetone	IS	G^{o}	P	IS	G^{o}*	X	VL	P	P	VL	G^{o}	G^{o}
Acetonitrile	IS	G^{T}	X	IS	X	X	VL	G^{T}*	G^{o}	G^{T}	G^{C}	G^{C}
Dichloromethane	IS	G^{o}*	P	IS	P	P	IS	P	P	IS	P	P
Chloroform	IS	G^{C}	P	IS	P	P	IS	P	P	IS	P	P
1,4-dioxane	IS	G^{C}	P	P	G^{o}*	P	IS	G^{T}	G^{T}	IS	G^{T}	G^{T}
Benzene	IS	G^{o}	P	IS	P	P	IS	P	P	IS	P	G^{o}
Chlorobenzene	IS	G^{C}	P	PG^{Δ}	PG^{Δ}	P	PG^{Δ}	G^{T}	P	G^{T}	G^{T}	G^{T}
1,2-dichlorobenzene	P	G^{C}	P	G^{T}	G^{T}	P	G^{T}	G^{T}	G^{T}	G^{T}	G^{T}	G^{T}
1,3-dichlorobenzene	P	G^{C}	P	G^{T}	G^{T}	P	G^{T}	G^{T}	G^{T}	G^{T}	G^{T}	G^{T}
1,3,4-trichlorobenzene	P	G^{C}	P	G^{T}	G^{T}	P	G^{T}	G^{T}	G^{T}	G^{T}	G^{T}	G^{T}
Nitromethane	IS	G^{C}	X	G^{T}*	G^{o}*	P	G^{T}*	X	P	G^{T}	G^{T}	X
Nitrobenzene	P	G^{C}	P	G^{C}	G^{C}	G^{C}	G^{T}	G^{C}	G^{C}	G^{c}	G^{C}	G^{C}
Methanol	P	G^{o}*	X	P	S	X	P	P	X	X	X	X
Ethanol	IS	G^{T}	X	P	S	X	P	P	X	P	G^{T}*	X
1-propanol	IS	G^{T}	X	G^{T}	G^{T}*	P	G^{T}*	G^{T}*	P	G^{o}	G^{T}	X
2-propanol	IS	G^{T}	X	G^{T}	G^{T}*	P	G^{T}*	G^{T}*	P	G^{o}	G^{T}	X
1-butanol	IS	G^{T}	P	G^{T}	S	P	G^{T}*	G^{T}*	P	G^{o}	G^{T}	P
2-butanol	IS	G^{T}	P	G^{T}	S	P	G^{T}*	G^{T}*	P	G^{o}	G^{T}	P
1-pentanol	IS	G^{T}	P	PG^{Δ}	S	P	G^{T}	G^{T}*	P	G^{o}	G^{T}	P
2-pentanol	IS	G^{T}	P	PG^{Δ}	S	P	G^{T}	G^{T}*	P	G^{o}	G^{T}	P
Benzyl Alcohol	P	S	S	S	S	S	G^{T}	S	S	G^{T}	S	S
Ethylene Glycol	X	G^{T}	S	S	S	P	P	P	P	P	P	P
2-Butanone	IS	G^{T}	P	IS	G^{o}*	P	IS	G^{T}*	P	IS	G^{o}	P
Ethyl Acetate	IS	G^{o}	P	IS	P	P	IS	P	P	IS	G^{T}	P
Tetrahydrofuran	IS	G^{T}	P	PG^{Δ}	G^{o}*	P	IS	G^{T}*	G^{o}*	IS	G^{T}	G^{o}
Toluene	IS	G^{T}	P	IS	P	P	IS	PG^{Δ}	P	IS	G^{T}	P
o-xylene	IS	G^{T}	P	IS	P	P	IS	PG^{Δ}	P	IS	G^{T}	P
Mesitylene	IS	G^{T}	P	IS	P	P	IS	PG^{Δ}	P	IS	G^{T}	P
Pyridine	X	PG^{Δ}	S	X	S	P	X	S	P	X	S	S
Aniline	X	G^{C}	S	G^{T}	S	P	G^{T}	S	P	G^{T}	G^{T}	G^{T}
Cyclohexanone	IS	G^{T}	P	IS	P	P	IS	P	IS	IS	G^{o}	IS
Cyclopentanone	IS	G^{T}	P	IS	P	P	IS	P	IS	IS	P	IS
Cyclohexane	IS	G^{T}	P	IS	P	P	IS	P	IS	IS	P	IS
DMF	S	S	P	S	S	S	S	S	S	S	P	P
DMSO	S	S	S	S	S	S	S	S	S	S	S	S
DMA	S	S	P	S	S	S	S	S	S	S	P	P
2-Picoline	P	PG^{Δ}	X	X	S	X	X	S	P	X	S	P
3-Picoline	P	PG^{Δ}	X	X	S	X	X	S	P	X	S	P
4-Picoline	P	PG^{Δ}	X	X	S	X	X	S	P	X	S	P
Diethyl Ether	IS	IS	IS	IS	IS	IS	IS	IS	IS	IS	IS	IS
Water	IS	G^{T}*	P	IS	G^{T}*	P	IS	G^{o}*	IS	IS	IS	IS

As expected, the chiral aliphatic-spaced bis(acyl-semicarbazides) were more versatile molecular gels than their achiral counterparts, likely due to symmetry breaking which limits the viable space groups to Sohncke groups, potentially frustrating crystallisation and increasing the likelihood of gelation. R,R and S,S enantiomers exhibited identical gelation behaviour for all compounds. Gelators **4.1**$_{RR/SS}$ are highly versatile LMWGs, gelling 32 out of the 41 tested solvents and forming a further 4 partials gels in pyridine and the picolines at 2 % w/v. At concentrations above 5 % w/v these partial gels turn to a mixture of gel and precipitate and homogenous gelation is not achieved. Gelators **4.4**$_{RR/SS}$ are the next most versatile, gelling 24 solvents, followed by **4.3**$_{RR/SS}$ and **4.2**$_{RR/SS}$, which gel 16 and 12 solvents respectively, although it is worth noting that sonication was required to induce gel formation of these latter two LMWGs in most aliphatic solvents. Two general types of self-assembly behaviour are observed in the single crystals of aliphatic spaced bis(acyl-semicarbazides) presented in chapter 4 (**Figure 5-2**). These are urea α-tape assembly observed in crystal structures of **4.1**$_{RR}$, **4.2**$_{RR}$, **4.2**$_{Benz}$ and **4.4**$_{RR}$, whereby the molecules adopt an extended conformation, and bilayer assembly by folded conformers with an anti-syn urea group, observed in the **4.3**$_{SS}$, **4.3**$_{Rac}$ and metastable **4.2**$_{Rac}$ structures. It cannot be ruled out that the **4.3** derivatives can also adopt a linear conformation, and that **4.4** derivatives could also adopt a folded conformer. However, the two conformers observed for **4.2** and **4.3** derivatives provides the basis for a working hypothesis for why these compounds are less versatile gelators than the **4.1** and **4.4** derivatives. It is considered that the conversion from folded conformer to extended conformer is slow due to the requirement to overcome the energetically favourable intramolecular hydrogen bond in the folder conformer. This would hinder the ability of the **4.2** and **4.3** derivatives to assemble via unidirectional infinite α-tape synthons frequently associated with gelation. In contrast, only extended conformers assembling via α-tape synthons have been identified for **4.1** and **4.4** derivatives to date. Due to the diamide core, spacer **4.1** lacks the flexibility and length to enable intramolecular hydrogen bonds to form. Whilst spacer **4.4** does exhibit molecular flexibility that could enable an intramolecular hydrogen bond to form, the longer spacer in comparison with **4.2** and **4.3** derivatives, increases the entropic penalty and makes intramolecular hydrogen bond formation less energetically favourable. Therefore, it is proposed that the molecules of **4.4** readily

adopts an extended conformer, which can also rapidly self-assemble via urea tape synthons to form anisotropic fibrous aggregates.

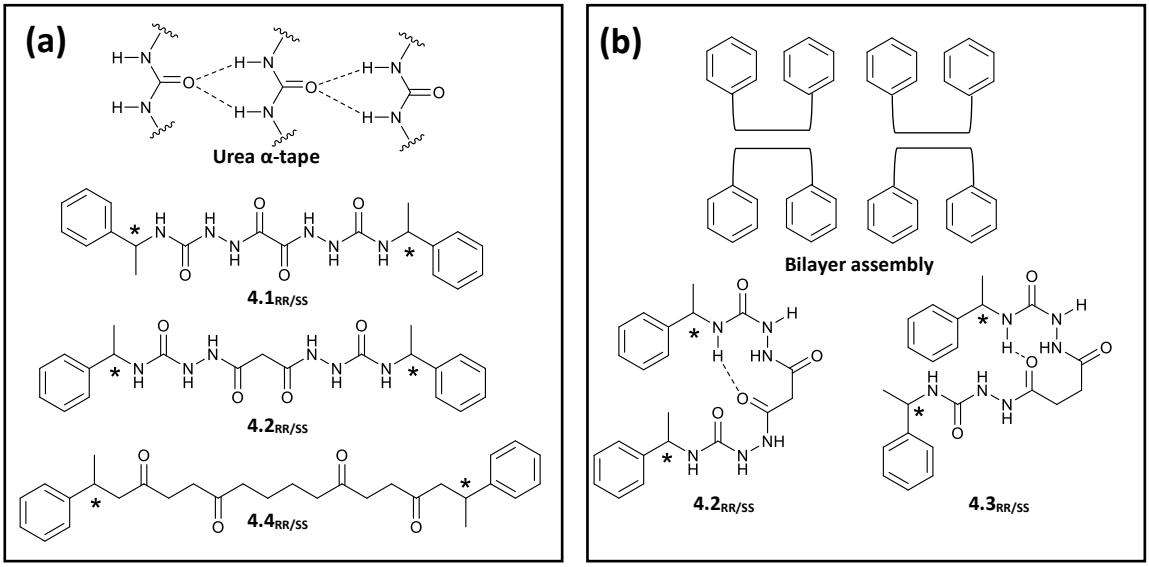

Figure 5-2. Summary of the general assembly behaviours observed in the single crystal structures of aliphatic-spaced bis(acyl-semicarbazides). **(a)** The urea tape synthon (top) and molecules observed forming urea tapes in the single crystal structures. **(b)** The bilayer assembly with the molecule core represented by lines (top) and the compounds that exhibited this assembly behaviour, drawn in their folded conformations.

Most LMWGs only gel a small selection of solvents,[1] but these compounds gelled a broad range, mutually gelling acetonitrile, 1,4-dioxane, the chlorobenzenes, nitrobenzene, aliphatic alcohols and THF. The versatility of these gelators is particularly useful for use as crystallisation media, as it increases the number of solvents, including mixtures, that can be used in the crystallisation screening procedure, which consequently increases the chance of elucidating novel polymorphic or solvate forms. Furthermore, gelators **4.1$_{RR/SS}$**, **4.2$_{RR/SS}$** and **4.3$_{RR/SS}$** can all be classed as ambidextrous as they also gel water (**Figure 5-3**). Ambidextrous gelators are relatively uncommon and tend to be amphiphiles,[2] since amphiphilicity can promote solubility in both organic solvents and water. Amphiphilicity is also important in enabling the interactions that drive both hydrogelation and organogelation to form, as hydrophobic aromatic-aromatic interactions are typically a major driving force for gelation of water,[3] whilst hydrogen bonding often plays a higher importance in driving fibre self-assembly in organic solvents.

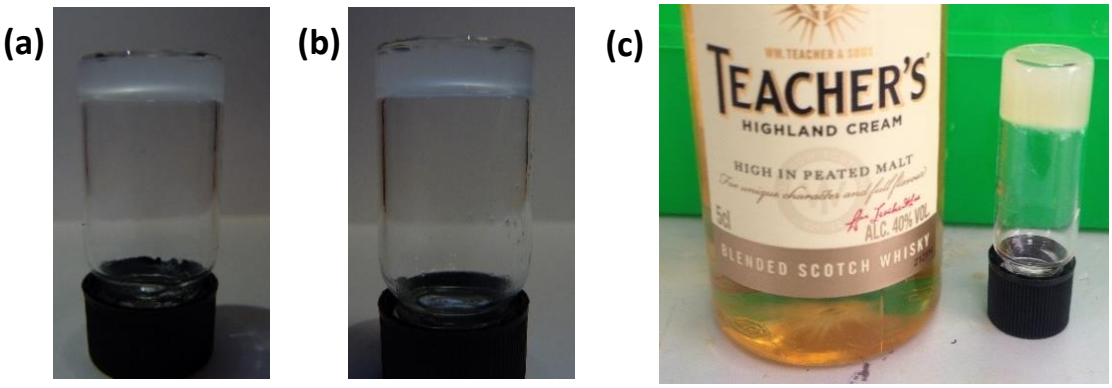

Figure 5-3. Images of **(a)** a 1 mL **4.1$_{RR}$** hydrogel at 0.1 % w/v, **(b)** a 1 mL **4.2$_{RR}$** hydrogel at 0.25 % w/v and **(c)** a 0.5 mL **4.1$_{RR}$** gel at 0.25 % w/v in a 40 % alcoholic aqueous solution. Photographs were taken 24 hours after vial inversion.

Molecular chirality is not a prerequisite for gelation of this series of bis(acyl-semicarbazides) and the achiral aliphatic-spaced compounds **4.2-4.4$_{Benz}$** also yield effective molecular gels (**Figure 5-4**). Compound **4.4$_{Benz}$** was the most versatile gelling 14 solvents, with **4.2$_{Benz}$** and **4.3$_{Benz}$** gelling 9 and 10 solvents, respectively. The solvents gelled by these compounds are typically aromatic or alcoholic solvents with relatively high boiling points which is due to the high temperature typically being required to achieve complete dissolution. This solubility difference between achiral and chiral derivatives is particularly stark when comparing the bis(*acyl*-semicarbazides) derived from the oxalyl spacer (n=0), with **4.1$_{Benz}$** displaying negligible solubility in most of the tested solvents, whilst **4.1$_{RR/SS}$** were highly versatile LMWGs. The higher relative solubility of the chiral compounds is expected, since both methylation and molecular chirality tend to increase the solubility of compounds.[4,5] However, the poor solubility of **4.1$_{Benz}$** indicates a potential limitation of spacer **4.1** in future LMWG designs and further bis(acyl-semicarbazides) derived from **4.1** utilising a range of structurally diverse end groups should be investigated to see how limiting this factor may be.

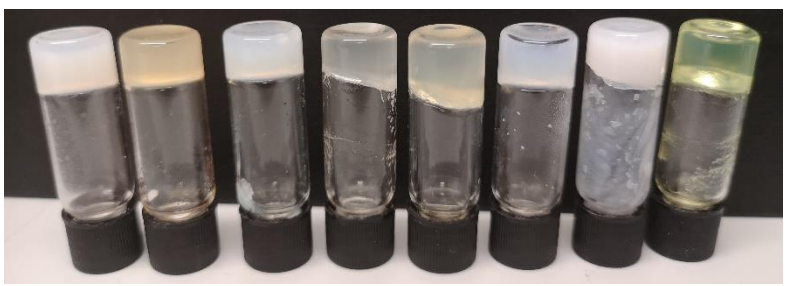

Figure 5-4. Gels of **4.4$_{Benz}$** at 1 % w/v in (left to right) 1-pentanol, 1,2-dichlorobenzene, acetonitrile, benzyl alcohol, 1,3-dichlorobenzene, nitromethane, propan-1-ol and nitrobenzene.

Racemic mixtures of enantiomers typically yield fewer gels than the enantiopure compounds, with exceedingly rare reports of racemic mixtures being more versatile and effective gelators than their homochiral forms.[6–9] Indeed, in this study racemic mixtures of the R,R and S,S enantiomers result in a reduction in the number of gels formed for each aliphatic-spaced derivative tested, with the effect becoming more pronounced as spacer chain length decreases (**Figure 5-5**). The racemic mixture of the most versatile gelators (**4.1$_{Rac}$**) resulted in a complete loss of gelation with zero gels forming and crystallisation or precipitation commonly observed instead. Whilst the effect is less marked for **4.4$_{rac}$**, there is still a significant drop in the number of gels formed; from 22 by the homochiral analogues to 11 by the racemic mixture. The sharp deterioration in gelation behaviours demonstrates there is a strong and preferential association between the two distinct enantiomers, which is expected as the formation of a racemic lattice overcomes the symmetry-breaking effect induced by molecular chirality and increasing the viable space groups promotes crystallisation over gelation. Indeed, this association between enantiomers was identified in the racemic crystal structures for **4.1**, **4.2** and **4.3** derivatives.

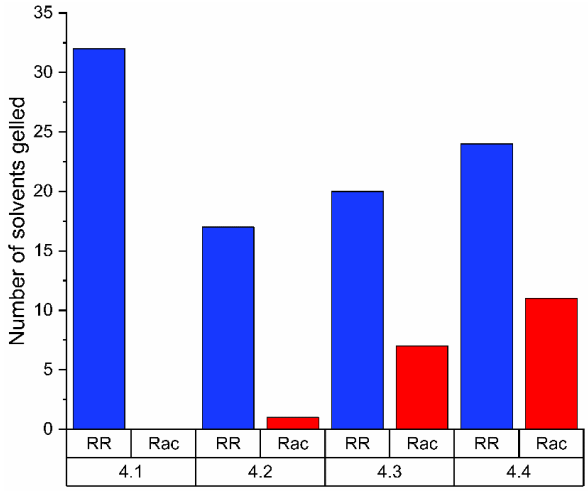

Figure 5-5. Comparison of the number of solvents gelled by homochiral (RR) and racemic mixtures (Rac) of 1-phenylethyl terminated bis(acyl-semicarbazides) derived from spacers **4.1**-**4.4**.

An intriguing phenomenon is observed when a single enantiomer of **4.2$_{RR}$** or **4.2$_{SS}$** is dissolved in acetone or 1,4-dioxane at concentrations above 0.5 % w/v via heating. This process results in the formation of spherical liquid crystalline droplets or spherulites within hours of cooling. These mesophases exhibit a birefringent Maltese cross that rotates with the polarisation axis of light (**Figure 5-6**). Sonication of the sol after heating and cooling but prior to mesophase formation results in gelation within

hours. Molecules that form liquid crystalline phases often consist of π-conjugated functionalities with hydrophilic or aliphatic chains, whilst flat structural features, such as aromatic rings, further increase the likelihood of liquid crystallinity.[10,11] Interestingly, sonication of this mesophase results in the formation of an opaque gel within seconds. Sonication can significantly impact fibre structure and morphology by cleaving supramolecular interactions, such as hydrogen bonds and π-π stacking, between gel molecules enabling assembly into new structures.[12–14] Additionally, sonication produces longitudinal pressure waves, which results in oscillating compression of the sol in the same direction as the wave.[49,50] This directional compression can promote the alignment of nanofibers enabling the formation of larger fibres, which can then entangle to form the fibrous network required for gelation. It is considered that the mesophase formed reported her likely corresponds to a metastable phase frustrating crystallisation, potentially with molecules of **4.2$_{RR}$** in the folded conformation as observed in the metastable **4.2$_{Rac}$** acetonitrile solvate. The restricted rotation around the amide bonds and favourability of the intramolecular S(9) hydrogen bond slows the transition from the folded conformer to the extended conformer associated with urea tape assembly. It may be that sonication here accelerates the conformational transition from folded to extended conformer, with the extended conformers assembling to form a gel. The competition between mesophase and gelation may also contribute to the inconsistent gelation behaviour of **4.2$_{RR}$** in 1,4-dioxane.

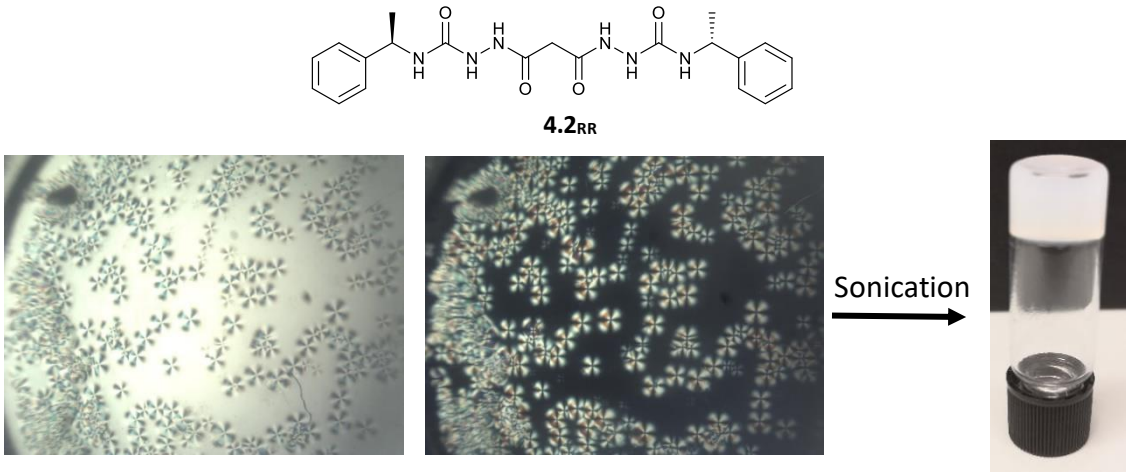

Figure 5-6. A photograph of liquid crystalline droplets formed by dissolving 5 mg of **4.2$_{RR}$** in 0.5 mL 1,4-dioxane. The Maltese cross rotates with the polarisation of light and sonication of this liquid crystalline phase results in an opaque gel forming.

The aromatic-spaced compounds are far less versatile as LMWGs compared to the aliphatic-spaced compounds (**Table 5-2**), which is anticipated due to the observed duplex assembly and lack of infinite, unidirectional hydrogen bond synthons in the crystal structures for these compounds, as reported in chapter 4 (**Figure 5-7**). Indeed, the p-phenylene-derivatives **4.6**$_{\mathbf{Benz}}$ and **4.6**$_{\mathbf{RR/SS}}$ were effectively non-gelators, with the chiral analogues exclusively gelling nitrobenzene at 2 % w/v and the achiral compound failing to yield any homogenous gels, despite forming 7 partial gels in aromatic solvents and pentanol. Increasing the concentration above 2 % w/v resulted in a crystalline precipitate forming rather than homogenous gelation. Meanwhile, both chiral and achiral isophthalic-derived gelators (**4.5**) gelled 7 solvents each, albeit only acetonitrile and 1,4-dioxane were gelled by both analogues.

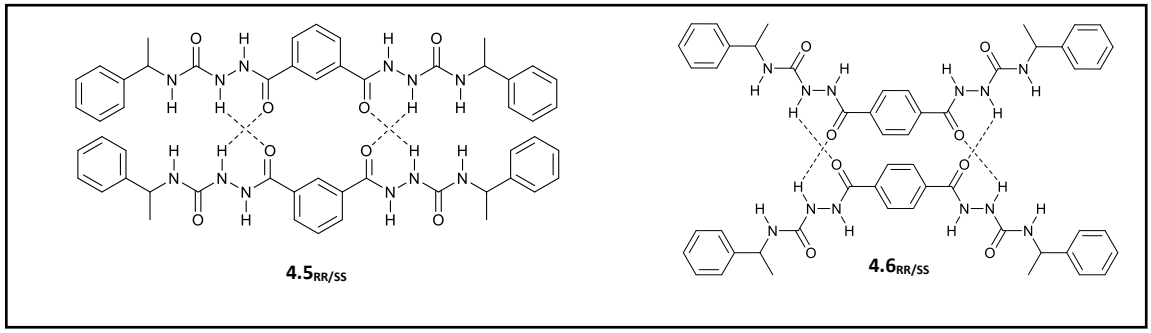

Figure 5-7. 2D-representations of the dimer assembly observed in the single crystals of the aromatic-spaced compounds **4.5**$_{\mathbf{RR/SS}}$ and **4.6**$_{\mathbf{RR/SS}}$. The lack of unidirectional infinite urea-tape synthon formation likely explains why the aromatic-spaced bis(acyl-semicarbazide) compounds are less effective gelators than the aliphatic-spaced compounds.

Table 5-2. The full gel screening results of aromatic-spaced bis(acyl-semicarbazides), derived from spacers **4.5 and 4.6** and the benzyl (**Benz**) and R-1-phenylethyl (**R,R**) end groups, at 1% w/v in a range of solvents. The R,R and S,S enantiomorphs exhibited identical gelation behaviour for each spacer. Results for 1:1 racemic mixtures of the R,R and S,S enantiomers (**Rac**) are also shown. IS = insoluble, X = crystallisation, P = precipitation, VL = viscous liquid, S= soluble, PG = partial gel G^{o}= opaque gel, G^{T}= translucent gel, G^{C}= transparent/clear gel. An asterisk indicates where sonication was required for gelation to occur.

	4.5			**4.6**		
	Benz	**R,R**	**Rac**	**Benz**	**R,R**	**Rac**
Acetone	P	G^{o}*	P	P	P	P
Acetonitrile	G^{o}	G^{o}	G^{o}	P	P	P
Dichloromethane	IS	IS	IS	IS	IS	IS
Chloroform	P	IS	IS	P	IS	IS
1,4-dioxane	G^{o}	G^{o}	X	IS	IS	IS
Benzene	P	S	P	IS	P	P
Chlorobenzene	P	P	P	PG	P	P
1,2-dichlorobenzene	P	P	P	PG	S	P
1,3-dichlorobenzene	P	P	P	PG	S	P
1,3,4-trichlorobenzene	P	S	S	PG	S	P
Nitromethane	IS	G^{o}*	P	IS	IS	IS
Nitrobenzene	G^{T}	G^{T}	PG	PG	$G^{T\Delta}$	P
Methanol	X	P	X	X	X	X
Ethanol	P	X	X	P	P	P
1-propanol	P	S	P	P	P	P
2-propanol	P	S	P	P	P	P
1-butanol	P	S	P	P	P	P
2-butanol	P	S	P	P	P	P
1-pentanol	P	S	P	PG	P	P
2-pentanol	P	S	P	PG	P	P
Benzyl Alcohol	G^{T}	S	S	P	X	X
Ethylene Glycol	G^{T}	S	S	P	X	X
2-Butanone	G^{o}	P	P	P	IS	IS
Ethyl Acetate	IS	IS	IS	IS	IS	IS
Tetrahydrofuran	G^{o}	P	P	P	IS	IS
Toluene	IS	P	P	IS	P	P
o-xylene	IS	P	P	IS	P	P
Mesitylene	IS	P	P	IS	P	P
Pyridine	X	S	P	S	S	S
Aniline	PG	PG	PG	PG	S	S
Cyclohexanone	IS	G^{o}	P	IS	IS	IS
Cyclopentanone	IS	G^{o}	P	IS	IS	IS
Cyclohexane	IS	G^{o}	P	IS	IS	IS
DMF	S	S	S	S	S	S
DMSO	S	S	S	S	S	S
DMA	S	S	S	S	S	S
2-Picoline	S	S	P	S	S	P
3-Picoline	S	S	P	S	S	P
4-Picoline	S	S	P	S	S	P
Diethyl Ether	IS	IS	IS	IS	IS	IS
Water	IS	IS	IS	IS	IS	IS

The critical concentration of gelation (CCG) was recorded for a range of gels for compounds **4.1-4.6$_{RR}$** (**Table 5-3**). The results show that **4.1$_{RR}$** and **4.4$_{RR}$** are the most potent gelators, capable forming gels below 0.5 % w/v in some solvents. Compound **4.1$_{RR}$** is also capable of forming gels at 0.05 % w/v in ethanol. Gelators **4.2$_{RR}$** and **4.3$_{RR}$** exhibit CCGs between 0.5-1 % w/v in the solvents tested, whilst the sole **4.6$_{RR}$** nitrobenzene gel required a relatively high concentration of 1.3 % w/v for gelation. The hydrogels of **4.1$_{RR}$**, **4.2$_{RR}$** and **4.3$_{RR}$** have significantly lower CCGs than the corresponding organogels, with **4.1$_{RR}$** being a particularly effective hydrogelator with a CCG of 0.08 %. This is expected to be due to the rigid structure of the oxalamide **4.1** spacer core, meaning the molecular maintains a linear conformation with aromatic functionalities at either end. The current hypothesis is that this results in large hydrophobic forces capable of immobilising water whilst urea α-tape synthons are maintained and drive fibril formation.

Table 5-3. Critical concentrations of gelation (% w/v) for gels of **4.1$_{RR}$-4.6$_{RR}$** in a range of solvents. NG signifies solvents in which the compound is a non-gelator.

	CCG / % w/v						
	Nitrobenzene	**Propan-1-ol**	**1,4-dioxane**	**Acetonitrile**	**THF**	**Toluene**	**H_2O**
4.1$_{RR}$	0.4	0.2	0.5	0.2	0.3	0.8	0.08
4.2$_{RR}$	0.8	1	0.8	1	1.2	NG	0.5
4.3$_{RR}$	0.5	0.5	0.5	0.5	0.8	1	0.2
4.4$_{RR}$	0.4	0.3	0.5	0.5	0.6	0.7	NG
4.5$_{RR}$	0.8	NG	0.9	0.9	NG	NG	NG
4.6$_{RR}$	1.3	NG	NG	NG	NG	NG	NG

5.2.2 Solid-state analysis

XRPD, IR spectroscopy and DSC were employed to compare the molecular packing and supramolecular interactions in the xerogel and crystalline phases.[15] The objective is to identify whether the supramolecular synthons observed in the SCXRD structures are also present in the gel state. The solvated nature of the single crystal structures means differences between the experimental XRPD patterns of xerogels formed from different solvents and calculated patterns from SCXRD data were anticipated but may be useful in identify any isostructural forms. It should be noted that the xerogel samples were typically dried under ambient conditions and transitions from

metastable forms to more stable crystalline forms cannot be ruled out. Gels formed from solvents with high boiling points and negligible evaporation at room temperature were dried in an oven between 50-70 ^{o}C or under vacuum.

Urea α-tape assembly can be correlated with gel fibre assembly by **4.1$_{RR}$**, with the IR spectra of xerogels and crystals matching with near-identical peaks in the NH regions (3300-3000 cm^{-1}) and C=O regions (1900-1600 cm^{-1}) (**Figure 5-8**). The DSC data reveals the crystals and xerogels all melt sharply at 219 ^{o}C, supporting the hypothesis that the same supramolecular synthons are present in the crystalline and gel phases. The XRPD patterns of the **4.1$_{RR}$** ethanol, nitrobenzene, chlorobenzene, chloroform and THF xerogels are all identical and further supports that they are isostructural forms. The rigidity of the oxalyl core [16] and preference for a **C**(O)$_{amide}$-**N**-**N**-**C**(O)$_{urea}$ torsion angle close to 90 ^{o} [17] likely explains this isostructural behaviour and reduces the likelihood of any conformational polymorphism or alternative molecular packing arrangements.

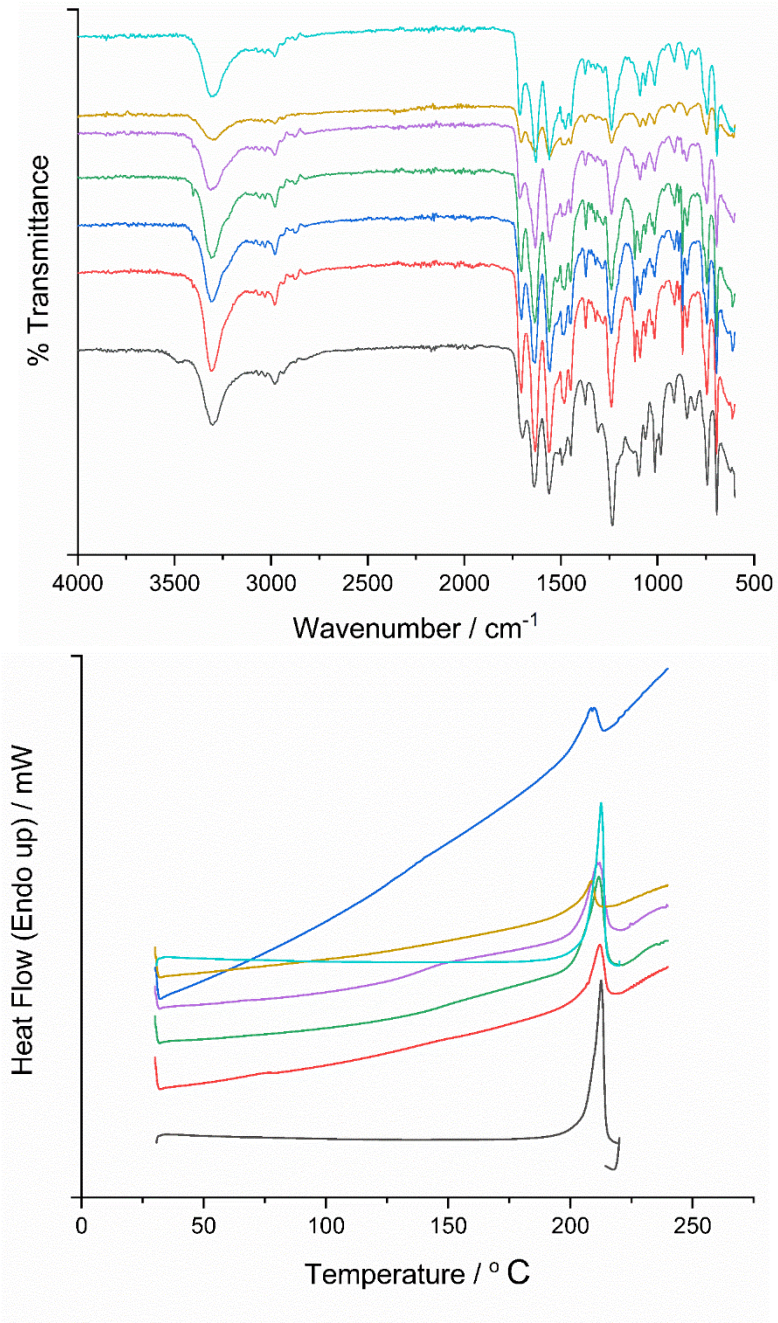

Figure 5-8. (a) IR spectra of **4.1$_{SS}$** crystals (in black) and **4.1$_{SS}$** xerogels formed from ethanol (red), THF (blue), chloroform (green), chlorobenzene (purple), nitrobenzene (yellow) and acetonitrile (light blue). **(b)** The DSC thermograms of the **4.1$_{SS}$** crystals and xerogels, all with the same colour schemes as in the IR spectra. The IR spectra are a good match, indicating the same supramolecular interactions in all xerogel and crystal forms. The DSC data shows similar melts around 219 °C for all forms.

No gels were formed by **4.1$_{Rac}$** but the precipitate obtained from nitrobenzene and ethanol both perfectly match the calculated XRPD pattern from the anhydrous **4.1$_{Rac}$** single crystal data (**Figure 5-9**). In this single crystal structure, molecules self-assemble via urea α-tapes, but also form N-H$_{(amide)}$···O=C$_{(urea)}$ hydrogen bonds perpendicular to the urea tape direction. This additional interaction likely weakens urea tape hydrogen

bonds and the combination of interactions results in 2-dimensional assembly as opposed to the 1-dimensional assembly typically required for fibre formation, thus this likely explains the non-gelator behaviour of **4.1$_{Rac}$**.

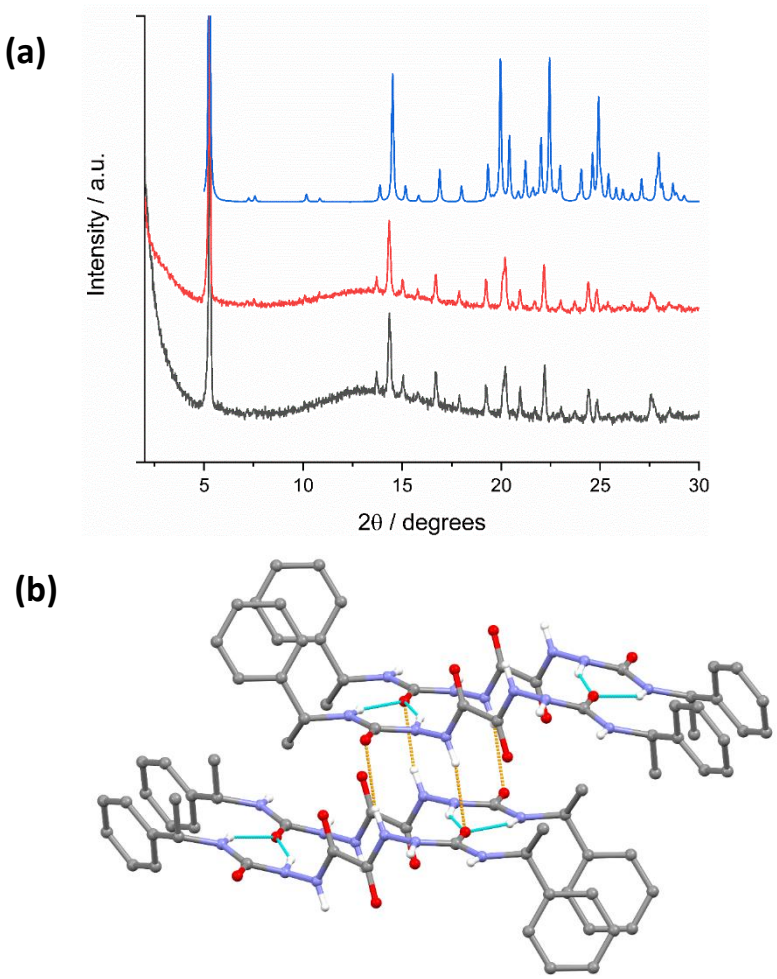

Figure 5-9. (a) The experimental XRPD patterns of **4.1$_{Rac}$** precipitate from nitrobenzene (black) and ethanol (red) are a good match with the calculated XRPD pattern from the **4.1$_{Rac}$** crystal structure. **(b)** The urea tape synthon (in light blue) and $NH_{(amide)}\cdots O_{(urea)}$ interactions (in orange) form perpendicular to one another and promote 2-dimensional assembly, which likely explains the lack of gelation of **4.1$_{Rac}$.**

Two distinct forms of **4.2$_{RR}$** can be observed in the XRPD data for xerogels depending on solvent formed from (**Figure 5-10**). The IR, XRPD and DSC data for the xerogel of **4.2$_{RR}$** formed from 1,4-dioxane matches the ethanol solvate, indicating parallel urea tapes drive this gel formation. However, xerogels formed from propan-1-ol, chlorobenzene and acetonitrile reveal different molecular packing arrangements. Interestingly, the XRPD pattern of the xerogel formed from a nitrobenzene sonogel reveals a mixture of the two distinct forms, with peaks matching both the calculated SCXRD pattern and experimental nitrobenzene xerogel (**Appendix 3**). This indicates

that either the **4.2$_{RR}$** fibres are polymorphic and some of the gels are a mixture of two distinct forms, or that they undergo a phase transition upon drying.

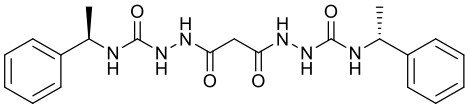

4.2$_{RR}$

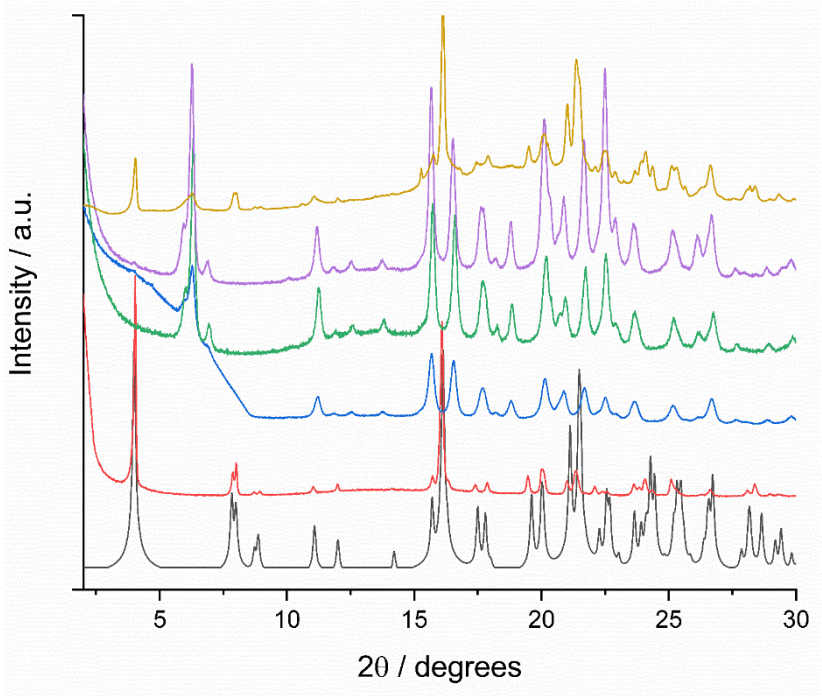

Figure 5-10. XRPD patterns of (top to bottom) xerogels of **4.2$_{RR}$** from nitrobenzene (yellow), acetonitrile (purple), propan-1-ol (green), chlorobenzene (blue) and 1,4-dioxane (red) and the calculated XRPD pattern from the **4.2$_{RR}$** ethanol solvate (black). The 1,4-dioxane xerogel closely matches the ethanol solvate pattern indicating identical molecular packing. The acetonitrile, chlorobenzene and propan-1-ol xerogels do not match the crystal pattern indicating an alternative molecular packing. The nitrobenzene xerogel exhibits peaks from both distinct patterns indicating it is a mixture of both polymorphic forms.

Only the xerogels of **4.4$_{RR}$** generated XRPD patterns with broad peaks that were inadequate for comparison between xerogel and crystal forms (**Appendix 3**). The IR spectra of **4.4$_{RR}$** xerogels however differ significantly in the NH stretch (3300-3000 cm^{-1}) and carbonyl peaks (1900-1600 cm^{-1}) which indicates that different xerogels exhibit different supramolecular environments (**Figure 5-11**). The this may be due to the extended length on the aliphatic spacer enabling a greater degree of conformational flexibility and a higher likelihood of polymorphism compared with the 4.1-derivatives.[18]

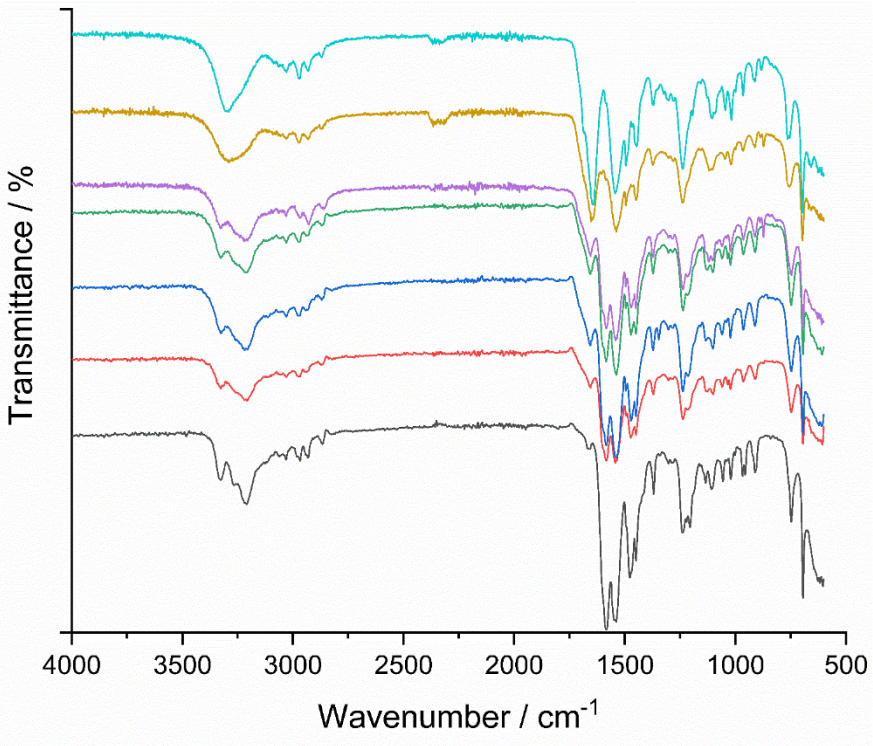

Figure 5-11. IR spectra of (from top to bottom) **4.4$_{SS}$** methanol solvate crystals (light blue), **4.4$_{RR}$** ethanol solvate (gold), and **4.4$_{RR}$** xerogels formed from nitrobenzene (purple), chlorobenzene (green), propan-1-ol (blue), 1,4-dioxane (red) and nitromethane (black). The spectra of the crystal forms are significantly different from the spectra of the xerogels, particularly at the NH stretch region (3300-3000 cm $^{-1}$) and the carbonyl region (1900-1600 cm^{-1}). This indicates the supramolecular interactions in gel and crystalline phases are different. The spectra of the xerogels are broadly the same regardless of solvent, indicating the supramolecular interactions in all **4.4$_{RR}$** gels are identical or remarkably similar.

The **4.3$_{RR}$** xerogels also appear to have two distinct forms. The XRPD of 1,4-dioxane and propanl-1-ol xerogels both exhibit peaks at identical 2θ values, but these do not match the calculated XRPD pattern of the **4.3$_{SS}$** water/methanol solvate (**Figure 5-12**). The XRPD pattern of the nitrobenzene xerogel only exhibits two peaks at 7.0 ° and 20.3 °, likely due to preferred orientation of the xerogel sample, but both peaks match with peaks in the calculated **4.3$_{SS}$** solvate pattern and are absent in the other xerogel patterns. This provides some evidence that the molecular packing in the nitrobenzene xerogel is the same as that in the crystal structure and is different from the other xerogels. This is further confirmed by comparison of the IR spectra with the spectra of the nitrobenzene xerogel and **4.3$_{SS}$** solvate being near identical (**Appendix 3**). This means the folded molecular conformation and bilayer assembly may drive gelation in nitrobenzene.

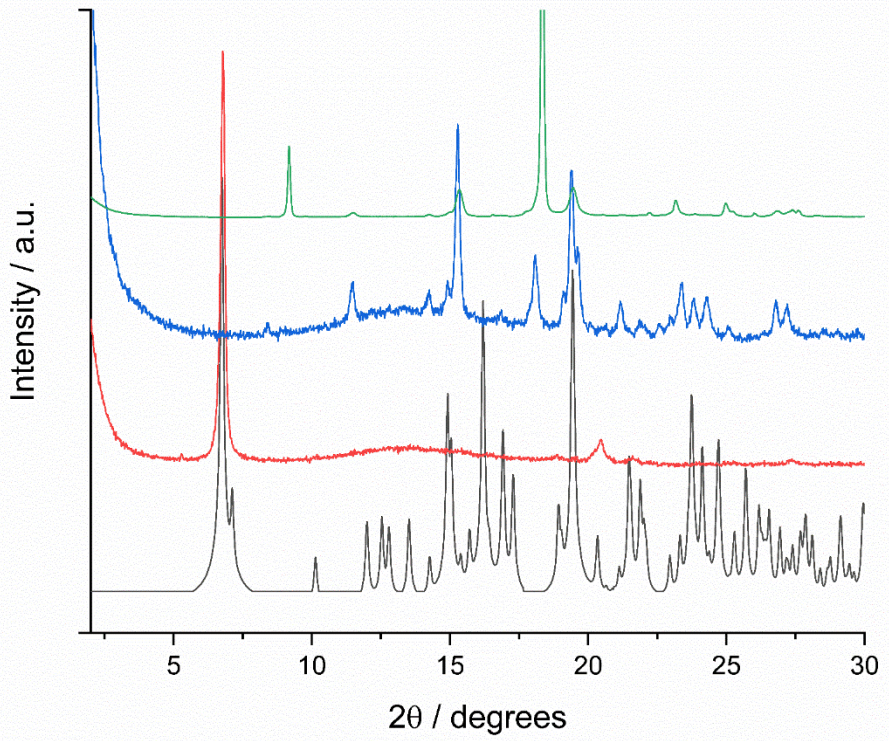

Figure 5-12. Experimental XRPD patterns of (top to bottom) **4.3$_{RR}$** xerogels formed from propan-1-ol (green), 1,4-dioxane (blue) and nitrobenzene (red), and the calculated XRPD pattern from the **4.3$_{SS}$** water/methanol solvate structure (black).

The **4.3$_{RR/SS}$** DSC data further confirms the similarities between nitrobenzene xerogel and solvate crystals, and the differences between these two forms and the 1,4-dioxane xerogel (**Figure 5-13**). Single high-intensity endothermic peaks with onset of melting at 153 ^{o}C for both the **4.3$_{SS}$** solvate crystals and the nitrobenzene xerogel, whilst an peak with onset of melting at 196 ^{o}C is observed for the 1,4-dioxane xerogel. This latter result likely reflects a more stable form of **4.3$_{SS}$**, potentially exhibiting an extended conformer, as opposed to the identified folded conformer. The 1,4-dioxane xerogel also has a miniscule endothermic peak with onset of melting at 153 ^{o}C indicating that trace impurity of the crystal form is also present in the sample, but not identifiable by XRPD/IR spectroscopy. The slight difference in melt point between the solvate and nitrobenzene xerogel may be due to the different in solvent nature.

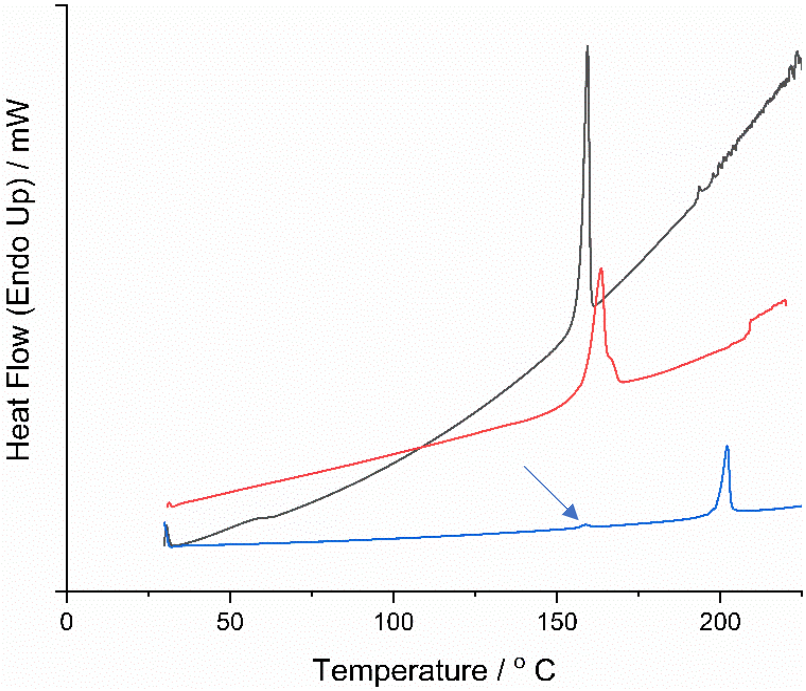

Figure 5-13. DSC thermograms of **4.3$_{SS}$** solvate crystals (black), the **4.3$_{RR}$** nitrobenzene xerogel (red) and **4.3$_{RR}$** 1,4-dioxane xerogel (blue). The profiles of the solvate and nitrobenzene xerogel are almost the same with onset of melting at 153 °C, whilst the 1,4-dioxane reveals a large endothermic peak at with onset of melting at 196 °C. The latter xerogel also reveals a minor endotherm peak with onset of melting at 153 °C, indicating a small amount of solvate form is also present in the sample.

Many of the gels formed by **4.2$_{RR/SS}$** and **4.3$_{RR/SS}$** required sonication to form. This supports the working hypothesis that the extended conformation and associated α-tape assembly of these bis(acyl-semicarbazide) compounds is associated with gelation, whilst the folded conformations are less like to promote gelation. Ultrasound has been shown to disrupt intramolecular hydrogen bonds[19] which can induce significant conformational changes that results in alternative intermolecular supramolecular synthons forming. Indeed, here it is anticipated that sonication breaks the S(9) and S(10) motifs in the folded conformers of **4.2** and **4.3** derivatives and overcomes the barrier to conversion to the extended conformer (**Figure 5-14**). The extended conformer can then rapidly form intermolecular synthons, such as urea α-tape synthons, to form fibrous aggregates. Crystallographic evidence of both folded and extended conformers for **4.2$_{RR}$** have discussed in Chapter 4. Only a folded conformer of **4.3$_{SS}$** has been identified through crystallography. However, the distinct XRPD patterns and DSC thermograms of the **4.3$_{SS}$** xerogels formed from sonogels means it is a possibility that ultrasound-induces a conformational change and drives an alternative self-assembly behaviour. SS-NMR was considered to further explore this possibility,

however, attempts to obtain adequate amounts of crystalline material were unsuccessful, particularly for the metastable **4.2$_{Rac}$** acetonitrile disolvate and **4.3$_{SS}$** methanol-water solvate.

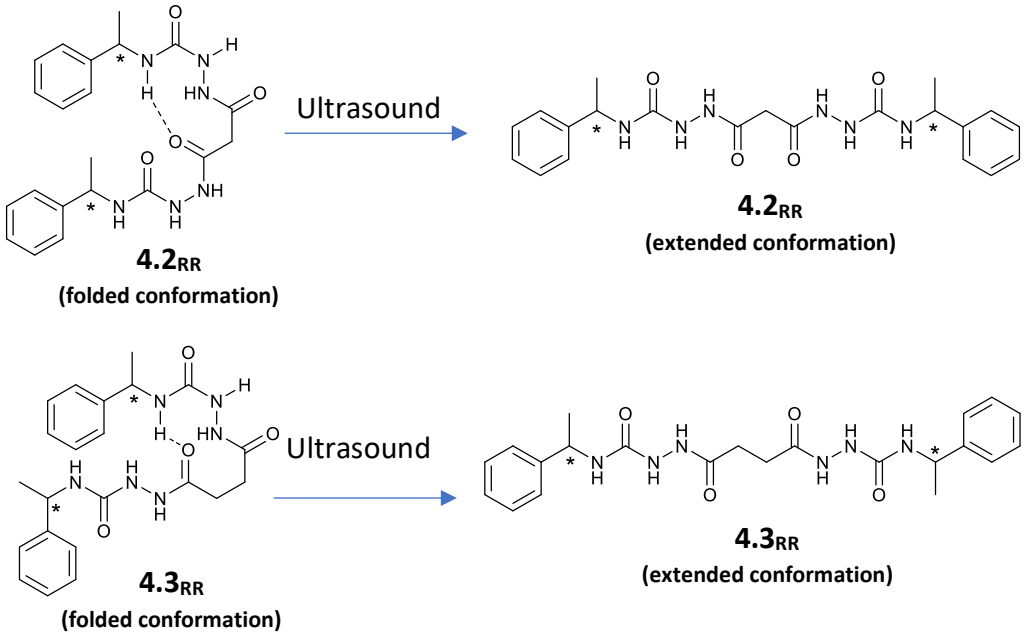

Figure 5-14. Proposed conformational change from folded to extended conformation for compounds **4.2$_{RR}$** and **4.3$_{RR}$** induced by ultrasound. Crystallographic evidence of both extended and folded conformation of **4.2$_{RR}$** were discussed in Chapter 4. Only the folded conformation of **4.3$_{RR}$** has been identified through crystallography. However, the XRPD patterns of the sonogels xerogels differ to those of the nitrobenzene xerogel with no ultrasound treatment and the calculated XRPD pattern from SCXRD data.

Finally, the XRPD patterns for the **4.5$_{SS}$** ethanol disolvate and **4.5$_{SS}$** xerogel formed from acetonitrile do not match, although have some peaks in common (**Figure 5-15**). Differences between the two may be due to the differences in solvent within the structures. However, the XRPD patterns for the **4.6$_{RR}$** benzyl alcohol solvate closely matches the pattern for corresponding nitrobenzene xerogel. This indicates that duplex assembly occurs in both gel and crystalline phases. Whilst finite molecular duplex assembly is not usually associated with gelation, a bis(acyl-semicarbazide) superorganogelator reported by Chen et al. was predicted to form gels via initial dimer assembly via the same amide-urea hydrogen bonds, via DFT calculations and NMR experiments.[20] This work supports their findings of gelation via duplex assemblies.

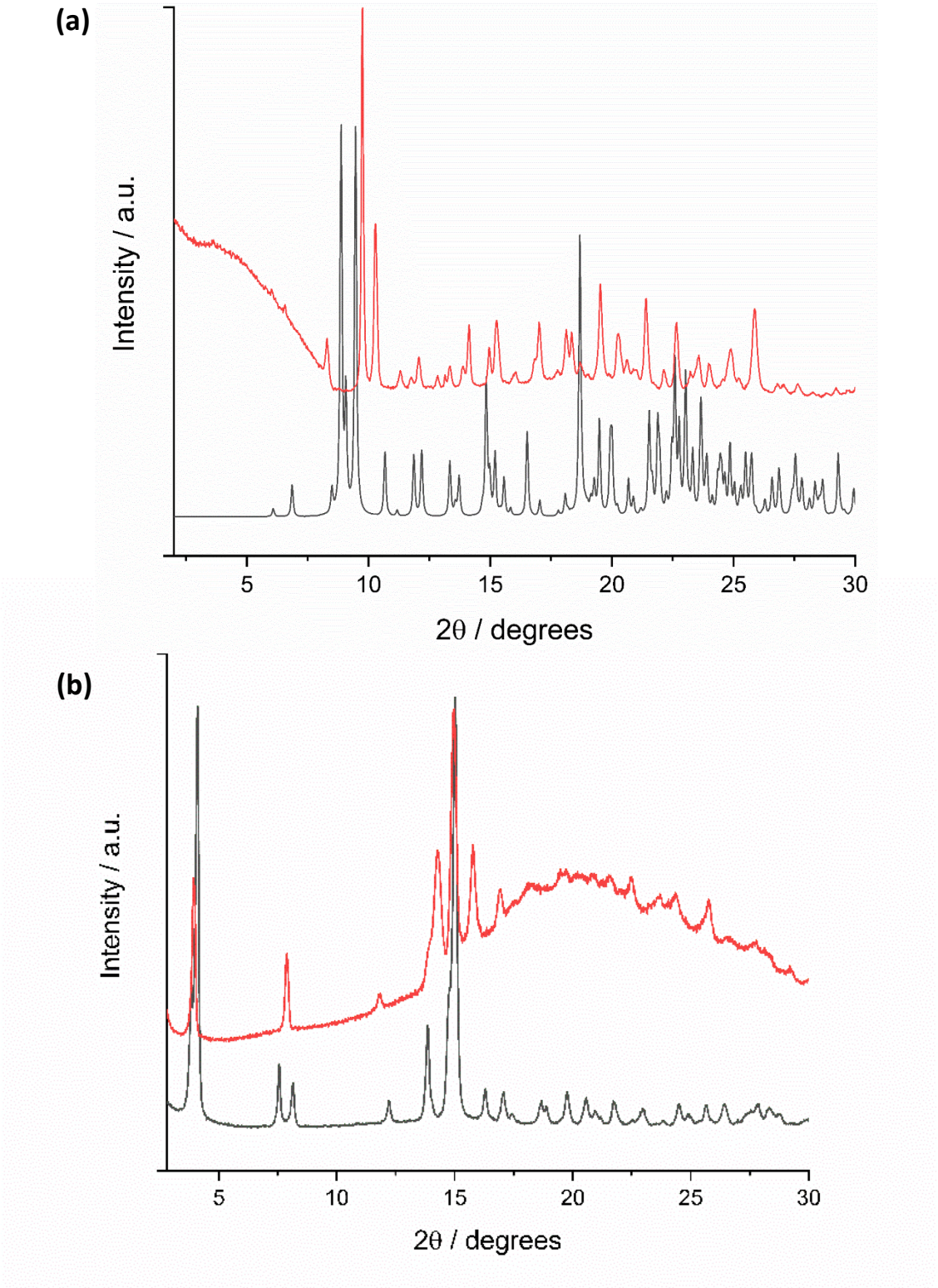

Figure 5-15. XRPD patterns of **(a)** the acetonitrile **4.5$_{SS}$** xerogel (red) and calculated from **4.5$_{SS}$** ethanol solvate (black), and **(b)** the **4.6$_{RR}$** nitrobenzene xerogel (red) and calculated from **4.6$_{RR}$** benzyl alcohol solvate (black). The patterns show numerous identical peaks in the crystal and fibrous phases, particularly between 0-20 °, indicating the same or highly similar molecular packing arrangements in both phases.

5.2.3 Rheological analysis

Rheological analyses of the 1 % w/v dioxane gels for compounds **4.1$_{RR}$**-**4.5$_{RR}$** were undertaken via frequency sweep and oscillatory stress experiments (**Figure 5-16**). Gels were pre-formed in vials on a 2 mL scale by heating until all solid was dissolved, allowed to cool before being sonicated for 30 seconds, due to the long gelation time for most of the gels on a larger scale (30 minutes to 12 hours) and requirement for sonication of **4.2$_{RR}$** and **4.3$_{RR}$** to form gels. Pre-forming the gels and transferring to the rheometry plate is not ideal as the transfer process can affect the gel integrity and means there is more variation between repeated experiments. However, some general observations can be made from the data. It is worth noting that rheological analysis of the **4.6$_{RR}$** gel was not undertaken due to harmful nature of nitrobenzene and a lack of adequate ventilation in the rheology instrument laboratory.

Rheometric frequency sweeps show the elastic modulus (G') is greater than the viscous modulus (G") by approximately one order of magnitude and is invariant to frequency for all samples, confirming the classification as gels. Increasing the applied stress ultimately results in an irreversible gel-sol transition with G" becoming greater than G'. The gels of **4.1$_{RR}$**, **4.3$_{RR}$** and **4.4$_{RR}$** were all relatively rigid, whilst the gels of **4.2$_{RR}$** and **4.5$_{RR}$** were significantly more labile with G' values reproducibly an order of magnitude lower. Meanwhile, the stress sweep experiments show that gels of **4.2$_{RR}$**, **4.3$_{RR}$** and **4.5$_{RR}$** are reproducibly and significantly weaker than those of **4.1$_{RR}$** and **4.4$_{RR}$**, with gel-sol transitions occurring under a lower stress for the former group. Both **4.1$_{RR}$** and **4.4$_{RR}$** form gels via anti-parallel urea α-tape assembly. The weaker nature of **4.5$_{RR}$** and **4.3$_{RR}$** gels are likely to the alternative molecular packing and supramolecular synthons involved in fibre formation, with **4.5$_{RR}$** forming fibres via duplex assembly and the folded conformer of **4.3$_{RR}$** unable to form two α-tapes due to one urea group adopting the *anti-syn* conformation. The weak nature of **4.2$_{RR}$** gels, which are formed by urea α-tape assembly of the extended conformer, was considered likely to be a consequence of two effects. Firstly, the transition from the folded conformer to extended conformer is anticipated to be slow due to the restricted amide rotation and favourability of the intramolecular hydrogen bond. The slow transition may mean that fewer 1D fibrils are formed, thus the fibrous network is less extensive and results in weaker gels. The second effect that may explain the weaker nature of **4.2$_{RR}$** gels is the odd-even effect,

whereby the behaviour of molecules with an odd number of methylene units in the spacer group differs to that of molecules with an even number of spacer methylene units. Odd-even effects have previously been shown to influence properties of the gels, such as gel appearance and rheological properties,[21] or can completely change self-assembly beahviour.[22,23] As shown by the crystal structures of the **4.2$_{RR}$** ethanol solvate and **4.2$_{Benz}$**, the urea groups orientate parallel to one another. Thus, it is likely that the weaker and less rigid nature of **4.2$_{RR}$** 1,4-dioxane gel is a variation of this odd-even effect. The gels of **4.3$_{RR}$** are also weaker than those of **4.1$_{RR}$** and **4.4$_{RR}$** which is hypothesised to be due to competition between linear and folded conformers and alternative supramolecular motifs dictating fibre formation.

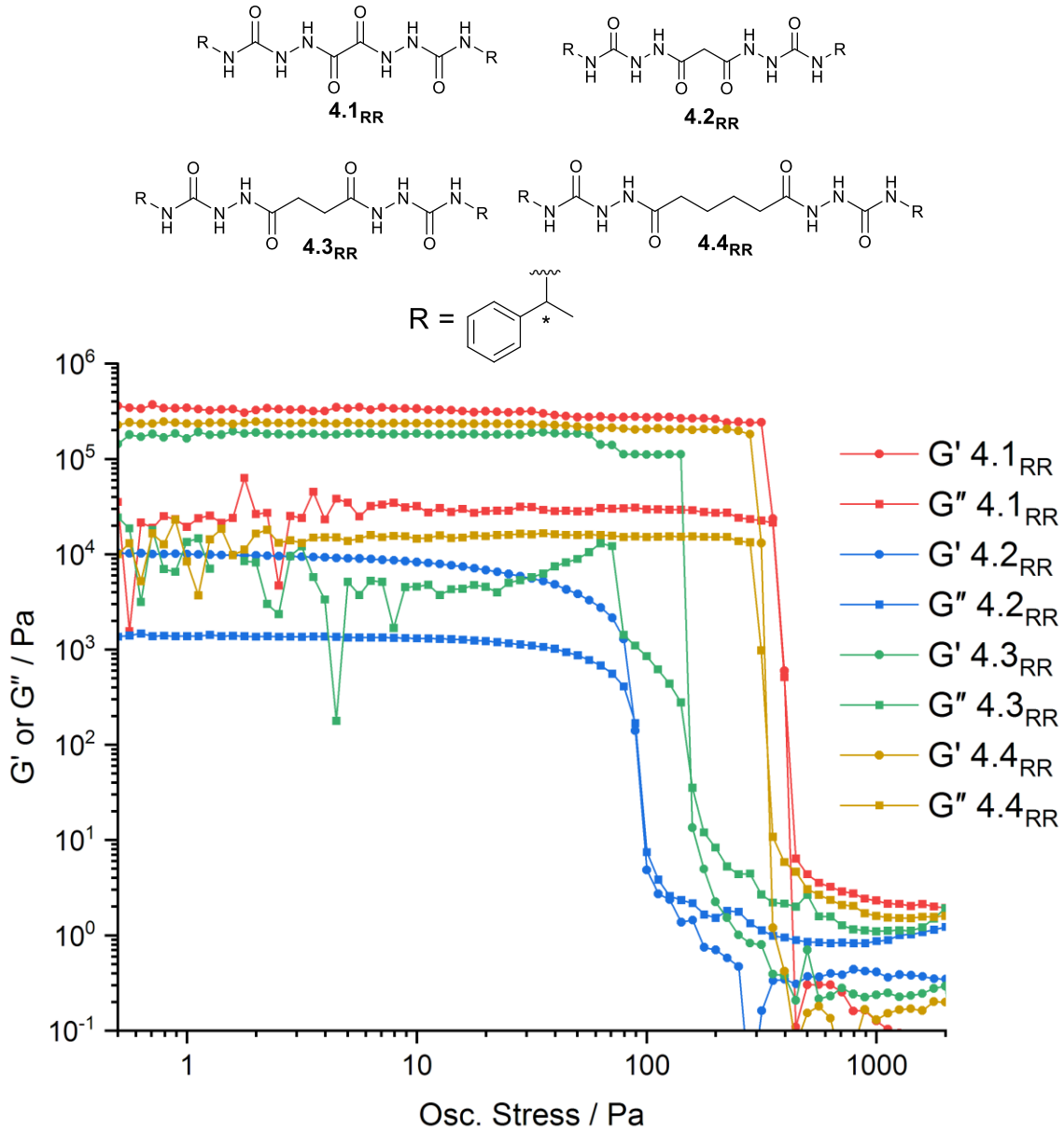

Figure 5-16. The stress-sweep rheometric experiments for 1 % w/v 1,4-dioxane gels of **4.1$_{RR}$** (red) **4.2$_{RR}$** (blue), **4.3$_{RR}$** (green) and **4.4$_{RR}$** (yellow).

A comparison of the stress-sweep rheometric measurements for the homochiral and racemic 1,4-dioxane gels of **4.3** and **4.4** derivatives show that the racemic gels are significantly weaker (**Figure 5-17**). This is consistent with most previous studies investigating racemic/homochiral gelators, with very few examples being reported where the racemic mixture is a more versatile gelator and yielding stronger gels than the homochiral forms.[6]

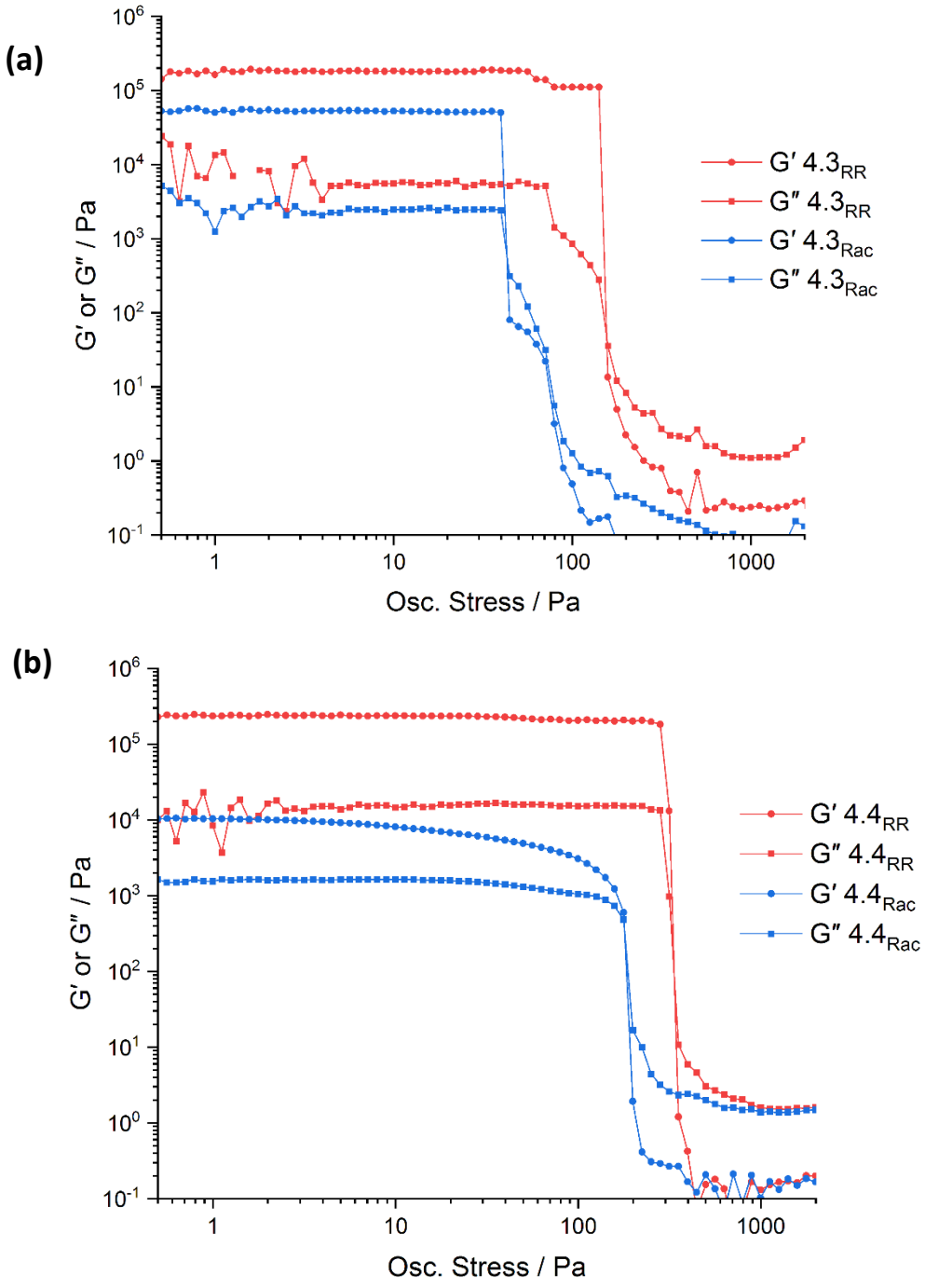

Figure 5-17. Stress-sweep rheometric measurements for 1% w/v 1,4-dioxane gels of **(a) 4.3$_{RR}$** and **4.3$_{Rac}$** and **(b) 4.4$_{RR}$** and **4.4$_{Rac}$**. The results show that the homochiral gels are significantly stronger than their racemic counterparts. Rheology was performed on a 2 mL scale with gels preformed and transfered to the rheometric plate.

Finally, the chiral gelators exhibit higher yield stresses than their achiral counterparts, indicating that the chiral bis(acyl-semicarbazides) resulted in stronger and more rigid gels (**Figure 5-18**). However, the gelation times of the achiral gelators are much shorter on the 2 mL scale that the chiral compounds, with homogenous gelation achieved within 30 minutes of dissolution via heat. Thus, the achiral gels did not have to be pre-formed and could be formed on the rheometry plate, thus avoiding the need to transfer from vial to plate.

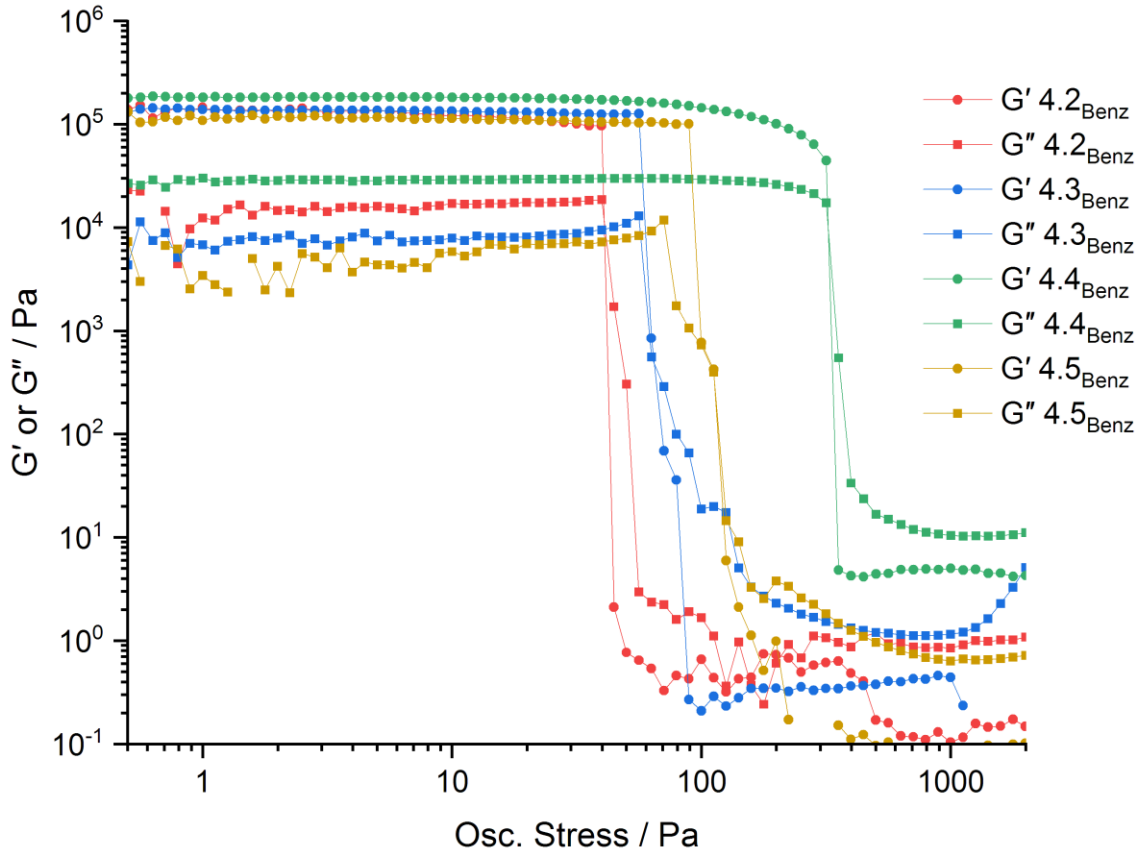

Figure 5-18. Stress-sweep rheometric experiments for 1 % w/v propan-1-ol gels of **4.2**$_{Benz}$ (red), **4.3**$_{Benz}$ (blue) and **4.4**$_{Benz}$ (green). The results for the 1 % w/v benzyl alcohol gel of **4.5**$_{Benz}$ is shown in yellow.

The bis(acyl-semicarbazide) gels were all thermo-reversible and gel-sol transitions temperatures for gels of each compound were measured via ball drop experiments (**Appendix 3**). The ball-drop experiments support the rheological evidence that the homochiral gels of **4.2**, **4.3** and **4.5** derivatives are significantly weaker than those of **4.1** and **4.4**, with sol-gel transitions occurring at lower temperatures. There were only significant differences in T_{gel} between racemic and homochiral gels of **4.3** and **4.4** derivatives, supporting the rheological evidence that the homochiral gels are stronger.

5.2.4 Aggregate morphologies

The morphologies of self-assembled aggregates formed by the bis(acyl-semicarbazide) compounds were investigated via SEM with a focus on identifying any chirality on the supramolecular level. This was considered to potentially provide insight to the effect of supramolecular chirality in the gels when utilised in enantioselective applications. Cryo-SEM was attempted to observe the solvated gel fibres. However adequate resolution was not achieved due to a leak in the cryo-rod, resulting in the sample vibrating and blurred images (**Appendix 3**). Thus, images of the dried xerogels were obtained instead. Again, it is worth noting that whilst imaging of xerogels can provide valuable insight to the nature of fibrous aggregates, but it cannot be ruled out that some observed features are artifacts of the drying process.[24]

Achiral xerogel fibres were observed for all the gels of **4.1**$_{RR/SS}$**, 4.5**$_{RR/SS}$ and **4.6**$_{RR/SS}$. The xerogel fibres for **4.1**$_{RR}$ are achiral flat ribbons or cylindrical fibres in aromatic solvents and aliphatic solvents respectively (**Figure 5-19**). The smaller fibres in the 1,4-dioxane gel correspond to the robust and transparent nature of the gel. The lack of chirality likely comes from the rigidity of the bis(acyl-semicarbazide) core, with the lack of methylene groups and restrictive nature of the amide groups likely the reason for the lack of translation of molecular to supramolecular chirality. SEM images of **4.1**$_{Rac}$ and **4.2**$_{Rac}$ precipitates reveal plate or spherulite nano-crystallites instead of fibrous networks (**Figure 5-20**).

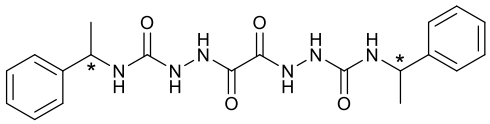

4.1$_{RR/S}$

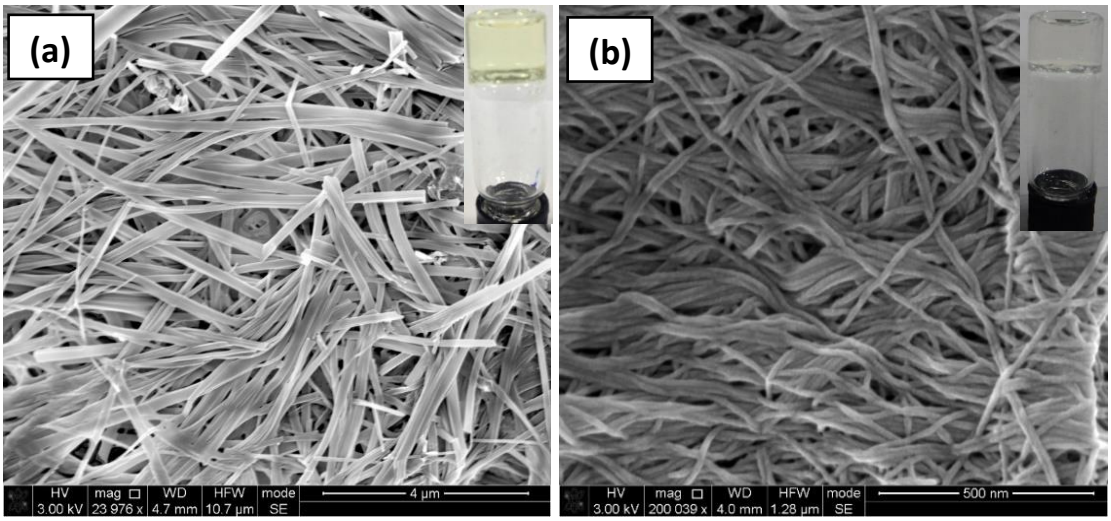

Figure 5-19. SEM images of 1 % w/v xerogel of **4.1$_{RR}$** in **(a)** nitrobenzene and **(b)** 1,4-dioxane. The nitrobenzene fibres have a larger diameter (approximately 500 nm) and are flatter ribbon architectures compared with the tubular ethanol fibres (approx. 20 nm). Images of the respective gels have been inserted. Samples are coated with 2.5 nm of platinum.

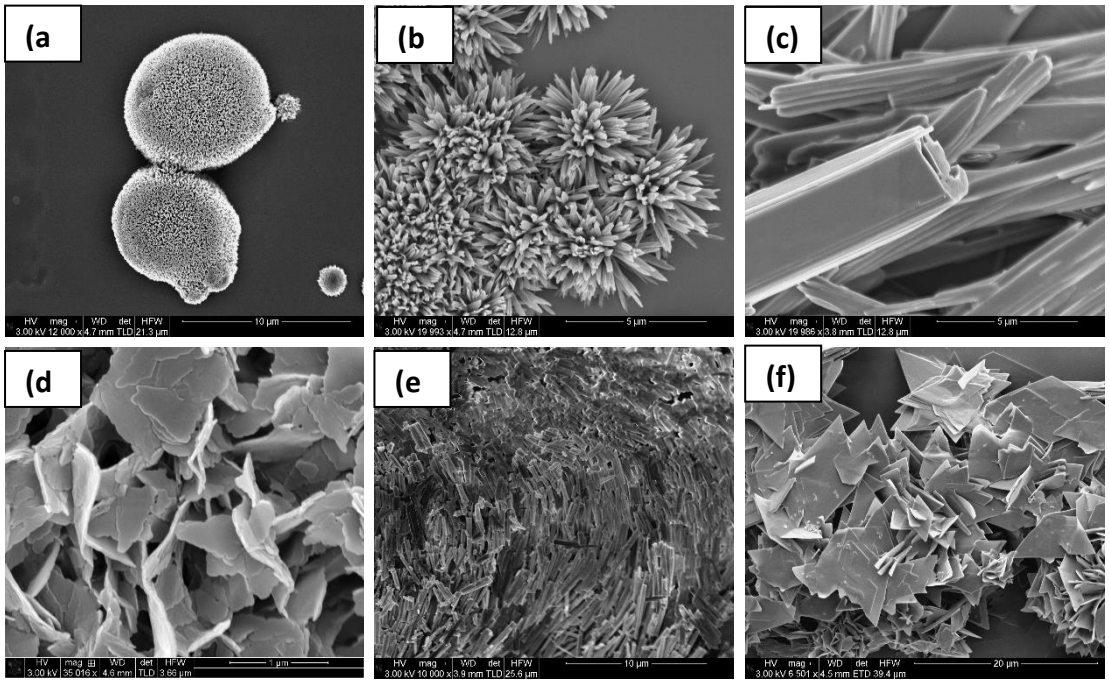

Figure 5-20. Top row: SEM images of the racemic aggregates of **4.1$_{Rac}$** in **(a)** nitrobenzene, **(b)** ethanol and **(c)** acetonitrile. The molecules self-assemble to form spherulites or defined rods rather than the fibrous aggregates observed for the enantiomerically pure compounds. Bottom row: SEM images of the racemic aggregates of **4.2$_{Rac}$** in **(d)** nitrobenzene, **(e)** 1-propanol and **(f)** acetonitrile. The molecules assemble into crystalline plates or shorts rods. Samples are coated with 2.5 nm of platinum.

Helical fibres were observed for homochiral **4.2**, **4.3** and **4.4**-derived molecular gels. SEM imaging of the xerogels of $\mathbf{4.2_{RR}}$ and $\mathbf{4.2_{SS}}$ dried from 1,4-dioxane, acetone or nitromethane sonogels reveal achiral fibres in addition to fascinating heliconical filaments (**Figure 5-21**), which can be characteristic of chiral bent-core liquid crystalline molecules, particularly mesogenic dimers with an odd-numbered aliphatic spacer unit.[11,25,26] Indeed, these fibres were exclusively observed in solvents in which liquid crystals formed and SEM images of the dried down $\mathbf{4.2_{RR/SS}}$ liquid crystals also reveal the heliconical fibres. Furthermore, gels formed via sonication of the liquid crystal phases for 5 seconds reveals the heliconical fibres almost exclusively (**Figure 5-22**). Xerogels of $\mathbf{4.2_{RR/SS}}$ in all other solvents in which gels formed reveal only the achiral tubular fibres (**Appendix 3**). These observations suggest that the heliconical fibres are related to the liquid crystal phase, which possibly form due to the frustrated conversion between folded and extended conformations.

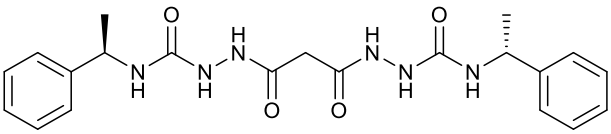

4.2$_{RR}$

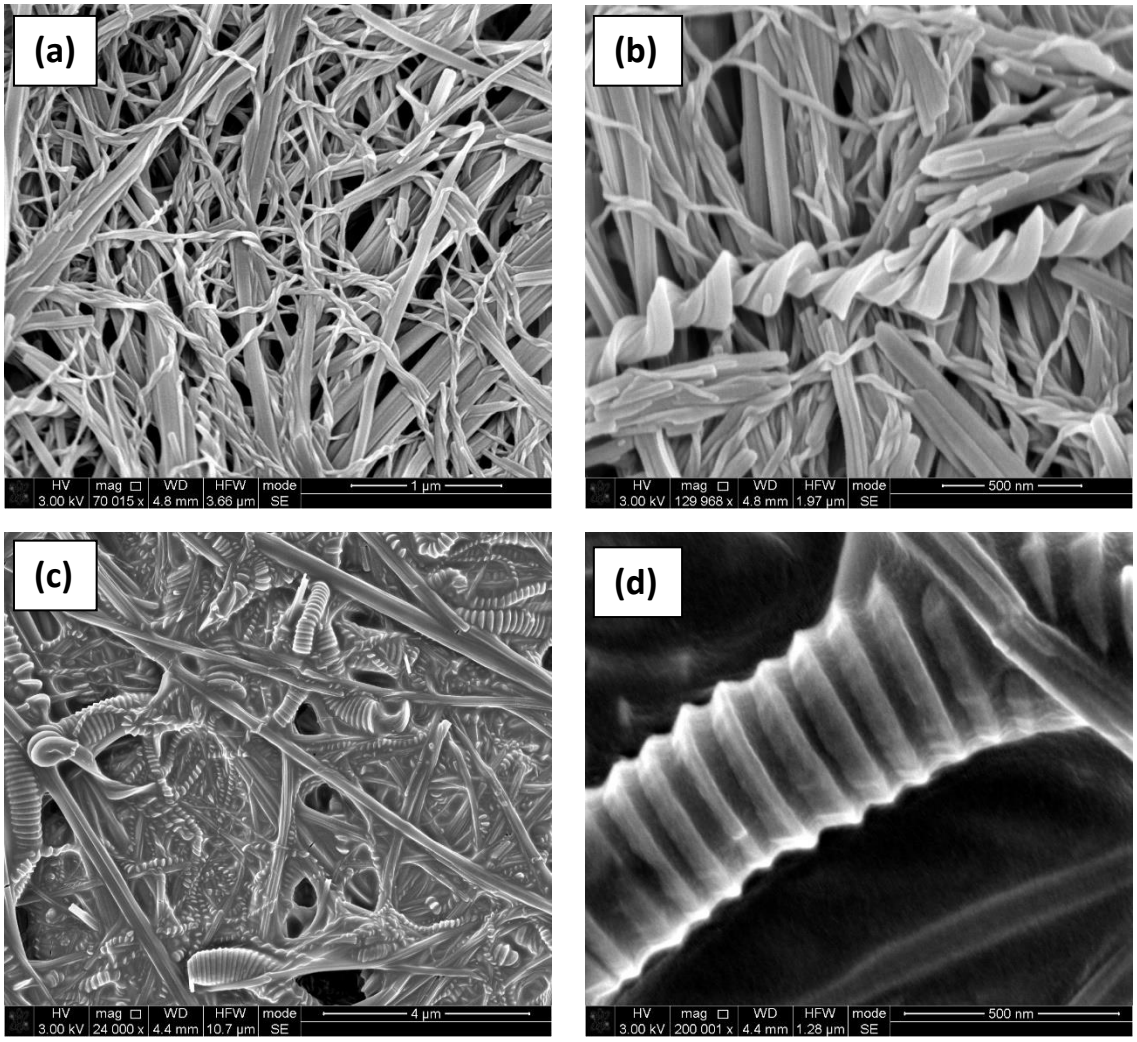

Figure 5-21. SEM images of xerogels of **4.2$_{RR}$** formed from **(a)** acetone, **(b)** nitromethane and **(c)** 1,4-dioxane. All three gels were initially formed by sonication of the sol, minutes after dissolution with heat. All xerogels reveal a mixture of achiral and heliconical fibres. The 'accordion-like' fibres in (c) are particularly fascinating due to their super coiled architecture. **(d)** A close-up image of the chiral 'accordion-like' fibres in the **4.2$_{RR}$** xerogel formed from 1,4-dioxane.

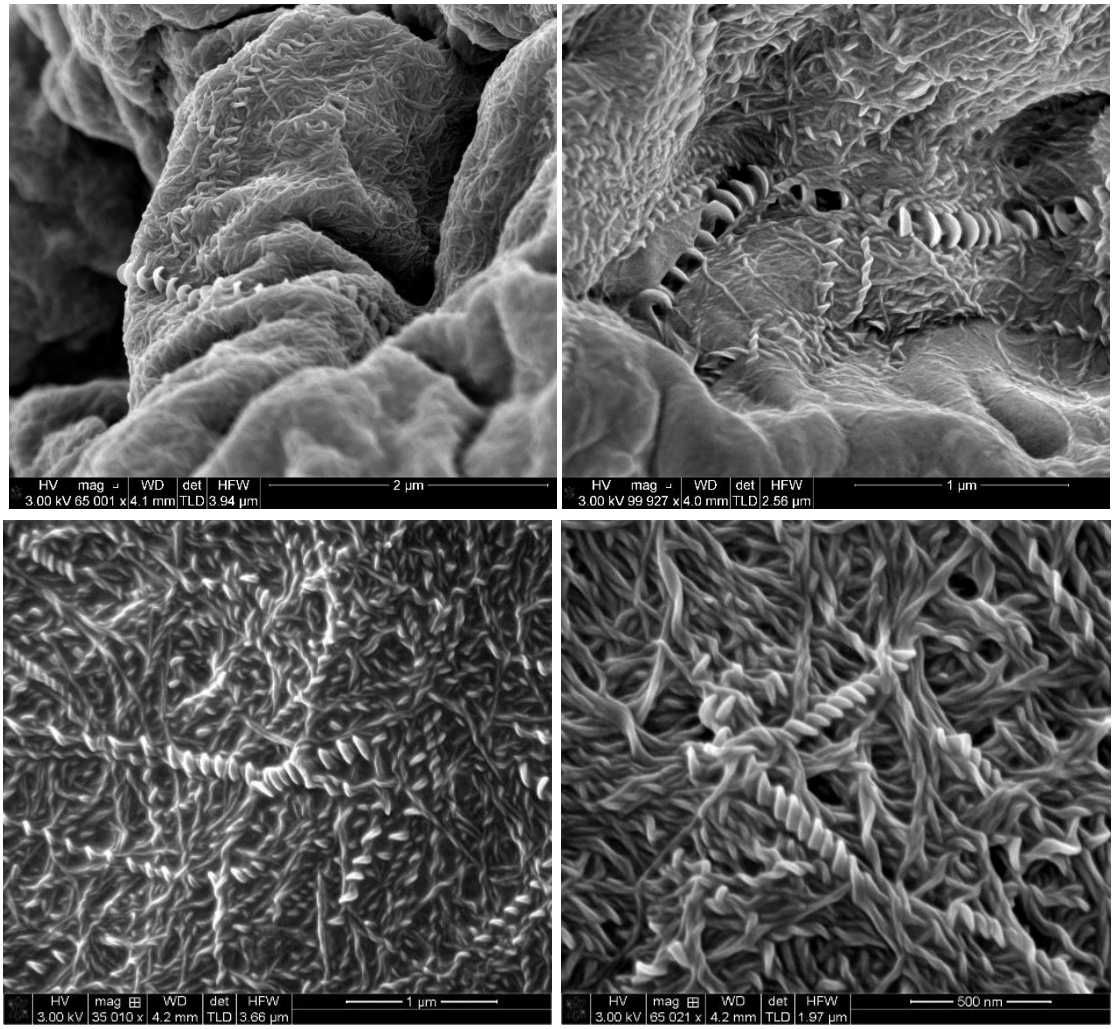

Figure 5-22. SEM images of **4.2$_{RR}$** xerogels formed from 1,4-dioxane gels formed by sonication of liquid crystalline droplets for 5 seconds. The fibrous network exhibits chiral heliconical fibres almost exclusively, as opposed to a mixture of achiral and chiral fibres as observed in gels formed by sonication of the sol prior to liquid crystal formation. Samples are coated with 2.5 nm of platinum.

The xerogels produced by drying down 1,4-dioxane gels of **4.3$_{RR}$** also exhibit fibres with helical twists present (**Figure 5-23**). However, the xerogels produced from 1,4-dioxane gels of **4.3$_{rac}$** reveal flat fibres exhibiting no chiral character. Chiral fibres are also observed in the xerogels of the homochiral **4.4$_{RR}$** and **4.4$_{SS}$** samples and achiral fibres observed in the **4.4$_{Rac}$** xerogels. This suggests that the racemic xerogel is not merely an entanglement of the same homochiral fibres, but the fibres are formed by an alternative molecular packing. Indeed, the XRPD patterns for the enantiomerically pure and racemic xerogels reveal clear differences that support this theory (**Appendix 3**).

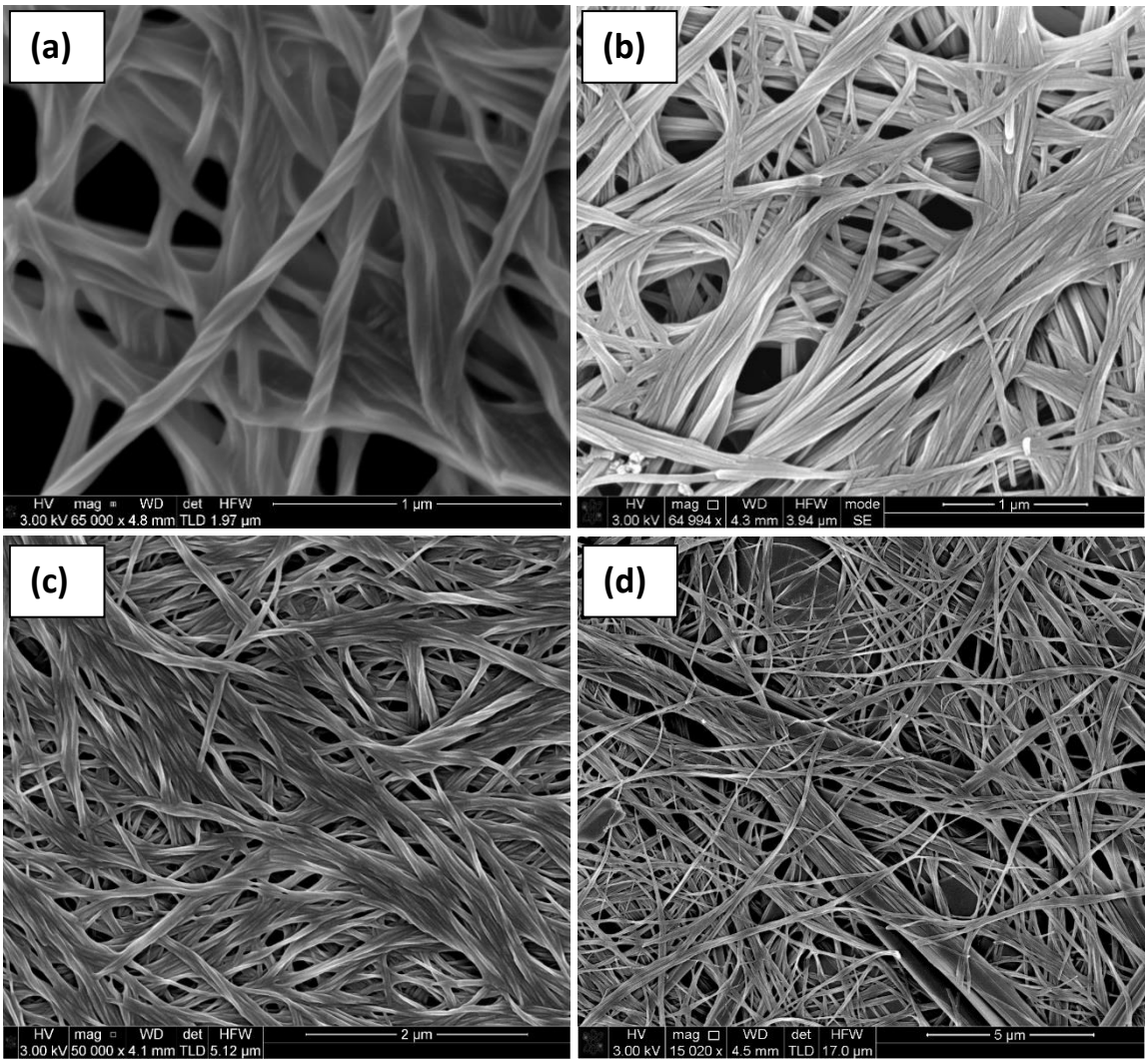

Figure 5-23. SEM images of the 1% w/v 1,4-dioxane xerogels of **(a) 4.3$_{SS}$** and **(b) 4.3$_{rac}$**. The enantiomerically pure fibres have a left-handed helical architecture, whilst the racemic dioxane xerogel shows achiral fibres of a similar diameter (approx .50-100 nm). SEM images of the 1 % w/v 1,4-dioxane xerogels of **(c) 4.4$_{RR}$** and **(d) 4.4$_{Rac}$** also reveal chiral and achiral fibres respectively.

Interestingly, whilst these small chiral fibres are also observed in the **4.3$_{RR}$** nitrobenzene xerogel, the xerogel also exhibits large flat ribbon fibres with diameters ranging from 20-50 µm (**Figure 5-24**). These differences between supramolecular architectures observed in the **4.3$_{RR}$** 1,4-dioxane and nitrobenzene xerogels may be due to the difference in molecular packing observed via XRPD. The nitrobenzene fibres were identified to form via bilayer assembly of the folded conformer as in the **4.3$_{SS}$** solvate form. This self-assembly behaviour involves hydrogen bond synthons in 2 dimensions, which may account for the larger and wider nature of these gel fibres in the nitrobenzene xerogel. All xerogels of **4.5$_{RR}$** and **4.6$_{RR}$** exhibit achiral tubular fibres (**Appendix 3**), with the racemic mixtures forming microcrystalline blocks as opposed to fibrous networks.

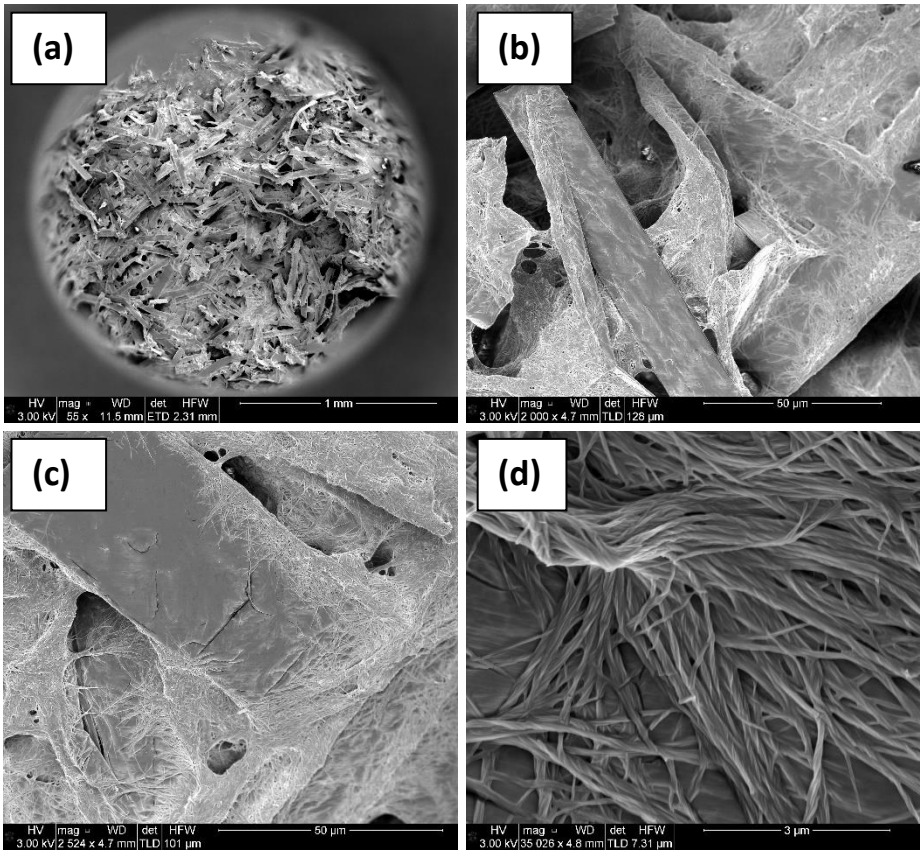

Figure 5-24. SEM images of the **4.3$_{RR}$** nitrobenzene xerogel revealing **(a)-(c)** large ribbon fibres (approximate diameter of 40 μm) and **(d)** smaller chiral fibres (diameters < 1 μm). These large ribbon fibres are not present in the other examined **4.3$_{RR}$** xerogels and only appear in the nitrobenzene xerogel, which appears to have the same underlying molecular packing arrangements as in the **4.3$_{SS}$** solvate form.

The aggregates formed by achiral benzyl-appended compounds vary drastically from their chiral 1-phenylethyl-appended counterparts (**Figure 5-25**). Comparison of the SEM images of aggregates from nitrobenzene reveal non-gelator **4.1$_{Benz}$** forms microcrystalline needles and planks. Achiral fibres are observed for **4.2$_{Benz}$** and **4.5$_{Benz}$**. In the former, narrow, flexible fibres are observed (diameter < 500 nm), which bundle to form thicker fibres (approximately 2.5 μm diameter), whilst more cross-linking is observed in **4. 5$_{Benz}$**. Achiral fibres were also observed for the **4.6$_{Benz}$** xerogel, formed from the nitrobenzene partial gel, but they form concomitantly with crystalline blocks, which demonstrates the competition between gelation and crystallisation and likely explains why homogenous gelation was not achieved. was formed by **4.6$_{Benz}$**.

Interestingly, **4.3$_{Benz}$** and **4.4$_{Benz}$** both form ribbon fibres with fibre diameters ranging between 2-10 μM. The networks reveal a mixture of achiral flat ribbons and chiral twisted ribbons, scrolls and heliconical fibres. Both left and right-handed helices are

observed, including inversions in chirality. These chiral ribbons were observed in all **4.3$_{Benz}$** and **4.4$_{Benz}$** xerogels regardless of solvent they were formed from (**Figure 5-26**). Whilst chiral architectures formed exclusively from the self-assembly of achiral molecules are not unheard of, they do remain highly unusual and relatively few examples have been reported.[27,28] Chiral supramolecular structures formed from achiral molecules arise from the breaking of mirror symmetry and this can be induced by variations in external physical factors, such as temperature, pH and the presence of metal ions,[29] or by multiple supramolecular synthons dictating self-assembly.[30,31] Studies to control the supramolecular chirality using polarised light,[32] magnetic fields[33] and hydrodynamic forces[34] have been reported along with numerous other methods.[29] Regrettably, for the achiral bis(acyl-semicarbazides) only a crystal structure of **4.2$_{Benz}$** was successfully elucidated, thus there is currently little insight to the potential supramolecular synthons and molecular packing arrangements underlying these chiral ribbons in xerogels of **4.3$_{Benz}$** and **4.4$_{Benz}$**.

Whilst the chiral supramolecular architectures observed are highly intriguing, they were not the primary focus on this investigation. Thus, this work is currently being continued by an EPSRC postdoctoral researcher to further understand these morphologies and to determine whether they are representative of the solvated fibres. This will be achieved through a combination of experimental methods, such as cryo-TEM and CD spectroscopy, and molecular dynamics calculations.

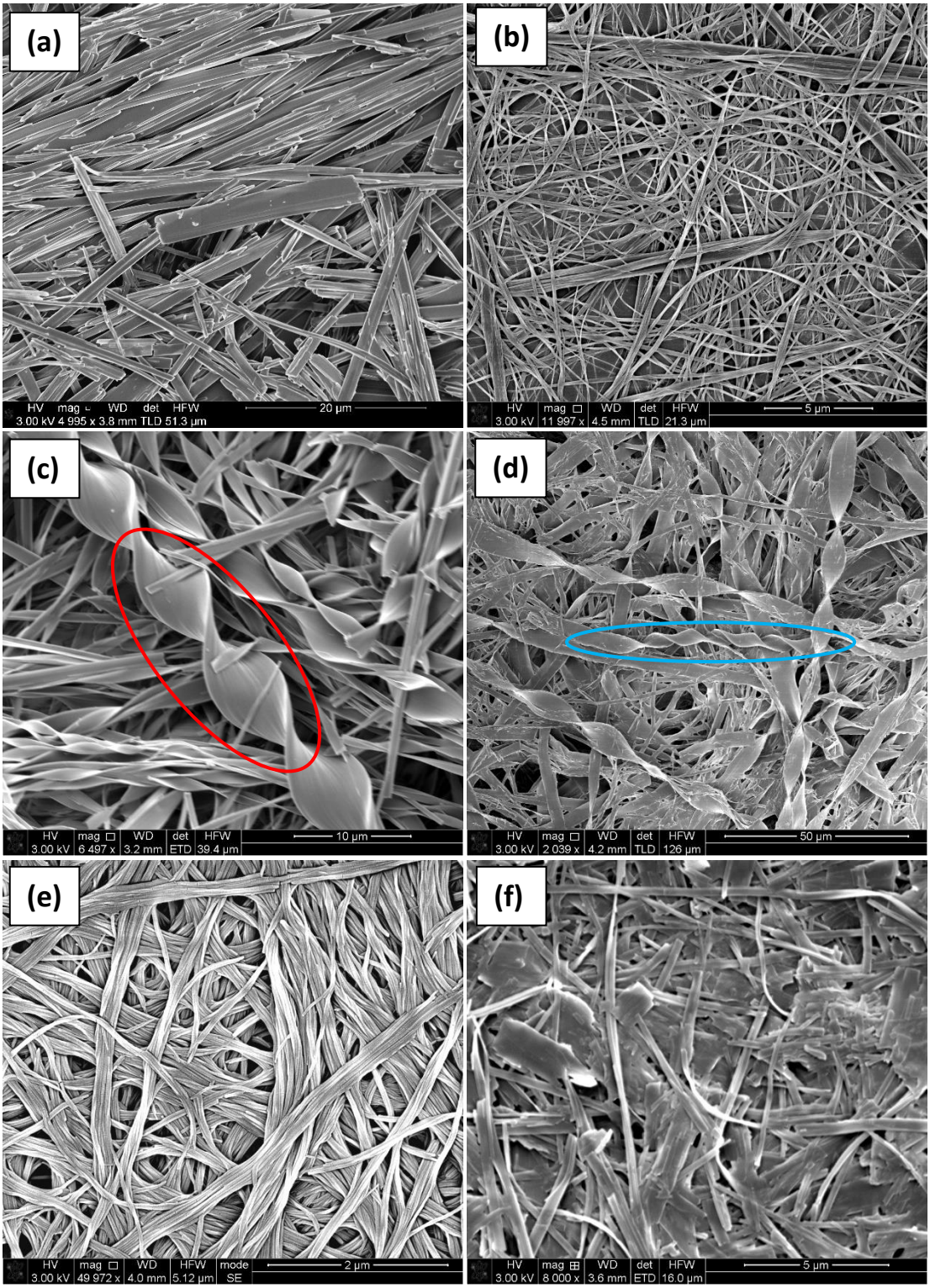

Figure 5-25. (a) Crystalline needle precipitate of **4.1**$_{\text{Benz}}$ from nitrobenzene and xerogels of **(b) 4.2**$_{\text{Benz}}$, **(c) 4.3**$_{\text{Benz}}$, **(d) 4.4**$_{\text{Benz}}$, **(e) 4.5**$_{\text{Benz}}$ and **(f) 4.6**$_{\text{Benz}}$ all formed from 1 % w/v nitrobenzene gels or partial gels. The images show **4.2**$_{\text{Benz}}$ and **4.5**$_{\text{Benz}}$ form achiral fibres, whilst **4.6**$_{\text{Benz}}$ forms mixture of achiral fibres and blocks, which likely explains the partial gel nature. Both **4.3**$_{\text{Benz}}$ and **4.4**$_{\text{Benz}}$ form ribbon fibres, including some chiral twisted ribbons and scrolls with examples of each circled in red and blue respectively. Samples are coated with 2.5 nm of platinum.

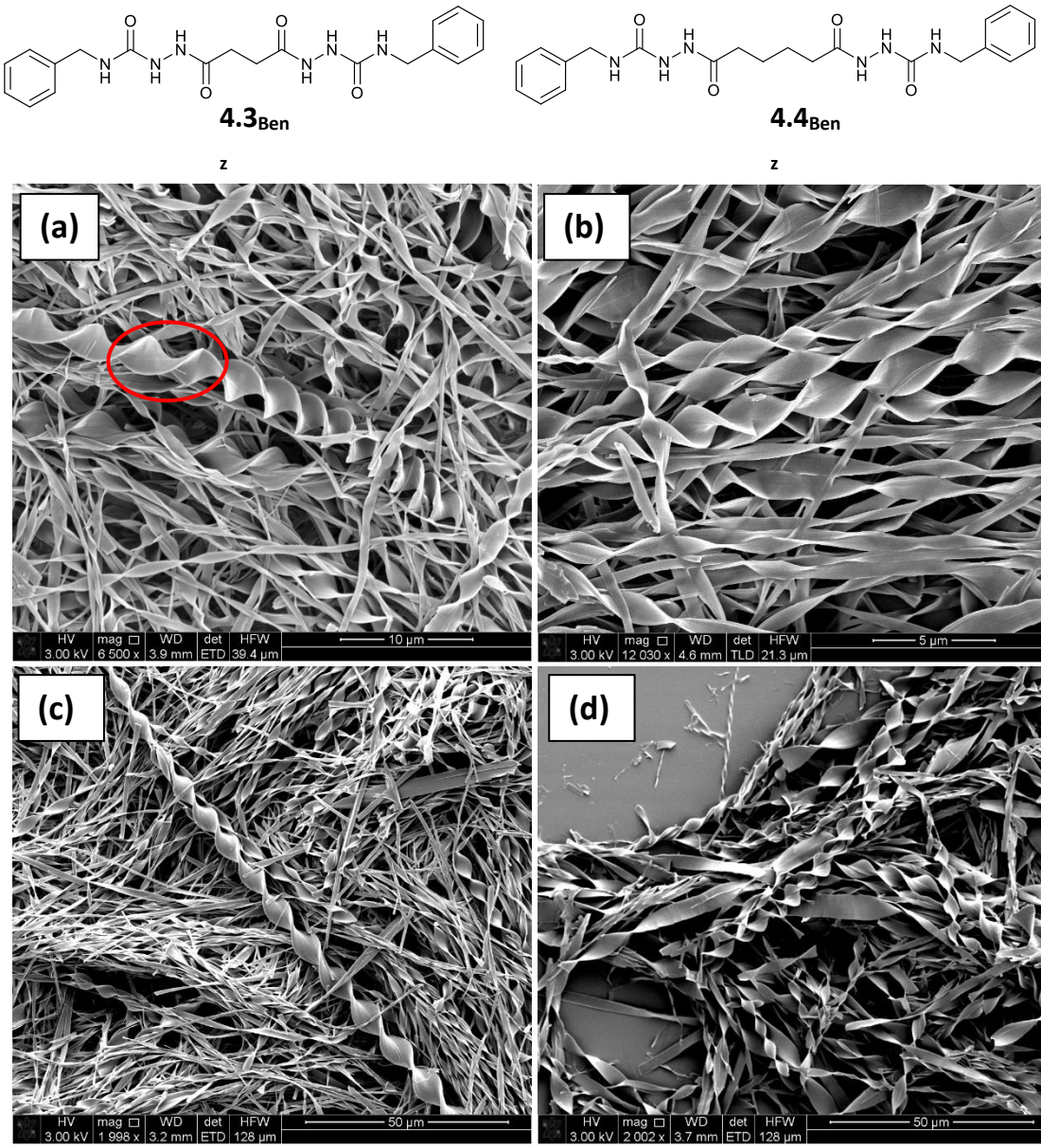

Figure 5-26. Chiral heliconical and twisted ribbon fibres were observed in xerogels of **4.3**$_{Benz}$, dried down from **(a)** aniline and **(b)** propan-1-ol, and xerogels of **4.4**$_{Benz}$ dried from **(c)** chlorobenzene and **(d)** nitromethane. Inversion of chirality in heliconical fibres were observed in **(a)** (circled in red). Chiral fibres of these gelators were observed in xerogels formed from all solvents in which gels formed. Samples are coated with 2.5 nm of platinum.

5.2.5 Gel Reversibility

It is well known that anions can induce gel-sol transitions by disrupting urea α-tape assemblies and other supramolecular motifs.[35] This can be useful in sensing applications and in enabling easy retrieval of crystals when utilised as crystallisation media. Indeed, addition of between 0.5 to 1 molar equivalents of tetrabutylammonium (TBA) salts induced gel-sol transitions in all gels of **4.2**–**4.6** derivatives, with 1 molar equivalent of fluoride, chloride, bromide, benzoate or acetate required for complete

gel-sol transition (**Appendix 3**). This switchable gel-sol behaviour is useful for applications of gels as crystallisation media as it allows easy retrieval of the crystals. However, the gels of **4.1$_{RR/SS}$** were relatively resistant to anion addition, with a negligible change in gel volume 48 hours after 5 molar equivalents of TBA AcO^-, Cl^-, Br^-, $Benz^-$, or F^- were added to 1 % w/v ethanol or 1,2-dichlorbenzene gels (**Figure 5-27**). The resilience of **4.1$_{RR/SS}$** to anion addition makes crystal isolation less convenient. However, these gels can be used as crystallisation for anionic API salts, which may not be possible in many other urea or acyl-semicarbazide gelators due to hydrogen bond disruption.

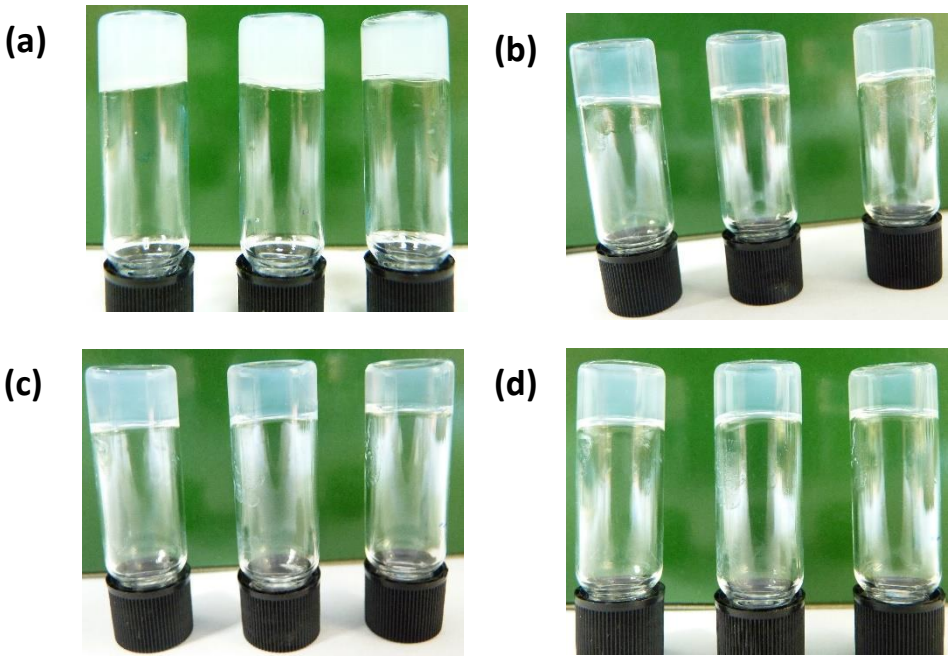

Figure 5-27. (a) Photographs of 2 % w/v 1,2-dichlorobenzene gels of **4.1$_{SS}$** with chloride ions added after gel formation at 1 molar, 2 molar and 5 molar equivalents (left to right). **(b)**, **(c)** and **(d)** all show 1 % w/v ethanol gels of **4.1$_{SS}$** with **(b)** fluoride, **(c)** benzoate and **(d)** acetate ions added post gel formation at 1, 2 and 5 molar equivalents (left to right in each image). All anions were added as tetrabutylammonium salts. Photographs were taken 48 hours after anion addition.

When 1 molar equivalent of anions are added to the sol prior to gelation for **4.2**–**4.6** derivatives, gelation is completely inhibited, and precipitates or stable solutions form instead. However, analogue **4.1$_{RR/SS}$** can form gels in ethanol and propan-1-ol in the presence of up to 10 molar equivalents of TBA chloride or TBA fluoride, with the gels increasing in transparency and decreasing in strength as the anion concentration increases (**Figure 5-28**). All these gels remain stable over 6 months. The rigidity of the gels remains similar up to 5 equivalents of TBA chloride. After this, G' decreases by an order or magnitude at 7.5 equivalents, and even further at 10 equivalents. These

experiments were repeated 3 times except for the 10 equivalents sample, where only two iterations were undertaken due to the challenge of transferring the preformed weak gel on to the rheometer plate. Whilst the reproducibility of this latter data is underdetermined, the fact the gels with 10 equiv. Cl^- kept breaking whilst the gels at lower anion concentrations did not, qualitatively supports their significantly weaker nature. SEM imaging of the xerogels with varying chloride concentrations revealed that fibre diameter decreased as chloride concentration increased (**Appendix 3**), which explains the increase in transparency as anion concentration increases. Attempts to grow single crystals of the bis(acyl-semicarbazides) with TBA salts to reveal more about the nature of their interactions with anions were unsuccessful. The ability of **4.1**$_{RR/SS}$ to gel in the presence of relatively high concentrations of anions can be useful for the crystallisation of API salts, where other urea-based gels cannot be used due to anion disruption of the gel driving synthons.

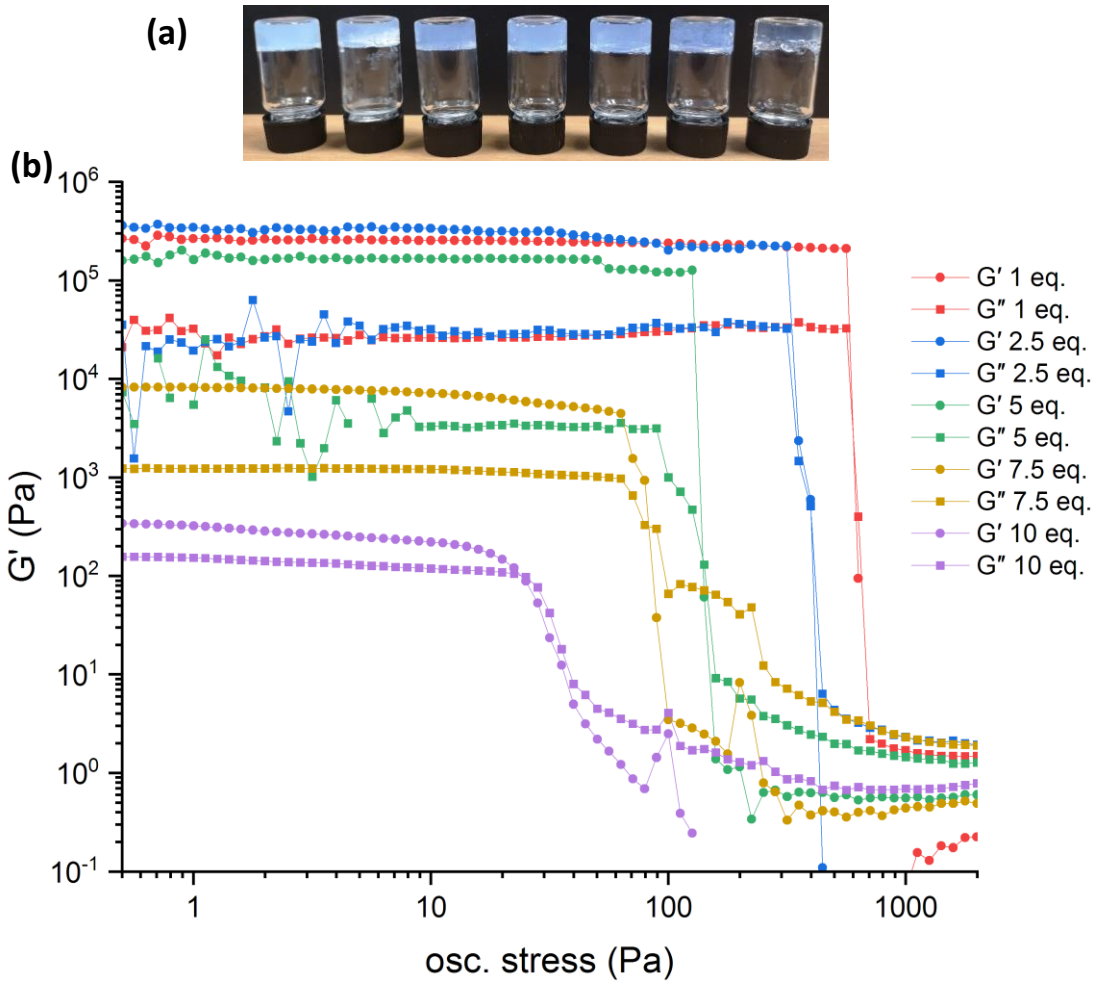

Figure 5-28. (a) 1 % w/v ethanol gels of **4.1**$_{SS}$ with (left to right) 0, 0.5, 1, 2.5, 5, 7.5 and 10 molar equivalents of TBA chloride added to the sol prior to gel formation. Gels were formed on a 2 mL scale and gelation occured between 2-48 hours after dissolution via heat. **(b)** Results of stress-sweep experiments undertaken on these gels with no anions and 1, 2.5, 5, 7.5 and 10 molar equivalents of TBA chloride present.

The lack of sensitivity of **4.1$_{RR}$** gels to anions may indicate that supramolecular interactions other than hydrogen bonds, and undisturbed by the presence of anions, play a significant role in gel formation. Alternatively, it may be that the amide functionalities hydrogen bond to the anions, as they do to hydrogen bond donors in solvent molecules, as observed in the single crystal structures for **4.1$_{RR}$** methanol solvate. This may enable the urea functionalities to form and maintain urea α-tapes until the concentration of anions in solution is high enough to overcome electronegative repulsion and enable both urea and amide functionalities to hydrogen bond to anions, resulting in the interruption of urea tapes. The nature of **4.1$_{RR}$** interactions with anions should be explored further via solution-state NMR titration experiments.

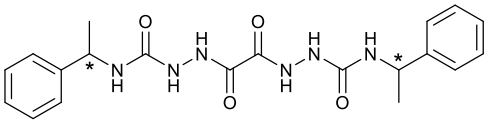

4.1$_{RR/S}$

5.3 Applications as Crystallisation media

The primary objective of this work was to investigate the application of bis(acyl-semicarbazides) gels as crystallisation media for APIs. Numerous APIs were utilised to explore whether the gels could influence crystallisation outcomes. As well as the APIs described below, the bis(acyl-semicarbazide) gels were also used to crystallise AstraZeneca drug compounds AZD-6140 and AZD-2281 to see if molecular or supramolecular chirality might influence the crystallisation of these achiral compounds. These gels all failed to influence crystallisation outcomes of these AstraZeneca compounds (**Appendix 3**).

5.3.1 Use as crystallisation media for salts

Formulating APIs as salts is a frequently employed strategy to enhance API aqueous solubility and bioavailability.[36,37] Salts can also yield polymorphic forms that can impact physicochemical properties and need to be thoroughly investigated for regulatory and market exclusivity purposes.[38] The use of urea-derived supramolecular gels to crystallise API salts as part of solid-state screening procedures can be limited because anions can disrupt fibre formation.[39] Procaine hydrochloride has one known

polymorphic form and was chosen as a test API salt. This is because a preliminary solution-phase screening revealed that crystals grew from solvents that are mutually gelled by the majority of the bis(acyl-semicarbazide) gelators, including acetone, acetonitrile, 1,4-dioxane and chlorobenzene. Concentrations required for crystallisation from solutions varied between 10-50 mg per 0.5 mL. Gel-phase crystallisations were attempted using aliphatic-spaced gelators **4.1$_{RR}$**–**4.4$_{RR}$** and **4.2$_{Benz}$**–**4.4$_{Benz}$**, however only **4.1$_{RR}$ and 4.1$_{SS}$** gelled these solvents in the presence of procaine HCl, likely due to the sensitivity of the other gelators to anions (**Figure 5-29**).

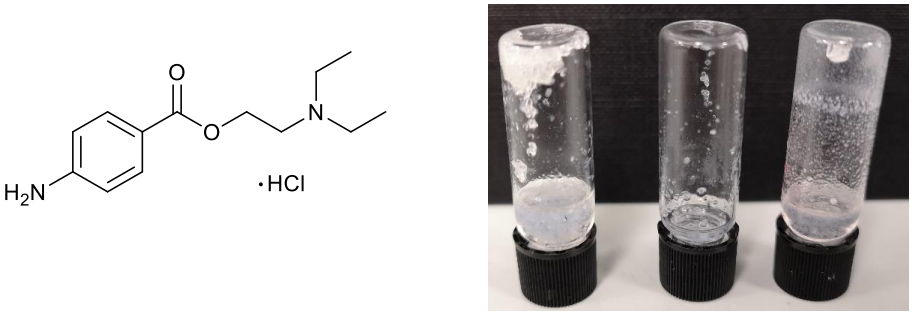

Figure 5-29. (a) Chemical diagram of procaine HCl. **(b)** 1 % w/v acetonitrile gels of **4.2$_{SS}$**, **4.3$_{SS}$** and **4.4$_{SS}$** with 10 mg procaine HCl (left to right). Gel formation was hindered by the presence of the chloride anions, rendering these gelators unsuitable for the crystallisation of organic salts.

All the gel-phase crystallisations from **4.1$_{RR/SS}$** gels yielded needles of the known form of procaine HCl, with gelator concentrations of 1 and 2% w/v being utilised and 10 to 100 mg of procaine HCl (**Appendix 3**). Whilst the crystallisation outcomes were not influenced by the gel-fibres, the fact that **4.1$_{RR}$** could be used to crystallise an anionic salt of an API means it may be used where highly anion-sensitive bis(urea) gelators are limited to investigate the crystallisation behaviour of other API-salts. Many of the crystals obtained at lower drug loading (< 25 mg/mL) were suitable for SCXRD analysis with a molybdenum radiation source (**Figure 5-30**).

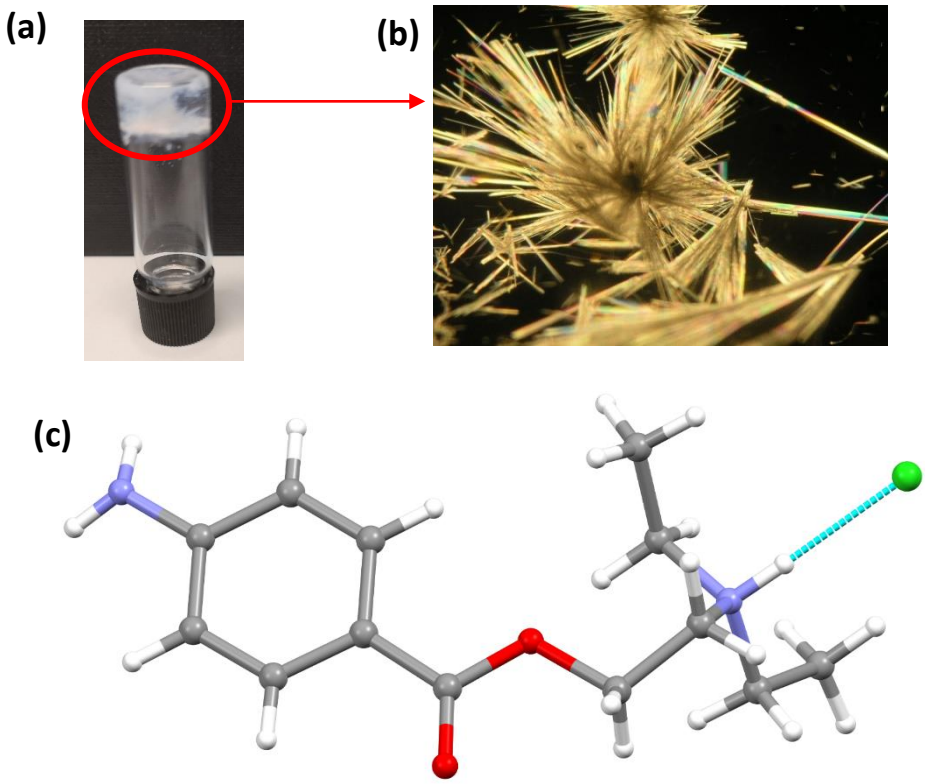

Figure 5-30. (a) A 0.5 mL **4.1$_{RR}$** acetonitrile gel (1 % w/v) with 50 mg procaine HCl crystallised within 12 hours of gelation. **(b)** The crystals were extracted with a spatula and washed with oil to remove excess gel to yield needle crystals. **(c)** At lower API concentrations, the crystals yielded were appropriate for SCXRD analysis. Full data was collected for one crystal and unit cell measurements for numerous other crystals. The known form of procaine HCl was always obtained from **4.1$_{RR}$** gel-phase crystallisations, regardless of gelator concentration, API concentration or solvent.

5.3.2 Use as API-mimetic and enantioselective crystallisation media

As discussed in the previous chapters, the use of API-mimetic gelators may influence crystallisation outcomes when utilised as crystallisation media. Here, ketoprofen and flurbiprofen were identified for API-mimetic crystallisations. Both compounds possess a methylated chiral centre as in the homochiral 1-phenylethyl gelators. Ketoprofen is currently thought to be monomorphic, whilst the racemic form of flurbiprofen is polymorphic with two known forms, forms I and II. Only one form of the enantiomerically pure (R)-flurbiprofen has been identified to date.

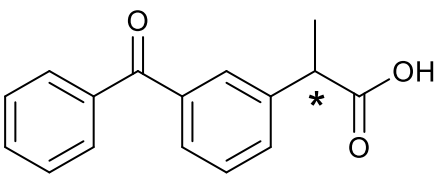

Ketoprofen

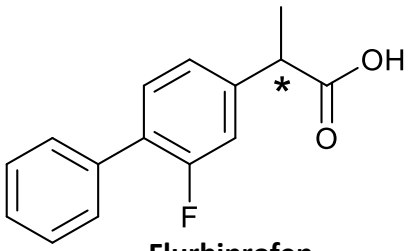

Flurbiprofen

The racemate of the APIs were used here to see whether enantiomeric separation could be achieved. Most drug molecules have at least one chiral centre and typically only one enantiomer exhibits the desired biological activity.[40–42] Therefore, methods to separate the enantiomers are highly desirable to minimise dosage size and avoid any adverse effects caused by the therapeutically inactive enantiomer. Currently, techniques such as chiral column chromatography are utilised to achieve enantiomer separation.[43] In this work, it was considered that chiral LMWG fibres may exhibit chiral microenvironments at their surface, which could facilitate preferential recognition for one enantiomer and potentially provide a heterogenous nucleation site for the homochiral crystal form. Indeed, a few examples of LMWGs demonstrating enantioselective recognition have been reported, but haven't reported homochiral crystallisations.[44–46] Here, homochiral gelators **4.1$_{RR}$**-**4.4$_{RR}$** were utilised to see if a chiral mimetic functionality in the gelator structure could result in enantiomer separation or influence the polymorph obtained. Achiral compounds **4.2$_{Benz}$**, **4.3$_{Benz}$** and **4.4$_{Benz}$** and racemic gels of **4.3$_{Rac}$** and **4.4$_{Rac}$** were utilised as gel-phase control experiments.

All solution-phase and gel-phase crystallisations of ketoprofen yielded the known racemate form (**Figure 5-31**). This was regardless of the gelator, solvent, gelator concentration or drug loading concentrations used (**Appendix 3**). All solution and gel-phase crystallisations yielded form I of the racemic (R,S)-flurbiprofen polymorphs (**Appendix 3**). This means the gels failed to influence the crystallisation outcomes. This may be due to several reasons, including the chiral moieties in the gelators being relatively small, thus not facilitating significantly strong interactions with one enantiomer. It is worth noting that gelation of some supersaturated ketoprofen or flurbiprofen solutions by **4.2$_{RR}$**, **4.3$_{RR}$** and **4.4$_{RR}$** was inhibited, potentially due to the acidic nature of the compounds and resulting disassociation resulting in charged species that interfere with gel-driving hydrogen bond formation. Gelation of **4.1$_{RR}$** was unaffected at the drug concentrations used.

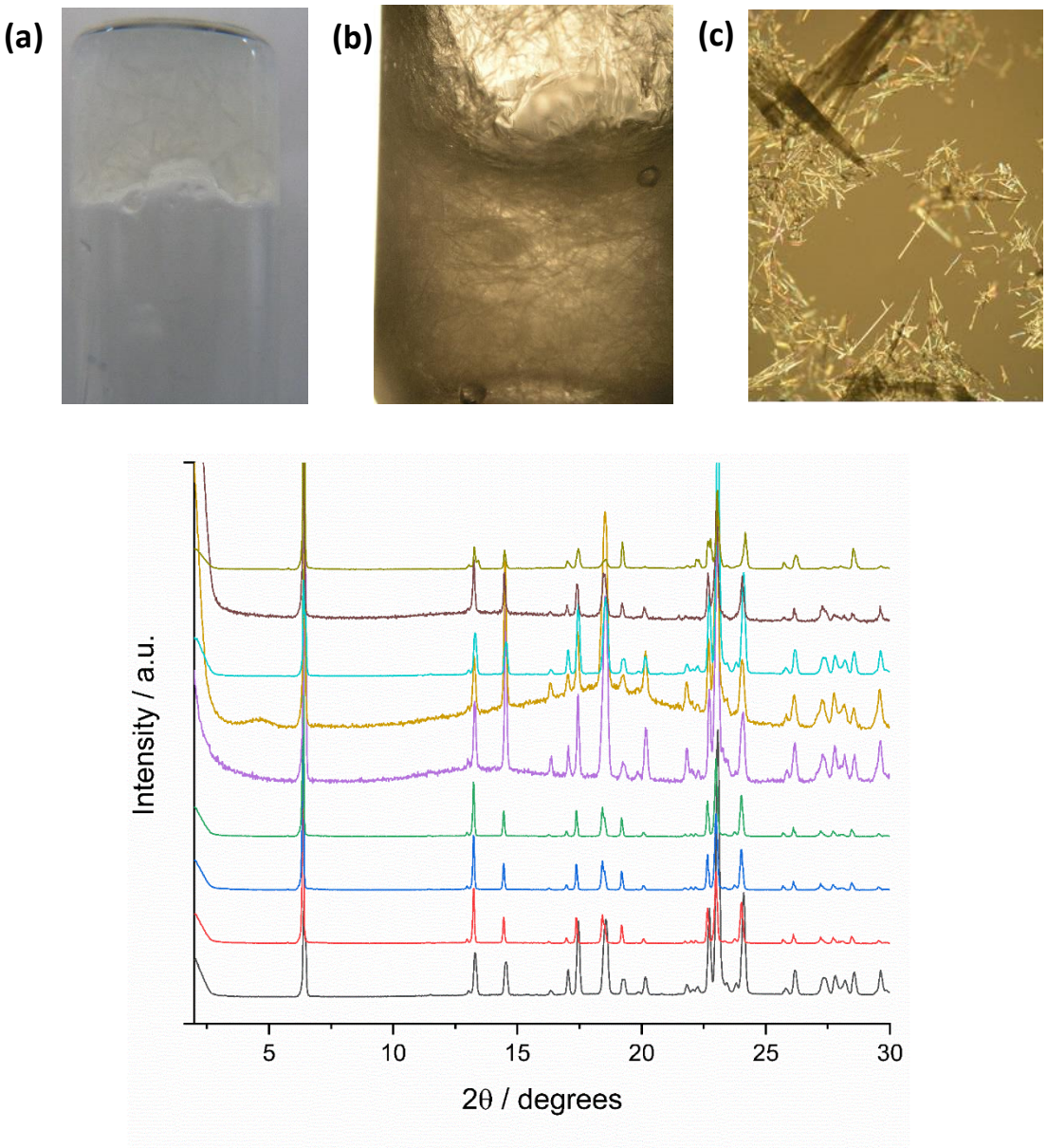

Figure 5-31. (a)-(c) Pictures of ketoprofen crystalline needles in a 1 % w/v **4.4$_{RR}$** 1,4-dioxane gel. **(d)** Experimental XRPD patterns of ketoprofen obtained from (top to bottom) nitrobenzene gels of **4.1$_{RR}$** (light green), **4.2$_{RR}$** (brown), **4.3$_{RR}$** (turquoise) and **4.4$_{RR}$** (yellow) and 1,4-dioxane gels of **4.1$_{RR}$** (purple), **4.2$_{RR}$** (green), **4.3$_{RR}$** (blue) and **4.4$_{RR}$** (red). All the patterns are identical and match that of the known R,S form of ketoprofen. The same form was obtained from **4.1$_{RR}$** gels of water/IPA 1:1 mixtures (black).

The versatility of ambidextrous gelators, like **4.1$_{RR}$** and **4.2$_{RR}$**, can be highly favourable when utilising the gels as crystallisation media, as it increases the likelihood of gelling solvents from which the crystallisation substrate exhibits suitable solubility to crystallise from. Furthermore, hydrates are the most important pharmaceutical solvate class due to their nontoxic and favourable stability, although they can be polymorphic with 20 % and 28 % of API non-salt and salt hydrates respectively being identified as polymorphic as of 2018.[47] Being able to crystallise APIs in LMWG hydrogels may

increase the chance of isolating hydrate forms that can be utilised in formulation and identifying any polymorphism of these forms. Finally, many drugs are poorly-water soluble, but water is frequently used as an anti-solvent to promote crystallisation. The ability to gel these aqueous-solvent mixtures allow investigations into whether gel fibres can influence the crystallisation outcomes. Hydrogels and gelled mixtures of organic solvents with water were used to crystallise ketoprofen and flurbiprofen (**Figure 5-32**). Although the fibres failed to influence crystallisation outcomes, the ability of these gelators to gel water and aqueous-organic mixtures, in addition to pure organic solvents, may increase the chances of identifying hydrate or solvate forms of other APIs, which can be used a safely in pharmaceutical formulations.

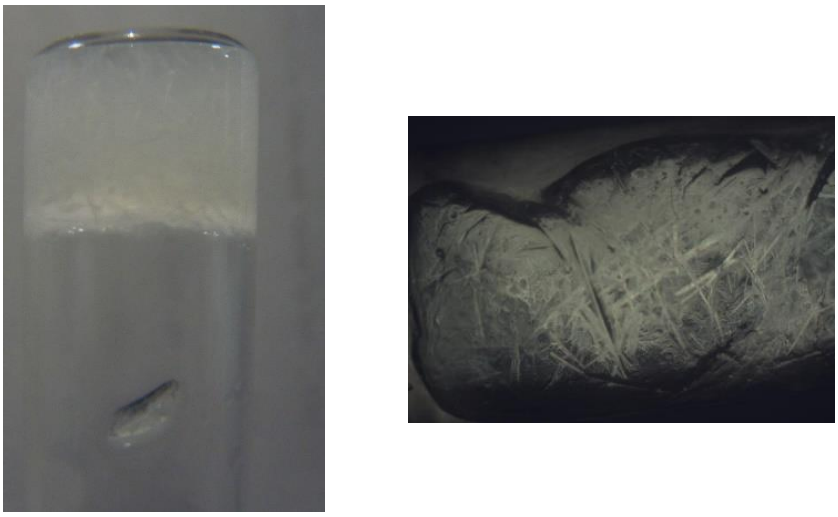

Figure 5-32. Ketoprofen crystals in a 1:1 H_2O:Propan-1-ol gel of **4.1$_{RR}$** at gelator concentration of 1 % w/v. An API concentration of 50 mg/0.5 mL was utilised.

5.3.3 High and Low temperature gel-phase crystallisations of RMOY

This section describes work in collaboration with the Preuss group at the University of Guelph. Work previously reported by Preuss *et al.* presented the crystallisation behaviour of 4-benzoyl-1,2,3-dithiazol-5-one, known as RMOY due to its structural similarity to ROY.[48] RMOY is an achiral molecule but undergoes a rare phenomenon whereby the molecule adopts transient chiral conformations in solution and crystallises in a racemic form from chlorobenzene at temperatures below 70 ^{o}C (**LT-1**), but in a homochiral form chlorobenzene at temperatures above 70 ^{o}C (**HT-1**). Racemisation of **HT-1** to **LT-1** occurs over several days when stored at ambient

temperature. We were interested to see whether chiral gelators could influence the crystallisation of RMOY at different temperatures and a sample of RMOY was kindly provided Dr. K. Preuss.

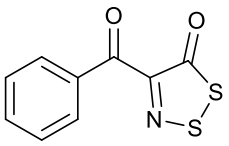

RMOY

Here, the crystallisation of RMOY from chlorobenzene solutions at 90 °C and ambient temperature was undertaken to ensure reproducibility. **HT-1** and **LT-1** were both obtained from the respective crystallisations and confirmed by XRPD. **HT-1** transitioned to **LT-1** within 4 days storage at ambient temperature.

Crystallisations of RMOY in chlorobenzene gels of **4.4$_{RR}$**, **4.4$_{Benz}$** and **4.4$_{Rac}$** were completed at an ambient temperature and at 90 °C on a 0.5 mL scale. Gel concentrations of 1 and 2 % w/v were employed and RMOY concentrations ranged between 25–75 mg / mL. Limited RMOY material was available, so only the **4.4** derivatives were used in these crystallisations. These gelators were selected as the chlorobenzene gels from gelators derived from **4.2** and **4.3**, collapsed above 70 °C, thus would not be suitable for high temperature crystallisations. Meanwhile, the chlorobenzene gels of **4.1$_{RR}$** were stable above 90 °C, but the lack of gelation of **4.1$_{Rac}$** and **4.1$_{Benz}$** were regarded as significant limitations in this study.

The **4.4$_{Benz}$** and **4.4$_{RR}$** gels yield the HT-1 when crystallised at 90 °C, whilst the **4.4$_{Rac}$** collapse at this temperature when supersaturated with RMOY. Under ambient conditions, **4.4$_{Benz}$** and **4.4$_{Rac}$** chlorobenzene gels yield the LT-1 form. Interestingly, the **4.4$_{RR}$** 1 % and 2 % chlorobenzene gels yielded crystals with XRPD patterns that do not match that of HT-1 or LT-1, potentially indicating a new form (**Figure 5-33**). Regrettably, DSC and IR data to confirm the novel nature of this form were not obtained due to a laboratory flood in December 2019, resulting in these samples being lost. Further work is required to test the reproducibility of these crystallisations, collect the IR and DSC data for this form and optimise conditions to grow a single crystal for SCXRD analysis if possible.

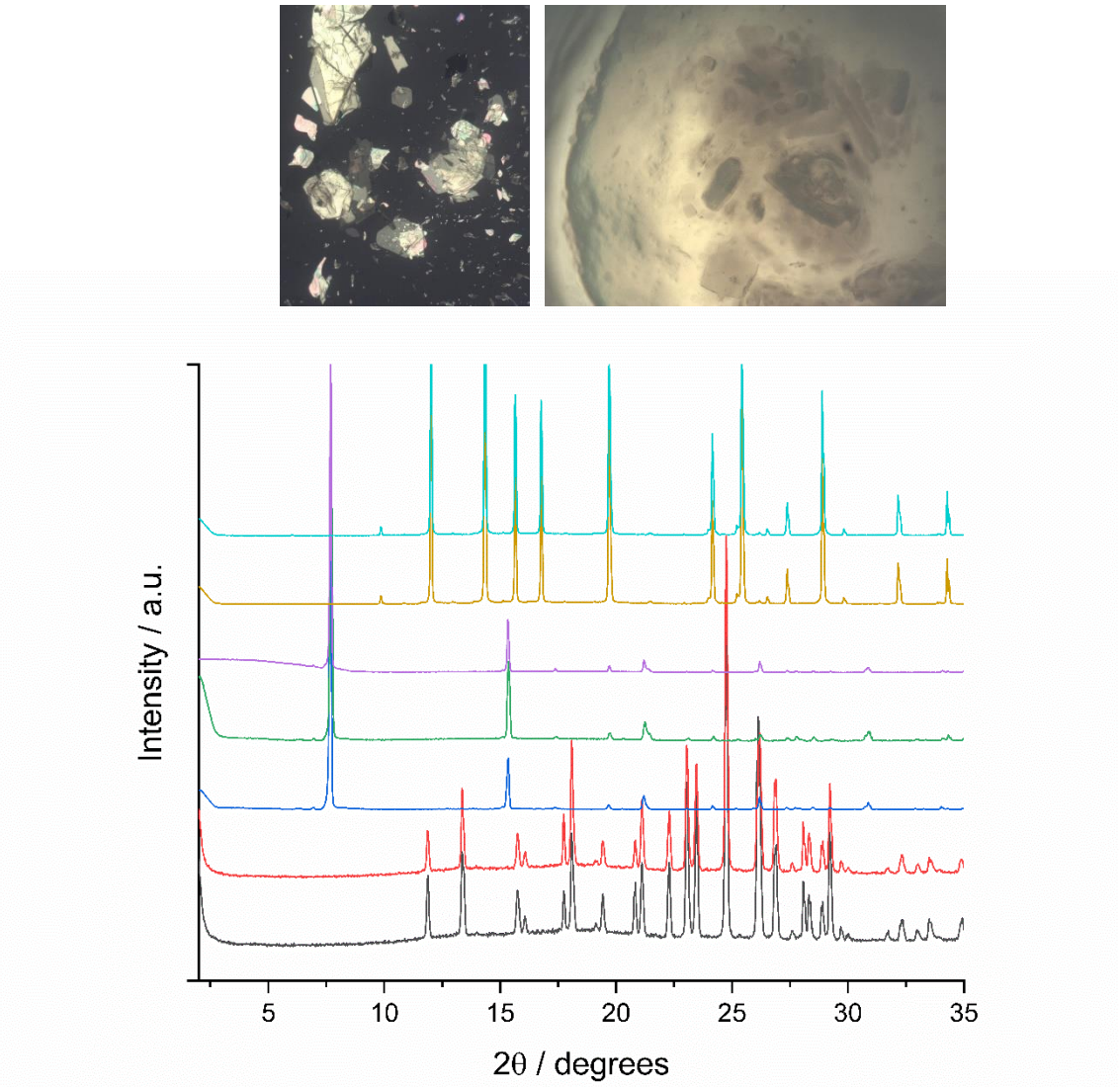

Figure 5-33. The XRPD patterns for RMOY crystallisation screening experiments. The HT form of RMOY obtained from chlorobenzene solution at 90 °C (black) and from 1 % w/v **4.4**$_{RR}$ chlorobenzene gels stored at 90 °C (red). The LT form was obtained from chlorobenzene solution at ambient temperature (blue) and 1 % w/v chlorobenzene gels of **4.4**$_{Benz}$ (green) and **4.4**$_{Rac}$ (purple) at room temperature. The patterns for these HT and LT forms match the previously reported patterns by the Preuss group. A potentially new form of RMOY was obtained from 1 % w/v **4.4**$_{SS}$ and **4.4**$_{RR}$ chlorobenzene gels (yellow and light blue respectively).

5.4 Conclusions

This work demonstrates that bis(acyl-semicarbazides) with varying aliphatic spacers are versatile gelators. The aromatic-spaced bis(acyl-semicarbazides) are less effective as gelators due to duplex assembly as observed in the corresponding single crystal structures. The impact of chirality on gelator performance was explored with molecular chirality increasing gelator versatility for all derivatives, but achiral compounds still yielded gels in most cases. Racemic mixture of the opposite R,R and

S,S enantiomers resulted in a significant drop in gelation for all compounds, particularly for **4.1** derivatives where the enantiopure compounds gelled 32 of 41 solvents, whilst the 50:50 mixture of R,R and S,S-enantiomers yielded zero gels. This was considered likely due to $N\text{-}H_{(amide)}\cdots O{=}C_{(urea)}$ hydrogen bonding which weakens urea α-tape interactions and form perpendicular to tape direction, resulting in 2D-assembly. This was confirmed by XRPD of the $\mathbf{4.1_{Rac}}$ precipitate. Solid-state techniques (IR, DSC and XRPD) were employed to compare molecular packing and interactions in crystal and xerogel forms and to explore polymorphism of gel fibres. Urea tape assembly could be correlated with gelation of $\mathbf{4.1_{RR}}$, whilst fibres of $\mathbf{4.2\text{-}4.4_{RR}}$ were either polymorphic or different to the identified crystal structures. XRPD, DSC and IR indicate that duplex assembly drive gel formation for the aromatic-spaced compounds, which is consistent with a previous study of aromatic-spaced bis(acyl-semicarbazides).

Rheology was used to confirm the SEM was also used to investigate the supramolecular architectures present in the xerogels. Use of SEM revealed that most xerogels exhibit achiral tubular fibres, however there were some notable chiral supramolecular structures observed. These include the 'accordion-like' fibres by chiral $\mathbf{4.2_{RR}}$ in 1,4-dioxane exclusively and twisted ribbons, heliconical fibres and scrolls observed in all gels of achiral compounds $\mathbf{4.3_{Benz}}$ and $\mathbf{4.4_{Benz}}$. The molecular mechanics underlying these structures is currently being further investigated by a postdoctoral fellow.

Most of the gels were sensitive to anions, with anion addition to pre-formed gels inducing gel-sol transitions, whilst adding anions to the sol prior to gelation inhibited gel formation. The exception was $\mathbf{4.1_{RR}}$, which could form gels with up to 10 molar equivalents of TBA fluoride or TBA chloride added to the sol. The gels became weaker and more transparent as anion concentration increased. This has applicability in the crystallisation of API salts, where anionic counterions may disrupt gelation of urea derivatives and limit the use of urea LMWGs in crystallisation screening of API salts. This was demonstrated through the crystallisations of procaine HCl.

The bis(acyl-semicarbazide) gels were also used to crystallise flurbiprofen and ketoprofen in the aim to control polymorphism of the form and/or achieve chiral resolution of both compounds. The 1-phenylethyl functionality is mimicked in both gelators and API compounds and the influences of molecular chirality, supramolecular

chirality and API-mimetic functionalities could be compared. However, despite an extensive crystallisation procedure, all gel-phase crystallisations yielded the same forms and from the solution phases, indicating a failure of the gel fibres to influence crystallisation outcomes. This was considered potentially due to the weak

Finally, crystallisation of RMOY was undertaken to see if the chlorobenzene gels of **4.1$_{RR}$**, **4.1$_{Rac}$** and **4.4$_{Benz}$** could influence the crystallisation outcomes both at ambient temperature and at 90 ^{o}C. RMOY adopts transient chiral conformations and crystallises from chlorobenzene solutions as a racemic form below 70 ^{o}C but as a homochiral form above 90 ^{o}C, and aim of this investigation was to see if molecular chirality or supramolecular chirality could yield the homochiral form at ambient conditions. Whilst this was not achieved, a new form of RMOY may have been identified via XRPD from **4.4$_{RR}$** gel crystallisations.

5.5 Future Work

The work described in this chapter provides solid foundations for much future work to be completed. Employing computational methods to model the self-assembly behaviour of the bis(acyl-semicarbazide) gelators would be beneficial. This would be particularly interesting for the 4.2 compounds to understand the interplay between folded and extended conformers and their role in forming gels, liquid crystals and crystals. This could also be used to investigate whether indeed the proposed mechanism of sonication disrupting the intramolecular hydrogen bond results in a change in conformation and enables gel fibre formation via urea α-tape assembly. Circular Dichroism (CD) spectroscopy and modelling of the solvated gel fibres would enable us to see whether the chiral architectures observed in the SEM images of the xerogels are observed in the solvated form.

To investigate the anion-resistance of **4.1ss** and **4.1$_{RR}$** ^{1}H-NMR titrations could be employed to investigate the supramolecular interactions between gelators and anions. Computational prediction tools could also be useful in modelling and understanding the interactions and behaviour of the gelator compounds in the presence on anions. Crystallisations using these gels with a wider ranges of API salts would be interesting to see whether gelator-anion interactions can influence the crystallisation outcomes.

Finally, repeated experiments to isolate the apparent new form of RMOY via gel-phase crystallisations should be employed and the form fully characterised. Further crystallisation techniques could also be used to try to isolate this form. If the bis(acyl-semicarbazide) gels can reproduce isolating this form, work to understand how interactions between gelator compounds and RMOY could be undertaken (both experimentally and computationally) to understand why the potential new form crystallises from these gels.

5.6 Experimental Details

Extended crystallisation details and outcomes are provided below. Please refer to Chapter 6– General Experimental for additional experimental details, including the general method employed for gel-phase API mimetic crystallisations.

Crystallisation of AZD-2281 and AZD-6140

The bis(acyl-semicarbazide) gelators were used to crystallise AZD-2281 and AZD-6140. This was a generic crystallisation tool to see whether the non-mimetic fibres could influence crystallisation outcomes, particularly as their versatility enabled gel-phase crystallisations to be undertaken in a wider range of solvents than the API-mimetic gelators. For AZD-6140, the gel fibres failed to influence crystallisation outcomes.

Table 5-4. Crystallisation outcomes when using the bis(acyl-semicarbazide) gels as crystallisation media for AZD-6140. All these experiments were undertaken on a 0.5 mL scale and repeated up to 3 times, consistently obtaining the stable form 2 of AZD-6140 (confirmed by XRPD). All solution phase crystallisations also yielded form 2. Polymorphic form was determined via IR, XRPD or SCXRD unit cell measurements.

Gelator	Solvent	Gel concentration / % w/v	Drug loading / mg	Crystallisation outcome
4.1$_{RR}$	Nitrobenzene	1	10	Form II
		1	25	Form II
	1,4-dioxane	1	10	Form II
		2	10	Form II
	Ethanol	1	25	Form II
		2	25	Form II
	Chloroform	1	10	Form II
		2	10	Form II
	Acetonitrile	1	10	Form II
		2	10	Form II
	Cyclohexane	1	10	Form II
		2	10	Form II
	Propan-1-ol	1	25	Form II
		2	25	Form II
	Chlorobenzene	1	25	Form II
		2	25	Form II
4.2$_{RR}$	1,4-dioxane	1	10	Form II
		2	10	Form II
	Nitrobenzene	1	10	Form II
		2	10	Form II
4.3$_{RR}$	1,4-dioxane	1	10	Form II
		2	10	Form II
	Nitrobenzene	1	10	Form II
		2	10	Form II
	Acetonitrile	1	10	Form II
		2	10	Form II
4.4$_{RR}$	Nitrobenzene	1	10	Form II
		2	10	Form II
	Acetonitrile	1	10	Form II
		2	10	Form II
	1,4-dioxane	1	10	Form II
		2	10	Form II
	Chlorobenzene	1	25	Form II
		2	25	Form II
4.5$_{RR}$	Nitrobenzene	2	25	Form II
		2	25	Form II
4.6$_{RR}$	Nitrobenzene	2	25	Form II
		2	25	Form II

This was also the case for AZD-2281, with gel fibres failing to influence the crystal form when compared to solution-phase crystallisations. The gels either yielded kinetically stable form A or the known isostructural solvates.

Table 5-5. Crystallisation outcomes when using the bis(acyl-semicarbazide) gels as crystallisation media for AZD-2281. All the experiments were undertaken on a 0.5 mL scale and repeated up to 3 times, consistently obtaining the kinetically stable form A of AZD-2281 (confirmed by XRPD) or the isostructural solvate form. All solution phase crystallisations also yielded form A or the isostructural solvates. Polymorphic form was determined via IR, XRPD or SCXRD unit cell measurements.

Gelator	Solvent	Gel concentration / % w/v	Drug loading / mg	Crystallisation outcome
4.1$_{RR}$	Nitrobenzene	1	10	Solvate
		1	25	Solvate
	1,4-dioxane	1	10	Form A
		2	10	Form A
	Ethanol	1	25	Form A
		2	25	Form A
	Chloroform	1	10	Form A
		2	10	Form A
	Acetonitrile	1	15	Form A
		2	15	Form A
	DCM	1	10	Solvate
		2	10	Solvate
	Propan-1-ol	1	25	Form A
		2	25	Form A
	Chlorobenzene	1	50	Form A
		2	50	Form A
4.2$_{RR}$	1,4-dioxane	1	10	Form A
		2	10	Form A
	Nitrobenzene	1	10	Solvate
		2	25	Solvate
4.3$_{RR}$	1,4-dioxane	1	10	Form A
		2	10	Form A
	Nitrobenzene	1	10	Solvate
		2	25	Solvate
	Acetonitrile	1	15	Form A
		2	15	Form A
4.4$_{RR}$	Nitrobenzene	1	10	Solvate
		2	25	Solvate
	Acetonitrile	1	15	Form A
		2	15	Form A
	1,4-dioxane	1	10	Form A
		2	10	Form A
	Chlorobenzene	1	25	Form A
		2	25	Form A
4.5$_{RR}$	Nitrobenzene	2	10	Solvate
		2	25	Solvate
4.6$_{RR}$	Nitrobenzene	2	10	Solvate
		2	25	Solvate

Table 5-6. Representative Crystallisation conditions and outcomes when using the bis(acyl-semicarbazide) gels as crystallisation media for AZD-procaine HCl. All These experiments were undertaken on a 0.5 mL scale and repeated up to 3 times, yielding the same outcomes with each iteration. For gelation outcomes, NG = no gelation, PG = partial gel, GT = translucent gel. For crystallisation outcomes, NC = no crystals after 4 weeks, X = crystals of the known form of Procaine HCl were obtained. Polymorphic form was determined via IR, XRPD or SCXRD unit cell measurements.

Gelator	Solvent	Gel concentration / % w/v	Drug loading / mg	Gelation outcome	Crystallisation outcome
4.1$_{RR}$	Acetonitrile	1	5	G^T	NC
		1	10	G^T	X
		1	25	G^T	X
		1	50	G^T	X
		1	100	NG	X
		2	25	G^T	X
		2	50	G^T	X
		2	100	NG	X
	Ethanol	1	10	G^T	NC
		1	25	G^T	NC
		1	50	G^T	X
		1	75	G^T	X
		1	100	G^T	X
		2	25	G^T	NC
		2	50	G^T	NC
		2	100	G^T	X
	1,4-dioxane	1	10	G^T	X
		1	25	G^T	X
		1	50	G^T	X
		1	100	NG	X
4.2$_{RR}$	Acetonitrile	1	10	NG	X
		1	25	NG	X
		1	10	PG	X
		1	25	NG	X
4.3$_{RR}$	1,4-dioxane	1	10	NG	X
		1	25	NG	X
	Acetonitrile	1	10	NG	X
		1	25	NG	X
4.4$_{RR}$	Acetonitrile	1	10	NG	X
		1	25	NG	X
	1,4-dioxane	1	10	NG	X
		1	25	NG	X
	Propan-1-ol	1	10	NG	NC
		1	25	NG	X
	Chlorobenzene	1	10	PG	NC
		1	25	PG	X

Table 5-7. Representative crystallisation conditions and outcomes when using the bis(acyl-semicarbazide) gels as crystallisation media for ketoprofen. All these experiments were undertaken on a 0.5 mL scale and repeated up to 3 times, yielding the same outcomes with each iteration. For gelation outcomes, NG = no gelation, PG = partial gel, Gc = transparent gel, GT = translucent gel. For crystallisation outcomes, NC = no crystals after 4 weeks, X = crystals of the known racemate form of ketoprofen. Polymorphic form was determined via IR or XRPD.

Gelator	Solvent	Gel concentration / % w/v	Drug loading / mg	Gelation Outcome	Crystallisation Outcome
4.1$_{RR}$	Chlorobenzene	2	25	G^T	X
		2	50	G^T	X
	Propan-2-ol	1	50	G^T	X
		1	75	G^T	X
	1,4-dioxane	1	25	G^T	X
		1	50	G^T	X
	Nitrobenzene	1	75	G^C	NC
		2	100	PG	X
	H2O:PrOH 1:1	1	50	G^T	NC
		1	75	G^T	X
4.2$_{RR}$	Nitrobenzene	2	75	G^T	NC
		2	100	NG	X
	1,4-dioxane	2	10	NG	NC
		2	25	NG	X
4.3$_{RR}$	Chlorobenzene	1	25	G^T	NC
		1	50	PG	X
	Propan-2-ol	1	50	PG	NC
		1	75	NG	X
	1,4-dioxane	2	25	G^T	NC
		2	50	G^T	X
4.4$_{RR}$	Chlorobenzene	1	25	G^T	NC
		1	50	PG	X
	Propan-2-ol	1	50	PG	NC
		1	75	NG	X
	1,4-dioxane	2	25	G^T	NC
		2	50	PG	X
	Nitrobenzene	2	75	NG	NC
		2	100	NG	X
4.5$_{RR}$	Nitrobenzene	2	75	NG	NC
		2	100	NG	X
4.6$_{RR}$	Nitrobenzene	2	75	NG	
4.2$_{Benz}$	Nitrobenzene	1	75	PG	NC
		1	100	PG	X
	Propan-2-ol	1	50	G^T	NC
		1	75	G^T	X
4.3$_{Benz}$	Nitrobenzene	1	75	G^T	NC
		1	100	PG	X
	Propan-2-ol	2	50	G^T	X
		2	75	NG	X
4.4$_{Benz}$	Nitrobenzene	1	75	G^c	NC
		1	100	G^c	X
	Propan-2-ol	2	50	G^T	NC
		2	75	NG	X
	1,4-dioxane	1	25	NG	NC

4.3$_{Rac}$		1	50	NG	X
	Nitrobenzene	1	75	G^c	X
		1	100	NG	NC
4.4$_{Rac}$	1,4-dioxane	1	25	G^T	NC
		1	50	PG	X
	Nitrobenzene	1	75	G^c	NC
		1	100	NG	X

Crystallisation of Flurbiprofen

Table 5-8. Representative Crystallisation conditions and outcomes when using the bis(acyl-semicarbazide) gels as crystallisation media for flurbiprofen. All These experiments were repeated up to 3 times, yielding the same outcomes with each iteration. For gelation outcomes, NG = no gelation, PG = partial gel, G^c = transparent gel and G^T = translucent gel. For crystallisation outcomes, NC = no crystallisation after 4 weeks, X = crystals of racemate form 1 of R,S-flurbiprofen. Polymorphic form was determined via IR, XRPD or SCXRD unit cell measurements.

Gelator	Solvent	Gel concentration / % w/v	Drug loading / mg	Gelation outcome	Crystallisation outcome
4.1$_{RR}$	Acetonitrile	1	25	G^T	NC
		1	50	PG	X
		2	25	G^T	NC
		2	50	G^T	X
	1,4-dioxane	1	10	G^T	NC
		1	25	G^T	X
	Nitrobenzene	1	50	G^c	X
		1	75	G^c	X
	Propan-2-ol	1	25	G^T	X
		1	50	G^T	X
	H_2O:Propan-2-ol (1:1)	1	25	G^T	X
		1	50	G^T	X
	Chlorobenzene	1	25	G^T	X
		1	50	G^T	X
		2	25	G^T	X
		2	50	G^T	X
4.2$_{RR}$	1,4-dioxane	2	10	NG	NC
		2	25	NG	X
	Nitrobenzene	1	25	NG	NC
		2	50	NG	X
4.3$_{RR}$	1,4-dioxane	1	25	G^T	NC
		1	50	PG	X
	Nitrobenzene	1	50	G^c	X
		1	75	G^c	X
	Acetonitrile	1	25	G^T	NC
		1	50	NG	X
4.4$_{RR}$	Acetonitrile	1	25	G^T	NC
		1	50	NG	X
	1,4-dioxane	1	10	G^T	NC
		1	25	PG	X
	Nitrobenzene	1	50	G^c	NC
		1	75	PG	X

		2	75	G^c	X
	Propan-2-ol	2	25	G^T	X
		2	50	PG	X
	Chlorobenzene	1	25	G^T	X
		1	50	G^T	X
4.5$_{RR}$	Nitrobenzene	2	50	NG	X
		2	75	NG	X
4.6$_{RR}$	Nitrobenzene	2	50	NG	X
4.2$_{Benz}$	Nitrobenzene	1	50	G^T	NC
		1	75	G^T	X
	Propan-2-ol	1	75	G^T	X
		1	10	G^T	X
4.3$_{Benz}$	Nitrobenzene	1	50	G^T	NC
		1	75	G^T	NC
	Propan-2-ol	1	25	G^T	X
		1	50	NG	X
4.4$_{Benz}$	Nitrobenzene	1	50	G^c	NC
		1	75	G^c	X
	Propan-2-ol	1	25	G^T	NC
		1	50	NG	X
4.3$_{Rac}$	1,4-dioxane	1	10	NG	NC
		1	25	NG	X
	Nitrobenzene	1	50	G^c	X
		1	75	NG	NC
4.4$_{Rac}$	1,4-dioxane	1	10	G^T	NC
		1	25	PG	X
	Nitrobenzene	1	50	G^c	NC
		1	75	NG	X

Crystallisation of RMOY

Table 5-9. Representative crystallisation conditions and outcomes when using the 4.4-derived bis(acyl-semicarbazide) chlorobenzene gels as crystallisation media for RMOY. All gels were on a 0.25 mL scale with 50 mg RMOY. HT = high temperature form, LT = low temperature form, NG = collapsed gel and X^n = potential new polymorphic form of RMOY. Repeats are required.

Gelator	Gel concentration / % w/v	Storage temperature	Crystallisation outcome
4.4$_{RR}$	1	25 °C	X^n
	2	25 °C	X^n
	1	90 °C	HT
	2	90 °C	HT
4.4$_{Benz}$	1	25 °C	LT
	2	25 °C	LT
	1	90 °C	HT
	2	90 °C	HT
4.4$_{Rac}$	1	25 °C	LT
	2	25 °C	LT
	1	90 °C	NG
	2	90 °C	NG

5.7 References

1 R. G. Weiss, *J. Am. Chem. Soc.*, 2014, **136**, 7519-7530

2 J. Bachl, D. Sampedro, J. Mayr and D. Díaz Díaz, *Phys. Chem. Chem. Phys.*, 2017, **19**, 22981-22994

3 X. Du, J. Zhou, J. Shi and B. Xu, *Chem. Rev.*, 2015, **115**, 13165-13307.

4 M. A. Walker, *Bioorganic Med. Chem. Lett.*, 2017, **27**, 5100–5108.

5 M. Ishikawa and Y. Hashimoto, *J. Med. Chem.*, 2011, **54**, 1539–1554.

6 W. Edwards and D. Smith, *Gels*, 2018, **4**, 31-48.

7 D. A. Tómasson, D. Ghosh, Z. Kržišnik, L. H. Fasolin, A. A. Vicente, A. D. Martin, P. Thordarson and K. K. Damodaran, *Langmuir*, 2018, **34**, 12957-12967

8 V. Čaplar, L. Frkanec, N. Š. Vujičić and M. Žinić, *Chem. A Eur. J.*, 2010, **16**, 3066-3082.

9 K. McAulay, B. Dietrich, H. Su, M. T. Scott, S. Rogers, Y. K. Al-Hilaly, H. Cui, L. C. Serpell, A. M. Seddon, E. R. Draper and D. J. Adams, *Chem. Sci.*, 2019, **10**, 7801-7806.

10 D. Andrienko, *J. Mol. Liq.*, 2018, **267**, 520–541.

11 R. A. Reddy and C. Tschierske, *J. Mater. Chem.*, 2006, **16**, 907-961

12 X. Yu, Q. Liu, J. Wu, M. Zhang, X. Cao, S. Zhang, Q. Wang, L. Chen and T. Yi, *Chem. - A Eur. J.*, 2010, **9**, 9099–9106.

13 F. Ye, S. Chen, G. D. Tang and X. Wang, *Colloids Surfaces A Physicochem. Eng. Asp.*, 2014, **452**, 165-172.

14 M. Luo, S. Wang, C. Li, W. Miao and X. Ma, *Dye. Pigment.*, 2019, **165**, 436-443.

15 P. Dastidar, *Gels*, 2019, **5**, 15-25.

16 S. Ahn, F. Guo, B. M. Kariuki and K. D. M. Harris, *J. Am. Chem. Soc.*, 2006, **128**, 8441–8452.

17 R. Centore, M. Causà, F. Cerciello, F. Capone and S. Fusco, *CrystEngComm*, 2014, **16**, 9168–9175.

18 A. J. Cruz-Cabeza and J. Bernstein, *Chem. Rev.*, 2014, **114**, 2170–2191.

19 Y. Wang, C. Zhan, H. Fu, X. Li, X. Sheng, Y. Zhao, D. Xiao, Y. Ma, J. S. Ma and J. Yao, *Langmuir*, 2008, **24**, 7635–7638.

20 W. J. Chu and C. F. Chen, *Chinese Sci. Bull.*, 2012, **57**, 4278–4283.

21 N. Fujita, Y. Sakamoto, M. Shirakawa, M. Ojima, A. Fujii, M. Ozaki and S. Shinkai, *J. Am. Chem. Soc.,* 2007, **129**, 4134–4135

22 P. Yadav and A. Ballabh, *New J. Chem.*, 2015, **39**, 721-730

23 M. O. M. Piepenbrock, G. O. Lloyd, N. Clarke and J. W. Steed, *Chem. Commun.*, 2011, **47**, 2095-2097.

24 L. L. E. Mears, E. R. Draper, A. M. Castilla, H. Su, Zhuola, B. Dietrich, M. C. Nolan, G. N. Smith, J. Doutch, S. Rogers, R. Akhtar, H. Cui and D. J. Adams, *Biomacromolecules*, 2017, **18**, 3531–3540.

25 W. Park, T. Ha, T. T. Kim, A. Zep, H. Ahn, T. J. Shin, K. I. Sim, T. S. Jung, J. H. Kim, D. Pociecha, E. Gorecka and D. K. Yoon, *NPG Asia Mater.*, 2019, **11**, https://doi.org/10.1038/s41427-019-0146-6.

26 C. Tschierske, *Liq. Cryst.*, 2018, **45**, 2221-2252.

27 S. J. James, A. Perrin, C. D. Jones, D. S. Yufit and J. W. Steed, *Chem. Commun.*, 2014, **50**, 12851–12854.

28 Z. Shen, Y. Jiang, T. Wang and M. Liu, *J. Am. Chem. Soc.*, 2015, **137**, 16109–16115.

29 D. N. Nadimetla, M. Al Kobaisi, S. T. Bugde and S. V. Bhosale, *Chem. Rec.*, 2020, **20**, 793–819.

30 P. Xing, Y. Li, S. Xue, S. Z. Fiona Phua, C. Ding, H. Chen and Y. Zhao, *J. Am. Chem. Soc.*, 2019, **141**, 9946–9954.

31 C. D. Jones, H. T. D. Simmons, K. E. Horner, K. Liu, R. L. Thompson and J. W. Steed, *Nat. Chem.*, 2019, **11**, 375–381.

32 C. Park, J. Lee, T. Kim, J. Lim, J. Park, W. Y. Kim and S. Y. Kim, *Molecules*, 2020, **25**, 402-415.

33 N. Micali, H. Engelkamp, P. G. Van Rhee, P. C. M. Christianen, L. M. Scolaro and J. C. Maan, *Nat. Chem.*, 2012, **4**, 201–207.

34 J. Sun, Y. Li, F. Yan, C. Liu, Y. Sang, F. Tian, Q. Feng, P. Duan, L. Zhang, X. Shi, B. Ding and M. Liu, *Nat. Commun.*, 2018, **9**, Article number: 2599.

35 J. W. Steed, *Chem. Soc. Rev.*, 2010, **39**, 3686–3699.

36 D. Gupta, D. Bhatia, V. Dave, V. Sutariya and S. V. Gupta, *Molecules*, 2018, **23**, 1719–1734.

37 D. P. Elder, R. Holm and H. L. De Diego, *Int. J. Pharm.*, 2013, **50**, 6665-6672.

38 S. Hiendrawan, E. Widjojokusumo, B. Veriansyah and R. R. Tjandrawinata, *AAPS PharmSciTech*, 2017, **18**, 1417–1425.

39 J. A. Foster, M. O. M. Piepenbrock, G. O. Lloyd, N. Clarke, J. A. K. Howard and J. W. Steed, *Nat. Chem.*,2010, **2**, 1037-1043.

40 H. Alkadi and R. Jbeily, *Infect. Disord. - Drug Targets*, 2018, **18**, 88–95.

41 A. Calcaterra and I. D'Acquarica, *J. Pharm. Biomed. Anal.*, 2018, **147**, 323–340.

42 M. Budău, G. Hancu, A. Rusu, M. Cârcu-Dobrin and D. L. Muntean, *Adv. Pharm. Bull.*, 2017, **8**, 353–364.

43 F. Phourcq, C. Jarry and B. Bannwarth, *Biomed. Chromatogr.*, 2001, **15**, 217–222.

44 L. Zhang, Q. Jin and M. Liu, *Chem. Asian. J.*, 2016, **11**, 2642.

45 W. Edwards and D. K. Smith, *J. Am. Chem. Soc.*, 2014, **136**, 1116–1124.

46 X. Xu, L. Qu, J. Song, D. Wu, X. Zhou and H. Xiang, *Chem. Commun.*, 2019, **13**, 9873–9876.

47 S. M. Reutzel-Edens, D. E. Braun and A. W. Newman, in *Polymorphism in the Pharmaceutical Industry: Solid Form and Drug Development*, eds. R. Hilfiker and M. von Raumer, Wiley VCH, Berlin, 1st edn., 2018, pp. 159–188.

48 R. A. Mayo, D. J. Sullivan, T. A. P. Fillion, S. W. Kycia, D. V. Soldatov and K. E. Preuss, *Chem. Commun.*, 2017, **53**, 3964–3966.

49 C. G. Pappas, P. W. Frederix, T. Mutasa, S. Fleming, Y. M. Abul-Haija, S. M. Kelly, A. Gachagan, D. Kalafatovic, J. Trevino, R. V. Ulijn, S. Bai, *Chem Commun (Camb).*, 2015, **51**, 8465-8.

50 A. M. Hung and S. I. Stupp, *Langmuir*, 2009, **25**, 7085-7089

Chapter 6 - Closing Remarks

This work primarily focuses on the design of novel LMWGs and using solid-state analysis, including crystallography, to understand the self-assembly behaviour of these compounds on the molecular scale. The designed LMWGs include those that exhibit structural mimicry to target APIs. This work aims to contribute to the eventual goal of producing a 'toolkit' of structurally diverse LMWGs that solid-state chemists can select and use to crystallise a target API based on structural similarity and likelihood that the gelator and API will interact. These gels, under certain conditions, could potentially influence crystallisation outcomes, such as controlling the polymorphic form. The work highlights some key considerations regarding gelator design and the use of supramolecular gels as crystallisation media.

Firstly, discoveries of LMWGs have historically relied upon serendipity or synthesising structurally related analogues of known gelators and hoping the gelation functionality is preserved. Indeed, the Steed group has heavily relied upon the 4,4-MDEP (magic spacer) group as a gelation functionality to yield effective supramolecular gels. One issue with being reliant on few core gelation functionalities is that sometimes when incorporating a desirable substructure or functionality into your core structure, the resulting compound may exhibit poor or no gelation behaviour. This was demonstrated in chapter 3, whereby a selection of bis(urea) compounds synthesised using the typical gelation functionalities utilised by the Steed group were proven to be non-gelators. The work in chapter 4 and 5 presents the first reports yield highly effective and versatile bis(acyl-semicarbazides) gelators, particularly those derived from spacers **4.1-4.4**. This can limit the structure features that can be incorporated into LMWGs. The more core-gelation functionalities known and available to researchers the more options they have available to design and synthesise diverse structurally related analogues, which increases the likelihood that an effective gelator will be obtained. Future work should further investigate the use of these bis(acyl-semicarbazide) gelation functionalities in supramolecular gels by synthesising other novel bis(acyl-semicarbazide) compounds, with structurally diverse end groups and charactering their gelation/crystallisation behaviour.

Secondly, whilst crystallising effective LMWGs is often considered challenging this work demonstrates that often a delicate balance exists between crystallisation and gelation, and that refining experimental conditions can determine whether gelation or crystallisation will be observed. Specifically, this work demonstrates that crystallisation can often be promoted over gelation by decreasing gelator concentration below the critical concentration for gelation and carefully controlling conditions. This was especially demonstrated in chapter 1, where the first crystal structure of a bis(urea) derived from 4,4-MDEP is reported, and via the crystallisation of the versatile bis(acyl-semicarbazide) gelators in chapter 4. The resulting crystal structures provides detailed insight to the molecular packing and supramolecular interactions dictating self-assembly. Whilst it is crucial to note that assembly behaviour observed in the crystal form may not represent those in the gel phase, the crystal structures can still provide valuable insight to the general behaviours of LMWG compounds on the molecular level. Such insights can enable working hypotheses regarding any observed gelation behaviour (or lack of) to be formulated. The hypotheses can, and indeed should, then be tested via the employment of other techniques, including employing computational tools, such as molecular dynamics, to understand the underlying kinetics of gel formation and factors affecting it. This will further aid intelligent and directed design of LMWGs. Molecular dynamics should be employed in future work to further explore the interesting gelation properties of the bis(acyl-semicarbazides) presented in this work, including the accordion-like fibres exhibited in xerogels of **4.2$_{RR/SS}$** and the ability of **4.1$_{RR/SS}$** gels to maintain gelation in the presence of high quantities of anions.

The API-mimetic LMWGs presented in this work were designed and synthesised by simply appending mimetic moieties to known gelation functionalities and anticipating that the resulting molecules would gel based on previous gelation behaviour exhibited by structurally related compounds. Unfortunately, a number of these compounds were non-gelators or gelled solvents not considered appropriate for use in pharmaceutical development. The gold standard for the supramolecular gel field would be the development of computational methods that can universally be applied to accurately predict whether a designer molecule can gel a specific set of solvents, however this is currently proving a challenge to achieve due to the structural diversity of LMWGs and the complexity of factors dictating gelation behaviour, including the polarity of the solvent, solvent-gelator interactions and how the solvent impacts gelator-gelator

interactions, which are still not fully understood.[1] Currently the field is limited to developing methods to predict gelation behaviour on solubility parameters, which can provide accurate predictions for a series of structurally-related analogues.[2] Indeed, one such model for predicting the gelation behaviour based on the solubility parameters of 4,4-MDEP analogues and bis(acyl-semicarbazide) analogues would be highly desirable and would significantly aid the development of novel LMWGs that could be used for API crystallisation. This approach may also enable researchers to design gelators to gel a specific solvent, for example a solvent in which a target API is known to crystallise from.

Finally, on the topic of using supramolecular gels designed to mimic or interact with crystallisation substrates, this thesis highlights some of the complications with this approach. The gels used as crystallisation media in chapters 3 and 5 typically failed to significantly influence crystallisation outcomes, except for a potential new form of RMOY which remains inconclusive and requires further investigation. Incorporating API-mimetic structural moieties into LMWG compounds is a rational approach to encourage interaction between the gelator and crystallisation substrate and has previously yielded significant success.[3,4] However, many other factors determine whether crystallisation outcomes will be impacted, including the rates of nucleation of each component, which in turn are affected by gelator-substrate concentrations and external factors, such as temperature.[5] Producing a 'toolkit' of supramolecular gelators with a wide range of structural moieties/functionalities that can be used to screen APIs exhibiting structural similarities has potential to be useful for early-phase solid-state screening in industries. However, this work highlights that often gels fail to influence the crystallisation of the target substrate, despite numerous different conditions being tested. This lack of impact could be observed for a number of reasons, such as insufficient interaction/recognition between gelator and crystallisation substrates or there being a narrow window of conditions under which the gelator can significantly impact crystallisation of the substrate which could easily be overlooked. Additionally, the approach of experimentally testing numerous API-mimetic LMWGs and gel-phase crystallisation conditions in the hope that they will influence crystallisation outcomes, without using a method or protocol to determine which experimental conditions should be tested, is inefficient. Indeed, it would be particularly problematic to adopt the approach presented in this work for early-phase solid-state screening of

pharmaceutical candidates when available masses of the crystallisation substrate can be very limited. As such, future work in this field should shift towards using computational modelling methods, such as crystal structure prediction and molecular dynamics, to direct API-mimetic gelator design and predict whether significant interaction would be expected between gelator and target substrate. These models could then help to identify the gelators and experimental crystallisation conditions that are most likely to influence crystallisation outcomes and enable supramolecular gels.

6.1 References

1 Y. Lan, M. G. Corradini, X. Liu, T. E. May, F. Borondics, R. G. Weiss and M. A. Rogers, Langmuir, 2014, **30**, 14128–14142.

2 D. Rosa Nunes, M. Raynal, B. Isare, P. A. Albouy and L. Bouteiller, Soft Matter, 2018, **14**, 4805–4809.

3 A. Dawn, K. S. Andrew, D. S. Yufit, Y. Hong, J. P. Reddy, C. D. Jones, J. A. Aguilar and J. W. Steed, Cryst. Growth Des., 2015, **15**, 4591–4599.

4 S. R. Kennedy, C. D. Jones, D. S. Yufit, C. E. Nicholson, S. J. Cooper and J. W. Steed, CrystEngComm, 2018, **20**, 1390–1398.

5 A. Dawn, M. Mirzamani, C. D. Jones, D. S. Yufit, S. Qian, J. W. Steed and H. Kumari, Soft Matter, 2018, **14**, 9489.

Chapter 7 – General Experimental

7.1 Materials

API compounds AZD-6140 and AZD-2281 were provided in solid powder form by AstraZeneca and were used without further purification. AZD-6140 was supplied as crystalline form I, whilst AZD-2281 was supplied as crystalline form A. RMOY was provided by the Preuss Group at the University of Guelph as the crystalline low temperature form. All other materials were purchased from licensed commercial sources and used without further purification.

7.2 Instrumentation for the characterisation of compounds

7.2.1 Nuclear Magnetic Spectroscopy (NMR)

Solution-state NMR spectra were recorded in DMSO-d6 or $CDCl_3$, without an internal reference, using either a Bruker Avance III-HD-400 spectrometer with operating frequencies of 399.95 MHz for ^{1}H and 100.57 MHz for ^{13}C or a Varian VNMRS-600 spectrometer with operating frequencies of 599.42 MHz for ^{1}H and 150.72 MHz for ^{13}C. Data on the latter was collected by Dr Juan Aguilar Malavia. Samples were typically 0.7 mL in volume and concentrations of 1-3 % (w/v) were used.

Solid-state spectra Solid-state ^{13}C spectra were recorded at 100.63 MHz using a Bruker Avance III HD spectrometer and a 4 mm (rotor o.d.) magic-angle spinning probe. They were obtained using cross-polarisation with a 1 s recycle delay, 10 ms contact time, at ambient probe temperature (approximately 25 ^{o}C) and at a sample spin-rate of 10 kHz. Between 3000-3600 repetitions were accumulated. Spectral referencing was with respect to an external sample of neat tetramethylsilane. Data was collected by Dr. David Apperley.

7.2.2 Mass Spectroscopy

Electrospray-ionisation mass spectra were obtained using a Waters SQD mass spectrometer. Samples were prepared by diluting <1 mg in 1 cm^{-3} of acetonitrile or

methanol. The mobile phase was either formic acid (0.1 % v /v aqueous solution):methanol or formic acid (0.1 % v/v aqueous solution):acetonitrile, eluted at a flow rate at 0.6 mL min^{-1}. A solvent gradient was used, changing from 95 % water and 5 % organic solvent to 5 % water and 95 % organic solvent over 4.5 minutes.

7.2.3 Elemental Analysis

Elemental analysis was completed on dried materials using an Exeter CE-440 Elemental Analyser. Data was collected by Dr Emily R. Unsworth.

7.2.4 Rheological Analysis

Rheometry measurements were acquired using a TA Instrument AR 2000. A rough Peltier plate with a 25 mm rough plate geometry were used for all samples, with a 2.5 mm gap between them. The Peltier plate was cooled at 10 ^{o}C to minimize solvent evaporation. For samples in chapters 2 and 3, the required quantity of gelator was dissolved in 2 mL of solvent via heating in a sealed 7 cm^{-3} vial. The hot sol was then poured into a glass mould on the Peltier plate and left for 30 minutes to 1 hour until gelation was achieved. The mould was then removed and measurements taken. For the gel samples in chapter 5, most gels were pre-formed due to the requirement for sonication to induce gelation. In these cases, the gels were formed on a 2 mL scale in seals vials via heat and sonication. The gels were then carefully extracted from the vial using a spatula and placed on the Peltier plate. For all frequency sweep experiments, a constant applied stress of 1 Pa was used. For stress-sweep experiments, a constant frequency of 1 Hz was applied.

7.2.5 X-ray Powder Diffraction (XRPD)

Samples for XRPD were mounted on a silicon single-crystal wafer and diffraction patterns obtained using a Bruker D8 powder x-ray diffractometer with Cu-Kα radiation at a wavelength of 1.5406 Å. The diffractometer was operated with a voltage of 40 kV and current of 40 mA. Samples were typically scanned over 2-40 ^{o} 2θ with a scan rate between 0.5-1.5 second per step and a step size of 0.02 ^{o}.

7.2.6 Single-Crystal X-ray Diffraction (SCXRD)

Most single crystal data in this work was collected at 120 K on a Bruker D8 Venture (CMOS area detector) equipped with a Cryostream 700+ (Oxford Cryosystems) open-flow nitrogen cryostat, using MoKα (λ = 0.71073 Å) or CuKα (λ = 1.54178 Å) radiation. Data for poorly diffracting crystals was obtained at 100 K using Rigaku Saturn 724+ diffractometer at station I19 of the Diamond Light Source synchrotron (undulator, λ = 0.6889 Å, ω-scan, 1.0°/frame). Data were processed using the Bruker APEX II software and solved and refined using the SHELX suite of programs[1] in Olex2.[2] Structures were solved and refined by the author and/or Dr Dmitry S. Yufit.

7.2.7 Infrared Spectroscopy (IR)

Fourier transform IF spectra were collected using a Perkin Elmer Spectrum 100 spectrometer, fitted with a diamond universal Attenuated Total Reflectance (ATR) accessory. Eight scans were collected for each sample at a resolution of 2 cm^{-1} over a wavenumber region of 4000 cm^{-1} to 600 cm^{-1}.

7.2.8 Differential Scanning Calorimetry (DSC)

Differential scanning calorimetry (DSC) data was collected using a Perkin Elmer 8500 calorimeter, calibrated using an indium standard (melting point onset = 156.6 °C, heat of fusion = 28.57 J g^{-1}). Between 1 and 3 mg of sample was weighed accurately (±0.01 mg) into sealed aluminium pans and hermetically sealed. Dry nitrogen was used as the purge gas (flow rate: 50 mL min^{-1}). Data was collected by Mr Douglas W. Carswell.

7.2.9 Scanning Electron Microscopy (SEM)

SEM samples were prepared on silicon wafers and dried in air for up to 3 days. Prior to imaging, the samples were coated with 2 nm of platinum using a Cressington 328 Ultra High Resolution EM Coating System. Images were acquired using a FEI Helios NanoLab

DualBeam microscope in immersion mode with typical beam settings of 1.5 kV and 0.17 nA. Cryo-SEM imaging was performed using a Hitachi S5200 In-Lens FESEM. The samples were prepared and coated as described above, before being mounted on a cryo-stage and loaded into the microscope chamber.

7.3 Synthesis of 4,4-methylenebis(2,6-diethylphenyl isocyanate)

The compound 4,4-methylenebis(2,6-diethylphenyl isocyanate) (referred to in this work as 4,4-MDEP) is a key reagent in the synthesis of bis(urea) compounds described in chapters 2 and 3. It was synthesised from the commercially available diamine via a procedure previously reported.[3] A solution of di-*tert*-butyl dicarbamate (6.0 g, 27.5 mmol) in 20 cm^3 dry acetonitrile was treated with a solution of 4-dimethylaminopyridine (1.56 g, 12.8 mmol) in dry acetonitrile and a solution of 2,2',6,6'-tetraethyl-4,4'-methylenediphenyl (4 g, 12.8 mmol) in 20 cm^3 dry acetonitrile. The resulting mixture was stirred for 10 minutes at room temperature. Sulfuric acid (7 eq.) as a 40% solution in dry acetonitrile was added to the reaction mixture and stirred for 2 minutes. The mixture was then extracted three times with hexane. The combined hexane layers were dried over magnesium sulfate before the solvent was removed under vacuum. The resulting solid was dissolved in 10 cm^3 dichloromethane and passed through a filter. The dichloromethane was removed under vacuum to give an oily white precipitate. Finally, 20 cm^3 acetone was added to the oily precipitate and left to evaporate overnight to yield pure tetraethyl-4,4'-methylenediphenyl isocyanate as a white solid (3.294 g, 9.08 mmol, 71% yield). The product was used without further purification to synthesis gelators in chapters 2 and 3.

^{1}H NMR (400 MHz, DMSO-d_6) δ 7.00 (s, 4H, ArH), 3.84 (s, 2H, CH_2), 2.54 (q, J = 7.5 Hz, 8H, CH_2), 1.14 (t, J = 7.5 Hz, 12H, CH_3).

7.4 Compound Characterisation

Compounds were initially characterised by ^{1}H-NMR spectroscopy and mass spectrometry. Pure shift ^{1}H-NMR was used to improve the resolution of complex multiplets to enable assignments.[4] D_2O shakes were frequently employed to identify signals corresponding to labile protons (primarily urea NH signals). Once the spectra

looked free of impurities samples were submitted for elemental analysis. Solution state ^{13}C spectra were also then obtained where possible but the low solubility of many gelators meant this was often challenging. Instead, solid-state ^{13}C spectra were obtained for many of the compounds synthesised. The characterisation data for specific compounds can be found in the relevant chapters 2-5.

7.5 General method for gel screens

Potential LMWGs were initially screened at 1 % w/v in a selection of 41 solvents ranging the polarity spectrum (See **Table 5-1** for the full list). The dry gelator powder was initial ground in a pestle and mortar to reduce particle size which could facilitate more rapid dissolution. The gelator (5 mg) was then weighed out into vials before 0.5 mL of selected solvent was added. The vial was then sealed and carefully heated using a heat gun until either all the solid had dissolved by eye, or the boiling point of the solvent was reached. The vial was then allowed to cool to ambient temperature on the benchtop. After 24 hours, the vial was inverted to see if gel-like rheology was observed. If the compound dissolved upon heating but formed a solution upon cooling, the experiment was repeated at 2 % w/v to see if higher concentrations of compound could result in gelation. If the compound dissolved upon heating but formed a precipitate upon cooling (at either 1 % w/v or 2 % w/v), then the sample was heated again until all the solid redissolved and then was sonicated for 10-60 seconds to see if sonication could trigger gelation.

7.6 General approach for crystallisation of APIs

Initially the solubility of crystallisation substrates were tested in various organic solvents by adding 0.1 mL aliquots of solvent to 10 mg of API and heating with a heating gun to see if dissolution occurred. If dissolution were achieved, the sample was left to determine whether crystallisation or precipitation would occur. If rapid precipitation occurred, the conditions were fine-tuned using lower extents of supersaturation to try to improve the crystallisation process and grow single crystals. The concentrations that yielded crystalline material from a given solvent were then used for gel-phase crystallisations of the API using the same solvent system.

Gel-phase crystallisations of APIs were all performed by dissolving the required mass of API in the selected solvent with heat. The API solution was then added to a vial containing the required mass of gelator and heated again with a heat gun until all solid particulates had seemingly dissolved and were no longer visible by eye, or until the solvent boiled. The vial was then left to stand and cool until a gel formed. Gels were then kept at ambient temperature for days to weeks and carefully checked on a frequent basis to check if crystals had grown. Crystals were removed from gels either by the addition of tetrabutylammonium acetate to the gel and filtering the resulting sol, or by extracting them directly from the gel with a spatula.

7.6 References

1 G. M. Sheldrick, *Acta Crystallogr. Sect. C Struct. Chem.*, 2015, **71**, 3–8.

2 O. V. Dolomanov, L. J. Bourhis, R. J. Gildea, J. A. K. Howard and H. Puschmann, *J. Appl. Crystallogr.*, 2009, **42**, 339–341.

3 H. J. Knolker, T. Braxmeier and G. Schlechtingen, *Angew. Chem. Int. Ed. Engl.*, 1995, **34**, 2497–2500.

4 J. A. Aguilar, S. Faulkner, M. Nilsson and G. A. Morris, *Angew. Chemie - Int. Ed.*, 2010, **49**, 3901–3903

Chapter 8 - Appendices

Appendix 1 – Supplementary data for Chapter 2

This appendix provides supplementary data and experimental conditions for chapter 2.

Rheology – Frequency-sweep measurements

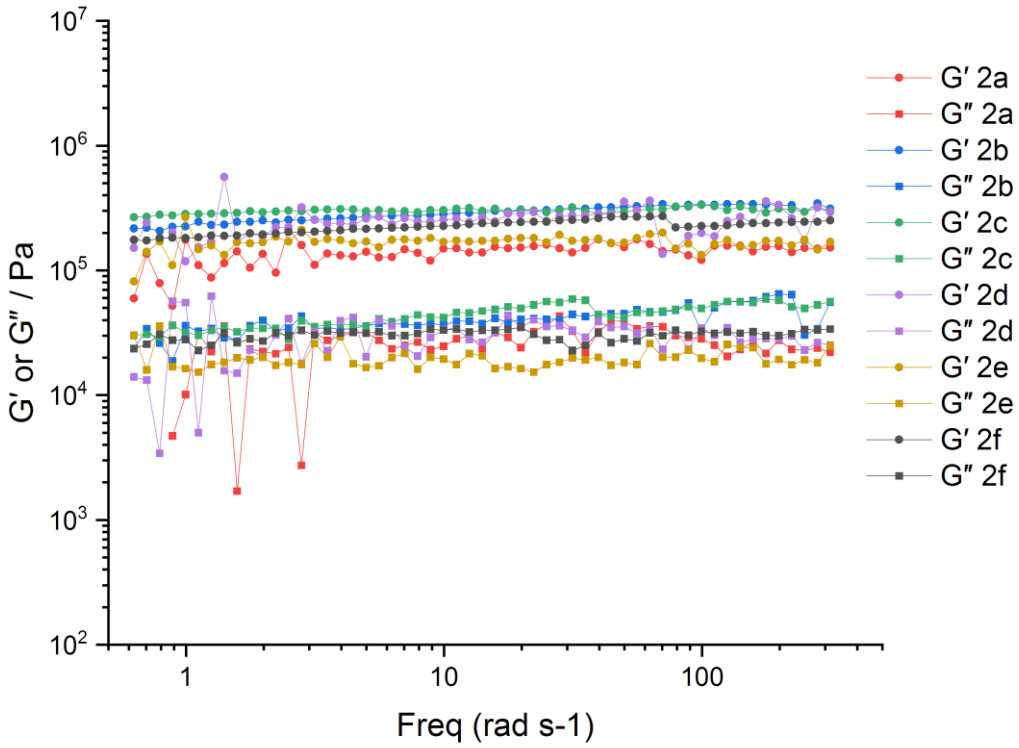

Figure 8-1. Frequency-sweep measurements for 1 % w/v gels of **2a-2f**. The G' and G" values are essentially constant across the frequency range, and G" is approximately an order or magnitude lower than G' for all gels. The solvent used was 1,4-dioxane for all gels, except **2e** where 1,2-dichlorobenzene was used instead due to a lack of gelation in 1,4-dioxane. Measurements were taken at 10 °C to minimize solvent evaporation.

Ball Drop Experiments

Table 8-1. The results of ball-experiments undertaken to determine T_{gel} (°C). Ball-drops were undertaken on a 2 mL scale using a 500 mg ball bearing. NG = no gel in this solvent.

	2a	**2b**	**2c**	**2d**	**2e**	**2f**
1,4-dioxane	83	67	58	50	NG	41
1,2-dichlorobenzene	NG	112	108	95	88	90

Table 8-2. Representative examples of crystallisation experiments that failed to yield crystalline material for **2a**-**2g**. P = precipitate, S = solution, PG = partial gel, O= oil.

Compound	Solvent	Procedure	Outcome
2a	Chloroform	Compound **2a** (4 mg) dissolved in chloroform (4 mL) with heat and allowed to cool to ambient temperature. Left undisturbed for 3 days.	P
	Methanol	Compound **2a** (4 mg) dissolved in methanol (3 mL) with heat and allowed to cool to ambient temperature. Left undisturbed for 3 days.	P
2b	1,4-dioxane	Compound **2b** (4 mg) dissolved in 1,4-dioxane (2 mL) with heat and slow-cooled from 100 ^{o}C to 50 ^{o}C over 5 days.	PG
	Methanol	Compound **2b** (2 mg) dissolved in methanol (6 mL) with heat and allowed to cool to ambient temperature. The vial was then covered with pinpricked parafilm and left undisturbed for 5 days to slowly evaporate.	P
2c	DMF	Compound **2c** (4 mg) dissolved in DMF (2 mL) allowed to passively cool to room temperature and left undisturbed for 3 days.	PG
	Ethanol	Compound **2c** (2 mg) dissolved in ethanol (6 mL) with heat and allowed to cool to ambient temperature. The vial was then covered with pinpricked parafilm and left undisturbed for 7 days to slowly evaporate.	P
2d	Chlorobenzene	Compound **2d** (2 mg) dissolved in chlorobenzene (4 mL) with heat and slow cooled from 95 ^{o}C to 50 ^{o}C over 10 days.	P
	Ethanol	Compound **2d** (2 mg) dissolved in ethanol (6 mL) with heat and allowed to cool to ambient temperature. The vial was then covered with pinpricked parafilm and left undisturbed for 7 days to slowly evaporate.	P
2e	Acetonitrile	Compound **2e** (3 mg) dissolved in acetonitrile (5 mL) with heat and slow cooled from 76 ^{o}C to 50 ^{o}C over 7 days.	P
	Ethanol	Compound **2e** (2 mg) dissolved in acetonitrile (8 mL) with heat and allowed to cool to ambient temperature. The vial was then covered with pinpricked parafilm and left undisturbed for 5 days to slowly evaporate, during which a powder precipitate had formed.	P
2f	Nitrobenzene	Compound **2f** (5 mg) dissolved in nitrobenzene (3 mL) with heat and slow cooled from 150 ^{o}C to 50 ^{o}C over 14 days, after which time the solvent was partially immobilised.	PG
	Acetonitrile	Compound 2f (2 mg) dissolved in acetonitrile (7 mL) with heat and allowed to cool to ambient temperature. The vial was then covered with pinpricked parafilm and left undisturbed for 5 days to slowly evaporate.	P
2g	THF	Compound **2g** (2 mg) dissolved in THF (4 mL) allowed to passively cool to room temperature. The vial was then covered with pinpricked parafilm and left undisturbed for 5 days to slowly evaporate.	O
	Acetonitrile	Compound **2g** (4 mg) dissolved in acetonitrile (6 mL) allowed to passively cool to room temperature and left undisturbed for 3 days.	P

Appendix 2 – Supplementary data for Chapter 3

This appendix provides supplementary data and experimental conditions for chapter 3.

SEM Images of Xerogels

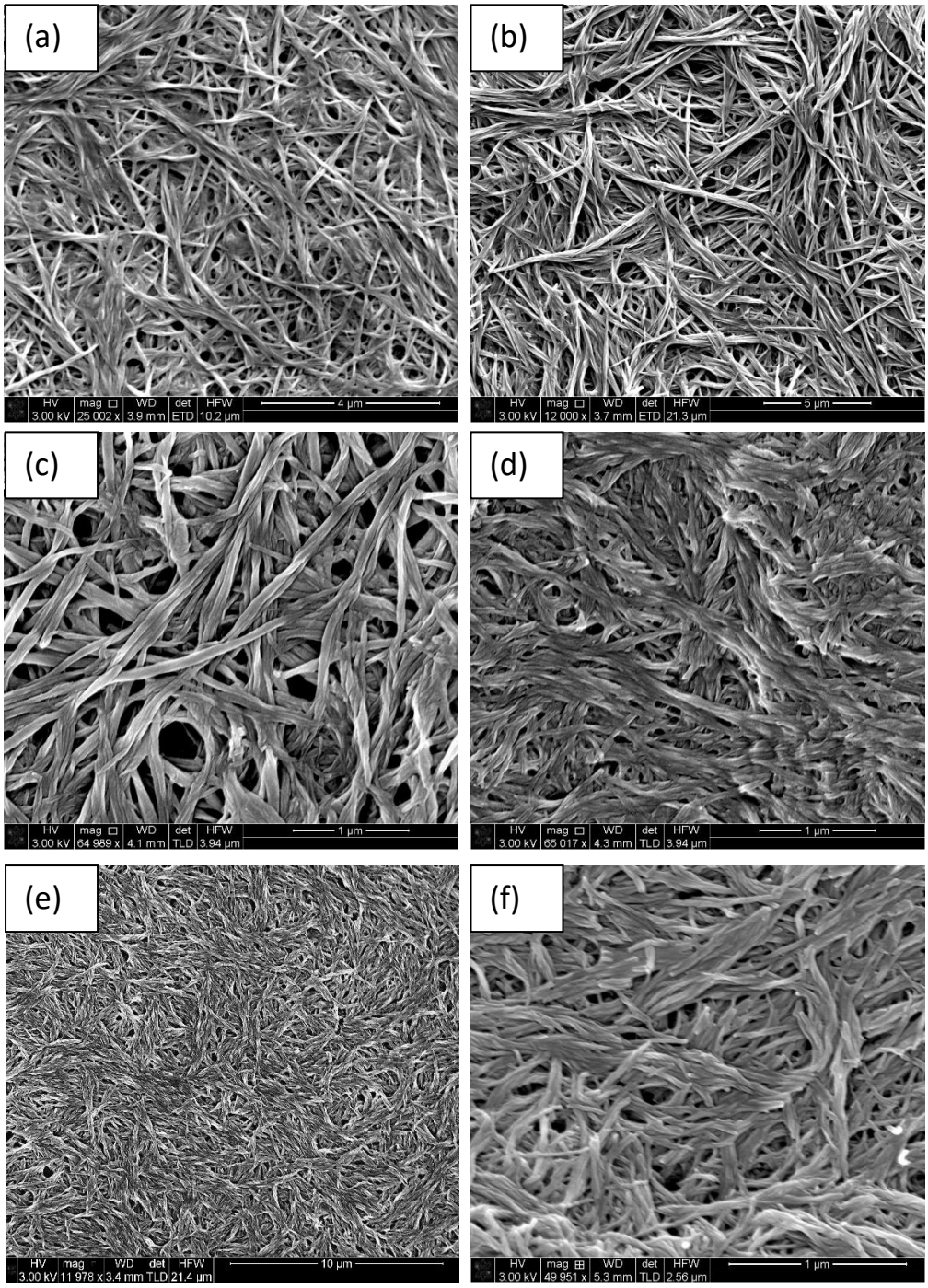

Figure 8-2. SEM Images of the nitrobenzene xerogels of (a) **3.2e**, (b) **3.2h**, (c) **3.1c**, (d) **3.1d**, (e) **3.1e** and (f) **3.1h**. All xerogels were dried down from 1 % w/v nitrobenzene gels of the relevant compound.

AZD-2281 Nitrobenzene Solvate Structure

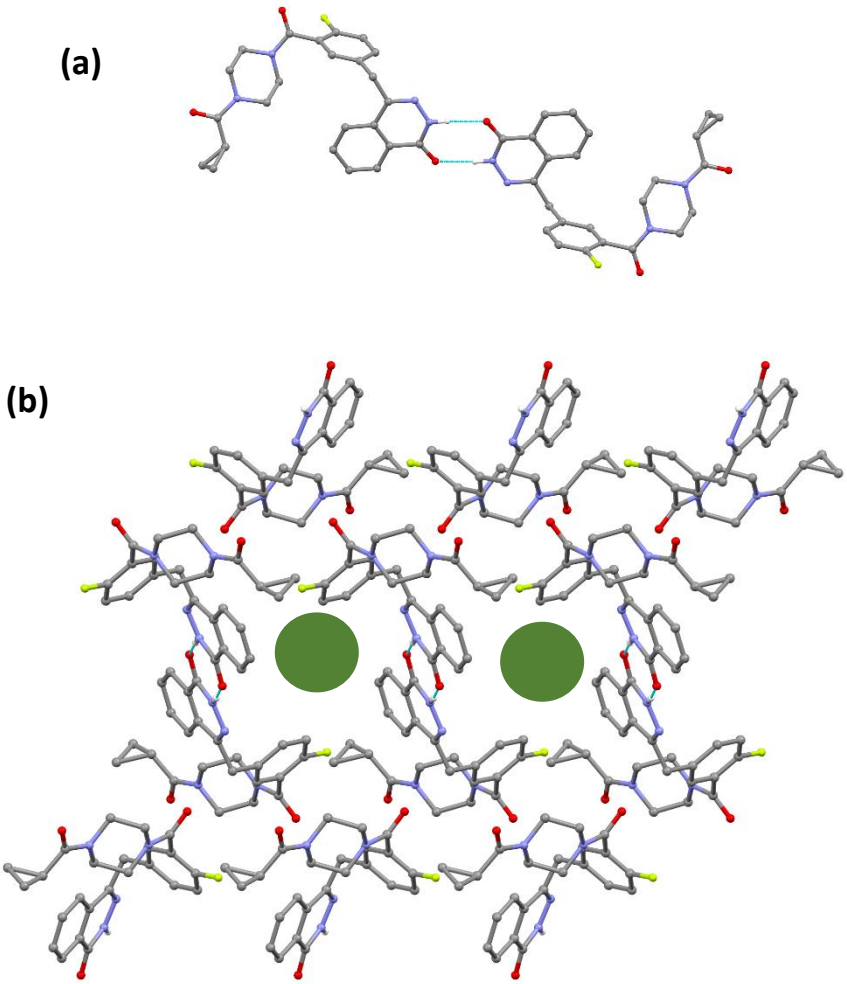

Figure 8-3. (a) Image of the $R_2^2(8)$ dimer formed by molecules of AZD-2281 in the nitrobenzene and isostructural solvates. **(b)** The packing in these solvate structures exhibits the formation of pores which contain disordered solvent molecules (represented by the green circles).

Appendix 3 – Supplementary data for Chapter 5

This appendix provides supplementary data and experimental conditions for chapter 4.

Ball Drop Experiments

Table 8-3. Table showing the T_{gel} values for 1 % w/v propan-2-ol, nitrobenzene and 1,4-dioxane gels of the bis(acyl-semicarbazides). These values were measured through ball drop experiments performed on a 0.5 mL scale. NG = no gel in specified solvent.

Gelator	**T_{gel} / °C**		
	Propan-2-ol	**Nitrobenzene**	**1,4-dioxane**
4.1$_{RR}$	65	130	61
4.2$_{RR}$	40	64	39
4.2$_{Rac}$	NG	54	NG
4.2$_{Benz}$	37	55	NG
4.3$_{RR}$	49	83	42
4.3$_{Rac}$	NG	73	38
4.3$_{Benz}$	43	80	NG
4.4$_{RR}$	56	121	60
4.4$_{Rac}$	NG	99	58
4.4$_{Benz}$	51	109	NG
4.5$_{RR}$	NG	65	42
4.5$_{Rac}$	NG	36	NG
4.5$_{Benz}$	NG	60	40
4.6$_{RR}$	NG	54	NG

Additional solid-state data

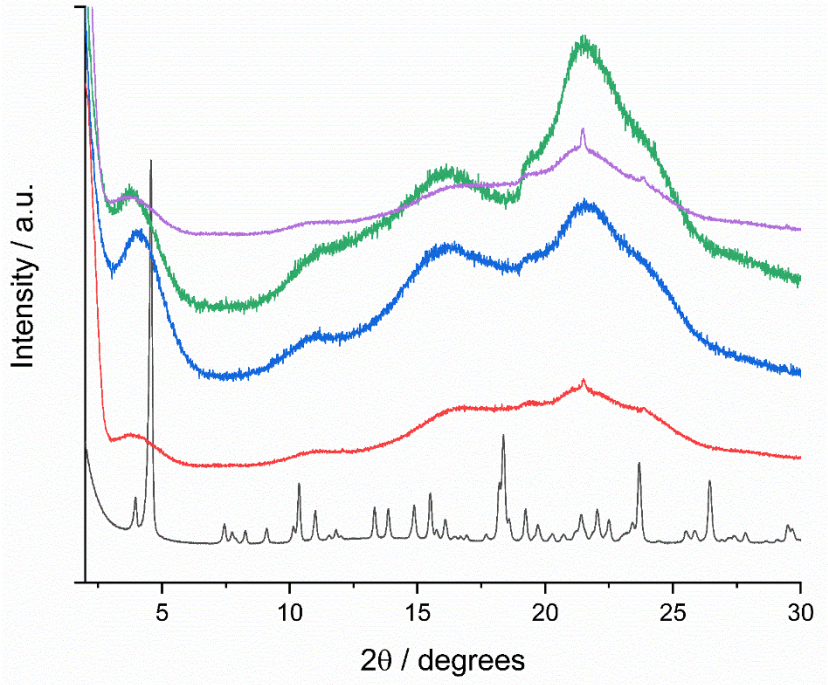

Figure 8-4. The XRPD patterns of xerogels of **4.4**$_{RR}$ from propan-1-ol (purple), 1,4-dioxane (green), nitrobenzene (blue) and acetonitrile (red) compared with the experimental XRPD pattern of the **4.4**$_{RR}$ methanol solvate. The xerogel XRPD patterns are broad but identical to one another. These xerogel samples diffracted insufficeintly for comparison with the crystal forms.

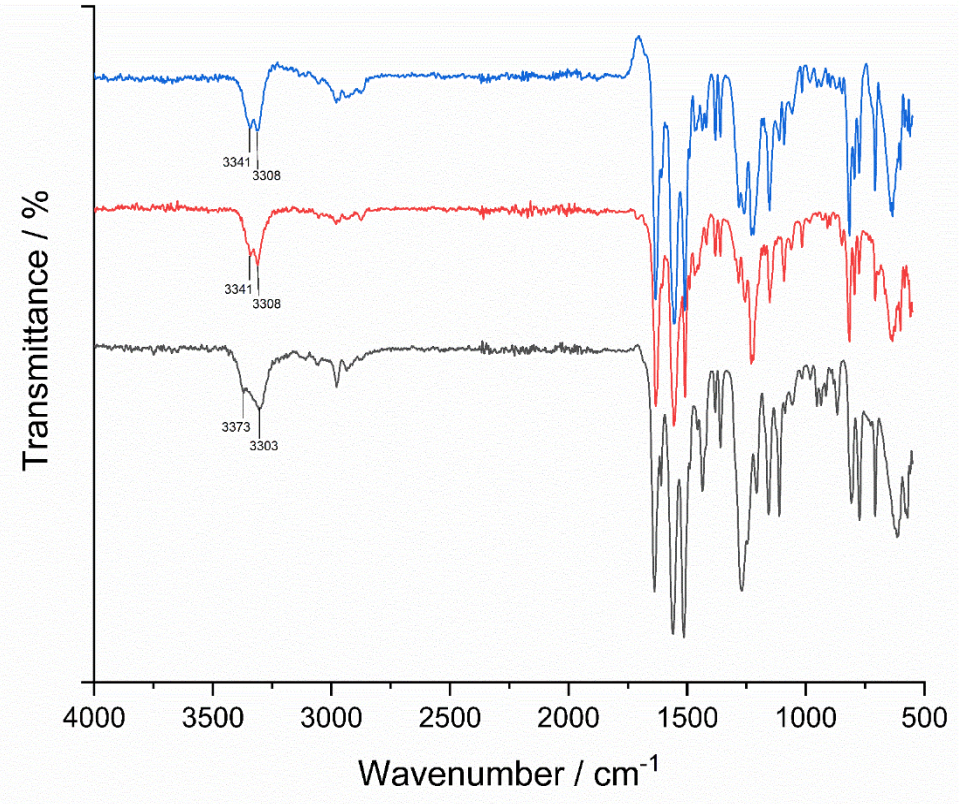

Figure 8-5. IR spectra of the **4.3**$_{SS}$ nitrobenzene xerogel (blue), **4.3**$_{SS}$ solvate single crystal (red) and the **4.3**$_{RR}$ 1,4-dioxane xerogel. The spectra show that the supramolecular interactions in the nitrobenzene xerogel and crystal solvate form are identical, but differ from the 1,4-dioxane xerogel. The difference and similarities are particularly clear when observing the NH stretch peaks aroudn 3300-3400 cm-1, which are labelled with the wavenumber values.

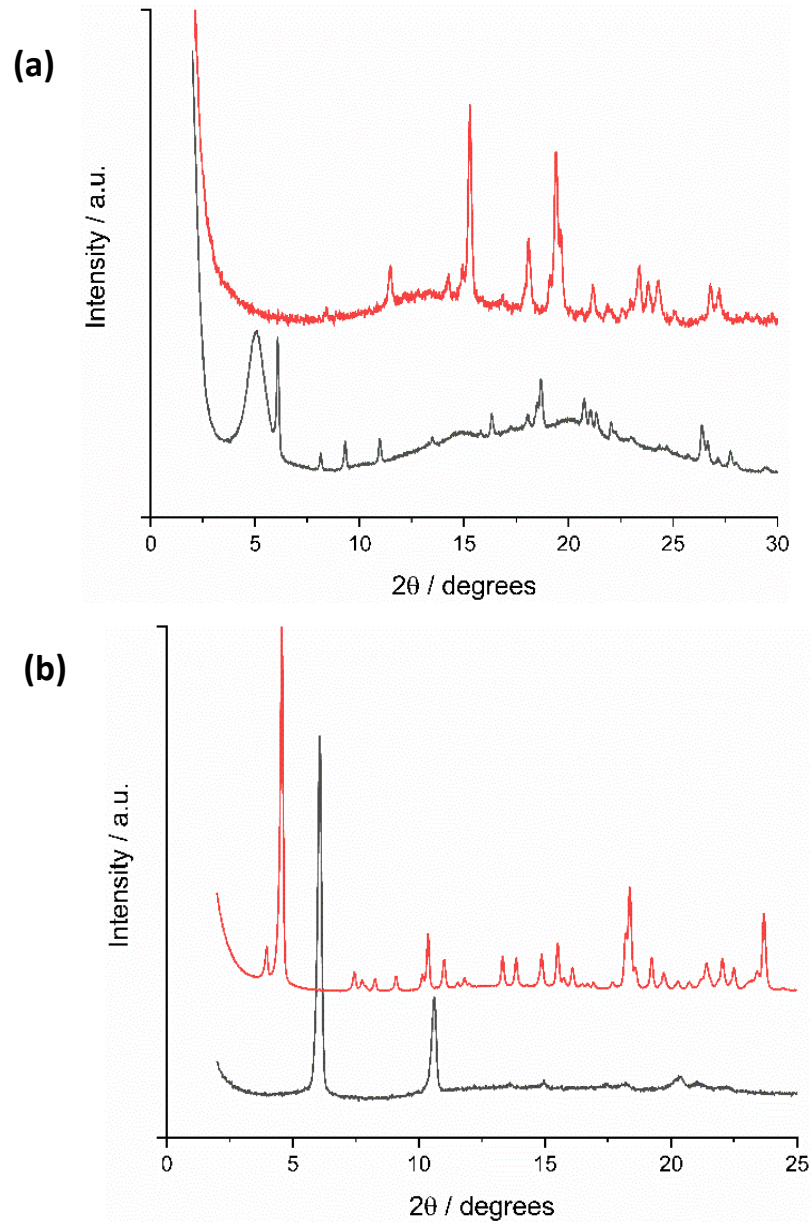

Figure 8-6. XRPD patterns of homochiral 1-phenyethyl xerogels (red) and racemic mixtures of the R,R and S,S enantiomers in 1,4-dioxane for **(a)** 4.3 derivatives and **(b)** 4.4 derivatives. The xerogels were dried down from the 1-butanol gels for each compounds.

Additional SEM Images

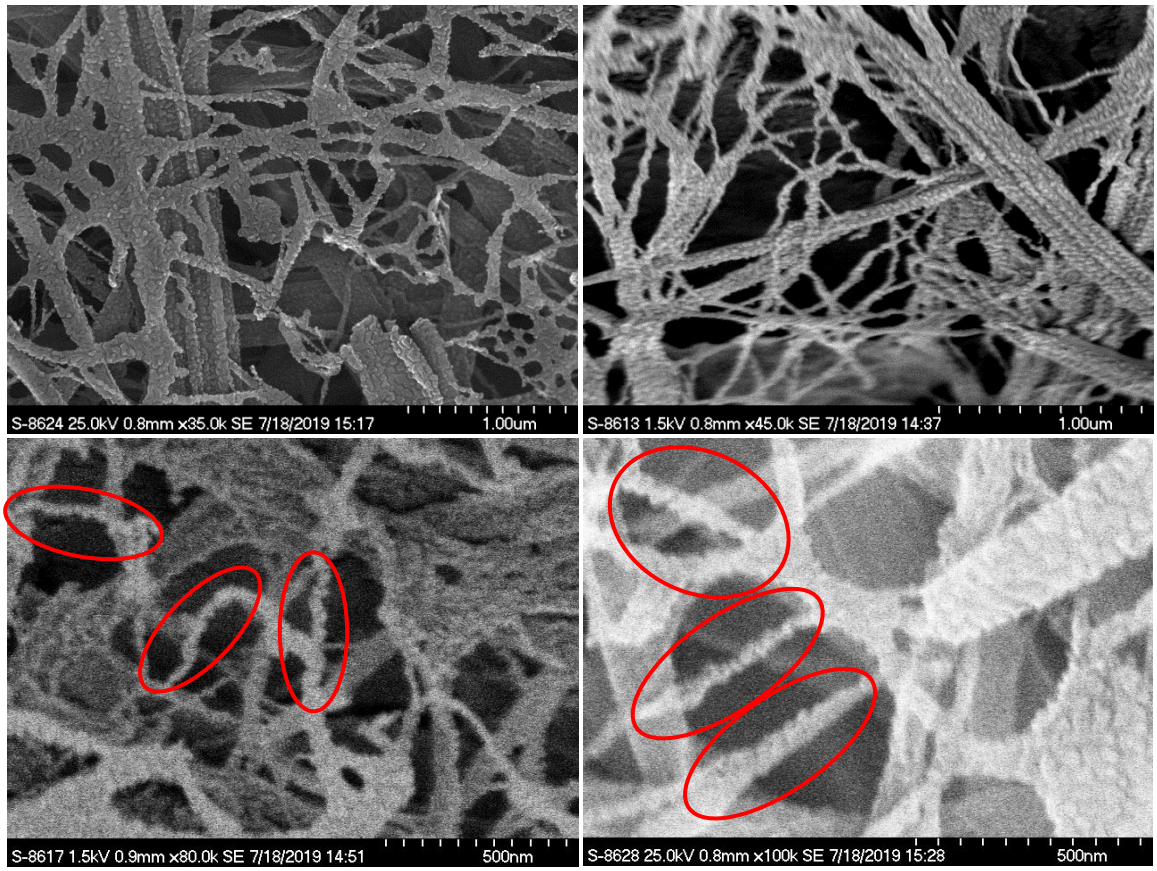

Figure 8-7. Images from cryo-SEM of **4.2$_{RR}$** 1,4-dioxane gels. A sample of the gel was frozen in liquid nitrogen and coated with 2.5 nm chromium prior to insertion into the SEM chamber via a cryo-rod sample holder. As the solvent sublimed, chiral fibres could be observed in real-time (circled in red), however the sublimation and a slight leak in the cryo-rod resulted in a loss of resolution during image collection time.

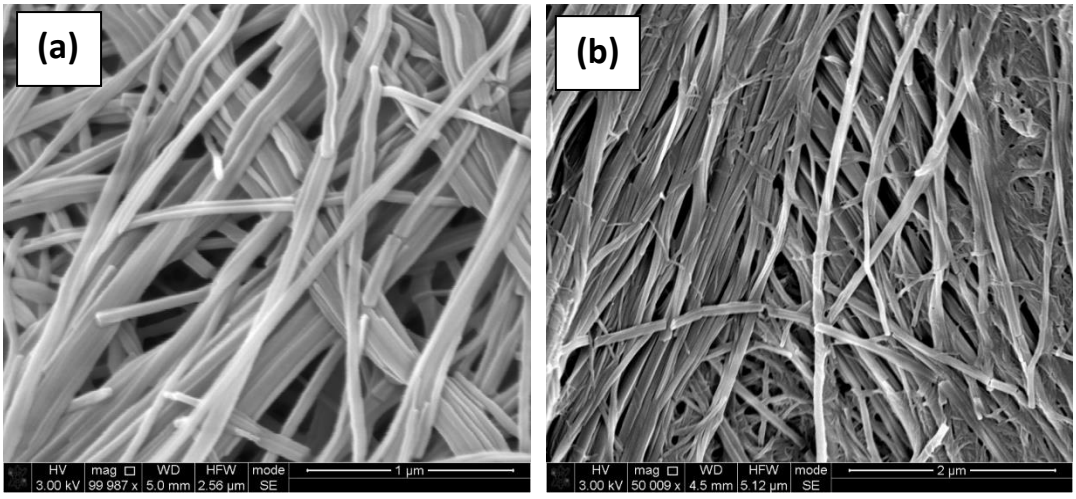

Figure 8-8. Achiral fibres observed in the **4.2$_{RR}$** butan-1-ol (a) and 1,2-dichlorobenzene (b) xerogels.

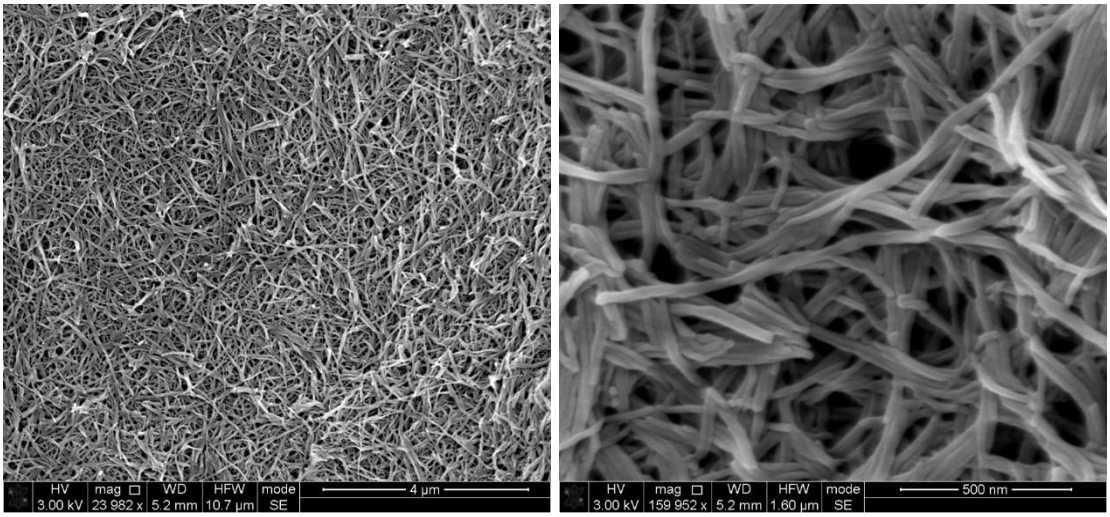

Figure 8-10. Images of a 0.5 % w/v **4.1$_{RR}$** xerogel formed from water. The xerogel reveals fibres with diameter < 100 nm.

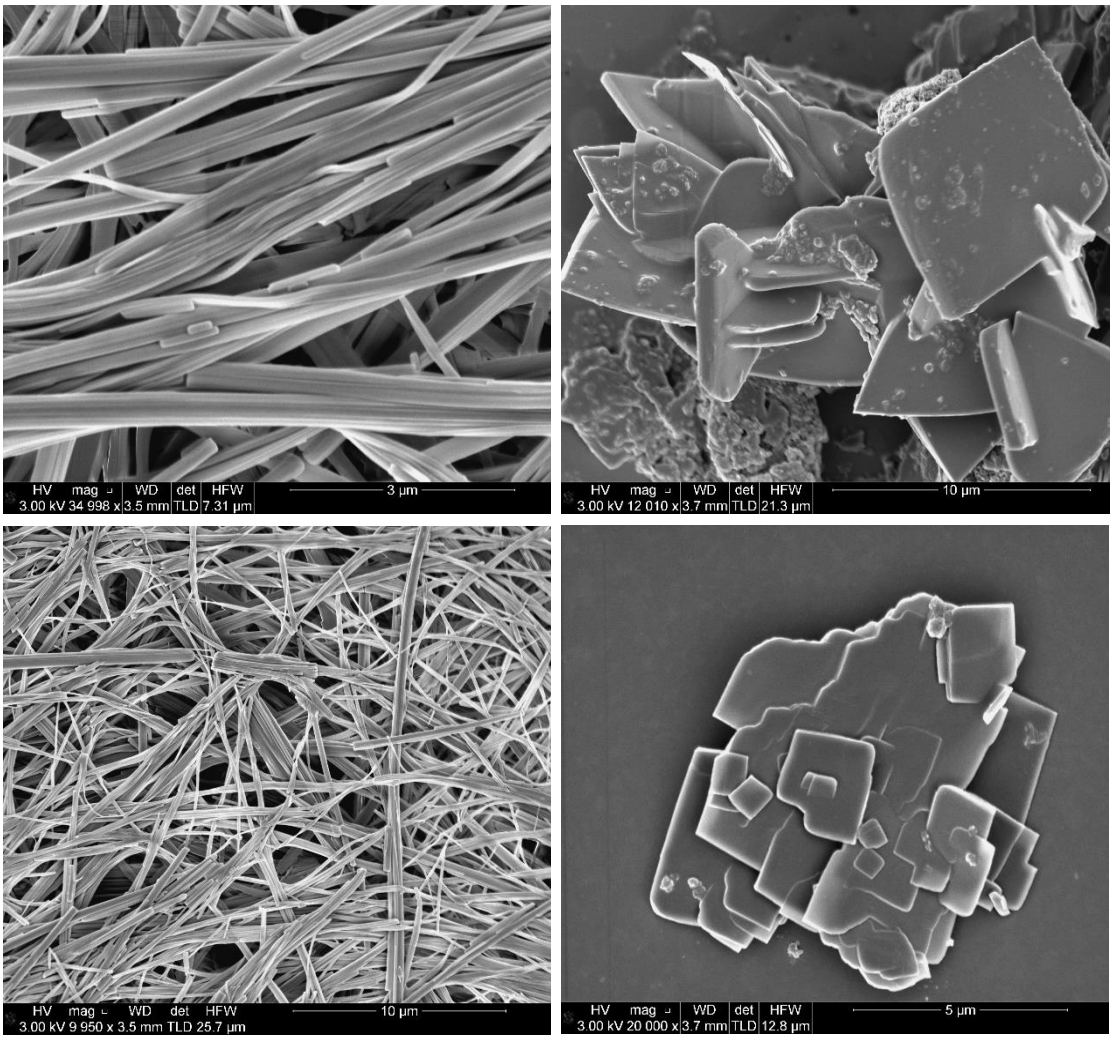

Figure 8-9. SEM images of **(a) 4.5$_{RR}$** xerogel, **(b) 4.5$_{Rac}$** precipitate, **(c) 4.6$_{RR}$** xerogel and **(d) 4.6$_{Rac}$** precipitate all formed from nitrobenzene. The aromatic-spaced bis(acyl-semicarbazides) form similar supramolecular architectures, with the homochiral aggregates both form achiral fibres with a diameter of approximately 1 µM, whilst racemic mixtures form microcrystalline blocks.

Anion Addition

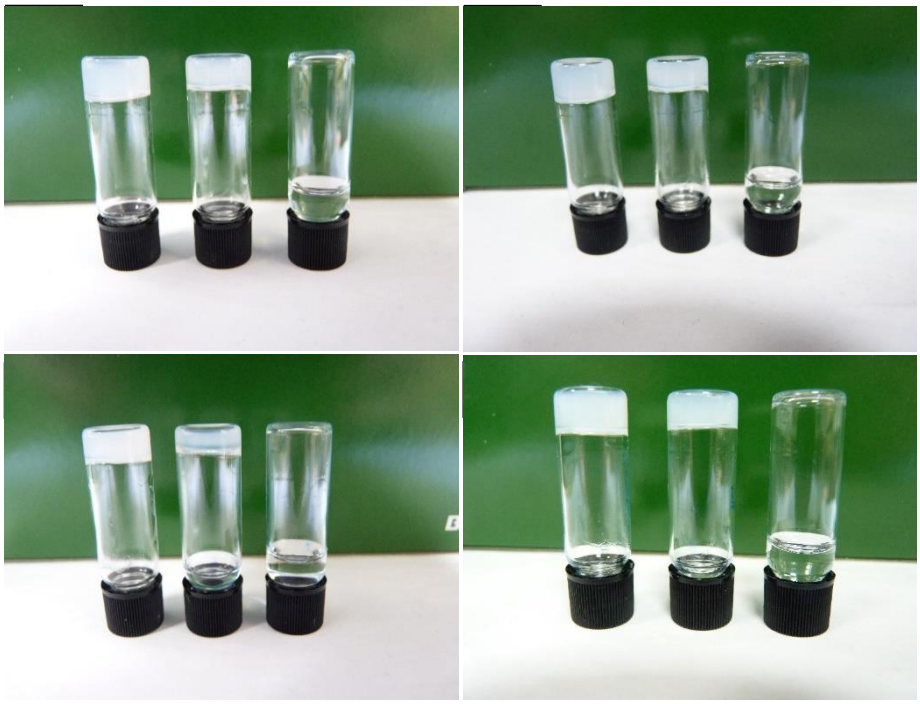

Figure 8-11. Pictures to show the effects of anion addition on gels of **4.2-4.4$_{RR}$**. Each image shows (left to right) gels with no anions added, 0.5 molar equivalents added, and 1 molar equivalent added. All photos were taken 24 hours after anion addition. **(a) 4.4$_{RR}$** 1 % w/v propan-1-ol with TBA fluoride added, **(b) 4.3$_{RR}$** 1 % w/v 1,4-dioxane with TBA benzoate added, **(c) 4.2$_{RR}$** 2% w/v 1,4-dioxane with TBA chloride added, **(d) 4.4$_{RR}$** 1 % w/v chlorobenzene gels with TBA acetate added.

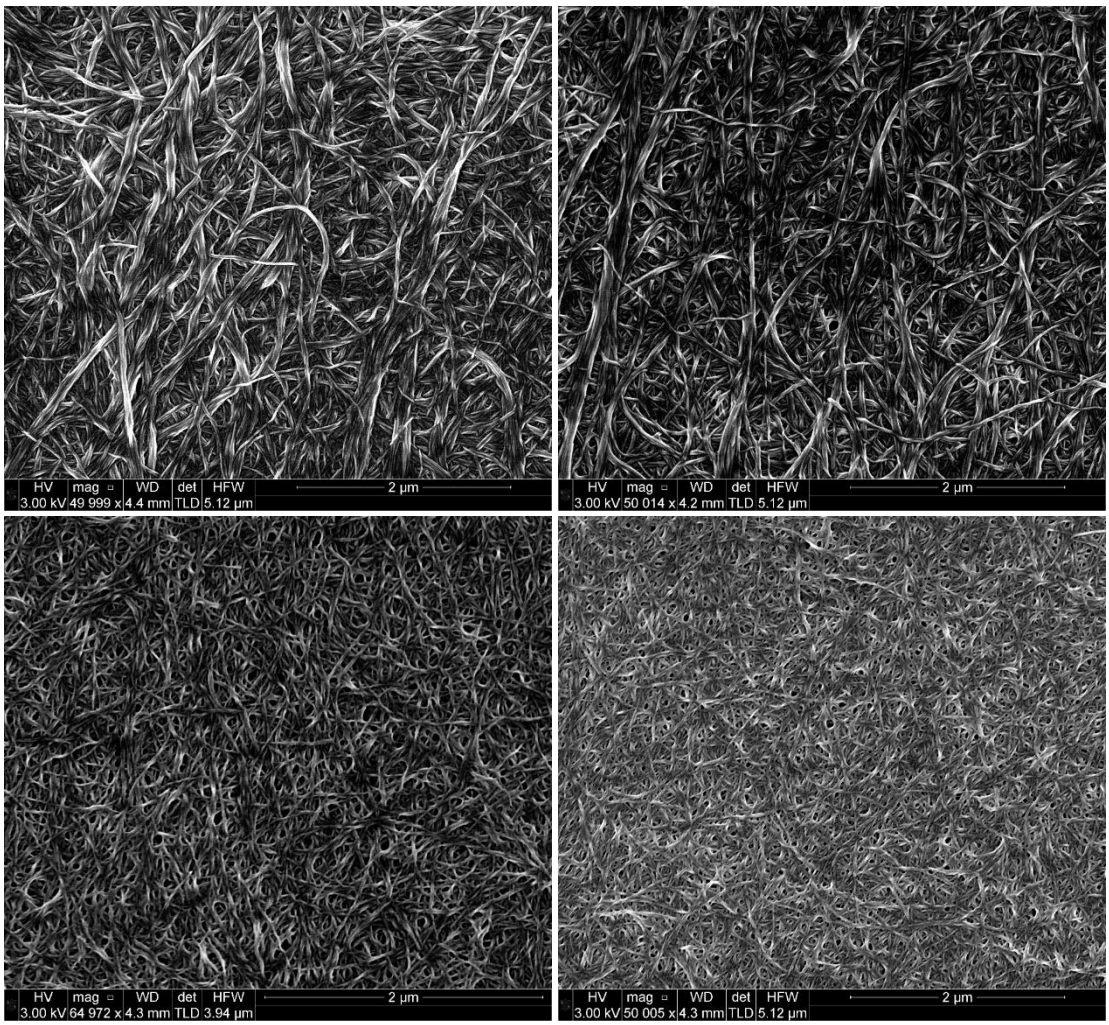

Figure 8-12. SEM images of **4.1$_{RR}$** ethanol xerogel at 1 % w/v with **(a)** no chloride present, **(b)** 0.5 equiv. chloride anions, **(c)** 7.5 equiv. chloride and (d) 10 equiv. chloride. The fibres become thinner in diameter as the chloride concentrations increases, which explains the increased transparency of the gels at high chloride concentrations.